STUDY OF MATERIALS DERIVED FROM $YMnO_3$-MANGANITE AS SOFC ELECTRODES

ZULMA LILIANA MORENO BOTELLO

UNIVERSIDAD INDUSTRIAL DE SANTANDER

FACULTAD DE INGENIERÍAS FISICOQUÍMICAS

ESCUELA DE INGENIERÍA METALÚRGICA Y CIENCIA DE LOS MATERIALES

DOCTORADO EN INGENIERÍA DE MATERIALES

BUCARAMANGA

2018

STUDY OF MATERIALS DERIVED FROM $YMnO_3$-MANGANITE AS SOFC ELECTRODES

ZULMA LILIANA MORENO BOTELLO

IN PARTIAL FULFILLMENT OF THE REQUIREMENTS OF THE DEGREE OF

DOCTOR EN INGENIERÍA DE MATERIALES

ADVISOR

GILLES HENRI GAUTHIER

Ph. D. IN PHYSICO-CHEMISTRY OF SOLID STATE

UNIVERSIDAD INDUSTRIAL DE SANTANDER

FACULTAD DE INGENIERÍAS FISICOQUÍMICAS

ESCUELA DE INGENIERÍA METALÚRGICA Y CIENCIA DE LOS MATERIALES

DOCTORADO EN INGENIERÍA DE MATERIALES

BUCARAMANGA

2018

TABLE OF CONTENT

Pag.

LIST OF TABLES

Pag.

LIST OF FIGURES

Pag.

LIST OF ANNEXES

Pag.

RESUMEN

TÍTULO: ESTUDIO DE MATERIALES DERIVADOS DE LA MANGANITA $YMnO_3$ COMO ELECTRODOS DE CELDAS DE COMBUSTIBLE SOFC*

AUTOR: ZULMA LILIANA MORENO BOTELLO**

Palabras clave: Electrodo, Celdas de Combustible de óxido sólido, Estructura hexagonal, celda simétrica.

Los compuestos $Y_{1-x}A_xMn_xB_yO_3$ (A=Zr, B=Ti) se estudiaron como posibles electrodos en Celdas de Combustible de Óxido Sólido, por su original estructura laminar de simetría hexagonal en la que los átomos de manganeso presentan coordinación bipiramidal trigonal de átomos de oxígeno. Los materiales se prepararon en aire con los métodos de reacción al estado sólido y/o Pechini, a T~1100-1300ºC y se caracterizaron por medio de Difracción de Rayos X y de Neutrones. Con DRX de alta temperatura en aire se pudo establecer la compatibilidad termo-mecánica del $YMnO_3$ (*P*6$_3$*cm*) con el electrolito YSZ, y se observó una transición de fase desde el tipo estructural *P*6$_3$*/mmc* a *P*6$_3$*cm* (T~360°C) para $Y_{0,9}Zr_{0,1}MnO_3$. Medidas de conductividad eléctrica usando la técnica de 4-puntas revelaron que la sustitución de Zr mejora las propiedades de conducción de la matriz $YMnO_3$, quizás como consecuencia de una diferente contribución de conductividad iónica. El estudio por Espectroscopia de Impedancia (EIS) de celdas simétricas en aire, con la configuración LSM/Y_{1-x}ZrxMnO$_3$/YSZ/Y_{1-x}ZrxMnO$_3$/LSM, reflejó una menor resistencia de polarización para el material $YMnO_3$, debido posiblemente a diferencias de orden microestructural entre los materiales; no obstante, el comportamiento en ambos casos se modeló con las misma contribuciones. Se pudo comprobar que los materiales $Y_{1-x}Zr_xMnO_3$ no son estables en atmósfera reductora para T>700°C; por tal motivo se sustituyó Ti en el sitio de Mn. Los materiales $YMn_xTi_yO_3$ (y=0,1; 0.2; 0,3) mostraron ser más estables en atmósfera reductora; específicamente la estequiometría $YMn_{0.6}Ti_{0.3}O_3$ no muestra descomposición hasta 800°C y sigue siendo compatible química y termomecánicamente con el electrolito YSZ. Además, mostró un valor de conductividad intermedio entre $YMnO_3$ e $Y_{0,9}Zr_{0,1}MnO_3$ en aire, aunque experimentan los mismos procesos; en atmósfera anódica la conductividad cae dos órdenes de magnitud por la disminución de concentración de portadores. Los valores de resistencia a la polarización $YMn_{0,6}Ti_{0,3}O_3$ también son superiores a los de $Y_{1-x}Zr_xMnO_3$.

---

* *Proyecto de Grado*

** *Facultad de Ingenierías Fisicoquímicas. Escuela de Ingeniería Metalúrgica y Ciencia de los materiales. Director: Dr. Gilles Henri Gauthier*

ABSTRACT

TÍTLE: STUDY OF MATERIALS DERIVED FROM THE MANGANITE $YMnO_3$ AS SOFC ELECTRODES[1]

AUTHOR: ZULMA LILIANA MORENO BOTELLO[**]

Keywords: Electrode, Solid Oxide Fuel Cells, Hexagonal structure, symmetrical cell.

$Y_{1-x}A_xMn_xB_yO_3$ (A=Zr, B=Ti) compounds were studied as possible Solid Oxide Fuel Cell electrodes, due to the original lamellar structure with hexagonal symmetry of the series, in which the manganese atoms present a trigonal bipyramidal coordination of oxygen atoms. The materials were prepared in air by solid-state reaction and/or the Pechini method at T~1100-1300°C and characterized by X-Ray and Neutron Diffraction. Using High-Temperature XRD, it was possible to establish the thermo-mechanical compatibility of $YMnO_3$ (*P*6$_3$*cm*) and YSZ electrolyte and a phase transition from *P*6$_3$*/mmc* to *P*6$_3$*cm* structure type (T~360°C) was observed for $Y_{0.9}Zr_{0.1}MnO_3$. Four-point probe electrical conductivity measurements revealed that Zr substitution improves the conduction properties of the $YMnO_3$ matrix, possibly due to a different contribution of ionic conductivity. The study using Electrochemical Impedance Spectroscopy (EIS) of symmetrical cells in air, with the configuration LSM/$Y_{1-x}ZrxMnO_3$/YSZ/$Y_{1-x}ZrxMnO_3$/LSM allows to observe that the polarization resistance for $YMnO_3$ is smaller than for $Y_{0.9}Zr_{0.1}MnO_3$, due to microstructural differences; nonetheless, the behavior in both cases were modeled by the same two contributions. We could demonstrate that $Y_{1-x}Zr_xMnO_3$ materials are not stable in reducing atmosphere for T>700°C; for that reason, Ti was substituted for Mn. The $YMn_xTi_yO_3$ (y=0.1, 0.2, 0.3) materials were found more stable in reducing atmosphere than $Y_{1-x}ZrxMnO_3$ compounds; specifically the $YMn_{0.6}Ti_{0.3}O_3$ stoichiometry does no exhibits decomposition up to 800°C and is still chemical and thermomechanically compatible with YSZ electrolyte. In addition, this compound shows an intermediate conductivity values between $YMnO_3$ and $Y_{0.9}Zr_{0.1}MnO_3$ in air, although they experience the same processes; in anodic atmosphere, the conductivity drops two orders of magnitude due to the decrease in the concentration of charge carriers. The polarization resistance values of $YMn_{0.6}Ti_{0.3}O_3$ are also higher than of $Y_{1-x}ZrxMnO_3$ materials.

[*] *Thesis*

[**] *Physicochemical Engineering Department. School of Metallurgical Engineering and Materials Science.*

INTRODUCTION

The increase in global energy requirements continues its vertiginous ascent due to the growth of the population and the improvement of its standard of living. This could cause the demand for hydrocarbon fuels exceeding in 2017 the average of the last decade [1], [2]. In this context, the overexploitation of fossil fuels has become a great concern, taking into account that, in the coming years, total depletion of oil is also expected [2]. As it happens, traditional energy sources continue to release large quantities of pollutants (CO_2, NO_x, CO, SO_2) into the environment and therefore these are considered as directly responsible for the current environmental deterioration [3]–[5].

This complex outlook poses enormous challenges for governments and research institutions, as they must ensure that countries achieve sustainable development by conserving and/or improving the existing quality of life. Consequently, it is essential to seek friendly ways of generating energy that do not compromise the economic or technological position of nations.

Specifically, people from the Latin American region has 93% access to the electricity grid, as a whole; however, in the rural sector only about 70% is covered. The above means that millions of people do not benefit from such service [6].

Colombia, on the other hand, was on the verge of a large energy rationing during 2016 due to the drought caused by the natural phenomenon called “El Niño” which returns every 4 or 5 years [7]. This fact revealed the inability of Colombia’s traditional way of energy production, mainly from hydroelectric sources (70%), to meet the demand. One of the biggest problems of such technology is its strong dependence on climatic phenomena and the dilemma that water should be used essentially for human consumption and agricultural industry. Additionally, during the twenty-first meeting of the Conference of the Parties (COP 21) of the United Nations Framework Convention on Climate Change (UNFCCC), Colombia committed reducing by 20% its emissions of greenhouse gases by 2030 [8], [9].

Therefore, it is evident that Colombia urgently needs a diversification of its energy matrix so that it increases the incorporation of renewable energies (0.2% today) [10], [11]. In this sense, the Unidad de Planeación Minero Energética, UPME, (Energy-Mining Planning Unit from its Spanish name) is planning an optimisation of the matrix, including unconventional sources such as solar or wind, to deal with the increase in energy requirements projected at 3.5% for the following decade [11], [12]. Another factor to take into account by the country, like others in the region, is that the strategy of extending power grids to remote locations cannot be thought of as a financially efficient solution; for this reason, isolated generation systems have become an important option [13].

In recent years, many countries, such as the United States, France, Italy, Spain, Germany, Japan, China, Taiwan, Korea and India, have devoted part of their efforts to the research and/or implementation of Solid Oxide Fuel Cells (SOFC). The above has the objective to try to reduce the use of fossil sources [14] and, at the same time, to diminish the emission of greenhouse gases [15]. These devices are operated from hydrogen or theoretically almost any fossil fuel, generating in the process zero or acceptable CO_2 emissions, respectively [16]. Additionally, SOFC's are basically used as stationary electrical power systems (100-250 kW) [17], which are easily adapted to residential or business areas [18] since they have no moving parts and therefore are very quiet [19]. On the other hand, they can operate for 3000-5000 hours so they are considered durable devices, although it is still needed to increase that duration to 40,000-80,000 hours to make them more competitive [18]. Finally, unlike other stationary generation systems, requiring sources such as wind or solar power, those based on fuel cells do not need to be built in zones with specific properties to operate [20].

Even with all these advantages, fuel cell technology, in general, has only been considered in Colombia by the scientific sector, largely due to their cost and because of the difficulty to change the defined consumption patterns [21]. Thus, amongst the few researches on the subject in this country we can find those that seek the

optimisation of existing devices, those who want to improve the materials or those that study the feasibility of using fuel cells in vehicles or in specific places, as part of what many have called the hydrogen economy [22], [23]. Some important results have been achieved: the development of commercial fuel cells at laboratory scale [21], and the realisation bringing energy to distant locations (1000 km or more) by transporting hydrogen through pipelines could be cheaper than transporting electricity in a conventional manner [24]. Obviously, the above consideration requires to build a robust infrastructure for production, storage and distribution of hydrogen [18]. On the other hand, it was also demonstrated the viability of producing hydrogen in hydroelectric plants to be used in fuel cells, as long as certain problems can be solved [24].

Bearing this in mind, it is not surprising to think that the government should pay more attention to this alternative form of energy production. However, it is important to remember that although hydrogen is one of the most abundant elements on earth [14], it presents the disadvantage that cannot be found isolated in nature and must be obtained from water or hydrocarbons [24]. In fact, hydrogen is currently obtained in 96% from fossil fuels [23]. It means that a complete abandonment of oil is not an easy task. Therefore, to begin the transition towards the extensive use of renewable sources with the use of natural gas (NG) in the anode of a fuel cell has been proposed. This is possible taking into account that one of the main advantage of the Solid Oxide Fuel Cell, among all the other kinds of fuel cells, is their high temperature of operation.

Indeed, Natural gas is considered a clean fuel, highly efficient and is an important Colombian resource, as it is used in thermo-electric plants during periods of drought and most of the homes in Colombia for cooking [25]. The largest reserves were found in 1991 and correspond to the Arauca (Cusiana) and Guajira deposits [7]. By 2011, the limit of the Guajira reserve was reached, which encouraged the development of Cusiana fields which supply grew from 5% to 40% in the period 2006-2014 [7]. It became indeed an issue because in Arauca, petroleum is extracted in the same

place of gas extraction, and priority is not given to NG; the latter is indeed in big part reinjected into the well to pump the crude oil. Moreover, the long periods of droughts, which were not foreseen in recent years, have made the situation critical for NG since 2012. From that moment, importing natural gas from Venezuela or Ecuador became necessary, with the aggravating situation that Colombia lacks robust infrastructure to do it. Fortunately, in 2017, one of the largest natural gas fields called Gorgon-1 has been discovered, in addition to the already existing Kronos-1 and Purple Angel-1 fields. Against all forecasts, such discovery will allow the country to deal with reserves of 4.4 cubic Terafeet providing NG for approximately 10 more years [26], [27].

It can be concluded that, at least now, Colombia is a great candidate to adopt Solid Oxide Fuel Cells within its energy matrix using natural gas. Therefore, it is worth participating in the improvement of these devices which although not completely new, still need work to be considered as optimal.

In particular, the state-of-the-art anode, made of Ni/YSZ (YSZ= Yttria-Stabilized Zirconia), outstands from other materials due to its excellent electrochemical performance when hydrogen is used as a fuel [28], [29]. Nevertheless, in presence of natural gas (or other hydrocarbon fuels of short chain), nickel generally promotes carbon coking and is easily poisoned by the sulphur contained in the fuel, what is detrimental to anode performance [30], [31]. Therefore, the development of Nickel-free anodes is of great relevance in order to solve the issues associated with such metal [31]. Ideally, these new kind of electrode should be able to conduce not only electrons but also oxygen ions (they are therefore referred to as Mixed Ionic and Electronic Conductors) and be efficient, durable, reliable and economically viable.

We chose to take a different way from most of the studies that have been performed in the SOFC area, most of them being focused on perovskite compounds, and $YMnO_3$-based materials, with the same stoichiometry as a perovskite (ABO_3) but with an unusual (five-fold) Mn coordination are studied in this project. In the first part of the manuscript, the structural, transport and electrochemical properties of pure

and Zr-doped $YMnO_3$ compounds are described in order to examine their suitability as electrode materials. In a second step, due to the instability of the first materials in reducing atmosphere, we tried to the stabilize them by Ti for Mn substitution. We thus considered the global objective to use the same material on both sides of a symmetrical Solid Oxide Fuel Cell. In the latter, the same compound can operate for both cathode and anode functions, what means the manufacturing process, maintenance and operation could be significantly simplified in comparison with the classical Solid Oxide Fuel Cell.

1. STATE OF THE ART

1.1 HISTORY OF SOLID OXIDE FUEL CELLS

Fuel cells in general have been developed since the 19th century and their development can be summarized in Figure 1.

i.) Initially, the construction of a simple fuel cell has been attributed to the British chemist Sir Humphrey Davy. However, his work on this subject is not fully documented [18].

ii.) Later, the scientist Christian Schönbein described the reverse-electrolysis process and his work was published in the "Philosophical Magazine" [18], [20].

iii.) Sir William Grove proved that it was possible to produce electrical energy using hydrogen and oxygen. This experiment was called "Gas battery" [18].

iv.) Subsequently, Ludwig Mond and Charles Langer worked on the construction of a practical version of the "gas battery" using air and coal-generated industrial gas and called it a “Fuel cell” [18].

v.) The history of Solid Oxide Fuel Cells specifically began with the demonstration of the ionic conductivity of the most important electrolyte: Yttria Stabilised Zirconia (YSZ) by the scientist W.H. Nernst. At that time, YSZ was known as the "Nernst mass", which was used to replace the carbon filaments of the incandescent light bulbs and only after 30 years this material could be considered as electrolyte in fuel cells [20], [32].

vi.) E. Baur and H. Preis made the first demonstration of a fuel cell constructed from ceramic materials. It used an electrolyte of zirconium oxide (doped with MgO or Y_2O_3), a cathode of Fe_3O_4 and an anode of iron or coal [20].

vii.) The great leap for fuel cells happened during the 1960s when NASA chose these devices to provide electricity to their manned space flights, since they were light, safer than nuclear energy and less expensive than solar.

viii.) At the same time, the development of the ceramic fuel cells continued this time for more practical applications. Thanks to investigation in this field, denser and

thinner electrolytes have been designed to avoid massive waste and in addition, different configurations were tested to stack the cells [18], [20].

Figure 1. Timeline of the history of Solid Oxide Fuell Cells.

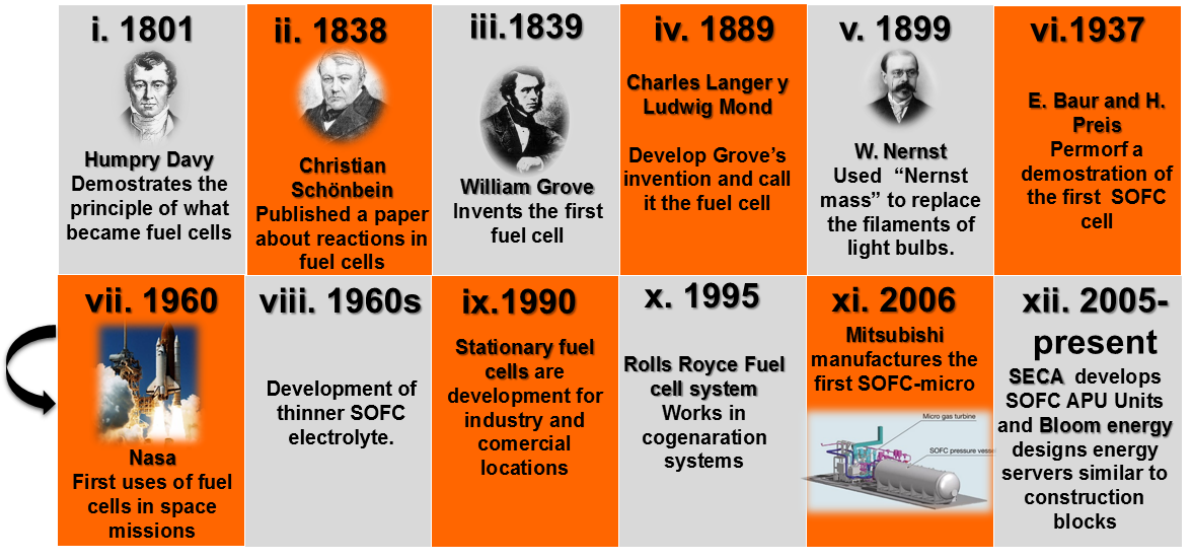

Adapted from [18], [20], [32]

ix.) Modern interest in ceramic cells took place several decades later when companies around the world began a race to bring to market large stationary power systems with SOFC cells for homes, hospitals and general facilities. Thanks to the above, the range of materials for the different parts of the cells was expanded [32].

x.) Rolls Royce focused on creating hybrid co-generation systems with Solid Oxide Fuel Cells using low cost manufacturing techniques [32].

xi.) It was only about a decade later that Mitsubishi succeeded in displaying the first combined cyclic power generation system coupling SOFC and a gas micro-turbine [32].

xii.) During the first years of the twenty-first century, many efforts were dedicated to the development of Solid Oxide Fuel Cell technology and, in addition, great attention has been given to power generation systems for portable applications. These include

SOFC APU (Auxiliary Power units) of the Department of the Energy Conversion Alliance (SECA) in the United States [32]. At the same time, the Bloom Energy company designs servers that produces 200-300 kW and also they can be clustered together in various configurations in order to get hundreds of kilowatts [33]. Some of the current challenges of SOFC technology and the contribution of the present work to overcome them will be discussed later. Before this, an initial description of the devices' main characteristics must be given.

1.2 SOLID OXIDE FUEL CELLS (SOFC)

A Solid Oxide Fuel Cell is an electrochemical device capable of producing energy without the intermediate step of combustion [34], with high efficiency (50-70%, and 80-90% when taking advantage of the cell heat) [24], [35], [36] and with low emissions of pollutants [35], even when using fossil fuels [37]. Generally, a SOFC is constituted of a dense electrolyte between two porous electrodes (anode and cathode); the continuous conversion of chemical to electrical energy is carried out as long as the reactants are continuously supplied: the hydrogen fuel and air fuel, normally [35]. However, it is relevant to say that SOFCs can also operate with simple hydrocarbon fuels (ethanol, methanol, natural gas, liquefied petroleum gas, diesel or biogas) [35], [38]. All the above depend on the chemical, physical and transport properties of the compounds forming the device as it will be described in the following sections of the chapter.

The operation of a Solid Oxide Fuel Cell, when operating with hydrogen (the theoretical fuel) is shown in Figure 2: The electrochemical half-reactions are carried out at each electrode/electrolyte interface since, in general, the electrodes are defined as electrical conductors [20].

Figure 2. Solid Oxide Fuel Cell operation.

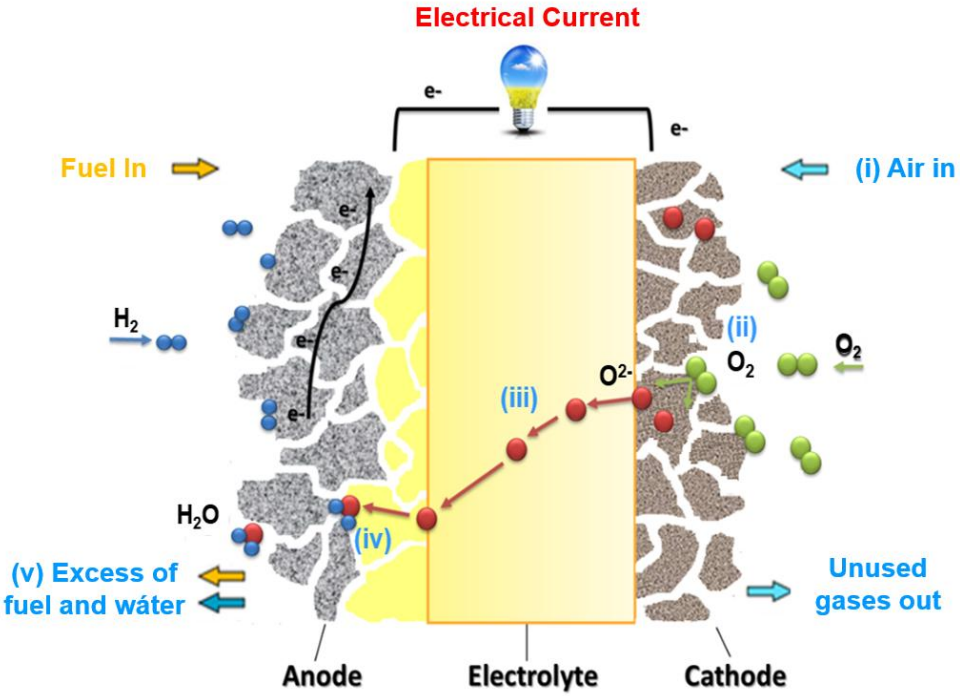

Thus, (i) the cathode is fed with air and (ii) the oxygen molecules are reduced to O^{2-} ions at the cathode/electrolyte interface with the electrons coming from the external circuit. Then, (iii) the anions diffuse selectively through the electrolyte towards the anode, since the difference in oxygen activity between the two gases in the electrodes gives the ions a driving force [35]. At the anode, (iv) O^{2-} ions meet with hydrogen and react catalytically, what occurs normally in the cell regions called “triple phase boundaries” (electrode/electrolyte/gas). (v) As a result, electrons, heat and water in the form of vapour are obtained. At this point, it is important to mention that the kinetics of oxygen ion transport is a thermally active process; hence, enough performance is achieved at the high operating temperatures (600-800°C). However, as will be seen later, this condition brings many problems to SOFC devices [39]. On the other hand, the electrochemical reactions in this process are carried out isothermally and therefore at each electrode separately [18]. When using H_2 (or CH_4), is used, the reactions are summarized in the following equations [34], [40]:

Cathode reaction: $$\frac{1}{2}O_2(g) + 2e^- \leftrightarrow O^{2-} \quad (1)$$

Anode reaction: $$O^{2-} + H_2(g) \leftrightarrow H_2O(g) + 2e^- \quad (2.1)$$

$$4O^{2-} + CH_4(g) \leftrightarrow 2H_2O(g) + CO_2(g) + 8e^- \quad (2.2)$$

Global reaction: $$H_2(g) + \frac{1}{2}O_2(g) \leftrightarrow H_2O(g) \quad (3.1)$$

$$CH_4(g) + 2O_2(g) \leftrightarrow 2H_2O(g) + CO_2(g) \quad (3.2)$$

Theoretically, thermodynamic voltage E_I is related to the variation of the free Gibbs energy $\Delta G^0$of the fuel oxidation reaction, in this way [40]:

$$E_I = -\frac{\Delta G^0}{nF} \quad (4)$$

Where
F is the Faraday's constant,
and n, the number of electrons in the reaction.

When power is applied, this same voltage can be expressed as follows [40]:

$$V = E - RI - \eta_C - \eta_A\ [=]V \quad (5)$$

Where
R is the electrolyte resistance,
η_C, the cathode overpotential,
η_A, the anode overpotential,
and I, the applied current.

The current is defined as [18]:

$$I = jFq = 2Fq \ [=]A \tag{6}$$

Where

j is the number of electrons which are generated from hydrogen

and q, the hydrogen flow

At this point, it is important to make clear that the voltage (or potential difference) and the current density that each fuel cell can provide is in the range 0.5-1 V and ~2000 A m^{-2}, respectively. That's why many cells are generally set in series or parallel to reach the requested power [14], [18].

On the other hand, the ideal performance of the cell when it is operating reversibly with hydrogen and pure oxygen in standard conditions is [40]:

$$\eta_{Ideal} = \frac{\Delta G^0}{\Delta H^0} = \frac{-273.2kJ/mol}{-286kJ/mol} = 0.83 \tag{7}$$

Since the maximum change in Gibbs free energy in standard conditions (ΔG^0) is -273.2 kJ/mol in a hydrogen cell and enthalpy change of the system, called Higher Heating Value (HHV) corresponds to a value of -286 kJ/mol. Meanwhile, the actual yield of the cell is given by Faraday's law which directly relates the current intensity produced in a reaction to the amount of fuel [41], and can be defined as:

$$\eta_{Real} = \frac{Useful\ energy}{\Delta H^0} \tag{8}$$

Then, clearing ΔH^0 from equation *(4)* and replacing in *(8),* we obtain:

$$\eta_{Real} = \frac{Useful\ energy}{\frac{\Delta G^0}{0.83}} \quad (9)$$

Therefore, the real yield can be expressed as the relationship between the voltage of the cell in operation and the ideal voltage; isolating ΔG^0 from equation *(8)* and replacing in *(9),* we have*:*

$$\eta_{Real} = \frac{Useful\ energy}{\frac{-E_I * nF}{0.83}} = \frac{-E_R * nF * 0.83}{-E_I * nF} \Rightarrow \eta_{Real} = \frac{E_R * 0.83}{E_I} \quad (10)$$

Notwithstanding the aforementioned considerations, the values of the potential difference and each cell's yield will deviate from the theoretical values by the following losses [18]:

i.) Activation loss, due to the energy that is spent to catalyse the electrochemical reactions.
ii.) Concentration loss, because of changes in concentration of the reagents in the electrodes.
iii.) Ohmic losses, because of the electrical resistances of the different components of the cell, in particular the electrolyte.
iv.) Losses by internal currents, which are given by the possible flow of electrons through the electrolyte.

Bearing in mind in which way each part of the cell must operate, the characteristics that should be fulfilled in order the cell to be considered as efficient, can be determined. Nowadays, the most common electrolyte is Yttria Stabilized Zirconia (YSZ) which works at high temperature, because it has not very high ionic conductivity at temperatures below 750°C [42]. In addition, the most widely used cathode $La_{1-x}Sr_xMnO_{3-\delta}$ (LSM) presents a higher activity as electrocatalyst at 900°C [42]. However, the Ni/YSZ cermet (composite between YSZ and Ni), anode par

excellence, does exhibit less carbon deposition if SOFC temperature is maintained below 750°C [43]. This discordance between the materials suggests that, despite the many advantages, developing an ideal SOFC requires more research concerning its main components.

1.3 DESCRIPTION OF SOFC ELECTROLYTE

The first thing to know is that the nature of the electrolyte determines the operating temperature of the device and allows the differentiation between the different types of fuel cells [44]. In the particular case of SOFC, the electrolyte is a ceramic compound that separates the electrodes so that the electrochemical reactions are carried out independently [45]. The material from which the electrolyte is made of must meet the characteristics shown below [18], [44]:

i.) Stability at the cell operation temperature.
ii.) High ionic conductivity to allow the diffusion of species from the cathode to the anode and limit ohmic drop.
iii.) Low electronic conductivity in a broad interval of oxygen partial pressure to avoid losses of current.
iv.) High density (over 90% of compactness) to prevent direct contact between reagent gases.
v.) Chemical and thermo-mechanical compatibility with electrodes and interconnect.

Yttria stabilized zirconia (YSZ) is the most famous electrolyte material for an SOFC device; it crystallizes in a cubic fluorite structure and its thermal expansion coefficient (TEC) is 10.9×10^{-6} K^{-1} [46]. This material has sufficiently high conductivity values at temperatures typically above 750°C, explaining why YSZ-based cells generally have to operate at high temperatures (4.59×10^{-2} S cm^{-1} at 800-1000°C) [19], [40], [43]. The operation of the cells in this temperature range allows the use of hydrocarbon fuels and benefits the kinetics of the reactions [18]. However, these conditions

impose the development of electrodes and interconnector compounds with certain specific characteristics for the operation of SOFC devices [40]. The main problem of high temperatures is the rapid degradation of all the components of the cell, particularly the standard cathode [19], [47], [48].

The aforementioned issue points out that it is essential to reduce the operating temperature of the cells to extend the life of the devices [44], [49], reduce the boot time of the cells so that they can be used in portable applications and, as an additional advantage, in order to use more economical materials, in particular, for interconnects [15]. This can be achieved by different strategies: reduce the thickness of the electrolyte [50] or develop electrolyte materials with higher ionic conductivity at low temperatures.

The first solution allows less ohmic losses [50]; however, it is relevant to remember that the smaller the thickness, the more brittle the electrolyte [47]. From the second option has born the SOFC classification according to the operating range of temperature: 500-800°C (intermediate temperatures, IT-SOFC) and 800-1000°C (high temperatures, HT-SOFC). Although at high temperatures the reforming reactions of hydrocarbon fuels are faster [51], IT-SOFCs are now preferred, since they can be used together with metallic interconnects, instead of ceramic. The first ones are usually Cr alloys that have higher electronic and thermal conductivity, and better mechanical properties (even at low temperatures), but they react with the oxygen of the cathode until deactivate it [48]. The electrolytes for IT-SOFC are normally made from doped-ceria, another fluorite material [40], [44], [47]. These include GDC (gadolinia doped ceria), SDC (samaria doped ceria) and YDC (yttria-doped ceria). Amongst these, GDC stands out because such material exhibits a higher conductivity at low temperature than YSZ ($\sigma_{i\text{-}YSZ} \approx 0.02$ S cm^{-1} and $\sigma_{i\text{-}GDC} \approx 0.08$ S cm^{-1} at 750°C) [52]–[54] and its TEC value is 12.7×10^{-6} K^{-1} [46]. Albeit this electrolyte based-Ce are unstable at low oxygen partial pressures and, under reducing atmosphere and high temperatures (T>700°C) suffer a short circuit, due to

Ce^{4+} changes to Ce^{3+} introducing electronical conductivity. For that reason, GDC cannot be used in the high temperature range [43], [55].

In a similar way, another zirconia- based electrolyte has been proposed, specifically SSZ (scandium stabilized zirconia) which is also more conducting than the classic YSZ ($\sigma_{i\text{-}SSZ} \approx 0.1$ S cm^{-1} at 800°C), but presents the disadvantage of having a high cost due to scandium [43].

Additionally, other electrolytes with more complex stoichiometry than the previous ones, have been postulated too; these are: BIMEVOX (derived from $Bi_4V_2O_{11}$ by partial substitution of vanadium; *e.g.* $Bi_2Mg_xV_{1-x}O_{5.5-3x/2-\delta}$ and $Bi_2V_{1.9}Cu_{0.1}O_{5.35}$) [40], [56] and $La_{0.9}Sr_{0.1}Ga_{0.8}Mg_{0.2}O_{3-\delta}$ (LSGM) [43]. Both have higher ionic conductivity than YSZ, even at moderate temperatures ($\sigma_{i\text{-}YSZ} \approx 0.008$ S cm^{-1} and $\sigma_{i\text{-}BiCuVOx} \approx 0.06$ S cm^{-1} at 500°C, $\sigma_{i\text{-}LSGM} \approx 0.03$ S cm^{-1} at 600°C) [53], [57]. However, BIVEMOX family shows low thermodynamic stability in reducing atmosphere [58] and LSGM has the drawback of forming additional phases at low temperature [40], [43]. The thermal coefficient of expansion of these materials are 11.49 x 10^{-6} K^{-1} for LSGM [46] and 16-19 x 10^{-6} K^{-1} for BIMEVOX [59].

To conclude this section, it is worth noting that the decrease of temperature, that is one the main target of SOFC researching, requires the search for better electrode materials. In fact, this is actually the issue that concerns the present work, which consists in studying a new compound that would replace one or both electrodes since, as it will be seen shortly, the materials that are currently used still have several critical problems.

1.4 ELECTROCHEMICAL REACTION MECHANISMS AT THE SOFC ELECTRODES

Taking into account the current challenge of decreasing SOFC operation temperature, it is important to know that as the temperature diminishes, the output voltage also does [44]. The above is because both electrolyte and electrodes' ohmic and activation overpotentials increase, respectively, reducing the electrochemical performance. To improve this behaviour, the reaction mechanisms at the interface between the electrode and the electrolyte have to be studied.

In general, for each electrode/electrolyte couple the limiting steps of the reaction depend on [47]:

i). The nature of the electrode compound: electronic or mixed conductor. In the first case, the compound only allows the flow of electronic charges. Therefore, the electrochemical half reactions can only be carried out at the electrode/electrolyte/gas triple points of contact [47], when the gaseous reactant enters the pores of the electrode and meets the electrode/electrolyte interface. On the other hand, the MIEC-type materials can conduct both ionic and electronic charge carriers [60]. Thus, the material carries electrons to the interconnect and at the same time the O^{2-} anions can follow their way through the bulk of the mixed conductor [61]. Therefore, such kind of electrode exhibits an electrochemical reaction delocalized on the entire electrode surface [40]. In this way, as will be seen in this section, some limiting steps of the reaction occurs simultaneously in a MIEC and, consequently, the polarization resistance is generally lower than for pure electronic conductor, *i.e.* the first kind of electrode has better performance [62]. Another important thing concerns the fact that for the compound to be considered as MIEC, the two conductivities must be in the minimum range of 10^{-4}-10^{-3} S cm^{-1}, or ideally it must reach an ionic conductivity of 0.1 S cm^{-1} and an electronic conductivity of 100 S cm^{-1} [63], [64].

ii). Temperature, oxygen partial pressure in the gas phase or carrier gas: since some limiting steps could be faster or (lower) depending on temperature or oxygen partial

pressure value. In addition, also some steps can be easily identified due to their impedance response increases when carrier gas change [47]
iii). Electrode morphology: different values of thickness, porosity or grain size can hinder (or promote) the apparition of one of other limiting step [44], [65]

Additionally, it is important to know that the mechanisms occur in several steps, in series or parallel, and some of them can be produced simultaneously. However, under some conditions, it is possible to suppose that the general rate reaction only depends on the rate of a few (limiting)-step, while others are considered infinitely fast and kept at thermodynamic equilibrium.

First, at the **cathode** side, the oxygen reduction reaction is carried out following the next global equation, in which three phases are included: oxygen gas, electrons from the electrode and electrolyte vacancies [47]:

$$\frac{1}{2}O_2^{gas} + 2e^{\prime,electrode} + V_o^{\bullet\bullet,electrolyte} \rightleftharpoons O_O^{\times,electrolyte} \qquad (11)$$

The limiting steps of the oxygen reduction reaction are depicted in Figure 3 and are discussed below [44], [47].

i). Molecular diffusion in free phase gas and/or inside electrode porosity, *i.e.* matter transport to gas/electrode interface:

$$O_2^{gas} \Leftrightarrow O_2^{Interface} \qquad (12)$$

ii). Adsorption/Desorption of molecular oxygen, which could be carried out in two steps: non-dissociative adsorption *(13)* and subsequent dissociation *(14)*. If *s* is an available adsorption site on the surface, we have:

$$O_2^{Interface} + s \Leftrightarrow O_2^{ad} \quad (13)$$

$$O_2^{ad} \Leftrightarrow 2O^{ad} \quad (14)$$

Figure 3. Limiting steps for the Oxygen Reduction Reaction.

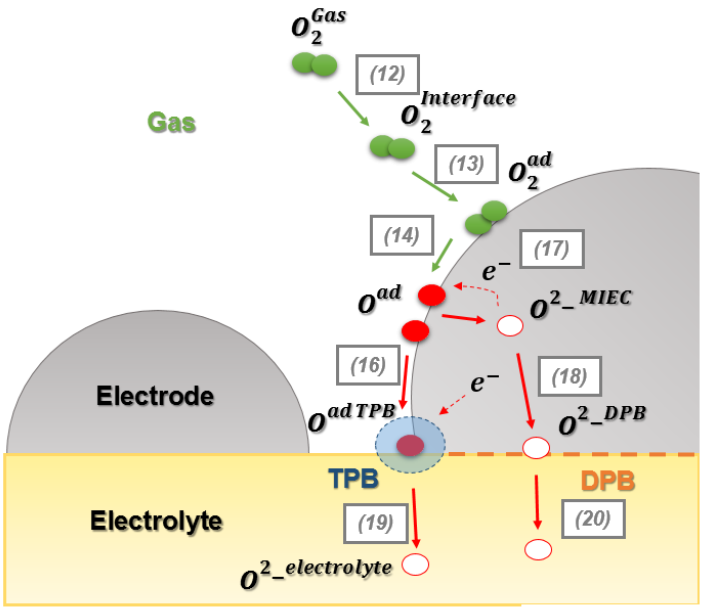

Adapted from [47]

However, a unique step for dissociative adsorption can also occur, as described by:

$$\frac{1}{2}O_2^{Interface} + s \Leftrightarrow O^{ad} \quad (15)$$

iii). Transport of oxygen and/or electroactive species toward electrode/electrolyte interface. This step strongly depends on the nature of the electrode. If the electrode material can only condut electrons, adsorbed oxygen diffuses through electrode surface up to TPB *(16)*.

$$O_2^{ad} \Leftrightarrow O_2^{ad,\mathrm{TPB},} \quad (16)$$

On the other hand, if the electrode compound can conduct electrons and ions, adsorbed oxygen is directly incorporated to the electrode by a charge transfer reaction *(17)* and then diffuse to electrode/electrolyte surface (double phase boundary, DBP) *(18)*.

$$O_2^{ad} + V_O^{\bullet\bullet,MIEC} + 2e'^{,MIEC} \Leftrightarrow O''^{,MIEC} + s \qquad (17)$$

$$O_2''^{,MIEC} \Leftrightarrow O_2''^{,DPB} \qquad (18)$$

iv). Oxygen incorporation into the electrolyte. In the same way, if electrode is a pure electronic conductor, this step needs a charge transfer reaction:

$$O^{ad,TPB} + V_O^{\bullet\bullet,electrolyte} + 2e'^{,electrode} \Leftrightarrow O''^{,electrolyte} + s \qquad (19)$$

However, if the electrode conducts electrons and ions, charge transfer already occurred and therefore only an ionic transfer at the electrode/electrolyte interface (DPB) is necessary:

$$O''^{,DPB} + V_O^{\bullet\bullet,electrolyte} \Leftrightarrow O''^{,electrolyte} \qquad (20)$$

At the **anode** side, the oxidation of hydrogen is carried out according to the next global reaction [62]:

$$H_2^{gas} + O''^{,electrolyte} \rightleftharpoons H_2O + 2e'^{,electrode} \qquad (21)$$

The limiting steps of this reaction in a cermet (composite made of ceramic and metal) and in a MIEC (Mixed ionic and electronic compound) are depicted in Figure 4 and are discussed below [62], [66]:

i.) Molecular diffusion in free phase gas and/or inside electrode porosity, *i.e.* matter transport to gas/electrode interface, according to:

$$H_2^{gas} \Leftrightarrow H_2^{Interface} \qquad (22)$$

Figure 4. Limiting steps for Hydrogen Oxidation Reaction in (a) Cermet material and (b) MIEC compound.

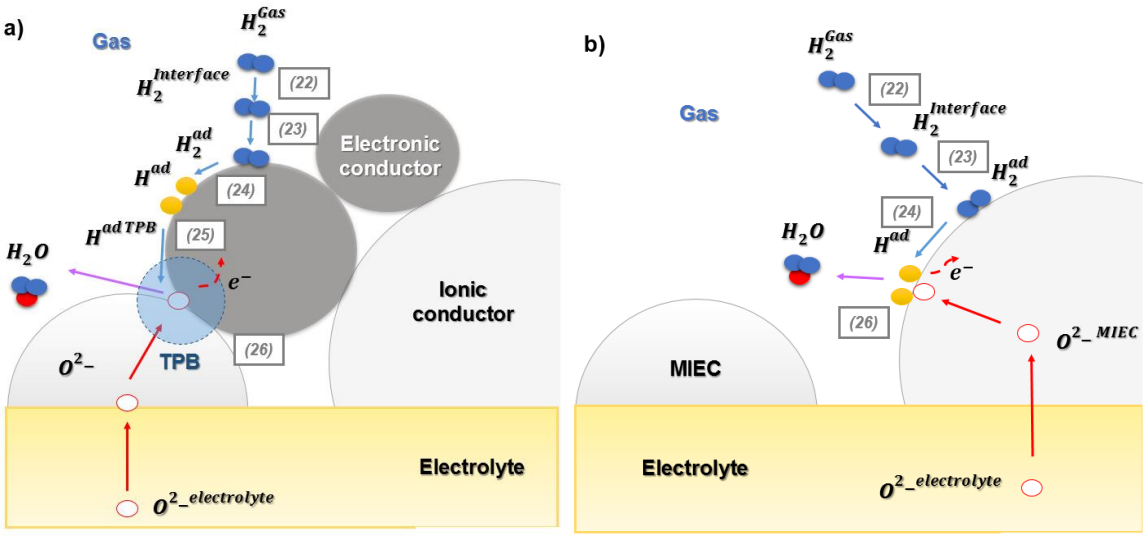

ii.) Adsorption of hydrogen at an *s* available site on the surface *(23)* (in the metal of cermet material or over the MIEC surface) and the dissociation *(24)*:

$$H_2^{Interface} + s \Leftrightarrow 2H^{ad} \qquad (23)$$

$$2H^{ad} \Leftrightarrow 2H^{\bullet,ad} + 2e' \qquad (24)$$

iii.) Hydrogen diffusion through electrode surface to the electrode/electrolyte interface (TPB) *(25)*.

$$H^{ad} \Leftrightarrow H^{ad,\mathrm{TPB}} \qquad (25)$$

iv.) Electronic transfer to the electrode

$$O_O^X + 2H^{ad} \Leftrightarrow H_2O + 2e'^{,electrode} + V_O^{\bullet\bullet,electrolyte} \qquad (26)$$

As a concluding point concerning the reaction mechanisms at the cathode/anode, it is worth noting that most of the efforts concerning the search of new materials has been devoted during the last decade to MIEC materials, that are theoretically the best option for such application and would avoid the use and optimization of composite electrodes.

1.5 CHARACTERISTICS OF THE SOFC CATHODE

In general, the cathode (or air electrode) is a porous but conducting ceramic material in charge of the oxygen reduction which must have the following properties [35], [67]:
i). Chemical and dimensional stability under operating conditions (high temperatures and oxidizing atmosphere) [67].
ii). Chemical and thermo-mechanical compatibility with electrolyte and interconnect [35].
iii). High electrical conductivity, possibly mixed between ionic and electronic (see below) considering that the main function of the electrode is to transfer electrons from the current collectors to the reaction sites [67].
iv). Electrocatalytic activity for the dissociation and reduction of oxygen molecules [35].

Usually, the cathode is made of noble metals or complex oxides. However, the high price of the former restricts its use in such devices. Consequently, most of the research has focused on the analysis and characterization of complex oxides, essentially of perovskite structure (ABO_3 stoichiometry). Many of these oxides have shown several of the expected cathode characteristics, such as thermal and mechanical stability, and compatibility with the electrolyte [42].

Initially, $LaMnO_3$ compound has been considered. Such material exhibits a thermal expansion coefficient of 11 x 10^{-6} K^{-1}, which is compatible with the TEC values of most common electrolytes and therefore does not induce dimensional issues [67]. When it is doped with divalent elements such as Ca and Sr in replacement of La, the electrical conductivity increases because Mn in these conditions adopts a mixed valence +3/+4, which allows the electronic hopping by a small polaron-type mechanism [35]. In fact, the family $La_{1-x}Sr_xMnO_{3-\delta}$ (LSM) are considered the most important cathode materials, since it is stable in an oxidizing atmosphere, its TEC is close to that of the YSZ electrolyte and its electronic conductivity is between 200-300 S cm^{-1} at 900°C [42]. However, LSM has shown high electrode polarization, therefore a mix with the YSZ electrolyte has been prepared in order to increases the reaction sites [43].

Later, compositions where the B site (*i.e.* Mn) has been totally or partially substituted have also been developed, especially using other transition metals like Fe or Co, [67]. First, the materials of the $La_{1-x}Sr_xCoO_{3-\delta}$ type (LSC) exhibit high oxygen diffusivity because such system can show a large concentration of oxygen vacancies, particularly interesting to generate a mixed ionic and electronic conductivity. Additionally, LSC has a high electronic conductivity (1600 S cm^{-1} at 800ºC). However, it is incompatible with many electrolyte materials since its TEC has a value almost twice that of YSZ and because both compounds react at high temperature [35], [67]. For its part, compounds with stoichiometry $La_{1-x}Sr_xFeO_{3-\delta}$ (LSF) have a lower coefficient of thermal expansion than their predecessors, but

exhibit a decrease of electronic conductivity [20]. Usually, potential cathodes including La or Sr react chemically with YSZ to form non-conducting phases; for this reason, the use of different electrolytes has been proposed. One of them is $LaGaO_3$ which seems to have better chemical compatibility with (La, Sr) perovskites, though existing cationic interdiffusion leads to long-term instability [67]. Another considered electrolyte is GDC (Gd-doped ceria) with which these materials do not present reactions, but as already mentioned, the devices are restricted to low temperatures [68].

The combined stoichiometry $La_{0.6}Sr_{0.4}Co_{0.2}Fe_{0.8}O_{3-\delta}$ (LSCF) achieves good values of ionic and electronic conductivity (around 10^{-2} and 10^{2} S cm^{-1} at 800°C, respectively); nonetheless, it still has a high TEC value (13.5-14.8 x 10^{-6} K^{-1}), and because of that, it is in the limit of thermomechanical compatibility with the most common electrolytes [35], [42], [69]. In general, strontium substitution in $La_{1-x}Sr_xCo_yFe_{1-y}O_{3-\delta}$ family increases the oxygen vacancy concentration, while cobalt doping increments the electronic conductivity although increases also the thermal expansion coefficient bringing mechanical problems [69].

In the last decade, an increasing interest has been observed in the study of materials derived from perovskite, in particular with layered structure. This is the case for the oxygen vacancy ordered double perovskites ($AA'B_2O_{5+\delta}$) like $NdBaCo_2O_{5+\delta}$, $GdBaCo_2O_{5+\delta}$, or $SmBaCo_2O_{5+\delta}$. In those materials, oxygen vacancies are stabilized and confined to the LnO plane, because the weak bonding energy of the Co-O bonds allows easy oxygen diffusion [70]. Likewise, these have more satisfactory conduction properties than perovskite compounds; therefore, they have better electrochemical performance. Despite these numerous attributes, double perovskites exhibit a high coefficient of thermal expansion compared to the most usual electrolytes, their long-term stability is low and cobalt its expensive [70]–[72]. However, in a $Pr_{1-x}BaCo_2O_{5+\delta}$ compound, the Pr content induce the reduction of TEC and polarization resistance values at the expenses of decrement of the electrical conductivity [73]. Another

optional double perovskite cathodes are the B site substituted $LnBaCo_{2-x}Fe_xO_{5+d}$ (Ln= Nd and Gd) system. This substitution reduces the TEC value that is a determinant disadvantage of double perovskites [74]. However, when Fe content increases in these compounds (oxygen and Co^{4+} concentrations decrease) there is a reduction of carrier concentration, whereby electrical conductivity and general electrocatalytical activity diminish [72], [74].

Other cathode materials that have been considered are those belonging to the Ruddlesden-Popper series (stoichiometry $A_{n+1}B_nO_{3n+1}$) which are layered structures formed of alternating perovskite and rock salt layers. Specifically, the $La_{n+1}Ni_nO_{3n+1}$ series (*n*= 1, 2 and 3) have been investigated as SOFC cathode. As *n* increases in these materials, the polarization resistance decreases (at 800°C) and conductivity increases (500-700°C), since there is an increment of the number of conduction pathways if increasing the thickness of the perovskite block within the structure [75]. However, this family has shown poor performance compared to LSM and LSF [76], and exhibits noticeable chemical reactivity with GDC and LSGM [77]. Particularly, $La_2NiO_{4+\delta}$ (*n*=1) presents a higher ionic conductivity than perovskites, has a reasonable electrical conductivity (~100 S cm^{-1}) and the TEC value (~13.4 x 10^{-6} K^{-1}) close to those of GDC and LSGM electrolytes; however, the compound is unstable in long-term operation and it seems to react with GDC [76].

After this revision, it becomes evident the importance of looking for SOFC cathodes that can be in particular chemically and thermomechanically compatible with existing electrolytes.

1.6 REQUIREMENTS OF THE SOFC ANODE

As for cathodes, anode materials must also be porous and conducting [35], and globally, they must fulfil the following characteristics:

i). Chemical and dimensional stability under operating conditions (high temperatures in reducing atmospheres) and during cycles in which the atmosphere abruptly changed from oxidizing to a reducing (redox cycles) [35], [78].
ii). Thermomechanical and chemical compatibility with electrolyte and interconnects, to preserve the electrode/electrolyte interface [42], [78].
iii). High electrical conductivity over a wide range of pO_2, and if possible with both electronic and ionic components [35].
iv). High reforming catalytic activity (if fuel is different from hydrogen) [35], [42] and electrocatalytic activity for hydrogen oxidation.

For many years, the interesting combination of properties of the Ni/YSZ cermet (a composite between nickel and YSZ ceramic) has made it the quintessential anode since it has high electrochemical performance [79], high porosity and a coefficient of thermal expansion similar to YSZ electrolyte [44]. This is achieved because Ni catalyses the oxidation of the fuel and promotes electronic conductivity, while YSZ allows ion conduction and thermomechanical compatibility with YSZ electrolyte [42]. However, this composite presents many disadvantages for long-term operation or considering complex fuels that make it unsuitable. With time, Ni tends to agglomerate causing the conductivity to decrease one third [42], [48], and if realistic hydrocarbon fuels are used, cermet is prone to sulphur poisoning [34], [42], [78]. Additionally, when the steam content is low, Ni can catalyse the formation of coke and cause clogging of the anode pores, resulting in a decrease in active sites for electrochemical reactions [42], [48], [80]. Likewise, another problematic aspect of this cermet is its inability to withstand the changes of temperature and atmosphere (redox cycling) that would occur during the start-up and, eventually, during the cleaning of SOFC devices [81]. This is because of the dramatic chemical expansion when Ni is re-oxidised to NiO and inversely, volumetric contraction when reduced again, *i.e.* the redox cycles are difficult to manage without deteriorating the Ni/YSZ cermets [48].

To lead to a decrease in the numerous drawbacks of Ni, the replacement by Cu has been explored. Therefore, a composite being more resistant to hydrocarbons and with large tolerance to sulphur has been obtained [35]. However, Cu/YSZ causes the cell to have poor performance and creates problems during the fabrication of the device, since it is not very thermally stable (due to the lower melting point of Cu) [35], [82]. Then, in order to improve the poor performance of the material, it has been necessary to incorporate ceria (CeO_2), leading to a Cu/CeO_2/YSZ combination. Such material turns out to have better properties because cerium oxide is able of conducing both O^{2-} ions and electrons in reducing conditions [35], [83]. Similarly, some authors reported that adding a Cu/CeO_2 layer between the electrolyte and Ni/YSZ would help to suppress carbon deposition [82].

Given the relative success of the latter case, and in particular the use of ceria at the anode, composites such as Ni/GDC and Ni/SDC (samarium doped ceria) were also tested; both showed good conduction properties when used in conjunction with LSGM electrolyte ($La_{0.9}Sr_{0.1}Ga_{0.8}Mg_{0.2}O_{3-\delta}$). However, with these combinations, the formation of insulating phases was observed as a result of a strong reaction of Ni with the electrolyte [35]. Nevertheless, if a cermet containing Ni-GDC/LSGM is used it is possible to eliminate coke formation [35]. Despite the good performance of the cermets and possible mitigation of the coking and poisoning issues, the conclusion obtained from all the studies concerning cermets is that some issues like redox cycling will never be solved as they stem from the presence of a metallic phase required to achieve electronic conductivity. For this reason, different works have been devoted to looking for anode materials that have the intrinsic ability to conduct ions and electrons, *i.e.* being mixed conductors, as for cathodes. These types of compounds are commonly referred to as MIECs (Mixed Ionic and Electronic Conductors) [60] and their greatest attribute is to have more catalytic points to achieve faster and cleaner reactions. Consequently, investigations to find Ni/YSZ cermet substitutes have been directed towards the study of complex monophasic

oxides of different structure types such as perovskite, spinel or fluorite [80]. In principle, the perovskite type compounds (ABO_3 stoichiometry) were exhaustively studied since the elements located at their B site, such as Mn, Fe, Ti and Cr, are multivalent and therefore can generate oxygen vacancies for conduction in a reducing atmosphere [42], [43], [84]. On the contrary for the A site, cations are preferred which tend to remain in a single valence state as La, Sr or Ca [43]. Thus, research on perovskite compounds usually includes a mix of several of these elements in order to find the ideal composition. One example is the pure $SrTiO_3$ material which has shown stability in reducing sulphur atmospheres but exhibits relatively low conductivity [35], [85]–[91]. The La-doped $La_xSr_{1-x}TiO_3$ (LST) compositions are also stable in sulphured environments [92] and achieve acceptable levels of mixed conductivity [42], [80]. Additionally, compounds where Y replaces Sr presents high electrical conductivity in the anode atmosphere and are compatible with YSZ and LSGM electrolytes [42]. On the other hand, when Nb replaces Ti ($Sr_{1-x}Ti_{1-x/2}Nb_xO_{3-\delta}$), the same conduction properties are achieved, even under more extreme conditions of oxygen partial pressure [42]. Nonetheless, if Ti is totally replaced by Nb, an increase in ionic conductivity is achieved at the expense of a reduction in the electronic conductivity [42].But, these kinds of materials have very low electrocatalytic activity for oxidation of hydrogen [93]. Similarly, with $SrVO_3$ compound a high conductivity value is obtained compared to the titanates mentioned above [42]. These kind of materials also are sulfur tolerant and coking resistance, however, they are unstable under oxidizing conditions which complicate their fabrication [94].

On the other hand, compositions corresponding to the $La_{1-x}Sr_xCr_{1-y}B_yO_3$ series (with B= Mn, Fe, Co, Ni) [35], [85] exhibit in particular good catalytic properties for the reforming of methane [42]. In fact, when B=Ni (10%), materials with low polarization resistances are obtained [42], whereas if the substitution is increased to 20%, an increase in electrical conductivity is observed both in air and in reducing atmosphere [95]. Similarly, the compositions $La_{1-x}Sr_xCr_{1-y}Mn_yO_3$ (LSCM) are stable in both

electrode environments [78], [80], allow an intermediate operating temperature (around 700°C) and do not catalyse carbon deposition [80]. Despite the above, the oxide which currently stands out amongst all the aforementioned compositions is the perovskite of stoichiometry $La_{0.75}Sr_{0.25}Cr_{0.5}Mn_{0.5}O_3$ (LSCM) [42], [96]–[98]. Some of its properties are: stability in the redox cycling and good catalytic performance yield for hydrogen (polarization resistance of 0.2 Ω cm^2 at 900°C in 97%H_2/3%H_2O[99]) and methane oxidation in low steam to hydrocarbon ratios [80], [100]. However, this material has some disadvantages: low conductivity in the anode environment ($9.6x10^{-1}$ S cm^{-1} under 5%H_2/Ar 0.025 atm H_2O at 800°C) [43], [97] and has still low electrochemical performance [42], [100]. For this reason, a doping strategy of the LSCM-type phases has been reported thus, a higher quantity of Sr in LSCM increase the electrical conductivity, although it could present chemical reactivity with Zr-based electrolytes [80]. Likewise, the case of $La_{0.75}Sr_{0.25}Cr_{0.2}Mn_{0.5}Ti_{0.3}O_{3-\delta}$ compound is interesting as the electrical conductivity exceeds that of LSCM [100]. Another choice is the $Ce_xLa_{0.75-x}Sr_{0.25}Cr_{0.25}Mn_{0.5}O_{3-\delta}$ series which shows a better electrochemical performance while maintaining the same electrical conductivity in anode atmosphere of the material without Ce [80], [100]. A further strategy to improve the LSCM anodes is the construction of layer composites with electrode/electrolyte interfaces with the ionic conductor YSZ or CGO. The above allows the electrocatalytic activity can be markedly improved. Nevertheless, these kind of mixtures exhibit poor electrical conductivity [80].

In the same way, double perovskites ($AA'BB'O_6$) are also shown as potential anodes. The $Sr_2Mg_{1-x}Mn_xMoO_{6-\delta}$ family can be used with natural gas in a temperature range of 600-1000°C, with wide thermal stability and sulphur tolerance [43]. Nevertheless, most of those materials are chemically incompatible with YSZ electrolyte at temperatures below 800°C, due to $SrMoO_4$ and $SrZrO_3$ impurities formation [78]. $Sr_2Fe_{1.5}Mo_{0.5}O_{6-\delta}$ material, specifically, is structurally stable under oxidizing and reducing environments; additionally, it has high performance but not better than materials such $La_{0.75}Sr_{0.25}Cr_{0.5}Mn_{0.5}O_{3-\delta}$ [78], [80].

Finally, another step in the way to enhance the anodic properties of the compounds is the incorporation of Ni metal by mixture, physical or chemical deposition, or recently by Ni-doping with subsequent Ni exsolution in reducing conditions [101]. The exsolution process, theoretically, takes advantage of the good properties of Ni while decreases the hydrocarbon-coking propensity [101], [102]. One example is the $La_{0.5}Sr_{0.5}Ni_{0.25}Ti_{0.75}O_{3-\delta}$ perovskite material, which has high conductivity at high temperatures (800-1000°C) and promising electrochemical performance, in both anodic and cathodic environments [102]. Although it has been observed for $La_{0.4}Sr_{0.4}Ni_yTi_{1-y}O_{3-y}$ (y=0.03) and $La_{0.4+2x}Sr_{0.4+2x}Ni_xTi_{1-x}O_3$ (x=0.06) sensibility to H_2S comparable to deposited Ni, an improvement of coking resistances is clearly evidenced [101]. The same strategy has been tested in other arrangements such as $Pr_{0.5}Ba_{0.5}Mn_{0.85}T_{0.15}O_{3-\delta}$ (T=Mn, Co, Ni and Fe) layered perovskites compounds which electrochemical performance is considered excellent compared to other ceramic anode [103]. In this sense, double perovskites such as $Sr_2FeMo_{0.65}Ni_{0.35}O_{6-\delta}$ present high electronic conductivity, good catalytic activity toward H_2 and hydrocarbon (CH_4) oxidation and good structural stability in reducing atmosphere, therefore has excellent electrochemical performance [104].

At this point it is necessary to particularly emphasise that the outstanding anode material $La_{0.75}Sr_{0.25}Cr_{0.5}Mn_{0.5}O_3$ is frequently interpreted as the stabilization in the reducing atmosphere of the cathode $La_{1-x}Sr_xMnO_{3-\delta}$ (LSM) by means of the incorporation of Cr [99]. Following this same idea, part of the development of this project is dedicated to the stabilization of a potential cathode to be used also as anode, all with the aim that this material can be used in practical way in symmetrical fuel cells. In these systems, a single compound operates as both electrodes, so the manufacturing process, maintenance and operation can be significantly simplified. Therefore, they are considered an evolution of the classical SOFC design, as described in the following section [19].

1.7 SYMMETRICAL SOFC OR S-SOFC

As already mentioned, in Symmetrical Solid Oxide Fuel Cells (S-SOFCs) the same compound operates simultaneously as anode and cathode. This technology is considered an important development because it allows to simplify the elaboration of the cells [105] and, at the same time, the manufacturing costs are reduced compared to the traditional SOFC [49]. It would only require a temperature to assemble the device and unlike SOFCs, in which compatibility between three materials must be sought under all conditions, only one type of electrode-electrolyte interface would have to be optimized [19]. More importantly, it is worth noting that problems with the use of hydrocarbon fuels would be completely eliminated since the deposited carbon or damages due to sulphur or cocking could be cleaned simply by reversing the flow of gases between the two electrodes [19], [49].

In general, it is desired that an electrode for S-SOFC presents the properties mentioned as it follows [19], [49] :

i) Chemical and physical stability in reducing and oxidizing environments.

ii) Chemical and thermomechanical compatibility with the components of the cell.

iii) Appropriate electrical conductivity, if possible mixed-typed in oxidizing and reducing atmosphere.

iv) Electrocatalytic activity for the reduction of oxygen and the oxidation of the fuel.

For that reason, very few candidates exist at this time for S-SOFC electrodes. These are derived from anode, cathode and even SOFC interconnects [19], in which some elements are preferred, *e.g.* Cr, Mn, Mo or Ti [106], and other have been avoided, *e.g.* Co [49]. The materials that have been considered for such application are no other than perovskites derived from $LaCrO_3$, $LaMnO_3$ and $SrTiO_3$; however, none of them are ideal given their low electronic conductivity in reducing or oxidizing atmosphere or insufficient electrocatalytic properties, especially as an anode [49]. [107]. The most studied perovskite compound for S-SOFC is the already mentioned

$La_{0.75}Sr_{0.25}Cr_{0.5}Mn_{0.5}O_3$ (LSCM). This material has been considered because presents adequate electrochemical properties in both reducing and oxidizing atmosphere, and in fact using CH_4 and H_2 [108], [109]. As an improvement of LSCM, Ni-doped $La_{0.75}Sr_{0.25}Cr_{0.5}Mn_{0.5}O_3$ compounds have been proposed as S-SOFC electrode, too. Those materials exhibit a higher conductivity than pure LSCM in air (13 and 20 S cm^{-1} at 800°C for pure and doped material, respectively), and comparable values in reducing environment when Ni partially exsolutes (0.96 and 0.75 S cm^{-1} at 800°C 5%H_2/Ar, 0.025 H_2O for pure and doped material, respectively). In addition, a composition like $La_{0.75}Sr_{0.25}Cr_{0.5}Mn_{0.3}Ni_{0.2}O_3$ results better than Ni-free LSCM, given that the former allows the total oxidation of methane for a wide range of oxygen contents while, for LSCM, the selectivity decreases as lattice oxygen stoichiometry diminishes [95]. Using the same strategy, a similar material with $La_{0.6}Sr_{0.4}Fe_{0.9}Ni_{0.1}O_{3-\delta}$ composition has been also developed. This compound shows also high performance and long term stability and is a promising electrode for low temperature SOFC [110].

Now, not only traditional perovskites materials have been proposed and studied as S-SOFC electrodes. Other interesting compounds like $Sr_2Fe_{1.5}Mo_{0.5}O_6$ (SFM) double perovskite show high conductivities in both anode and cathode environment [19], [106], but such compositions present the great disadvantage that they chemically reacts with YSZ electrolyte [106]. Other derived compositions with $SrFe_{0.75}B_{0.25}O_3$ stoichiometry (B= Mo^{6+}, Cr^{6+}, W^{6+}, Nb^{5+}, Ti^{4+} and Zr^{4+}) have also been considered due to their stability in the electrode atmospheres and their good cathode performance; however, because of their low compatibility with electrolyte and their poor performance as anode, those materials are not considered competitive [105]. Recently, materials with lamellar Ruddlesden-Popper structure have also been successfully tested as S-SOFC compound. Among these, stands out the $La_xSr_{2-x}MnO_{4\pm\delta}$ compounds, which have TEC values (in air and hydrogen) very close the commercial electrolytes and, particularly, $La_{0.5}Sr_{1.5}MnO_4$ composition presents acceptable electrochemical behavior in both cathodic and anodic environment [107].

1.8 AIM OF THE PRESENT STUDY - DESCRIPTION OF THE $YMnO_3$-TYPED COMPOUNDS

As discussed above, the materials currently used for Solid Oxide Fuel Cells have not been fully satisfactory in terms of efficiency, durability and catalytic activity, which delays the large-scale commercialization of the technology. Thus, the intent of the present research is to find one or more materials having better properties to those exhibited by the compounds described above within the $YMnO_3$-typed compounds. Those materials have never been considered as electrodes for SOFCs and through this work, we expect to develop new compositions that could even be used for S-SOFC, considering in particular the main issue of SOFC components, which is the reactivity with YSZ electrolyte.

As a first consideration, it is worth noting that most of the mixed materials that have been successfully developed as SOFC anode in replacement of Ni-cermet contain Manganese as the main active element. This transition metal is one of the only ones to adopt multiple oxidation states in oxidizing as in reducing atmospheres, but also different coordination sphere (commonly octahedral and tetrahedral but square-based pyramidal, or trigonal bipyramidal), what is probably one of the main aspect to take into account for the formation of oxygen vacancies and migration of oxide ions. Moreover, most of the materials that have been developed for S-SOFC electrode are indeed pure or stabilized manganites [95], [111], what is due to the fact that conducting Mn oxides can, in some extent, be stable or stabilized using adequate doping in reducing atmosphere.

The matrix that has been selected for this study is the hexagonal lamellar $YMnO_3$ (space group $P6_3cm$), which has been the subject of many recent studies due to its particular magnetic characteristics when in its pure form [112]–[115] or because it is capable of storing oxygen in with or without substitutions [116]–[119]. These multiple applications are the result of the unique structure that the material adopts. However,

as $YMnO_3$ generally crystallizes in the hexagonal lamellar symmetry [120], [121], the material has also been described in an orthorhombic distorted perovskite [122], because Y^{3+} cation has a small ionic radius with respect to other rare earth elements [120], [123]–[128]. It causes the tolerance factor (*t*) for $YMnO_3$ stoichiometry to be 0.854 [126]. The factor, also called Goldschmidt tolerance factor, is defined as shown in equation *(27)* [129]:

$$t = \frac{r_A + r_O}{\sqrt{2}(r_B + r_O)} \qquad (27)$$

Where

r_A is the ionic radius at the A site,

r_B corresponds to the ionic radius at the B site,

And r_O is the ionic radius of the oxygen anion.

The *t* value, which is used to know the tendency of ABO_3 materials to form one or another structure ($0.855 \leq t \leq 1$ perovskite, $t < 0.855$ hexagonal lamellar [126]), allows to understand that $YMnO_3$ compound can be synthesized in any of the two arrangements, depending on the preparation method. But the perovskite $YMnO_3$ is obtained at high pressure [130], while the compound of interest in this project (hexagonal lamellar phase) has been obtained in an oxidizing atmosphere, under normal pressure and by solid state reaction, epitaxial-growth techniques of thin film or with mild chemical ways [122], using normally temperatures between 1200 and 1550°C [84], [120], [121], [124], [131]–[134]. The resulting hexagonal structure exhibits the $P6_3cm$ space group, and it is worth noting that this is non-centrosymmetric. As shown in Figure 5, the structure can be described as built of layers of Y^{3+} ions separated by sheets of trigonal bipyramids of MnO_5. The latter polyhedra are formed with three O^{2-} ions located in the same equatorial plane and two arranged apically [123], [131].

Figure 5. Hexagonal $YMnO_3$ (*P6₃cm*) representation of. a) Laminar arrangement of tilted polyhedra, b) MnO_5 polyhedra joined by corners, c) trigonal bi-pyramids MnO_5. The atoms of Y (gray) are surrounded by 8 oxygens atoms (purple), whereas the cations of Mn only by 5 oxygens atoms (blue polyhedron).

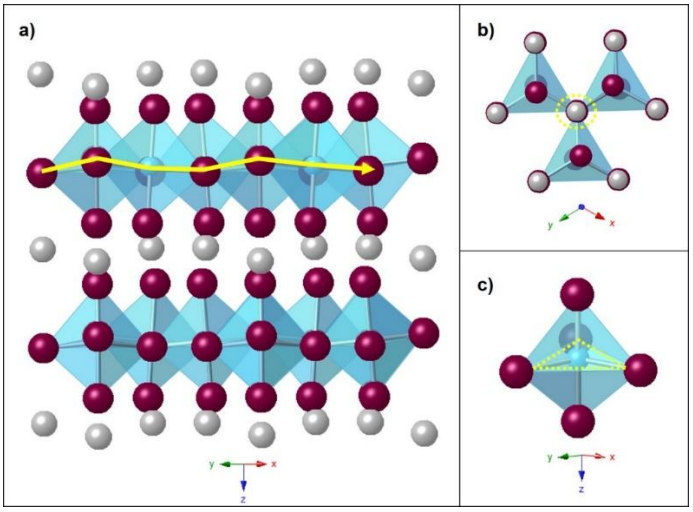

The polyhedra are joined by the corners to form a triangular network in the basal plane *ab*. Additionally, it is worth mentioning that the Y^{3+} layers are "buckled" [121], [135]; as a result, the structure exhibits two unequivalent Y-sites, and there are two different Y-O bond lengths, which cause a tilt of the bipyramids with respect to the *c*-axis [121], [124], [126].

Increasing the temperature in air, $YMnO_3$ becomes centrosymmetrical with *P6₃/mmc* space group at T~980°C [133], [136]–[139]. This transition occurs when, from of the crystallographic point of view, an inversion center is gained [112], [116], [136]. In other words, the structure becomes more symmetrical by increasing temperature and consequently, the high temperature arrangement have non-tilted polyhedral (Figure 6).

Figure 6. Hexagonal $YMnO_3$ (*P*6$_3$*/mmc*) representation. Laminar arrangement without tilting polyhedra. The atoms of Y (gray) are surrounded by 8 oxygens atoms (purple), whereas the cations of Mn by only 5 oxygens atoms (blue polyhedron).

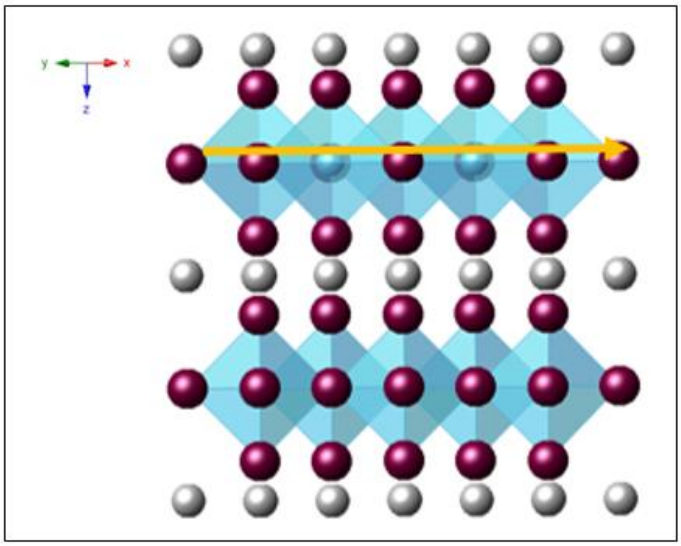

However, according to some authors, the structural arrangements mentioned above are not the only ones that can present this particular stoichiometry $YMnO_3$. Recently, it had been observed that $RMnO_{3+\delta}$ compounds with small or intermediate R^{3+} cations (Y, Dy, Ho, Er or Yb) have the ability to reversibly store different quantities of oxygen and adopt, as a consequence, distinct crystal structures. In general, these materials can absorb oxygen at critical temperatures and under normal pressure, both in air or higher pO_2. Therefore, at temperatures higher than T~350°C and in air, those compounds present their minimum oxygen content ($\delta \leq 0.13$) and remain generally in the *P6$_3$cm* space group. But in a narrow temperature range ~250<T<350°C, the materials exhibit a large oxygen absorption (up to δ~0.25-0.28), what induces a phase transition to an *R*3*c* arrangement. This structure can be understood as a tripling of the *P*6$_3$*cm* cell along the *c*-axis and presents six oxygen sites (instead of four oxygen sites in *P*6$_3$*cm*). Among them, the partially filled O6 site represents position of the overstoichiometric oxygen atom and is located in the

empty equatorial triangular sites of the parent $P6_3cm$ structure (Figure 7(a)). In that way, the extra oxygen induces a rearrangement in the stacking model of the Mn-O layers in hexagonal structure since, in the case of $R3c$, Mn trimers are not located exactly on top of each and are shifted by a vector 3/2 1/3 $C_h/2$ (in the hexagonal notation) [119], [140].

Figure 7. (a) R3c superstructure showing the oxygen ion intercalation site O6 in the *a-b* plane around the Mn sites; (b) $Pca2_1$ arrangement with eight oxygen around Mn.

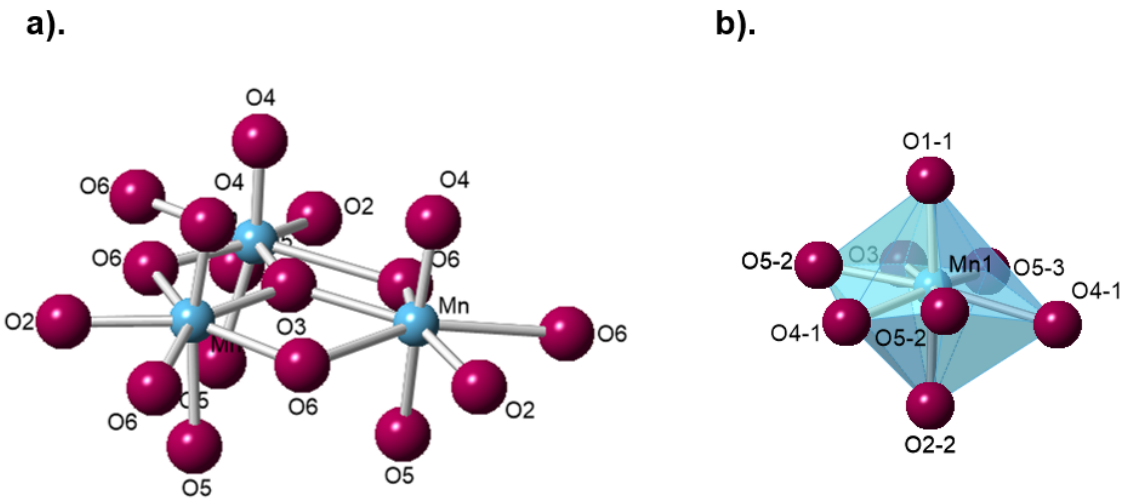

Adapted from [119], [140].

Finally, after annealing at 190 bar of oxygen pressure, the oxygen content can increase up to δ≈0.40 and at this point the structure transforms into another supercell of $Pca2_1$ space group [141]. In this arrangement, which is similar to the former but with a different symmetry, the oxygen excess is located in O5 sites, *i.e.* Mn atoms are bonded to one or more additional oxygen atoms (Figure 7(b)) [119].

As a summary, in both superstructures $R3c$ and $Pca2_1$, the oxygen is incorporated in the Mn-O layers (and apparent Mn coordination increases) [142], as a

consequence, the basal oxygens (O3 and O4, in *P*6$_3$*cm*) of MnO_5 polyhedra are under bonded, *i.e.* these oxygens can easily move or get out of the structure, being an interesting point in the search of MIEC behavior [116]. In addition, it is worth mentioning that the stability of these phases depends on the R ionic radius; the bigger the R^{3+} size, the slower the kinetics, the lower the absorbed oxygen content and the lower the transition temperature to *R*3*c* [119], [140], [143], [144]. Likewise, if some R ionic size promotes the formation of one or more phases, like for R=Ho, for example, it was impossible to obtain pure *R*3*c* single-phase for $YMnO_{3+\delta}$ [119], [145]. In Figure 8, we can observe the simulated X-Ray diffractograms of the aforementioned structures, using Cu-$K_{\alpha 1\text{-}2}$ incident radiation (λ_1=1.5406 Å and λ_2=1.5444 Å), with the aim to evidence their relationship showing similarities and/or differences, what will be helpful for the analysis of our own results.

Figure 8. Simulated X-Ray Diffraction patterns for $YMnO_3$ compound in their different possible structural arrangement.

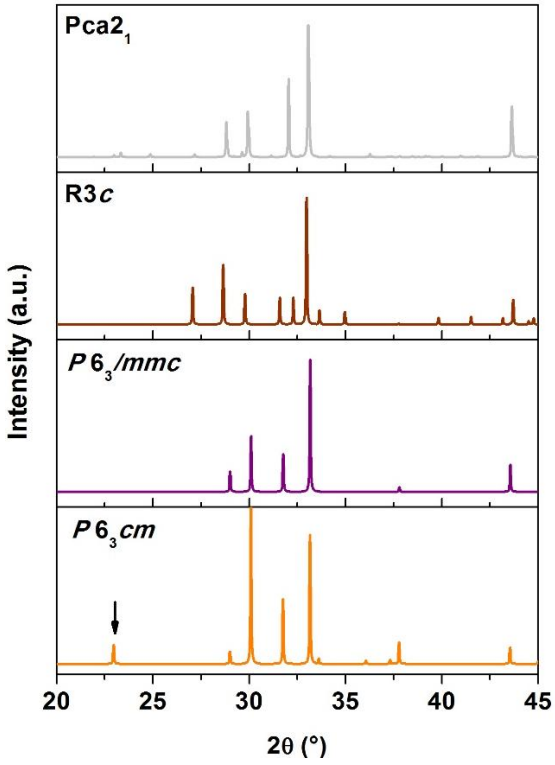

It is possible to see that the diffraction patterns of the two hexagonal and the orthorhombic (*Pca2₁*) structures are very similar, especially, in the more intense reflections (2θ~28-35°). Meanwhile, the diffractogram of the rhombohedral arrangement *R*3*c* show greater number of peaks. Additionally, the presence of 2θ~23° peak in the *P*6₃*cm* pattern is determinant to differentiate it from the *P*6₃/*mmc*.

In the particular case of $YMn_{0.875}Ti_{0.125}O_3$, different phase transitions related to an oxygen excess have been also described. Specifically, the X-Ray Diffraction data of the synthesized compound can be indexed in the *P*6₃*cm* arrangement; however, the Neutron Diffraction data of the same sample cannot be satisfactorily refined neither with the *P*6₃/*mmc* structure nor with the *P*6₃*cm* structure using isotropic atomic displacement parameters. The best results were obtained including the anisotropic refinement of atomic displacement parameters (ADPs) in the *P*6₃*cm* space group, except for the coordinates of Mn atoms which are displaced off the mirror planes due to additional interstitial oxygen atoms (O_I) having their centers locates on 3-fold symmetry axes (Wyckoff positions *6c*, (x; 0; z), x≈2/3, z≈0) notation (Figure 9) [116].

Figure 9. Atomic arrangement of as synthesized $YMn_{0.875}Ti_{0.125}O_3$ showing the interstitial oxygen atoms (O_I) on 3-fold symmetry axes.

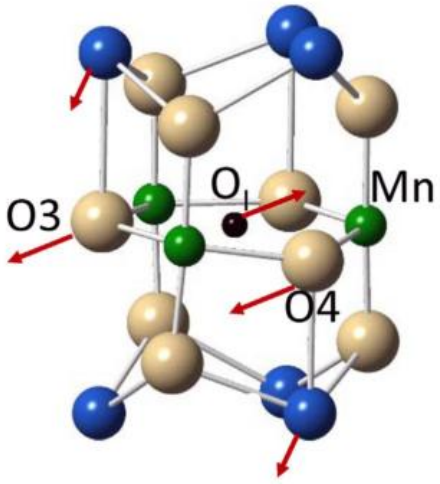

[116]

Then, it is possible to notice that, at difference from the cases discussed above, these authors consider that the presence of interstitial oxygen does not mean a transition to the complex *R*3*c* or *Pca2₁*, and they considered that a *P*6₃*cm* structure with an extra position O_I can explain the structure [116].

Several **substitutions** have been described for $YMnO_3$ material. In general, some doping elements are more favorable than others, the latter inducing the formation of biphasic samples when a limit of substitution of one element is achieved. Such phenomenon occurs generally when the A or B site replacement promotes the change of Mn^{3+} to Mn^{4+}. Since Mn^{4+} is much smaller in size than Mn^{3+} and the tolerance factor becomes higher [146], the hexagonal structure becomes unfavourable.

Recent research has shown the successful substitutions **at the Y^{3+} cation site** while retaining the *P*6₃*cm* hexagonal phase. Among these, Dy^{3+} can substitute Y^{3+} cation in the whole range of composition within the $Y_{1-x}Dy_xMnO_{3+\delta}$ series, what can be understood because $YMnO_3$ and $DyMnO_3$ have similar tolerance factors (t=0.857 for $DyMnO_3$) [117]. These compounds have similar behavior, present the aptitude for oxygen storage and can form hexagonal superstructures when Mn^{3+} is partially oxidized to Mn^{4+} and oxygen stoichiometry increases, as explained above [117], [126], [142]. In addition, it is worth to mentioning that Zr^{4+} or Ce^{4+} can partially replace Y^{3+} ($x \leq 0.1$) but, according to literature, they present a single-phase with *P*6₃/*mmc* space group [147], since these substitutions seem to diminish the transition temperature until room temperature.

Meanwhile, the substitutions **at the Mn site** that allow to conserve the *P*6₃*cm* structure are more numerous and cover elements with different oxidation states. First, concerning the **divalent** substituting elements, Zn^{2+} cation can be mentioned, which can lead to the formation of the hexagonal lamellar phase for low levels of doping ($x \leq 0.10$) [113]. On the contrary, a mixture of the hexagonal and orthorhombic perovskite has been reported for the following elements: Ni for $x \leq 0.20$ [120], [126],

[148], Co for x≤0.25 [120], [126], [149] and Cu for x≤0.30 [120], [150]. Beyond these limits perovskite structure prevails [120].

In order to achieve the pure hexagonal phase, some authors have tried to co-substitute the B site with elements that balance the charges of some divalent cations. Thus, materials of $YMn_{1-x}(B',B'')O_3$ stoichiometry with B' = divalent cation and B"= cation with an oxidation state greater than three have been prepared. Amongst these types of compounds we find those of the series $YMn_{1-x}(Zn_{2/3}V_{1/3})_xO_3$ whose solubility only extends up to approximately 25%; and the families $YMn_{1-x}(Cu_{2/3}V_{1/3})_xO_3$, $YMn_{1-x}(Cu_{3/4}W_{1/4})_xO_3$, $YMn_{1-x}(Zn_{2/3}V_{1/3})_xO_3$ and $YMn_{1-x}(Zn_{3/4}Mo_{1/4})_xO_3$ in which the substitution is limited to a value close to 50%. Only two series form a solid solution in the whole range: $YMn_{1-x}(Cu_{1/2}Ti_{1/2})_xO_3$ and $YMn_{1-x}(Cu_{3/4}Mo_{1/4})_xO_3$. The latter shows a complex cationic arrangement at low amounts of Mn [135], [151], [152].

The Mn site is also able to accept **trivalent** cations as B-site substituent. For example, with Al^{3+}, the hexagonal material (*P*6$_3$/*mmc*) is obtained up to a composition of x≈0.15 in $YMn_{1-x}Al_xO_3$. However, if the concentration of aluminum increases, an additional phase corresponding to an orthorhombic perovskite appears. Finally, when x>0.75 the sole perovskite structure remains [113], [147], [153]–[155]. On the other hand, if Mn is substituted with Ga, the hexagonal phase is obtained for x≤0.20 within the $YMn_{1-x}Ga_xO_3$ series [151]. The solubility limit is higher when the ion is Fe^{3+} since the substituting desired structure is achieved for x<0.30 in the $YMn_{1-x}Fe_xO_3$ materials; for higher iron quantities, the same mixture of phases as in the case of Al^{3+} observed and; when reaching x= 0.50 the stable structure is an orthorhombic perovskite [131], [151], [156]–[158]. In a similar way to what has been observed for the divalent cations, it is possible to carry out a co-substitution at Mn site considering, for example, the $YMn_{0.5}Fe_{0.5-x}Pd_xO_3$ series in the range 0≤x≤0.07 to obtain hexagonal single phases. However the most interesting case amongst trivalent cations is In^{3+}, since it is the only reported substitution at the Mn site that shows a complete miscibility in the whole $YMn_{1-x}In_xO_3$ solid solution, it

seems to be the result of similar In-O and Mn-O bond length in the basal plane for hexagonal $YInO_3$ and $YMnO_3$, respectively [135], [147], [151], [159], [160].

Finally, some **tetravalent** cations can replace Mn at the B site: for example, Re and Ru to name a few. With these elements, the phase crystallizes in the hexagonal structure for low contents of x<0.1 [113]. However, the substitution of more relevance is that of Ti^{4+}. Such cation can substitute the Mn site up to 0.15 (in the stoichiometry $YMn_{1-x}Ti_xO_3$) [161], [162] and even higher when a cation sub-stoichiometry is applied at the Mn site. For higher Ti concentration, a *R*-3*c* perovskite phase could be observed and both arrangements coexist above x= 0.2; when x= 0.3 the rhombohedral phase predominates [116], [137], [139], [163]. In case of B-site substoichiometry, *i.e.* when the B site is not completely filled considering $YMn_xTi_yO_3$ compositions with x+y<1, it is possible to synthesize samples adopting different hexagonal structures: for example, $YMn_{0.87}Ti_{0.1}O_3$ crystallizes in the *P*6$_3$*cm* space group and the compounds $YMn_{0.73}Ti_{0.2}O_3$, $YMn_{0.6}Ti_{0.3}O_3$ and $YMn_{0.3}Ti_{0.4}O_3$ with *P*6$_3$*/mmc* structure [164].

Considering the aforementioned information, and to conclude this part concerning the structural description of pure of doped $YMnO_3$, such original and flexible framework could make it an efficient electrode material, since it presents peculiar structural conditions for oxygen diffusion [123]. Exhibiting a combination of laminar arrangement and specific 5-fold coordination for Mn and bipyramids, instead of more classical octahedral in perovskite materials, and possibly extendable to “5+3”-fold (partially filled) coordination in case of oxygen excess, $YMnO_3$ is expected to be a mixed ionic and electronic conductor [42]. Concerning the layered structures, it is worth remembering again that anisotropic structures, *e.g.* Ruddlesden-popper ($A_{n+1}B_nO_{3n+1}$) and double perovskites ($AA'B_2O_{5+\delta}$) seem to present favorable situations for MIEC behavior [75], [165], [166]. The above mentioned materials exhibit high diffusivity of oxygen ions because they offer many "paths" for the movement of extra O^{2-} ions, instead of showing ion conduction via vacancies as occurs in the traditional perovskite materials [166].

Finally, considering the already described substitutions, in particular with B-site cations like In^{3+} or Ti^{4+} that are particularly stable in reducing atmosphere, opportunities seem to exist for the stabilization of $YMnO_3$ in anode conditions; in this sense, such framework seems to present all the chemical and structural features for potential application as a symmetrical SOFC electrode.

Figure 10. Flow diagram of the experimental procedure for the development and study of a new electrode material.

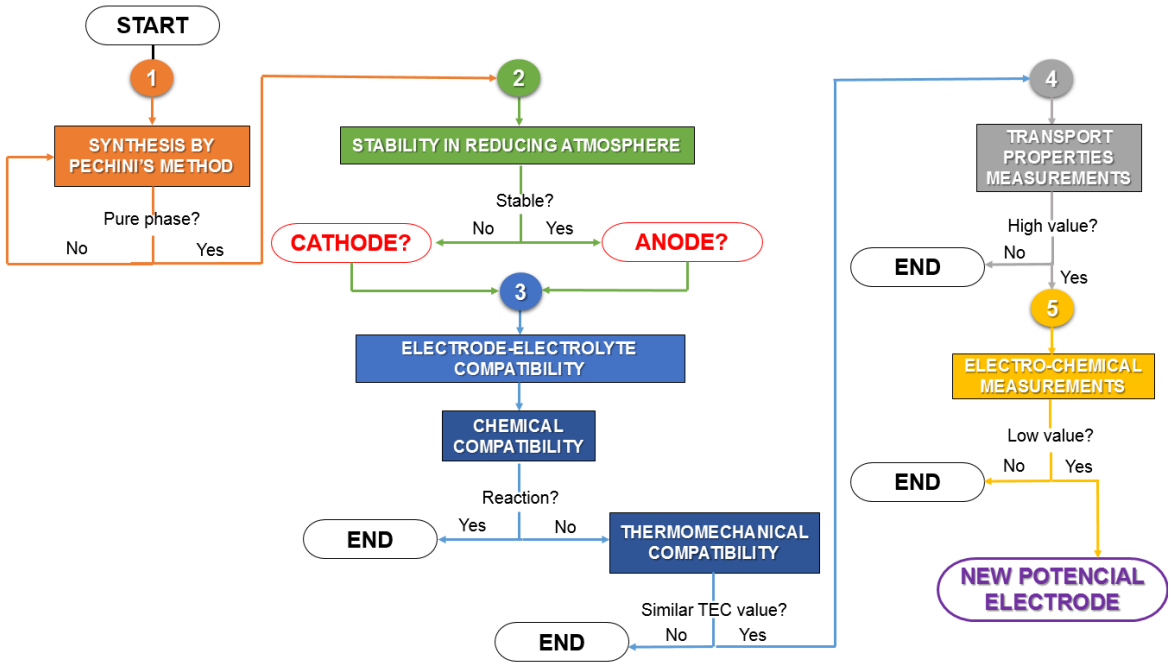

2.1 SYNTHESIS AND STRUCTURAL CHARACTERIZATION OF $YMnO_3$ AND $Y_{1-x}A_xMn_{1-y}B_yO_{3+\delta}$ (A = Zr or B = Ti) BY THE PECHINI METHOD

2.1.1 Description of the Pechini Method. It is considered the easiest and most elegant variation of the sol-gel method, since its implementation only requires a beaker, an agitator, a hot plate and an oven. This technique is classified within the procedures of soft synthesis and is preferred due to the lower temperature that is used; it allows the formation of smaller grains compared to other methods, such as the classic solid state reaction [167]. A further advantage is that it facilitates the doping of materials with multiple substituents, which is very important for the development of complex oxides like those considered in this work.

In general, this type of synthesis seeks to obtain a polymer network in which the metallic cations, which will form the final oxide, are homogeneously distributed and

intimately mixed. To accomplish this, a polyesterification reaction is carried out from a multifunctional organic acid capable of chelating metal ions in stable complexes, and a diol, which also acts as a solvent during the formation of the complexes (Figure 11).

Figure 11. Scheme for the transformation of the reagents into a mixed oxide by means of the Pechini method.

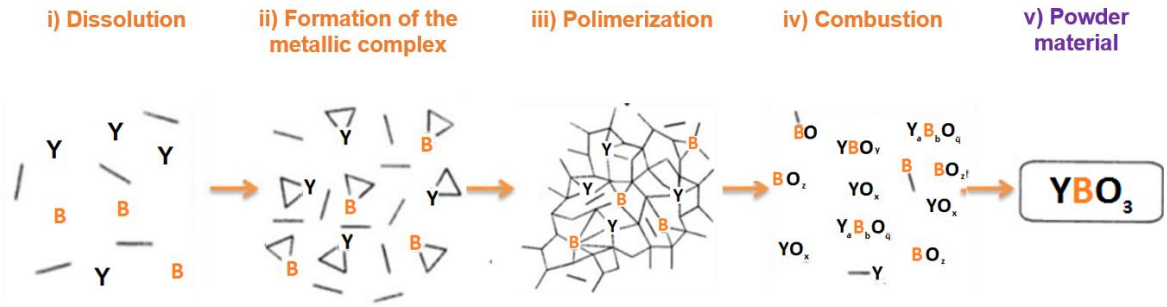

Adapted from [167].

Thus, in our particular case, cationic precursors in the form of nitrates, carbonates and oxides were used to synthesize the compounds. These reactants were mixed and transformed into a single-phased oxide, following the basic steps summarized in Figure 12.

Figure 12. Sequence of the Pechini method followed in the present work.

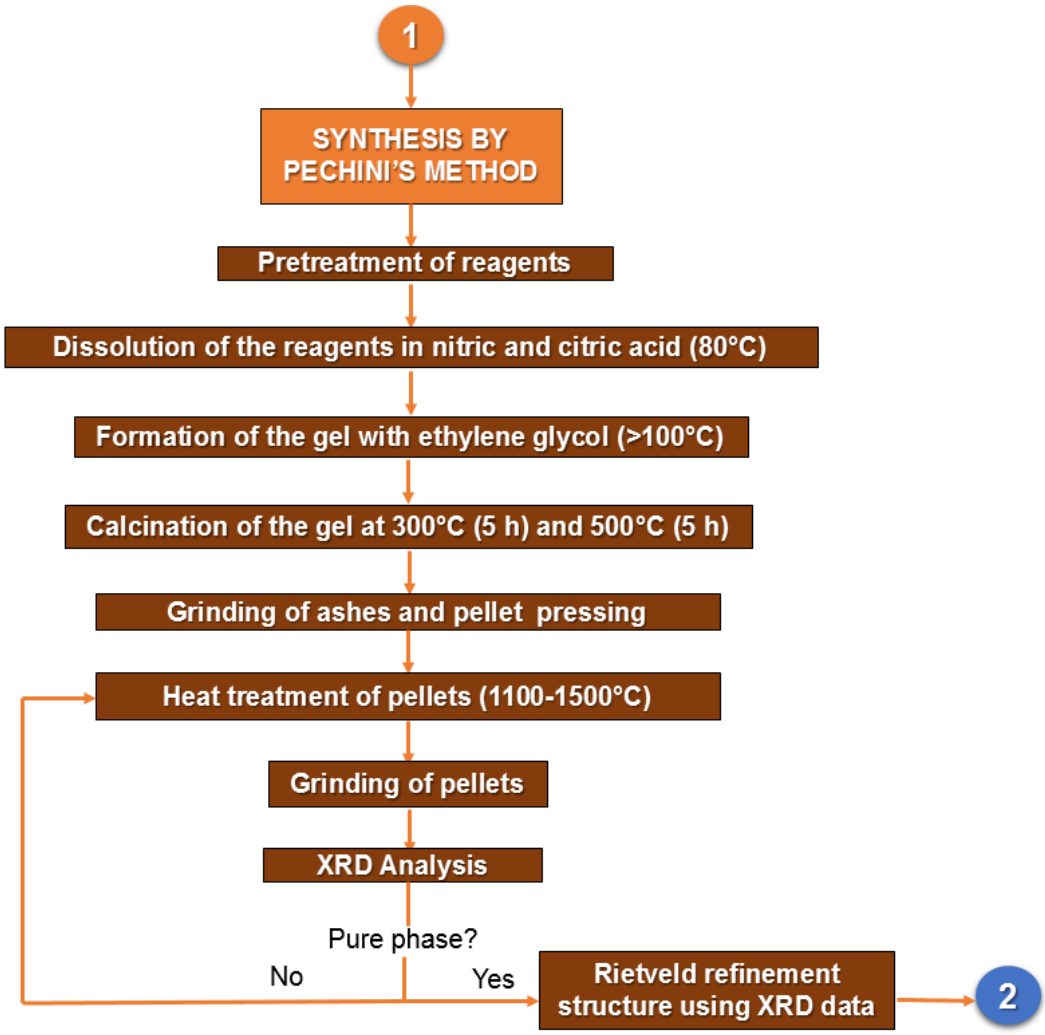

i.) First, the stoichiometric quantities of the reactants are dissolved in nitric and citric acid, and water until a homogeneous solution is obtained (T=80°C). ii) Thanks to the presence of the citric acid, metal- citrate complexes are formed at the same time. iii.) Ethylene glycol is added to this mixture and the temperature (T>100°C) is raised to induce the formation of a polyester, while the water evaporates. When the polymerization is completed, it is possible to observe a highly viscous organic mass (gel), with an ideal cations distribution. iv.) Subsequently, the gel is calcined at 300 and 500°C (for 5 hours) to decompose the organic species. The as-obtained precursor powder contains a mixture of metal oxides, carbonates or intermediate

monophasic compounds with appropriate stoichiometry, generally in an amorphous state. v.) Finally, the powder is pressed into pellets (CARVER mold and press, 9000 psi), which are thermally treated in air, on sheets of alumina and in a temperature range between 1100 and 1500°C (for 12 hours, with a heating ramp of 300°C h^{-1}, in a CARBOLITE furnace), depending on the stoichiometry of the desired oxide (Table 1).

Table 1. Synthesis temperature of the compounds studied in this project**.**

Compounds	Synthesis temperature
$YMnO_3$	1100°C
$Y_{1-x}Zr_xMnO_3$ (x=0,05; 0,1; 0,15)	1100-1200°C
$YMn_xTi_yO_3$ (x= 0,1- y=0.8; x= 0,2– y=0,65; 0,7; 0,73; 0,75; x=0,3- y=0,55; 0,6; 0,65)	1100-1200°C

2.1.2 Preparation of reagents. All the compounds studied in the present work were obtained from the precursors shown in Table 2. In order to ensure their correct weighing, some of them had to be heat treated for the removal of moisture and possibly ab/adsorbed volatiles. For other precursors, as in the case of reactants in the form of nitrates or carbonates, an oxide to carbonate and/or nitrate ratio was calculated by calcining a representative part of reagent and weighing it before and after treatment. This relationship is then used to determine the exact quantity to be weighed.

Table 2. Precursors used in the synthesis of the compounds.

Reagent	Formula	Purity (%p/p)	Supplier	Pre-treatment
Yttrium Oxide	Y_2O_3	99.9	Alfa Aesar	1000°C/ 2h
Manganese carbonate	$MnCO_3$	99.99	Sigma Aldrich	Weight loss (700°C/ 5h)
Hydrated zirconyl nitrate	$ZrO(NO_3)_2.H_2O$	99.9	Alfa Aesar	Weight loss (1000°C/ 5h)
Titanium isopropoxide	$C_{12}H_{28}O_4Ti$	99.995	Alfa Aesar	Stabilized in proportion Isopropoxide: Ethylene glycol: Citric acid = 1: 20: 4.3)
Citric acid monohydrate	$C_6H_8O_7*H_2O$	99.5	Emsure-Merck	-
Ethylene glycol	$C_2H_6O_2$	99.5	Emsure-Merck	-
Nitric acid	HNO_3	65	Emsure-Merck	-

2.1.3 Structural characterization of compounds with X-ray diffraction (XRD). After heat treatment, the compounds were characterised by the X-Ray Diffraction (XRD) technique to check their purity and determine/refine their structure. This method is very useful since each crystalline phase presents a characteristic pattern [168]. In general, the analysis consists of electromagnetically irradiating the crystallites of powdered materials with a beam whose wavelength is of the order of

magnitude of the distance between the atomic planes in the structure (X-Ray); then the intensity of the wave diffracted by the planes, is recorded. However, it must be taken into account that the diffraction phenomenon only occurs when the so-called Bragg law is fulfilled [169]:

$$2d_{hkl}sin\theta = n\lambda \qquad (28)$$

Where d_{hkl} is the distance between *(hkl)* planes,
θ, the angle between the incident beam and the planes hkl,
n, an integer,
and λ is the wavelength of the incident beam.

In our case, most of the diffractograms were measured with a D8-AVANCE diffractometer (BRUKER) with DaVinci Bragg Brentano geometry, Cu-$K_{\alpha 1\text{-}2}$ type radiation and under the following conditions: λ_1=1.5406 Å and λ_2=1.5444 Å; Voltage=40 kV; Current=40 mA. The data were obtained in a measurement interval of 2°-70 ° (2θ) (integration time of 0.2s per step) for qualitative analysis and 5-140 ° (2θ) for the quantitative (integration time 1s per step). The diffraction patterns were analysed using the SEARCHMATCH database (Version 2.0; 3.1, Oxford Cryosystems, www.oxcryo.com). When no additional phases were observed in the diffractograms, the lattice parameters and the atomic positions of the compounds were calculated using the LeBail or the Rietveld method described in Annex A (FULLPROF programme [170] and its WINPLOTR interface[171]). To carry it out such refinement procedure, it is necessary to interpolate the background points with a polynomial function of 6 coefficients. Then, the profile of the peaks is modelled by a Cagliotti function with variables U, V, W, the η parameter (Gaussian-Lorentzian mixture) and two parameters for peaks asymmetry at low theta. In our case, the standard deviation values were corrected according to the description made by Berar and Lelann [172].

2.2 MATERIALS' STABILITY IN REDUCING ATMOSPHERE

The study of stability of the synthesized materials in a reducing atmosphere allows the selection of compounds that can be used not only as cathode but also as anode and to establish their stability to redox cycles according to the procedure in Figure 13.

Figure 13. Flow diagram of the test of stability in reducing atmosphere.

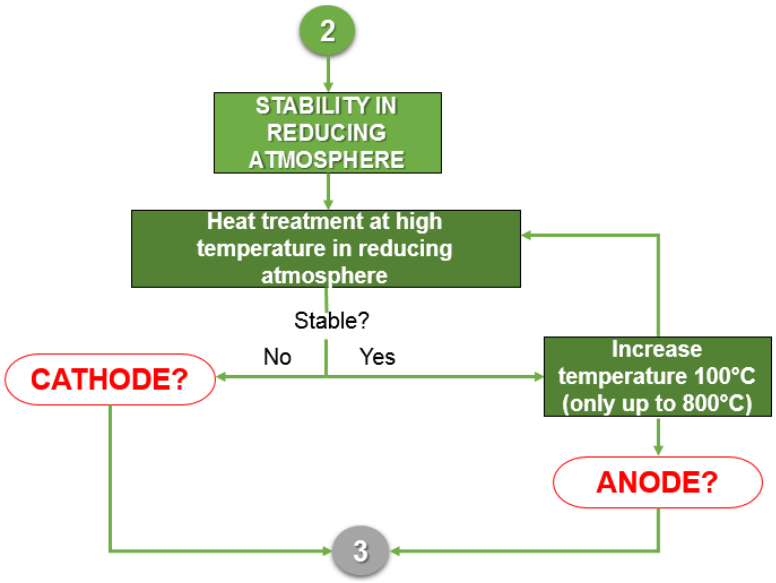

For the test, each material (~ 0.3 g) was placed homogeneously in an alumina crucible. The experiment was carried out at temperatures between 500 and 850°C and in cycles of 8, 16 or 48 hours, subject to the stability shown by each material. A tubular furnace (THERMOLYNE type 21100) with a quartz tube was used for the heat treatments. To begin the experiment, pure N_2 was allowed to flow for 20 minutes in order to purge the system. The system was then filled with a flow rate of 4 L h^{-1} of the wet (pH_2O~0.03 atm) or dry 3%H_2/N_2 (~2 bar pressure), also for 20 minutes. Once the purge and filling stage was over, the oven was set with a ramp of 300°C h^{-1} to the operating temperature, while maintaining a minimum flow of ~2 L h^{-1} of the

reducing mixture. When the desired temperature was reached, the flow of the anodic atmosphere was increased to 4 L h^{-1}. After these two steps, the amount of wet atmosphere (~2 L h^{-1}) was decreased and kept until the system was cooled. Finally, the obtained sample was analysed by means of XRD.

Subsequently and considering the preliminary results, a high temperature diffraction (HT-XRD) study was also carried out, but now in a humid anodic atmosphere of 3% H_2/Ar (pH_2O~0.03 atm). In this case, a Bruker D8 diffractometer equipped with an Anton Paar XRK900 camera was used. The composite was placed in a Macor® vitro-ceramic sample holder and the data were collected in a range of 2θ = 13-70° (15 min per scan), with a 0.015° step and in two segments: i) from room temperature to 500°C every 50°C and ii) from 500 to 800°C every 20°C. In all measurements, the same ramp rate of cooling and heating of 0.1°C s^{-1} was used. The lattice parameters were cyclically refined with the programme FullProf [170] and its graphic interface WinPLOTR [171]. The background was fitted with a polynomial function of 6 coefficients and the shape of the peaks with a pseudo-Voigt function. The latter includes a Cagliotti function with variables U, V, W, the η parameter (Gaussian-Lorentzian mixture) and 2 parameters for peaks asymmetry.

2.3 ELECTRODE-ELECTROLYTE COMPATIBILITY

2.3.1 Determination of chemical compatibility. In a SOFC cell, the electrodes come into direct contact with the electrolyte and may react chemically during cell elaboration and/or at the operating conditions of the device. For that reason, it is carried out the procedure describe in Figure 14. In first place, the compounds synthesized in this work were mixed in an agate mortar with the electrolyte powder (50%w/w). For this, Yttria-stabilized Zirconia in its cubic form was used, *i.e.* with fluorite structure of space group *Fm-3m* (8YSZ, 8mol% Y_2O_3 in ZrO_2, Fuel Cell Materials). Each electrode-electrolyte mixture was then: i.) examined by means of X-ray diffraction; ii.) compacted into pellets and heat-treated at 1200, 1300 or 1350°C

(for 8 h), depending on the projected temperature of sintering of the electrode; iii.) after calcination, the sample was characterized again by XRD, iv.) then, the diffraction patterns were compared to identify possible structural changes and/or the formation of new phases. Finally, if the case of a material that is stable in anodic atmosphere, the same experiment was performed again immediately after the air test, but in a reducing environment (3%H_2/N_2 wet or dry).The conditions corresponds to a temperature in the range 700-800°C and, a test duration of 6 or 16 h, depending on the particular characteristics of the compound.

Figure 14. Flow diagram for the Electrode-Electrolyte Compatibility.

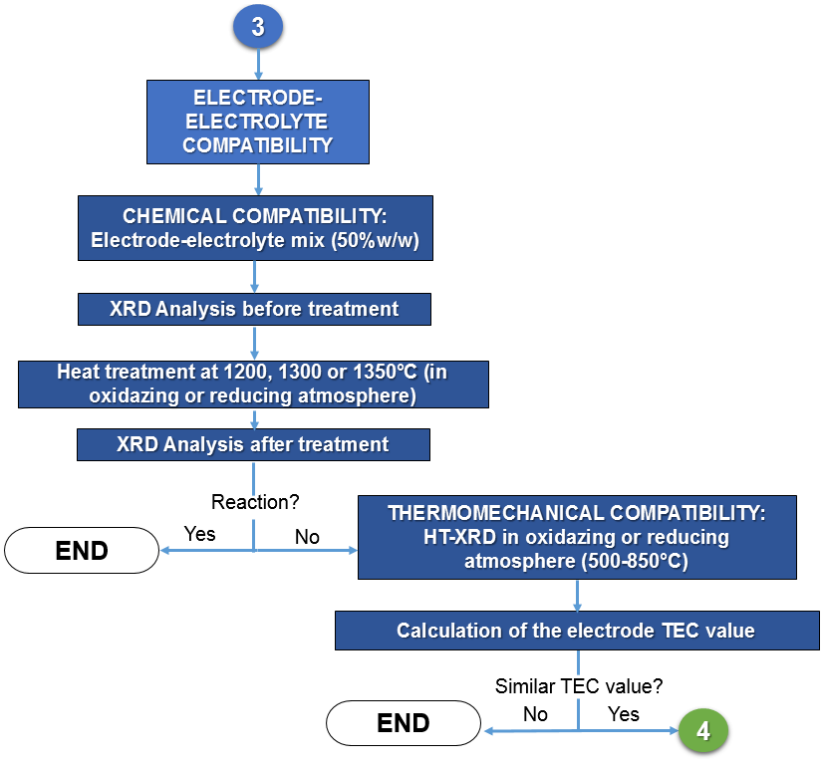

2.3.2 Analysis of the thermo-mechanical compatibility. The materials of a fuel cell are exposed to heating-cooling cycles, for this reason the thermal expansion coefficient (TEC) of the synthesized electrodes must be determined, for which the high temperature X-ray diffraction (HT-XRD) can be used. This particular kind of

measurement consists of collecting a diffractogram at different temperatures to observe the structural evolution of the studied phase. In this work, the patterns were measured with a Rigaku Smartlab diffractometer equipped with an Anton Paar DHS1100 heating device, under an air atmosphere and using an alumina support for the samples. Data were collected in the range of 2θ=13-64° or 2θ=13-70° (10 min per scan), with a 0.010° step and every 25°C from room temperature to 800 or 850°C. Then, the obtained diffractograms were cyclically refined with the programme FullProf [170] and its graphic interface WinPLOTR [171]. The background was fitted with a polynomial function of 6 coefficients and the shape of the peaks with a pseudo-Voigt function. The latter includes a Cagliotti function with variables U, V, W, the η parameter (Gaussian-Lorentzian mixture) and 2 parameters of asymmetry.

2.4 THERMOGRAVIMETRIC STUDY (TG) IN DIFFERENT ENVIRONMENTS

In order to study the oxygen stoichiometry and the evolution of the materials with the temperature in cathodic and anodic conditions, the mass variation of a representative sample was measured following several thermal treatments in different atmospheres. Essentially, the thermobalance consists of a high precision Cahn electrobalance 1000 (±10 μg) [47], a temperature controlled oven (20-1000°C) and a computerized recording system. The system consists of two arms, in each of which flow the same gas and a cylindrical crucible of alumina is placed (3x10 mm, Diameter x Length), but only one contains ~ 0.5 g of sample because the other serves as a reference. Thus, when the system is heated at a constant speed, the mass difference between the reference and the sample is recorded, and therefore can be quantified.

The experiments were carried out in air atmosphere (flow of 80 mL min^{-1}) from room temperature to 900°C (with heating/cooling ramp rates of 0.2°C min^{-1}). The same heat treatment was carried out, this time in an argon environment (flow of 40 mL min^{-1}). Additionally, the samples were exposed to a 50%H_2/Ar (flow of 80 mL min^{-1})

reducing atmosphere until the material was decomposed to its initial reagents, so that it was carried out up to 900°C or even 1000°C (with ramp rates of 5°C min^{-1}) if the sample proved to be very stable.

After this cycling procedure, the change in the oxygen stoichiometry ($3+\delta$) of the $ABO_{3+\delta}$ compound under all conditions, can be calculated each temperature. For example, $YMnO_{3+\delta}$ can be totally reduced into the oxides in diluted hydrogen according to:

$$YMnO_{3+\delta} + \delta H_2 \rightarrow \frac{1}{2}Y_2O_3 + MnO + \delta H_2O \qquad (29)$$

So, the oxygen stoichiometry equation includes the molecular weight of the obtained oxides and the atomic weight of the cations in the studied material and can be calculated by the following equation:

$$3 + \delta = \frac{\left(\left(\frac{m_i}{m_f}\right) * \left(M(MnO) + \frac{1}{2}M(Y_2O_3)\right)\right) - (M(Y) + M(Mn))}{M(O)} \qquad (30)$$

Where $3 + \delta$ is the oxygen content of the sample,

m_i is the weight of the sample at any measured point,

m_f corresponds to the weight of the totally reduced compound,

And $M(A)$ is the molecular weight of the reduction products or the elements constituting the mixed oxide.

2.5 TRANSPORT PROPERTIES

With the aim to know the conductivity of materials, it is necessary to follow the protocol in Figure 15:

Figure 15. Flow diagram to establish the electrical conductivity of the materials

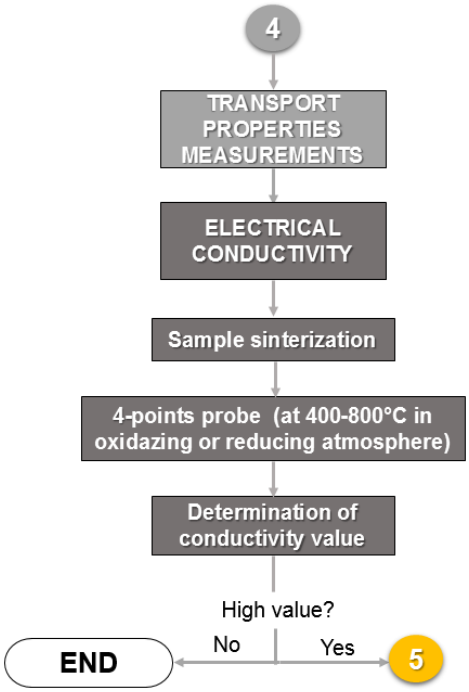

2.5.1 Electrical conductivity measurements. The 4-point probe technique is used to determine the electrical resistivity of the compounds. Those measurements were performed with the collaboration of UCCS (Lille, France). It consists in measuring the potential difference (V) between two internal points of a dense specimen, by which a current (I) is circulated between two external points (direct current, DC) [47]. By knowing these values, the ohmic resistance (R) can be determined, according to equation *(31)*:

$$R = \frac{\Delta V}{\Delta I} [=] \Omega \qquad (31)$$

From the resistance, the electrical resistivity ρ of the material can be defined

$$\rho = \frac{RS}{L} \; [=] \; \Omega * \mathrm{cm} \qquad (32)$$

Where *S* is the cross section of the sample [cm^2],
and *L* is the length [cm] between the points in which the potential difference is measured.
At the same time, it is possible to calculate the conductivity (σ), since it is the inverse value of the resistivity:

$$\sigma_{measured} = \frac{1}{\rho} \; [=] \frac{1}{\Omega * \mathrm{cm}} \qquad (33)$$

Finally, the measured conductivity data were normalized to take into account the fact that the sample is not fully dense, using the following empirical formula [173]:

$$\sigma_{corrected} = \frac{\sigma_{measured}}{\left(1 - \left(\frac{\pi_{total}}{100}\right)\right)^2} \; [=] \frac{1}{\Omega * \mathrm{cm}} \qquad (34)$$

Where π_{total} is the porosity (in %) of the sample and is calculated from the sample compactness knowing its theoretical and experimental density (see below).

2.5.1.1 Sintering procedure. In order to measure the conductivity of the materials, it is necessary to prepare highly dense samples. In our case, the best conditions to obtain full density were determined with a dilatometry curve. Thus, for each experiment, cylindrical specimens of the material were prepared by axial (Perkin-Helmer press) then isostatic pressing (1800 bar, Nova Swiss Ref: 7-100-306), with dimensions 5 x 8 mm (Diameter x Length). These cylinders were placed in a Netzsch DIL402C dilatometer and the experiments were carried out in air and in a temperature range of 50-1550°C.

From the dilatometry curve, several temperatures were chosen in the region of highest sintering rates (first derivative of dilatometry curve), this time using pressed pellets sintered in a furnace for 2 hours, with heating and cooling ramps of 5 °C min^{-1}. The above was performed in order to determine to which temperature the samples with highest percentage of compacity can be obtained, since their value must be between 80 and 100% in order to be able to adequately measure the conductivity of the material.

The compacity ($Comp[\%]$) is the parameter of comparison between the theoretical density (ρ_{theo}) and the experimental density (ρ_{exp}), and is defined as

$$Comp[\%] = \frac{\rho_{exp}}{\rho_{theo}} * 100 \qquad (35)$$

Meanwhile, the experimental density (ρ_{exp}) is:

$$\rho_{exp} = \frac{m_{exp}}{V_{exp}} \; [=] \; \frac{g}{cm^3} \qquad (36)$$

This was calculated from the weight of the specimen (m_{exp}) taken on an analytical balance (sensitivity 0.0001 g), and its volume (V_{exp}), which corresponds to that of a cylinder (digital caliber, sensitivity 0.01 mm), *i.e.*:

$$V_{exp} = \pi . R^2 . h \; [=] \; cm^3 \qquad (37)$$

Where
R is the cylinder radius [cm],
and h, the cylinder height [cm].

Finally, to calculate the theoretical density (ρ_{theo}) it is necessary to take into account the crystalline structure adopted by the studied materials. In this way, the following equation was used *(38)*:

$$\rho_T = \frac{Z*M}{N*V} \; [=] \; g \qquad (38)$$

Where M is the molecular weight [g mol^{-1}],
Z, the number of formula units per cell,
V, the cell volume [cm^3],
and N, the Avogadro number (6.022 x 10^{23} mol^{-1}).
It is important to remember that for a hexagonal ordering, the volume of the cell is:

$$V = a^2 c \frac{\sqrt{3}}{2} \; [=] \; Å^3 \qquad (39)$$

2.5.1.2 Sample preparation and measurement conditions. With the data obtained from the sintering study, the temperature was chosen to obtain the denser specimens for each compound. Then bars with dimensions of 5 x 10 mm (Diameter x Length) were pressed following the procedure described in the previous section. Two radial grooves were then fitted, and each face was covered with gold paint in order to improve the contact with the mounting elements. Then a curing step at 650°C (for 1 h) of the deposited paint was carried out to remove the organic compounds present in it. The prepared sample was connected to a circuit by surrounding it with gold filaments equatorially through the grooves previously drawn and then the whole assembly was introduced in a hermetic tubular furnace.

As shown in Figure 16, the potential difference between the gold wires (1) and (2) was measured when a current was applied between the electrodes (a) and (b) with a potentiostat (BioLogic-VSP) controlled by EC-Lab software V11.01 (March 2016).

Figure 16. Schematic diagram of the 4-point resistivity measurements assembly: (a) and (b) are the electrodes between which the current is applied; (1) and (2) represent the gold wires in which the potential difference is measured

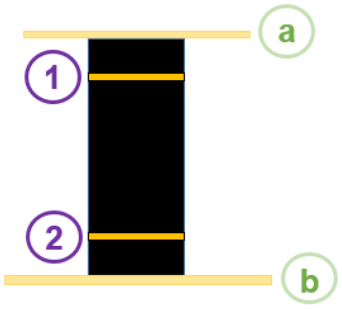

The tests were performed in the temperature range from 850 to 400°C, cooling down, the sample every 25°C, in air and, in case the material is stable in reducing atmosphere, also in a wet reducing environment (3%H_2/Ar), as explained below. At each condition, a CP (chronopotentiometric) staggered routine was performed with EC-Lab (Figure 17), varying the current between four selected values. Because of the measurements, multiple datasets of potential difference and intensity for each temperature were obtained.

Figure 17. . Illustration of the staggered chronopotentiometry routine.

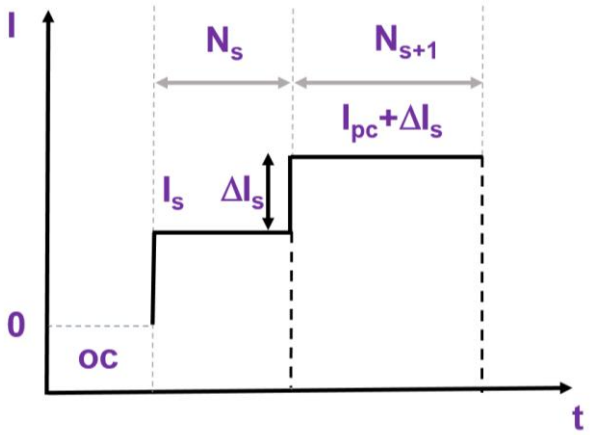

Adapted from [174]

The software saves the data in a text file that is treated with a series of Excel macros, since manual calculations would be very tedious for such a volume of information. After data treatment, we obtain four pairs of potential difference and intensity with which the resistance values, *R*, can be calculated according to equation *(31)*. Afterwards, the resistance values obtained are averaged (except if some strong deviation from linearity is observed at high current values). Finally, this calculated value is used to determinate the conductivity using equations *(32)* and *(33).*

2.5.1.3 Sample characterization by Scanning Electron Microscopy (SEM). The sintering study was complemented with the Scanning Electron Microscopy technique with which it was possible to observe the real porosity of the samples. In general, the microscope consists of an electron optical column, a vacuum system and a software (Figure 18).

Figure 18. Parts of the Scanning Electron Microscope.

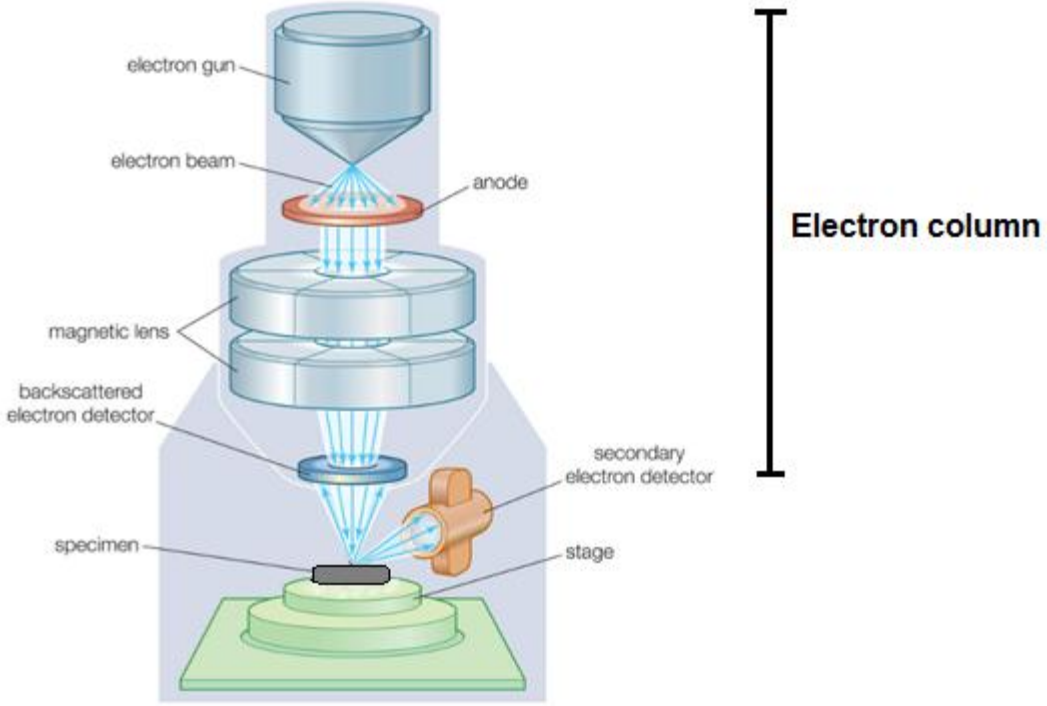

Adapted from [175]

The sample are covered with a thin carbon or metal layer to increase the electronic conduction properties of the sample, if necessary. The sample are scanned with the accelerated electrons from an electron gun. These constitute a very concentrated electron beam; specifically, of secondary electrons when you want to analyse the topography of an material [176], [177]. Thus, the beam is scanned in a rectangular raster over the specimen and the intensities of various signals created by interactions between the electrons and the specimen. A detector measure the amount of electrons sent from the sample and stored it in a computer memory [175], [177]. In this form, the scanning electron microscope can create an enlarged image of the surface of one object [176], [177] and it can provide information about microstructure, fractures, spatial variations in chemical compositions, among others [178]. Thus, in the particular case of this work, the Scanning Electron Microscopes used were (secondary electron mode): PHILIPS SEM 515 (with a W filament) equipped with a EDS GENESIS 2000 spectrometer (Centro Atómico de Bariloche, Argentina), SEM-FEG Nova Nano SEM 230 (Centro Atómico de Bariloche, Argentina) of field emission and a Hitachi S3400 (LILLE, France).

2.6 ELECTROCHEMICAL MEASUREMENTS.

The electrochemical behaviour of selected compounds was analysed by Electrochemical Impedance Spectroscopy. The spectra were obtained with a frequency response analyzer (FRA2) connected to a potentiostat AUTOLAB PGSTAT30 (EcoChemie). The measurements were made in a frequency range of 1MHz to 1mHz, with an alternating voltage (amplitude 10mV) and zero Bias voltage. The temperature range was 500-800°C. Subsequently, the data were adjusted by least squares method with equivalent circuits using the software Zview [179]. The flow diagram of the procedure is summarized in Figure 19.

Figure 19. Flow diagram to measure electrochemical properties of the compounds.

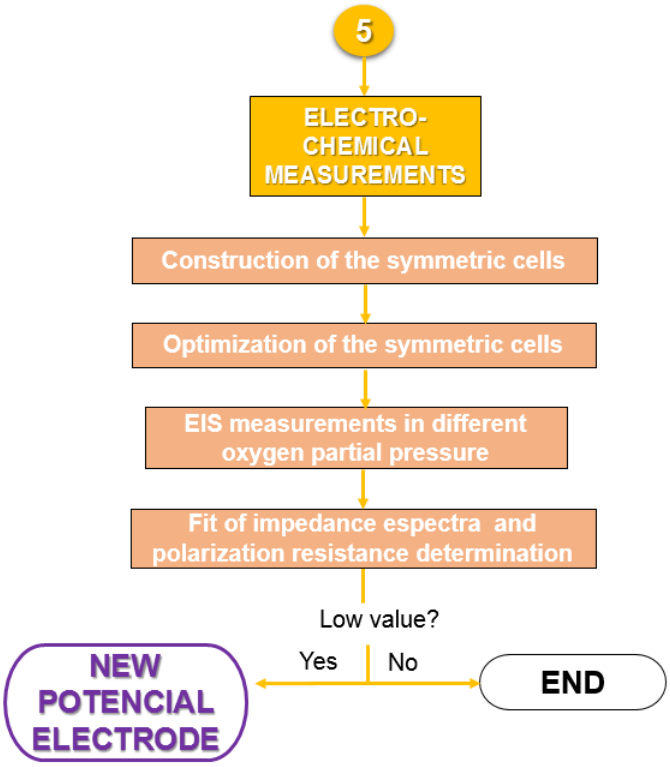

2.6.1.1 Definition of the Electrochemical Impedance Spectroscopy method (EIS). In general, impedance is the response of an electrochemical system to a potential which has been supplied [180]. The dependence of the frequency in relation to the impedance allows explaining the physicochemical processes, which are carried out inside the cell, since the impedance is the superposition of all these phenomena. The principle of the technique can be seen in Figure 20:

Figure 20. Principle of Electrochemical Impedance Spectroscopy measurement.

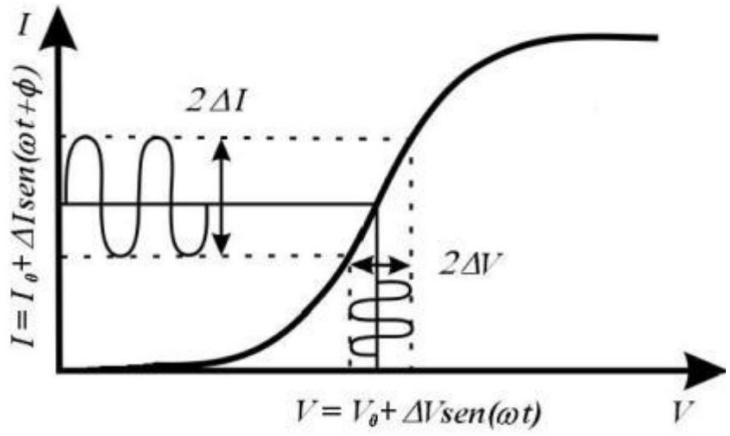

Adapted from [44].

First, a symmetric cell receives an electrical signal of small amplitude (ΔV, Alternating Voltage) and variable frequency (ω) which are defined as it follows:

$$V(\omega t) = V_0 + \Delta V sin(\omega t) \quad (42)$$

$$\omega = \frac{f}{2\pi} \quad (43)$$

Therefore, the ions and electrons within the system, can move inside the bulk of the constitutive materials or through the interfaces between them, generating in turn a potential drop [169]. The phase change φ and the amplitude, or the real and imaginary parts of the resulting current, I, at each frequency is given by:

$$I(\omega t) = I_0 + \Delta I sin(\omega t + \phi) \quad (44)$$

The relation between current and voltage [169], which is the impedance (Z) follows the equation:

$$Z(\omega) = \frac{V(\omega)}{I(\omega)} = Z' + jZ'' \qquad (45)$$

Particularly, in this work, the technique was used to study the polarisation resistance (Rp) of the electrodes. This value is determined using the representation of Nyquist where $-Z''$ vs Z' is plotted. R_p corresponds to the difference $Z'(\omega \to 0) - Z'(\omega \to \infty)$, which must be normalised according to the following equation [169]:

$$ASR = \frac{R_{p*}A}{2} \qquad (46)$$

Where
ASR is the Area Specific Resistance,
and A, the geometric area of the electrode.

2.6.1.2 Samples preparation. The cells were prepared using the following Symmetric configuration: Current collector/electrode/electrolyte/electrode/current collector as shown in Figure 21:

Figure 21. Configuration of symmetric cells to measure Electrochemical Impedance Spectroscopy data.

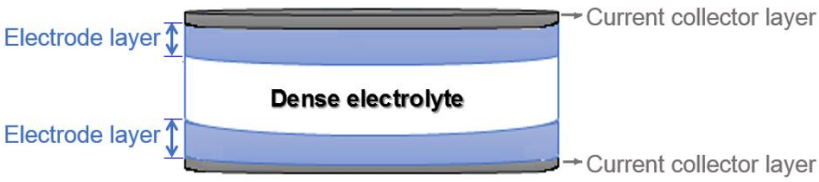

To this end, a pellet (0.9 cm diameter) of Yttria-stabilized zirconia (TZ-8Y, Tosoh Corporation) was densified with a heat treatment at 1300°C (heating and cooling ramp rates of 3.5°C min^{-1}) for 6 hours. Then, the electrode material and the current collector layers were deposited by means of the spin coating technique with the aim

of achieving a porous microstructure. This deposition method is widely used because it is carried out in only three steps, as shown in Figure 22.

Figure 22. Steps for the deposition of material by the spin coating technique.

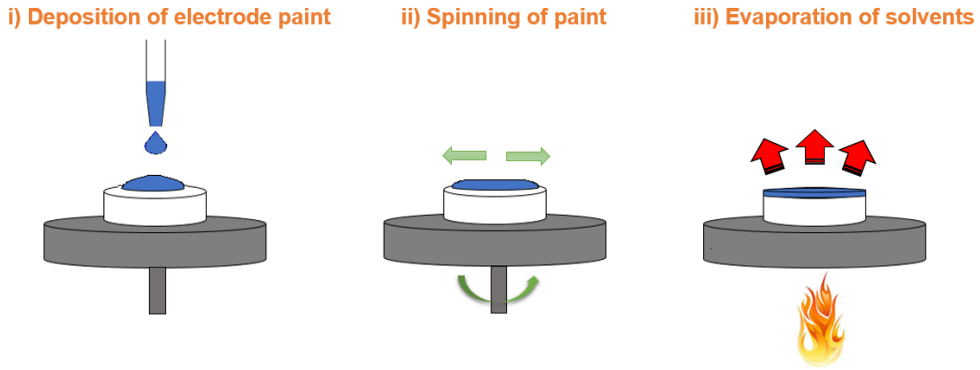

Adapted from [181].

i) To start, a solution is prepared with the desired material to coat. This is normally called ink [182] and its composition belongs to an empirical formula whose quantities are listed in Table 3. The ink is then prepared by mixing isopropanol with the electrode material and the PVB and PVP polymers until the alcohol evaporates. Subsequently, the alpha terpineol and isopropanol are added to the powder, until it is completely dispersed. In this way, a drop of this ink is applied on the electrolyte with the aid of a pipette Pasteur.

i) The densified pellet is then rotated at a speed of 2800 rpm for 15 s, which allows the ink to spread on the electrolyte although part of the ink is thrown by the edges due to the centripetal acceleration [183].

ii) Finally, the pellet is heated in an oven at 50°C to evaporate the solvents.

The process is repeated as many times as necessary until a desired thickness is obtained, and then a heat treatment (sintering) is made which allows the adhesion of the material and a certain level of porosity. The current collecting layer, which in this case is also a ceramic compound, was deposited in the same way using the spin-coating technique.

Table 3. Reagents used to prepare the spin coating ink.

Reactant	Function	Weight (%)	Supplier	Purity (%p/p)
Polyvinyl Butiral (PVB)	Binder	1.7	Aldrich	99.9
Polyvinylpirrolidone (PVP)	Dispersant	0.9	Alfa Aesar	99
Alfa Terpineol	Provides viscosity	23.6	Alfa Aesar	95
Isopropanol	Solvent	38.8	Sigma-Aldrich	99.8
Material to deposit	-	35	-	-

2.6.1.3 Description of the Electrochemical Impedance Spectroscopy Measurement System. Symmetrical cells are spring-secured to a head having the platinum current collectors in the form of grids. The head is then placed in a sealed alumina tube, which is inside a high temperature furnace (T<1000°C) and through which gases may flow. To avoid any interference between the measurements and the furnace feed, the assembly includes a Faraday box enclosing the samples [47]. The system is connected to a potentiostat and the spectra are obtained with a frequency analyser. The scheme of the system is shown in Figure 23.

Figure 23. Assembly for Electrochemical Impedance measurement in controlled atmosphere.

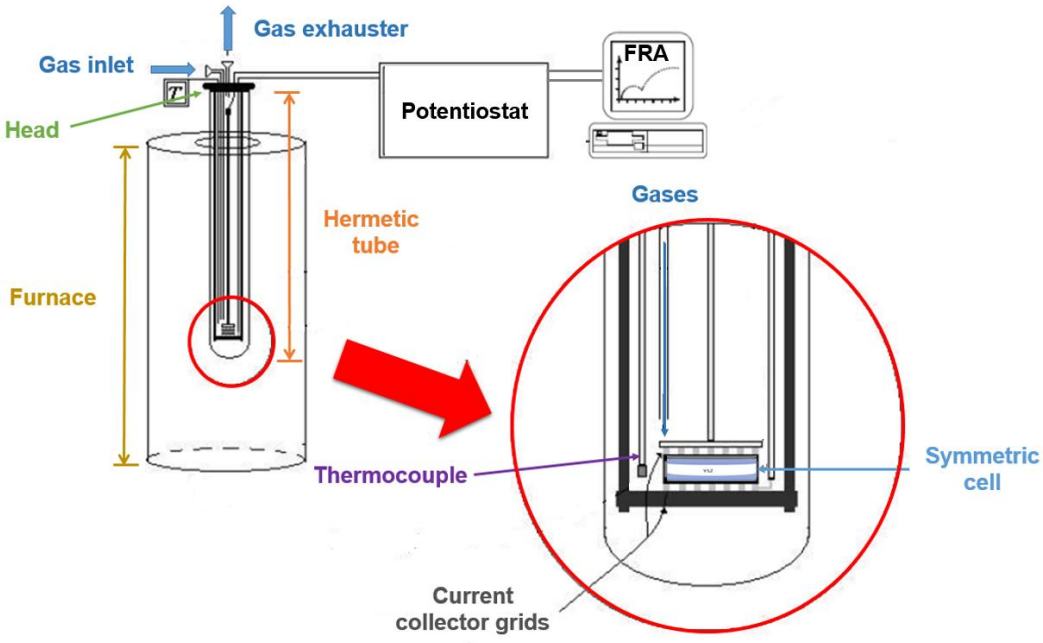

Adapted from [47].

2.5.3.4 Preliminary EIS measurements. The first symmetric cells which were measured were elaborated with different characteristics in order to determine two optimal conditions in oxidizing (cathode) conditions:

i) *The sintering temperature*: symmetric cells were prepared with 4 layers of the compound of interest (~20 µm) and 2 (~10 µm) of the current collector (LSM, $La_{0.8}Sr_{0.2}MnO_3$). They were heat-treated at temperatures around the synthesis temperature (1000-1300°C, the ramps and the dwell have the same duration of 1h). Afterwards, the cell with the lowest values of ASR was considered to be optimal with respect to the sintering temperature.

ii) *Number of layers*: cells were prepared at the optimum sintering temperature, with two layers of LSM current collector, but varying between 2, 4 and 6 the number of layers of the deposited electrode material. Similarly, the selection was based on the criterion of the lowest ASR value after measurements in air.

Such optimization provides the best symmetric cell configuration, which was measured in the temperature range of 500-800°C and an air atmosphere. However, due to time limitations, it is important to mention that the optimization of number of layers was only carried out for $YMnO_3$ and we assume that the same kind of behaviour would occur for the other composition

2.5.3.5 Study of EIS in pO2 vs temperature. To better establish the reaction mechanism that rules the behaviour of an electrode material, an Electrochemical Impedance Spectroscopy study is required varying the oxygen partial pressure (pO_2) at a constant temperature (600-800°C). This is due to the fact that, in these conditions, the relaxation times (and thus the relaxation frequencies) of each process can be separated and the limiting steps cease to overlap and can be analysed individually [40]. Thus, the optimal symmetric cells were analyzed in different atmospheres in the range of $10^{-6} < pO_2 < 1$ atm. This environment is produced and measured with an electrochemical pump-oxygen sensor system coupled to the thermobalance as described in 2.4. Particularly, the oxygen pump is made with an yttria-stabilized zirconia tube, on the outer and inner surfaces of which porous Pt electrodes are deposited. In the latter, a current (I) is applied and at the same time an inert carrier gas is circulated, Ar in this case (flow of 100 mL min^{-1}). Given that zirconia is an ionic conductor, it is able to transfer oxygen atoms from the outside to the inside (or *vice versa*) when the current is applied, thereby modifying the pO_2 of the carrier gas. The stabilized zirconia tube, which acts as the oxygen sensor, can determine the partial pressure of oxygen (pO_2^{system}) by measuring with one electrode the electric potential of the gas circulating inside it, the other side (outside) being at a fixed potential (air) [47].

In this way, the oxygen content is accurately controlled if the value of the resulting equilibrium potential difference (10-600 mA) is known after the current has been applied. This potential difference relates to Nernst's Law according to:

$$\mathrm{pO}_2^{system} = \mathrm{pO}_2^{air} * e^{\left(\frac{F*\Delta V}{RT}\right)} [=] atm \qquad (47)$$

Where pO_2^{system} is the measured partial oxygen pressure [atm],
pO_2^{air}, the air partial oxygen pressure [atm],
ΔV, the potential difference at equilibrium [Volt],
F, the Faraday constant 96485 [Coulomb/mol],
R, the gas constant 8.3144 [(Coulomb*volt)/(mol*K)],
and T, the system temperature [K].

These conditions are applied to the symmetric cells in the previously described assembly. Subsequently, the obtained impedance spectra are interpreted with physical models using equivalent circuits [40].

2.5.3.6 EIS Measurements in a reducing atmosphere. The optimized cells made of materials with potential anode application were also measured in a reducing atmosphere (10%H_2/Ar, dry), after the air measurements. In this case, the experiments were carried out in the same range of temperature 500-800°C, but using LBM ($La_{0.8}Ba_{0.2}MnO_3$) instead of LSM as current collecting material because the latter decomposes in reducing environment [184]. Then, using the same symmetric cell arrangement, the test was realized at constant temperature 800°C and with different atmospheres (10, 20, 50 and 80%H_2/Ar, dry) in order to better understand the reaction mechanism varying the pH_2.

2.5.3.7 EIS data adjustment. The collected spectra were fitted with equivalent circuits built from deep analysis of impedance data, and taking into account in particular their shape; subsequently, one element was attributed to one physic process according to the dependance with pO_2, capacitance values and frequency ranges [44]. The equivalent circuit generally presents ideal resistance and capacitances, and in some occasion inductances; they are disposed in series and/or

parallel. A resistance represents a conductor path and a resistor describes volume conductivity and a electrode reaction. For its part, the capacitances and inductances are asociated to adsorption processes in the electrode or spatial charge polarization regions [185].

3. STUDY OF PURE AND Zr-DOPED $YMnO_3$ COMPOUNDS AS SOLID OXIDE FUEL CELLS ELECTRODE

3.1 SYNTHESIS AND STRUCTURAL CHARACTERIZATION OF $Y_{1-x}Zr_xMnO_{3+\delta}$ (x=0, 0.05, 0.10, 0.15) MATERIALS.

The synthesis of $Y_{1-x}Zr_xMnO_{3+\delta}$ (x=0, 0.05, 0.10, 0.15) materials has been initially studied by the solid-state method, using high temperatures up to 1400°C to get single-phased compounds. When the XRD patterns of the prepared samples are analyzed, using a specialized database, we can confirm the obtention of the desired hexagonal structure of space group $P6_3cm$, for each of them (Figure 24).

Figure 24. X-Ray diffraction patterns of $Y_{1-x}Zr_xMnO_3$ ($0 \leq x \leq 0.15$) (with hkl indices).

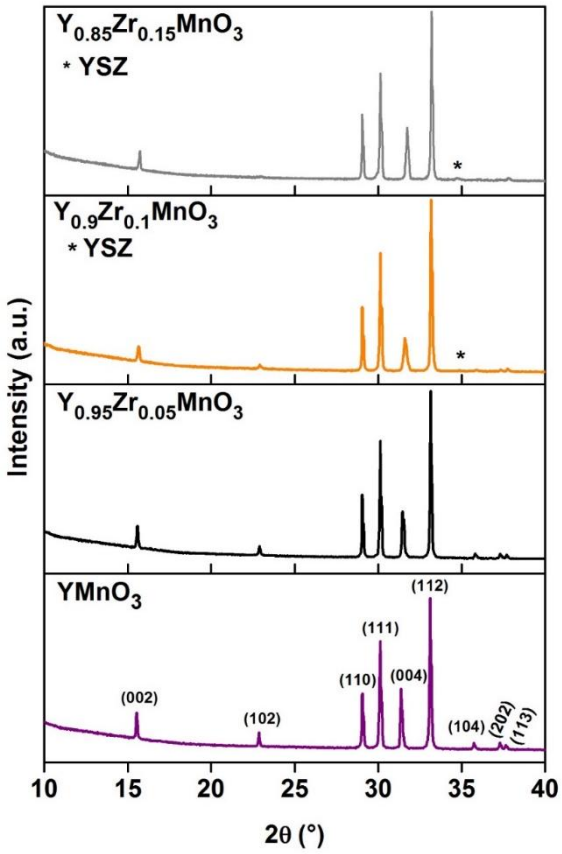

Nevertheless, for x=0.1 compositions, we can observe an additional peak that appears in the diffraction patterns around 2θ≈34.9º position. This reflection belongs to a YSZ-type impurity that crystallizes in a cubic space group (F*m-3m*). The presence of such phase contradicts the results obtained by Van Aken *et al.* who claim that pure $Y_{1-x}Zr_xMnO_{3+\delta}$ materials could be synthesized in contents up to x=0.3 [186]. However, our results agree with the work of Katsufuji *et al.*, in which the authors describe a solubility limit of Zr around x~0.10 in $YMnO_3$ matrix [187]. At this point, it is worth emphasizing that although we are looking for single-phase electrode materials, the amount of YSZ that is present as "impurity" is minimal and would not be indeed problematic for the application as SOFC electrode. As discussed in the state of the art, YSZ is a common SOFC electrolyte, and in many occasions, it is added to the electrodes to improve the ionic conductivity of the latter or to make them more thermally or chemically compatible with the same electrolyte. When comparing now the diffractograms of the compounds with different Zr-doping, it seems that the *(hk0)* peaks, such as *(110)*, remain in their positions. Nonetheless, *(00l)* type peaks, such as *(004)*, move towards high values of 2θ as the degree of substitution is increased (Figure 25), suggesting that *a* cell parameter remains nearly constant while *c* becomes smaller as the concentration of Zr increases.

Figure 25. Evolution of the *(110)* and *(004)* peaks for x=0 (purple line), x=0.05 (black line) and x=0.10 (orange line).

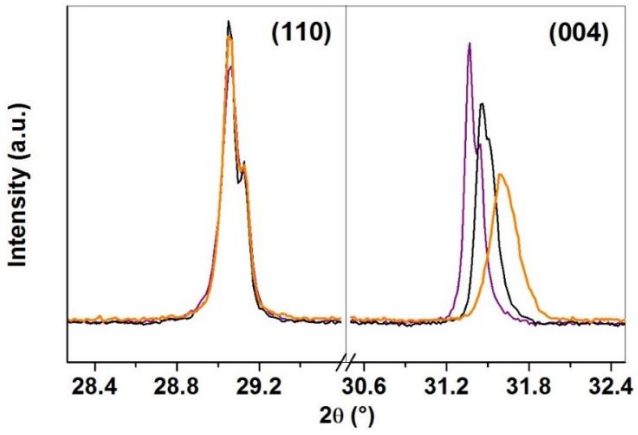

To understand the influence of these changes within the materials series, the crystal structure have been refined in each case using the Rietveld method and the X-ray diffraction data; in particular, the lattice parameters of the synthesized compounds have been determined. The results of those calculations are summarized in Table 4 (atomic positions are listed in Annex B).

Table 4. Structural parameters of *P*6$_3$*cm* $Y_{1-x}Zr_xMnO_3$ (x= 0, 0.05 and 0.10) after synthesis, as obtained from Rietveld refinement using XRD data.

Sample	**a (Å)**	**c(Å)**	**V(Å^3)**	**Reliability factors**
x=0	6.1403(3)	11.3952(5)	372.08(3)	R_p(%)=2.37 GOF=1.45
				R_{wp}(%)=3.20 R_B=5.20
x=0.05	6.1398(3)	11.3637(6)	370.084(3)	R_p(%)= 3.12 GOF=1.56
				R_{wp}(%)=4.35 R_B=4.74
x=0.10	6.1405(4)	11.3171(8)	369.55(4)	R_p(%)=3.16 GOF=1.74
				R_{wp}(%)=4.49 R_B=9.46
R_p: profile factor R_{wp}: weighted-profile factor GOF: goodness of fit R_B: Bragg factor				

First, for $YMnO_3$, we can conclude that the refined lattice parameters exhibit values that are close to those obtained by other authors (Table 5).

Table 5. Comparison between previously reported lattice parameters of $YMnO_3$ and our work.

Reference	a (Å)	c(Å)	Synthesis technique
Van Aken *et al.*[112]	6.1387	11.4074	Flux method
Gibbs *et al.*[136]	6.14151(3)	11.40134(8)	Solid state reaction
Overton *et al.* [188]	6.155	11.40	Solid state reaction
This work	6.1403(3)	11.3952(5)	Solid state reaction

Concerning the evolution of the lattice parametes with x, as observed in Figure 26, there is an appreciable difference depending on the *a* or *c* directions.

Figure 26. Evolution as a function of x of the cell parameters *a*, *c* and volume V along the $Y_{1-x}Zr_xMnO_3$ series.

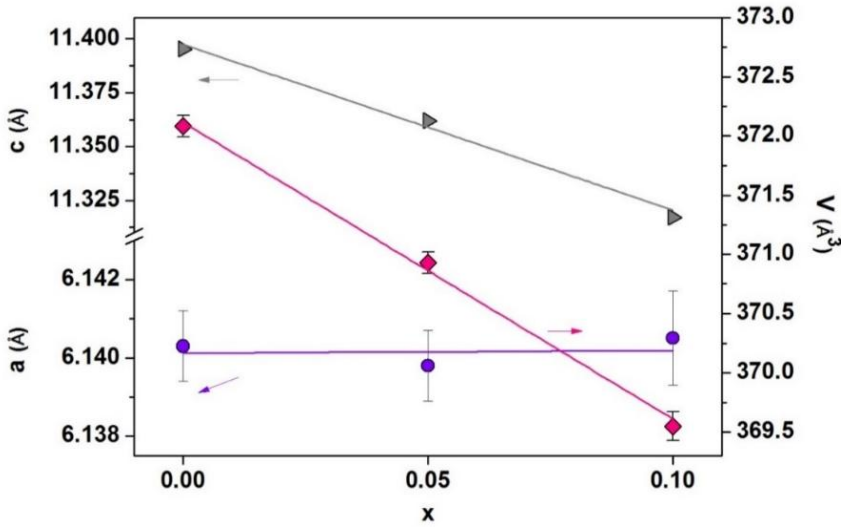

As already described after the qualitative inspection of the patterns, there is an overall decrease of the cell volume as x increases in $Y_{1-x}Zr_xMnO_{3+\delta}$, as a result of a strong decrease in the *c* lattice parameter. Meanwhile, *a* parameter remains about the same. Taking into account the previous trends, we can tentatively describe the effect of the insertion of Zr^{4+} in the $YMnO_3$ matrix, at a structural level. In a first instance, the decrease of the volume for the substituted compounds can be a consequence of the fact that part of the Y^{3+} cation (r_{Y3+}=1.019 Å) is replaced by a smaller Zr^{4+} cation (r_{Zr4+}=0.84 Å)[189]. Nevertheless, such explanation is not completely obvious, as it must be remembered that to observe the replacement of Zr^{4+} at the site of Y^{3+}, a charge compensation is required [186]. A first hypothesis would be to consider that the charge equilibrium occurs according to the following reaction in which Mn_{Mn}^{X} and Mn'_{Mn} means Mn^{3+} and Mn^{2+} cations at the manganese crystallographic site in $YMnO_3$:

$$Y_Y^X + Mn_{Mn}^X + 3O_O^X + ZrO_2 \rightarrow Zr_Y^{\bullet} + Mn'_{Mn} + 3O_O^X + {}^1/_2\, Y_2O_3 + {}^1/_4\, O_2 \qquad (48)$$

In that way, it may look that the balance of these structures is achieved when a part of the Mn^{3+} cations are reduced to Mn^{2+} [187], [190]. Considering that the latter cation has a greater ionic radius than Mn^{3+} (r_{Mn3+}=0.58 Å and r_{Mn2+}=0.75 Å)[189], it becomes clear that the change of the transition metal-ionic size by itself does not explain the observed data, unless the effect is negligible with respect to the already discussed direct size effect due to Zr for Y substitution. Another hypothesis would be to consider that there is no manganese reduction due to Zr for Y substitution, but the insertion of oxygen excess interstitially, as described in the following equation:

$$Y_Y^X + Mn_{Mn}^X + 3O_O^X + ZrO_2 \rightarrow Zr_Y^{\bullet} + Mn'_{Mn} + 3O_O^X + {}^1/_2\, Y_2O_3 + {}^1/_2\, O_i'' \qquad (49)$$

In order to prove the veracity of one or the other hypothesis, the absolute oxygen content (3+δ) of $Y_{0.9}Zr_{0.1}MnO_{3+\delta}$ sample was determined in different conditions. For this purpose, the compound was thermally treated in air then, reduced to the corresponding precursors: $(Y,Zr)_2O_3$ and MnO using 50%H_2/Ar. Subsequently, the data were normalized calculating the difference between the weight of each point in

the cycles and the reduction products. The results of this study are shown in Figure 27.

Figure 27. Thermogravimetrical analysis (TGA) measurements of oxygen content for $Y_{0.9}Zr_{0.1}MnO_3$ and $YMnO_3$ as a function of temperature in air (heating and cooling rates= 0.2°C min^{-1}).

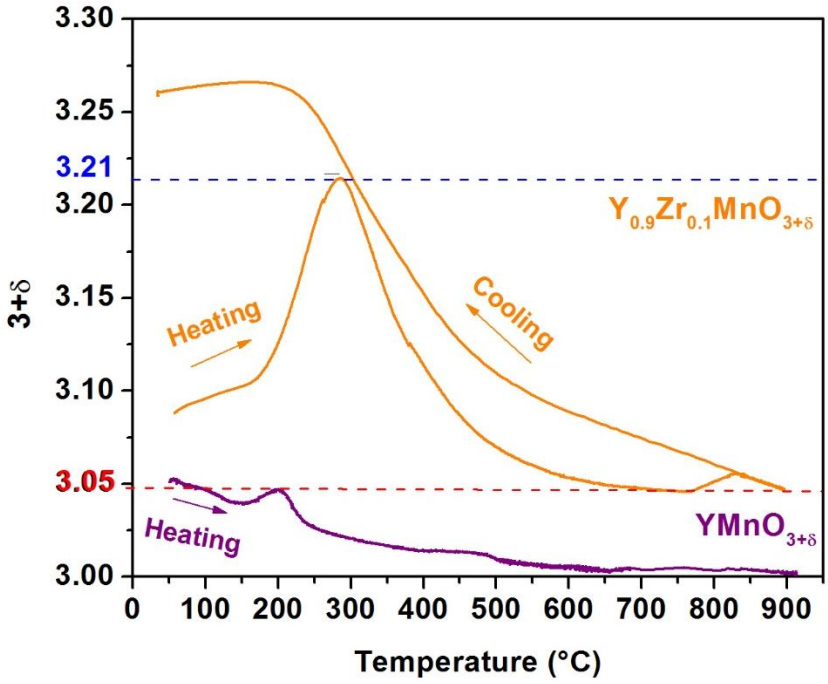

After analysis, the (3+δ) value is ~3.05 at temperatures higher than 550°C in air. Such result allows discarding the first hypothesis, since the stoichiometric oxygen content of the compound is deduced as $Y_{0.9}^{+3}Zr_{0.1}^{+4}Mn^{3+}O_{3.05}^{-2}$ and not $Y_{0.9}^{+3}Zr_{0.1}^{+4}Mn_{0.9}^{3+}Mn_{0.1}^{2+}O_{3.0}^{-2}$, that would correspond to the second and the first hypotheses, respectively. At the same time, the deduced oxygen content value of ~3.1 before TGA measurements (*i.e.* after synthesis) confirms the second affirmation. We may conclude that the initial stoichiometry of the material should be $Y_{0.9}^{+3}Zr_{0.1}^{+4}Mn_{0.9}^{3+}Mn_{0.1}^{4+}O_{3.1}^{-2}$, possibly due to the fact that a small fraction of Mn^{3+} cations are oxidized to Mn^{4+}, which in turn implies this sample exhibits an excess of oxygen.

During cooling, and specifically from T=400 To 200°C, the compound shows a weight uptake that is logically related to oxygen absorption due to manganese oxidation in air, a maximum of oxygen content of ~3.21 finally obtained that remains in that state until the lowest (room) temperature. The final material stoichiometry $Y_{0.9}^{+3}Zr_{0.1}^{+4}Mn_{0.68}^{3+}Mn_{0.32}^{4+}O_{3.21}^{-2}$ is reached after TGA, *i.e.* a greater oxygen excess than after synthesis. As a summary, we can affirm that Zr-doped $YMnO_3$ can absorbs/desorbs different amounts of oxygen depending on the temperature. This behavior seems common to all $AMnO_3$ hexagonal manganites, including the matrix $YMnO_3$, as briefly discussed in the state of the art. However, as shown in Figure 27, we can observe that the storage ability is much more pronounced for $Y_{0.9}Zr_{0.1}MnO_{3+\delta}$ in comparison to $YMnO_{3+\delta}$. For Zr-doped compounds, the oxygen content significantly raises in air (~3.21) and reaches values that, are only evidenced for $YMnO_3$ (or $ErMnO_3$ and $HoMnO_3$) under high pressures of oxygen and not in air under ambient pressure (~3.25 in pure oxygen and ~3.38 after high-pressure oxygen annealing at 190 bar at 400°C) [191]. Aiming to further study the origin of the differences between those materials and at the same time trying to obtain them at a lower temperature and using less thermal treatments, the classic solid-state technique was replaced by the Pechini method with heat treatment at 1100°C. The X-ray diffractograms of $YMnO_3$ and $Y_{0.9}Zr_{0.1}MnO_3$ samples synthesized using such technique can be found in Figure 28.

Figure 28. X-Ray diffraction patterns of $YMnO_3$ and $Y_{0.9}Zr_{0.1}MnO_3$ synthesized by the Pechini method (with (*hkl)* indices).

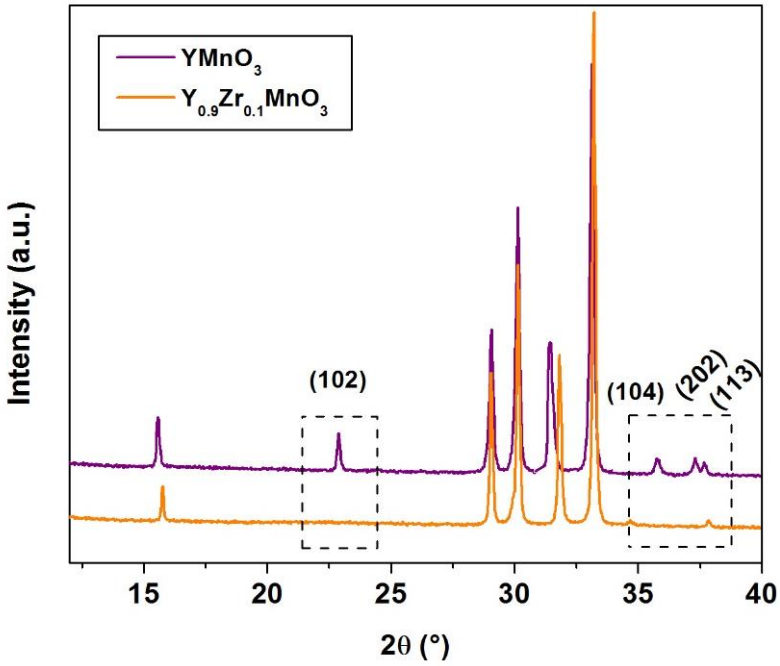

$YMnO_3$ diffraction pattern exhibits the same peaks sequence as for the samples prepared by the solid-state method, *i.e.*, a structure corresponding to the space group $P6_3cm$. Nevertheless, in the diffractogram of $Y_{0.9}Zr_{0.1}MnO_3$ prepared by the sol-gel technique, the peak located at $2\theta \approx 22.9°$ disappears completely, like some the reflections in the range of $2\theta \approx 35\text{-}38°$. Indeed, these modifications confirm that the structure has changed for the x=0.10 and the absence of any impurity proves the efficiency of the Pechini method to obtain pure materials at lower temperature. The lattice parameters of both materials refined the Full Pattern Matching (FPM) method are listed in Table 6.

Table 6. Structural parameters of $YMnO_3$ and $Y_{0.9}Zr_{0.1}MnO_3$ synthesized by the Pechini method, as obtained from FPM refinement using XRD data.

Space group	***a* (Å)**	***c*(Å)**	***V*(Å^3)**	**Reliability factors**
$YMnO_3$				
*P*6$_3$*cm*	6.1446(3)	11.3843(6)	372.23(3)	R_p(%)=2.67 GOF=1.51 R_{wp}(%)=3.59
$Y_{0.9}Zr_{0.1}MnO_3$				
*P*6$_3$/*mmc*	3.5503(3)	11.2513(9)	122.82(2)	R_p(%)=2.68 GOF=1.56 R_{wp}(%)=3.66
*P*6$_3$*cm*	6.1491	11.2513(9)	368.46	
R_p: profile factor R_{wp}: weighted-profile factor GOF: goodness of fit				

In Table 6, two sets of lattice parameter values for $Y_{0.9}Zr_{0.1}MnO_3$ are included, making easier the comparison with the case of $YMnO_3$. The above is possible since the parameters and the volume of the non-centrosymmetric and the centrosymmetric phases, are mathematically related according to [114]:

a lattice parameter (*P*6$_3$*cm*):

$$a=\sqrt{3}*a' \text{ [=] Å} \qquad (50)$$

c lattice parameter (*P*6$_3$*cm*):

$$c= c' \text{ [=] Å} \qquad (51)$$

Volume (*P*6$_3$*cm*):

$$V=3V' \text{ [=] } Å^3 \quad (52)$$

Where a', c' and V' are the cell parameters for the *P*6$_3$*/mmc* lattice.

This conversion shows, contrary to the samples prepared by solid state technique, a slight increase in *a* parameter and a significant decrease of the volume caused by the dramatic decrease in *c*, as a consequence of the Zr^{4+} for Y^{3+} substitution. Beyond that, Zr-doped $YMnO_3$ at the new synthesis conditions adopts a *P*6$_3$*/mmc* space group, mainly evidenced by the disappearance of *(102)* peaks. The same arrangement is indeed observed for $YMnO_3$ at temperatures higher than 980°C, and an increase of *a* parameter and decrease of *c* parameter are observed during such transition due to the fact that the bipyramids, initially buckled, are now perfectly aligned in the *P*6$_3$*/mmc* structure [133], [136]–[139]. In both cases, from a crystallographic point of view, an inversion center appears, *i.e.* the structure becomes more symmetrical due to the atoms displacement with temperature [112], [116], [136]. Indeed, in a compound of similar stoichiometry, $YMn_{0.875}Ti_{0.125}O_{3+\delta}$, the *(102)* peak which was present for the pattern of the as-prepared sample also disappears in the range of low temperatures (T=300-400°C) for which the maximum oxygen uptake was evidenced in air [116]. Thus, it is possible to infer that the structural change in $Y_{0.9}Zr_{0.1}MnO_{3+\delta}$ can be in the same way associated with the oxygen excess that has been clearly evidenced by TGA. In order to establish where these oxygens atoms are located in the structure and why the structure turns more symmetrical, Neutron diffraction (ND) analysis was carried out for as-synthesized Zr-doped $YMnO_3$ (it is worth noting that, for experimental reasons, the samples were prepared well before recording ND data). Using only FPM refinement, *i.e.* without including the cell content, the neutron diffraction pattern can be indifferently indexed using either *P*6$_3$*cm* or *P*6$_3$*/mmc* space groups, with quite good R-factors; however, using the literature data for atomic positions, the corresponding Rietveld refinements yield high values of reliability factors in both cases (Annex C). Performing a difference Fourier map using one or the other space groups, additional electron

density around Mn atoms was found that was attributed to the oxygen excess based on the classical Mn-O length, in agreement with TGA curves. Then, the best reliability factors were obtained refining the oxygen occupancy of all oxygen atoms in $Y_{0.9}Zr_{0.1}MnO_{3+\delta}$ and, in particular for the *P*6$_3$*/mmc* structure, the addition of a partially filled extra oxygen site (O3) was taken into account. It is worth noting that all refinement were performed not only in the *P*6$_3$*/mmc* space group, but also in the less symmetric *P*6$_3$*cm* model. We also tried to carry out refinements using the other two models that have been described in literature for oxygen overstoichiometric compounds, *i.e.* with space groups *R*-3*c* and *P*ca2$_1$, respectively [140], [191], the results were exactly the same as for the hexagonal cells with additional oxygen atoms and, as a basic rule of crystallography, the simplest model was finally chosen, *i.e.* the *P*6$_3$*/mmc* overstoichiometric structure.

A coupled Rietveld refinement using both neutron and X-Ray diffraction data was finally performed, and the graphical result is shown in Figure 29. The structural parameters are listed in Table 7. It is worth noting that such behavior was clearly evidenced with the sample prepared by Pechini technique, and not to solid state synthesis, probably evidencing the importance of the powder microstructure (grain size in particular) on the kinetic of oxygen absorption, making it difficult to observe in our first experiments.

Figure 29. Coupled Rietveld refinement for $Y_{0.9}Zr_{0.1}MnO_{3+\delta}$ (a) Neutron Diffraction and (b). X-Ray powder diffraction.

a).

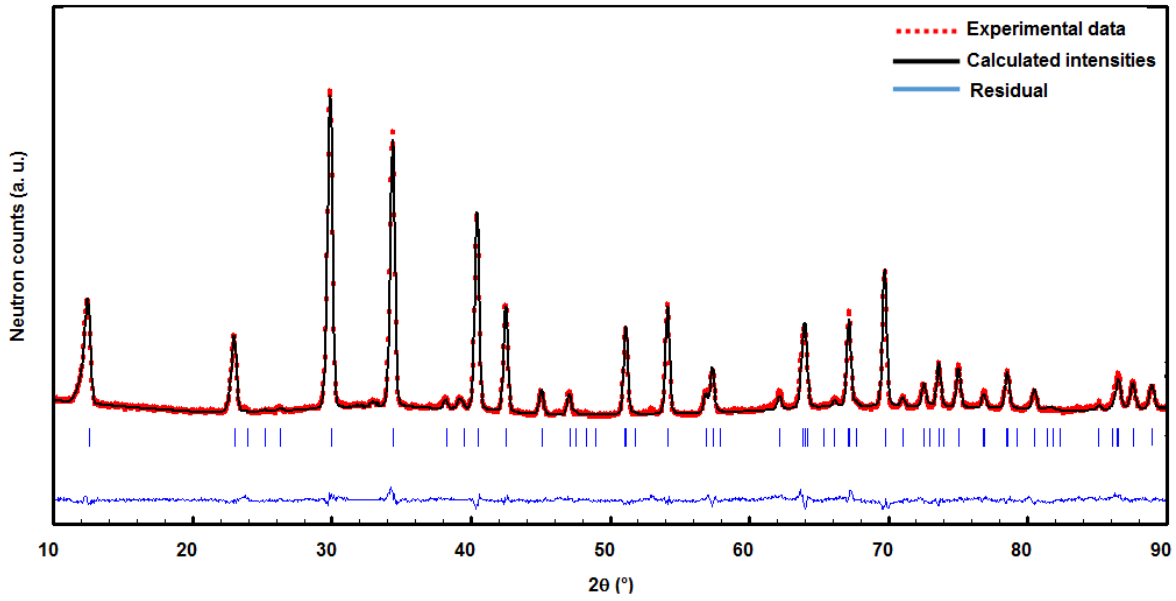

b).

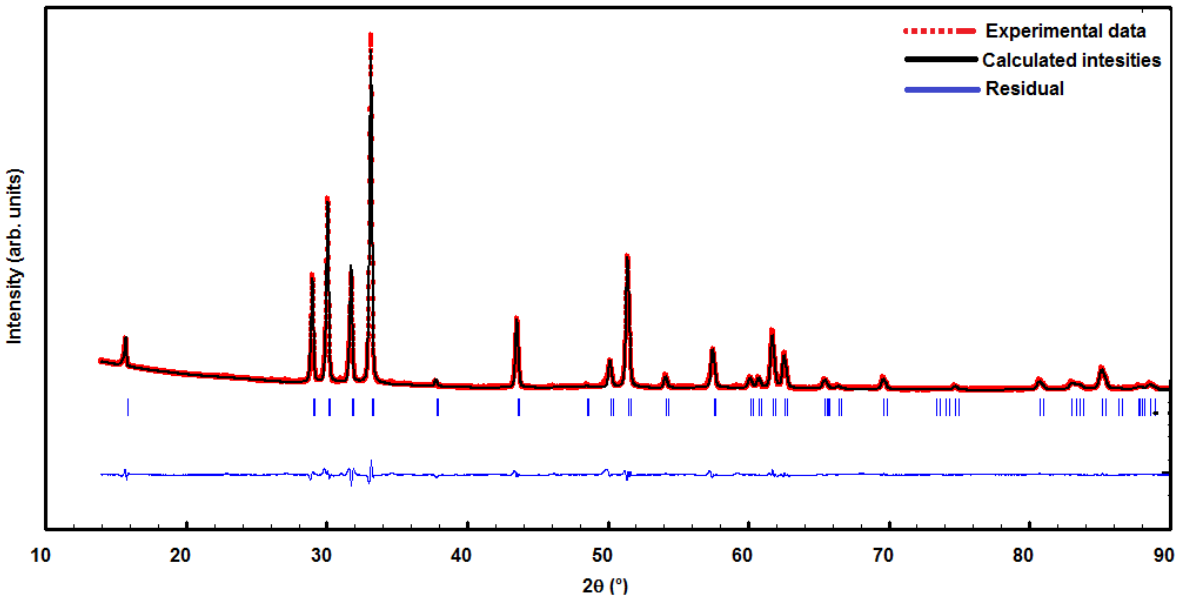

Table 7. Structural parameters for $Y_{0.9}Zr_{0.9}MnO_{3+\delta}$ (RT) with an additional interstitial position O3 position (s.g.: *P*6$_3$/*mmc;* lattice parameters: a=3.5506(1) Å, c=11.2559(4) Å).

Atom	**Wyckoff position**	***x***	***y***	***z***	**Occupancy**	**U_{eq}**
Y	4e	0	0	0.0214(3)	0.9	0.0151(8)
Zr	4e	0	0	0.0214(3)	0.1	0.0151(8)
Mn	2c	1/3	2/3	1/4	1	0.0197(5)
O1	4f	1/3	2/3	0.0847(1)	1	0.0144(2)
O2	2b	0	0	1/4	0.85954	0.0416(8)
O3*	6h	0.4883(2)	0.2441	1/4	0.135244	0.0668(6)
Reliability factors		**Neutrons**	R_p(%)=2.84, R_{wp}=3.55, GOF=1.94, R_B=7.88			
		X-Ray	R_p(%)=4.90, R_{wp}=6.31, GOF=1.34, R_B=9.23			

In Table 7, it can be appreciated that oxygen excess O3 is located indeed in a *6h* Wyckoff position at the same z-values than for O2-atoms (z=1/4 and 3/4), *i.e.* in the basal planes of the MnO_5 trigonal bipyramids. The oxygen excess is accommodated in the hexagonal interstices formed by three bipyramids, normally empty, as depicted in (Figure 30(a) and 30(b).

Figure 30. Structural representation of (a) $YMnO_3$ (*P*6$_3$*cm*) and (b) $Y_{0.9}Zr_{0.1}MnO_{3+\delta}$ with oxygen overstoichiometry (*P*6$_3$/*mmc*). Mn cations are light blue, host oxygen are purple, Y/Zr cations are light gray and interstitial oxygens O3 are yellow. Mn-O bond lengths (given in Å) are also given.

a). $YMnO_3$

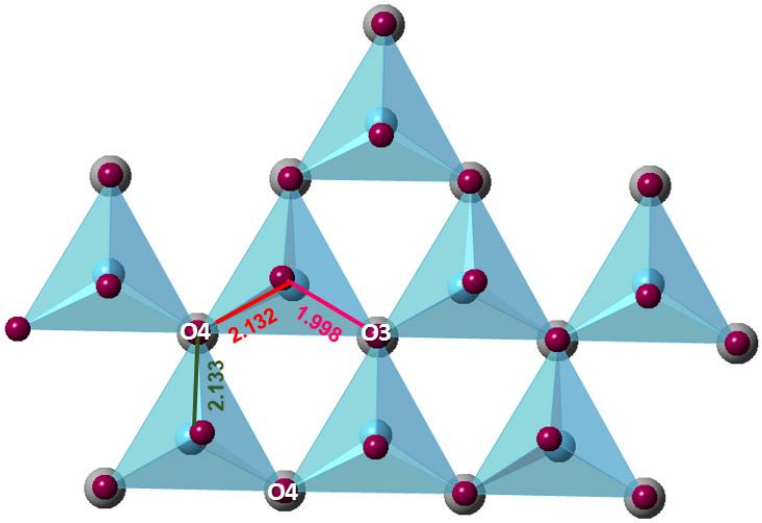

b). $Y_{0.9}Zr_{0.1}MnO_{3+\delta}$

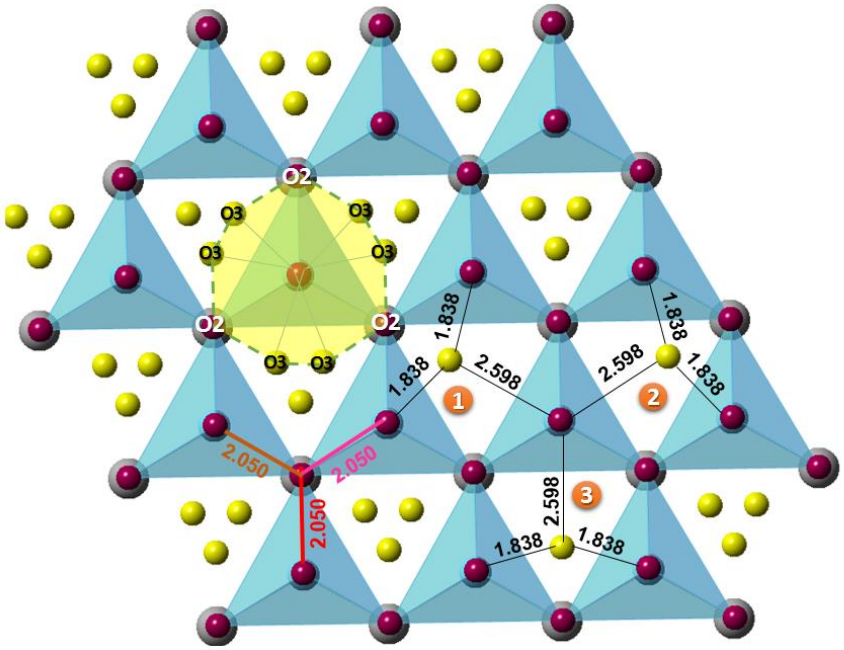

Apparently, such phenomenon is possible because in $YMnO_3$ as in the Zr-doped structure, the basal oxygens of MnO_5 bipyramids are under-bonded with Mn and, consequently, can easily move in the lattice [116]. Thus, in presence of an oxidizing atmosphere and temperature, these basal oxygen atoms can move in the Mn-O plane filling triangular interstitials sites of the trimers [192]. Specifically, in $Y_{0.9}Zr_{0.1}MnO_3$, the additional O3 atoms can occupy any of the six *6h* equivalent sites: (0.49, 0.24, 1/4), (0.76, 0.24, 1/4), (0.75, 0.51, 1/4), (0.24, 0.76, 3/4), (0.24, B1.49, 3/4) and (0.51, 0.76, 3/4) in the triangular interstitial space. In everyone, the O3 atoms can be arranged in three ways as observed in Figure 30(b). However, depending on the $3+\delta$ value, the sites could be only partially occupied [192]. As a result, Mn cations can virtually increase their coordination and form polygons different from the original trigonal bipyramids, similar to what happens in the overstoichiometric $AMnO_{3+\delta}$ structures with of *R*-3*c* and *P*ca2_1 space group [142]. It is noting that the extra oxygen atom is closer to two of the three bipyramids (or Mn atoms) that surround it (Mn-O3 bond lengths are 1.838 Å while Mn-O2 bonds are 2.050 Å).

As a summary, we can say that the presence of Zr in the $YMnO_3$ matrix makes the structure more symmetrical. In addition, the samples obtained by both methods (solid-state and Pechini) are in average the same, the only difference stemming from the fact that oxygen excess is more easily/rapidly absorb and desorb in the second kind of materials, due to lower synthesis conditions, *i.e.* to finer small grains. On the other hand, in air atmosphere, the amount of interstitial oxygen that can hold the pure $YMnO_3$ material is minimal due to its kinetic properties (diffusion length seems large compared with the low ionic mobility) and for that reason the material keeps a *P*6$_3$*cm* structural arrangement [192]. In the case of Zr-doped compound, the absorption kinetics seems fast. The above stems maybe from the former presence of interstitial oxygen after synthesis ($3+\delta \geq 3.05$), which could promote the diffusion of oxygen when the material is equilibrated in air at room temperature. Finally, it is worth highlighting that most of the following characterizations were carried out using

the samples obtained by Pechini method, in particular the electrochemical properties- since the corresponding microstructure seems to have a strong influence on the kinetics of oxygen absorption and the crystal structure

3.2 ANALYSIS OF THE MATERIALS STABILITY IN REDUCING ATMOSPHERE

To probe the stability of the synthesized materials in reducing atmosphere, the materials were placed at 800°C in wet diluted hydrogen atmosphere characteristic of the SOFC anode compartment. The XRD diagrams of the as-obtained materials are plotted in Figure 31.

Figure 31. XRD patterns of $Y_{1-x}Zr_xMnO_3$ ($0 \leq x \leq 0.10$) series (a-c) before and (d-e) after thermal treatment in wet diluted H_2 at 800°C for 8 hours.

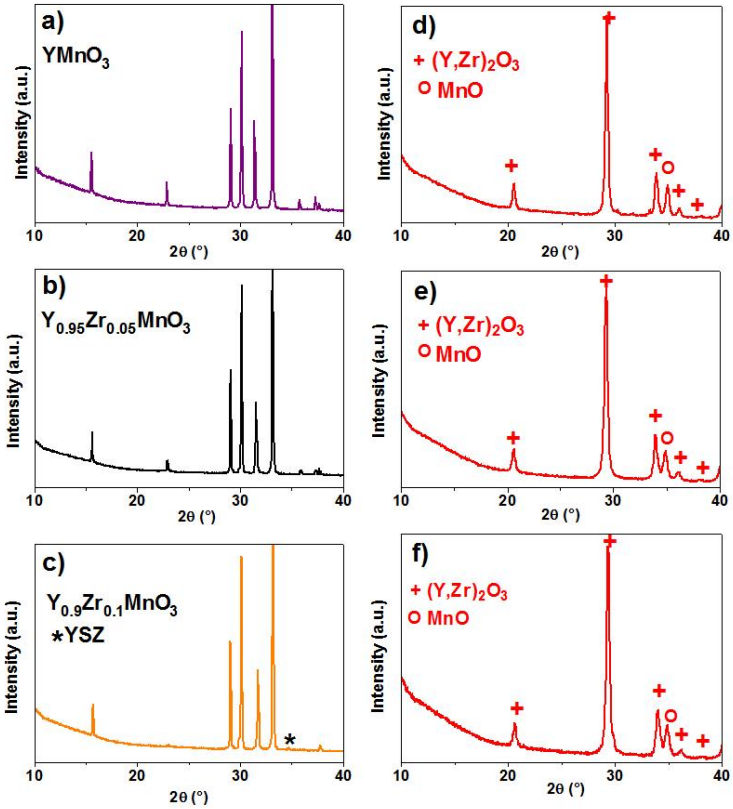

As can be observed, no $Y_{1-x}Zr_xMnO_3$ family members is stable in such conditions, regardless the presence of Zr or not at the Y site, since all are decomposed into their precursors: MnO and $(Y, Zr)_2O_3$. Such results preclude their use as anode materials in Solid Oxide Fuel Cells. However, to study the possibility of using those materials at lower temperature, HT-XRD experiments of a $YMnO_3$ sample has been carried out in dry H_2/N_2=3/97 atm up to 800°C, that allowed observing the temperature at which the material loses stability. The results are depicted in Figure 32 (the same experiment was also carried out in wet reducing atmosphere without significant changes neither in the behavior nor in the refined cell parameters).

Figure 32. HT-XRD patterns of $YMnO_3$ in dry H_2/N_2=3/97 reducing atmosphere.

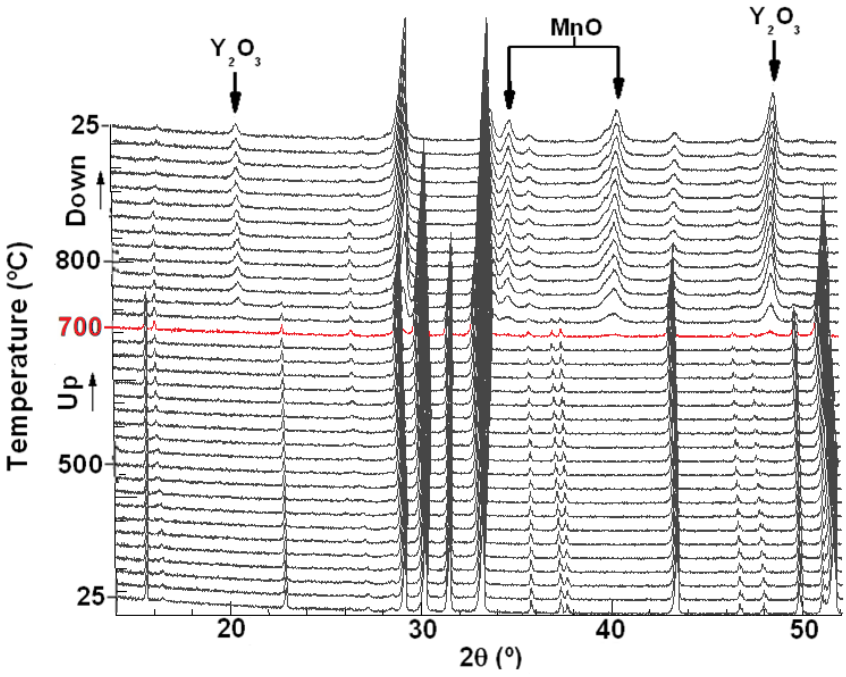

The first comment that can be made is that in dry reducing conditions, from RT to 700°C, $YMnO_3$ seems to remain stable. The latter, because most of the diffraction peaks shift with temperature but there is no obvious general trend of increase or

decrease of the cell parameters as a whole. Using cyclic structure refinement, the evolution of cell parameters can be plotted as a function of temperature as depicted in Figure 33.

Figure 33. Temperature dependence in dry H_2/N_2=3/97 of lattice parameters for $YMnO_3$.

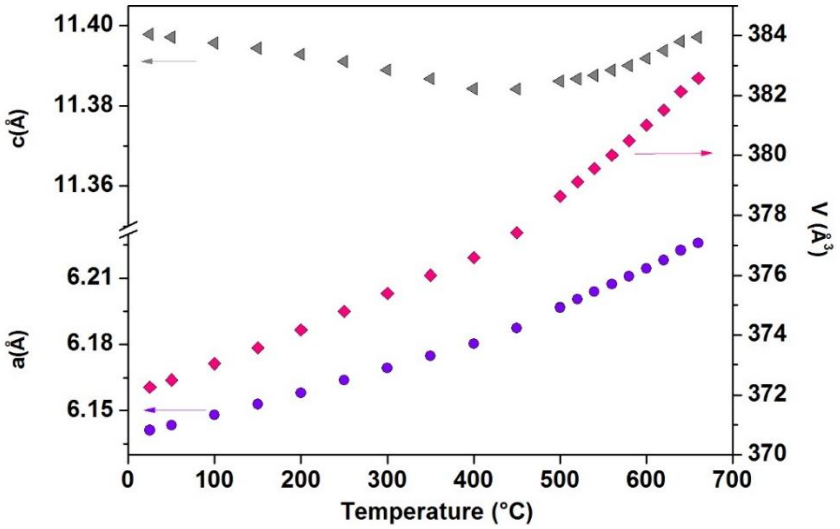

As observed in Figure 33, *a* and *c*-axis parameters behaves differently: *a* value strongly increases from 6.1403 to 6.1964 Å corresponding to a $\Delta a/a$=1.3% thermal expansion between RT and 500°C, while *c* parameter smoothly drops from 11.3952 to 11.3856 Å, *i.e.* a thermal contraction of $\Delta c/c$=-0.00596%. Globally, a positive mean volumetric expansion of $\Delta V/V$=2.76% is observed. According to Fu *et al.* [193], such redox expansion would induce strong stresses on the adjacent components, especially on the electrolyte layer in an anode supported cell or in large size cells, and would then be redhibitory. A solution to such issue would be the use of graded electrode $Y_{1-x}Zr_xMnO_3$ /YSZ, if the chemical compatibility between both materials allows the use of such composite; this will be the object of one of the sections described below.

Beyond T=500°C, a deviation from the linear thermal behavior of the lattice parameter is observed. The increase of the slope indicates a possible chemical contribution to the thermal expansion coefficient (TEC) maybe related to an oxygen loss. This assumption is supported by the thermogravimetrical behavior of the $Y_{1-x}Zr_xMnO_3$ materials in reducing atmosphere described in Figure 34.

Figure 34. Thermogravimetrical analysis (TGA) measurements $YMnO_3$ and $Y_{0.9}Zr_{0.1}MnO_{3+\delta}$ as a function of temperature in reducing atmosphere (wet 3%H_2/Ar, heating and cooling rates= 0.1°C min^{-1})

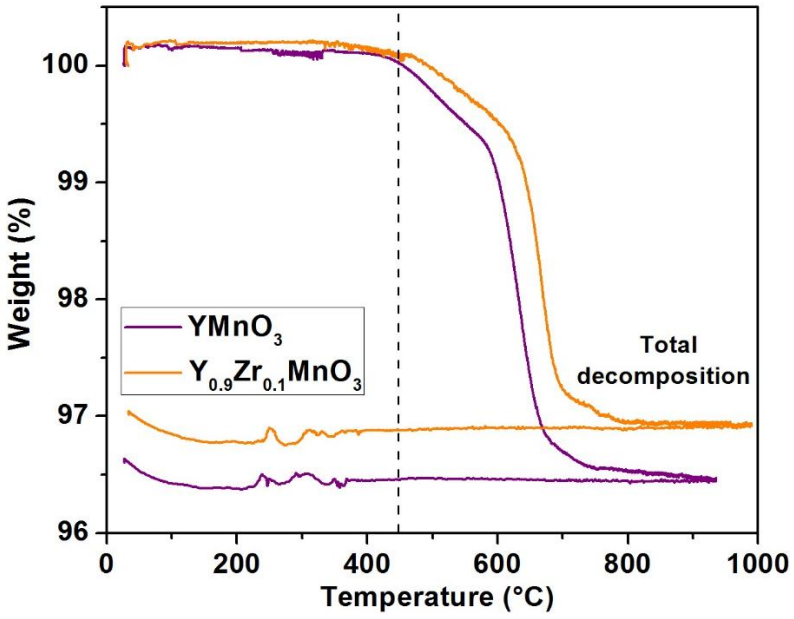

Clearly, we can distinguish the same zones observed in Figure 33. First, from RT to T~500°C, where the weight does not change significantly but the material thermally dilates (no chemical contribution to dimensional changes in the structure). However, for temperatures higher than 500°C, a weight loss is evidenced and at the same time the slope of both lattice parameters variation increases with temperature. This is associated to a partial reduction of Mn^{3+} into Mn^{2+} due to oxygen loss (and maybe a

few amount of Mn^{4+} reduced to Mn^{3+}), since the higher ionic radius of Mn^{2+} compare to that of Mn^{3+} (r_{Mn2+}=0.75 Å and r_{Mn3+}=0.58 Å) [189]. The structure finally decomposes around T~700°C, forming a mixture of MnO and $(Y,Zr)_2O_3$ oxides, what definitely discard $Y_{1-x}Zr_xMnO_3$ compounds for a possible use as SOFC anode materials, a device for which a minimum temperature of 600°C, and often higher than 700°C, is generally considered. The stabilization of the $YMnO_3$ matrix by substitution of the B-site (Mn) element to mitigate the effect of the reductions is precisely the object of the following chapter.

3.3 STUDY OF THE ELECTRODE-ELECTROLYTE COMPATIBILITY

3.3.1 Determination of the chemical compatibility. The XRD patterns of electrode/electrolyte ($Y_{1-x}Zr_xMnO_3$/YSZ) mixtures, with x=0 to 0.10 and a 50/50 wt ratio are depicted in Figure 35, before and after heat treatment at 1300°C in air.

Figure 35. XRD patterns of electrode-electrolyte mixtures before (purple) and after (light gray) chemical reactivity tests.

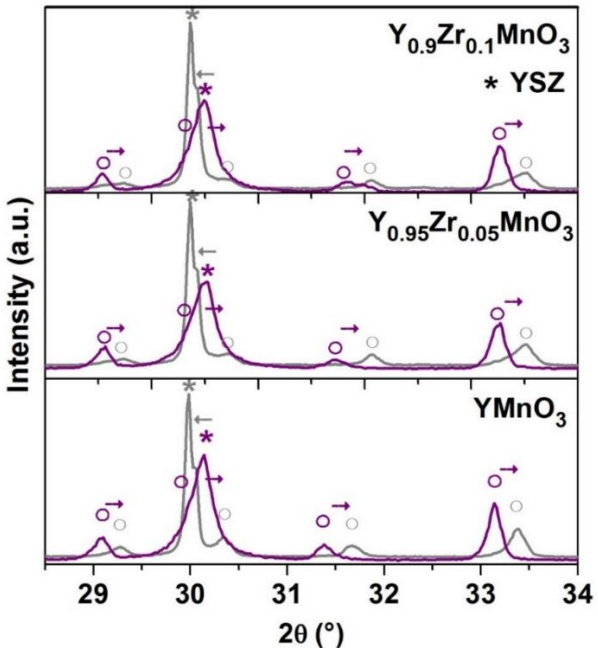

The samples used for this test were the same as prepared by the solid-state method. No detrimental reactivity between both phases is observed, as no impurity phase is formed, even at such high temperature of reaction. This confirms, in the case of $YMnO_3$, the first result obtained by Huang *et al.* [194]. The diffraction peaks of the hexagonal phase are shifted to higher angles after reactivity test, *i.e*. the refined lattice parameters *a* and *c*, listed in Table 8, are considerably reduced in comparison to the original values. On the other hand, the YSZ lattice parameter increases after heat treatment. Such behavior suggests a cross-diffusion phenomenon at the interface between the grains of YSZ and $Y_{1-x}Zr_xMnO_3$, in which Y^{3+} cations, larger than Zr^{4+}, migrate to the electrolyte, while Zr^{4+} cations move toward the manganite.

Table 8. Structural parameters of mixtures of $Y_{1-x}Zr_xMnO_3$ (x= 0, 0.05 and 0.10) and YSZ heat treated at 1300°C, as obtained from FPM refinement using XRD data.

Sample	a (Å)	c(Å)	V(Å^3)	Reliability factors
x=0	6.0996(3)	11.2955(7)	369.95(3)	R_p(%)=2.85 GOF=1.22
YSZ	5.1584(1)	-	137.26(2)	R_{wp}(%)=3.79
x=0.05	6.0971(8)	11.2279(13)	361.48(7)	R_p(%)=3.28 GOF=1.45
YSZ	5.1558(2)	-	137.06(6)	R_{wp}(%)=4.35
x=0.10	6.1044(8)	11.233(2)	362.50(9)	R_p(%)=3.40 GOF=1.43
YSZ	5.1545(2)	-	136.95(6)	R_{wp}(%)=4.54
R_p: profile factor R_{wp}: weighted-profile factor GOF: goodness of fit				

Such behavior means an absence of risk for long-term degradation of the electrode-electrolyte interface because in case of reaching the limit of Zr in the manganite, the thermodynamic equilibrium at the electrode/electrolyte ($Y_{1-x}Zr_xMnO_3$/YSZ) interface

would not involve any (possibly insulating) third phase. It would not be detrimental to zirconia conductivity since XRD data suggest an increase in Y^{3+} concentration within the electrolyte material and not the contrary. In addition, the diffusion of $Mn^{2+/3+}$ cations (r_{Mn3+}=0.58 Å)[189] into YSZ material, with possible mixed Mn^{3+} valence in the zirconia, cannot be ruled out, too, as some authors indicate that the solubility of Mn in 8YSZ varies between 5mol% at 1000°C and 15mol% at 1500°C [195]. Such doping of YSZ with manganese has been shown to decrease the ionic conductivity, and increase the electronic conductivity of the material in the entire oxygen chemical potential range from 10^{-15}-10^{5} Pa, but with still high oxygen ion transport numbers (*e.g* t_{io}=0.99 for 4mol% Mn doped YSZ)[196]. Finally, the cross diffusion of Zr^{4+} and Y^{3+} at the electrode/electrolyte interface can also be viewed as a benefit in terms of adhesion of the two layers, when sintering one over the other. The aforementioned behavior constitutes a really interesting result, considering that the electrode-electrolyte reactivity has been for a long time considered as one of the major issues to be solved in SOFC, in part solved in $(La,Sr)MnO_{3-\delta}$ using an A-site sub-stoichiometry and/or limited sintering temperatures [193], [197], [198]. On the contrary, due to their yttrium and zirconium common elements, $Y_{1-x}Zr_xMnO_3$ and YSZ are able to coexist under the referred conditions and probably also in long-term conditions, meaning that it would be possible to prepare $Y_{1-x}Zr_xMnO_3$/YSZ composites in case of insufficient electrocatalytic activity of the manganite.

3.3.2 Analysis of the thermo-mechanical compatibility. In Figure 36, the evolution in air of the X-ray diffraction pattern for $YMnO_3$ is shown as a function of temperature (HT-XRD). As can be observed, no structural change is evidenced, since no additional reflection in the diffraction patterns appears and no peak disappears. The material keeps the same structure of *P*6_3*cm* space group up to 850°C.

Figure 36. HT-XRD patterns of $YMnO_3$ recorded in air from RT to 850°C.

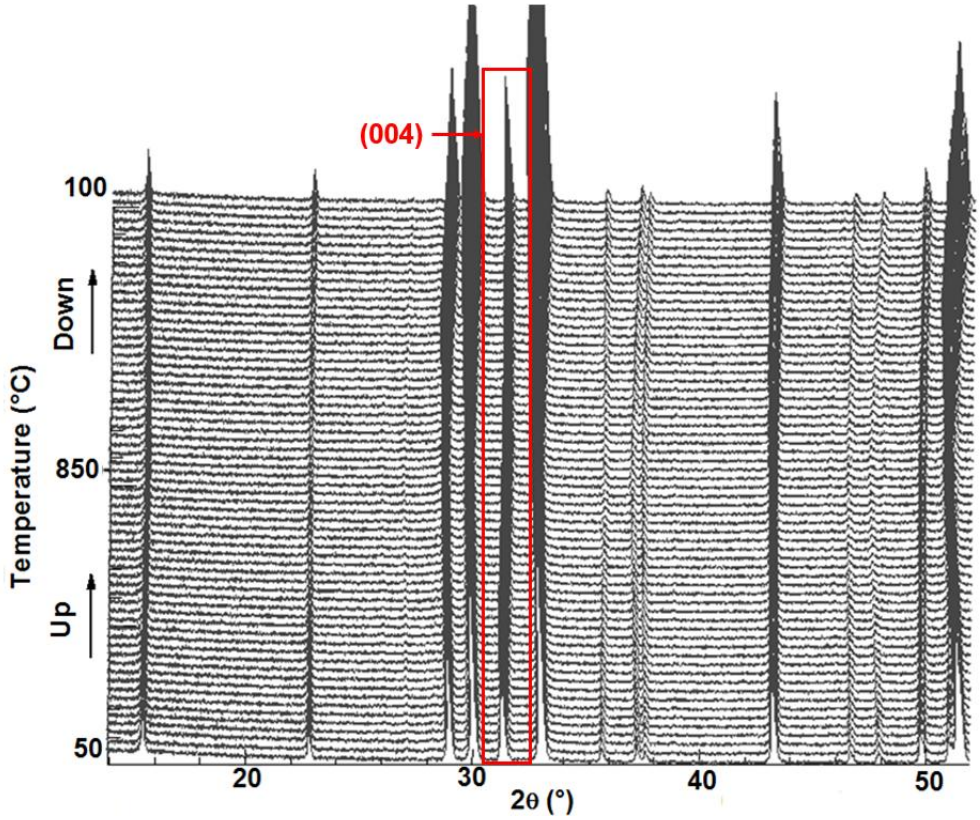

Into details, it is worth noting that instead of a general movement of the peaks to low angles, as expected for classical thermal expansion, a subtle displacement is indeed observed, especially of the *(004)* reflection. The structural anisotropy of the material makes the family of planes *(00l)* behaves differently with respect to other planes, leading to a contraction of the *c* parameter. With the aim to understand what occurs structurally in the material, a cyclic cell parameter refinement was carried out throughout the interval of temperature of the HT-XRD experiment. The evolution of the refined parameters is shown in Figure 37.

Figure 37. Temperature dependence in air of lattice parameters for $YMnO_3$. Colored symbols indicate the evolution during heating and black ones during cooling.

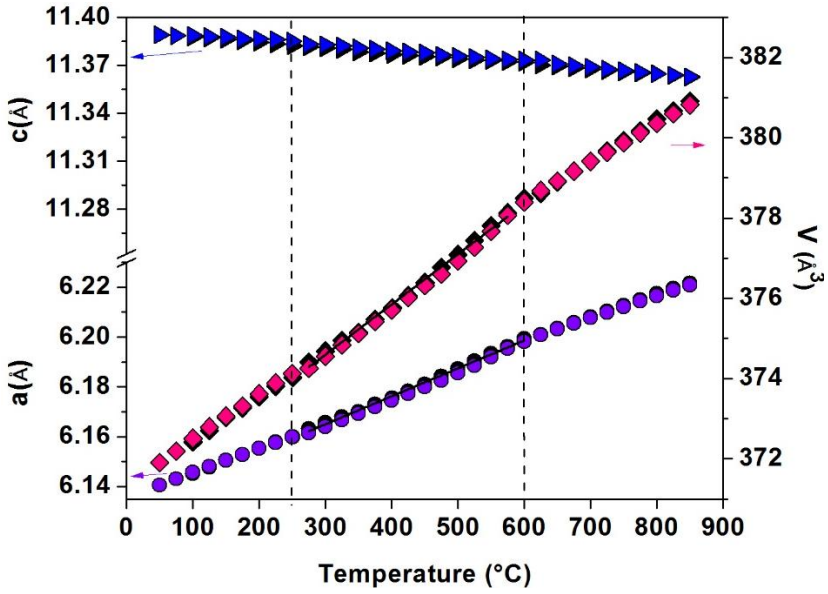

In the previous figure, it is possible to appreciate that *a* lattice parameter increases with the temperature in the whole range and in a quite linear way. At the same time, *c* parameter decreases linearly, but it changes less sharply than *a*; as a consequence, the overall volume of the cell increases with the temperature.

Based on those structural trends, several comments can be made. The first of them, concerns the behavior with temperature of *c* lattice parameter that is not common but stems from the anisotropic feature of the material structure. In literature, such kind of behavior has been described but seems to depend on the size of the rare earth ion in the $AMnO_3$ hexagonal compounds, what can be understood when a comparison is made for A= Sc^{3+} (r_{Sc3+}=0.87 Å), Lu^{3+} (r_{Lu3+}=0.977 Å) and Y^{3+} (r_{Y3+}=1.019 Å) [189]. For the smaller Sc^{3+} cation, *c* parameter increases with temperature, for Lu^{3+} it remains almost constant and for Y^{3+}, the same trend as we observed is described by the authors, *i.e. c* decreases with T. Indeed, although all these compounds undergo a transition to the *P*6$_3$*/mmc* phase (~980°C), and

therefore the polyhedral tilting and the layers buckling decreases when the temperature increases, in $YMnO_3$ these changes are more prominent due to its higher ionic radius [187].

On the contrary, the increase of *a* parameter in $YMnO_3$ seems to be solely due to the thermal expansion of the bonds because as already reported, albeit the size of the A ions differs, this parameter always tends to increase with temperature [187]. However, it cannot be left out that although the dependence of this parameter is almost linear [136], in the same Figure 37, we can observed a range of temperature (~250-600°C) in which the slope of the thermal dilatation slightly changes. This jump seems to be related with the fact that around T=250°C the material absorbs oxygen and then desorbs it up to ~600°C, where the material reaches its stoichiometric oxygen content ($YMnO_{3.0}$), as was discussed in the first section of this chapter. Some authors claim that this extra oxygen promotes phase transition to other structure types, but in our case the presence of secondary phases of *R-3c* and *P*ca2$_1$ space group could be discarded, probably because the amount of oxygen excess storage in air atmosphere is really low and must only slightly affects the atomic arrangement.

Back to the parameter evolution with temperature, and notwithstanding the previous analysis, it is worth noting that the heating and cooling curves of Figure 37 remarkably overlap, making it possible to determine the coefficient of thermal expansion (TEC) of $YMnO_3$, one of the main objectives of this section. For this, it must be taken into account that the material does not present a cubic structure, so linear thermal expansion coefficients (α_i) in each main directions of the structure must be calculated first:

$$\alpha_i = \frac{1}{\Delta T}\frac{(i_f - i_0)}{i_0}\ [=]K^{-1} \qquad (53)$$

Where,

ΔT is the temperature delta in which the coefficient is calculated,

i_0 corresponds to the initial value adopted by the lattice parameter,

i_f is the final value reached by the lattice parameter.

In the case of the hexagonal manganite $YMnO_3$, two main directions can be defined, *i.e.* along *a* and *c* axis, linear coefficients α_a and α_c are obtained, respectively. From that, we can deduce the coefficient of volumetric expansion (β), as follows:

$$\beta = \frac{1}{\Delta T}\frac{(V_f - V_0)}{V_0} = (2\alpha_a + \alpha_c)\ [=]K^{-1} \qquad (54)$$

However, given the aforementioned variations in the trendy of lattice parameters, two different β values can be calculated for this material (at low and at high temperature), as shown in Table 9. In the intermediate temperature range, where the change in oxygen content increases, a chemical expansion content could be calculated, as will be seen shortly.

Table 9. TEC values for low and high temperature $YMnO_{3+\delta}$

Temperature (°C)	**Space group**	**α_a (x10^{-6} K^{-1})**	**α_c (x10^{-6} K^{-1})**	**β (x10^{-6} K^{-1})**
50-250	*P*6$_3$*cm*	15.72	-1.71	29.73
600-850	*P*6$_3$*cm*	14.37	-4.06	24.64

Then, it could be observed that β value at low temperature is close to the most common SOFC electrolyte, *i.e.* 8YSZ (β~31-33 x 10^{-6} K^{-1}) [199], because only have differences between ~2%. This difference is even less than the exhibited by the most

commonly used cathode materials, *i.e.* La/Sr manganites (β~33-36 x 10^{-6} K^{-1})[198], with discrepancies in a range of ~5 -17 %. The fact that these values comparable, guarantees to a certain extent that during the elaboration and future operation of the SOFC cell, there would be a limited stress in particular at the electrode-electrolyte interface. At highest temperatures, the volumetric TEC of $YMnO_3$ decreases, and hence the difference with the value of 8YSZ increases (~20-25%). The above increments the risk of cell fracture due to TEC mismatch. Nevertheless, $YMnO_3$ compound could be used as electrode considering the perfect chemical compatibility with the most common electrolyte and because the thermomechanical issues could be solved easier. Indeed, a strategy would be to use $YMnO_3$/YSZ mixtures for the electrode elaboration instead of pure manganite, these could modify the β value. A couple of examples of this are the decrement of β to 39 x 10^{-6} K^{-1} for LSF/YSZ composites and the change from 61.5 x 10^{-6} K^{-1} to 51 x 10^{-6} K^{-1} in LSC ($La_{1-x}Sr_xCoO_3$)/YSZ mixture [200].

In a similar way, we carried out HT-XRD experiments with $Y_{0.9}Zr_{0.1}MnO_{3+\delta}$ compound in order to establish if with a small amount of Zr-doping, this material can still be considered compatible with the state-of-the-art electrolyte YSZ. The results of HT-XRD experiments and the corresponding diffraction patterns are presented in Figure 38. First, it must be remembered that the substituted compound, unlike $YMnO_3$, crystallizes in the heavily oxidized $P6_3/mmc$ structure when prepared by the Pechini method, what means that some diffraction peaks as at $2\theta \approx 23°$ and around $2\theta \approx 36$ are not present at the beginning of the experiment. Nonetheless, in Figure 38, we can observed that above T~350°C these reflections clearly re-appear. The latter indicates that the material experiences a phase transition towards the $P6_3cm$ structure, probably due to the loss of extra interstitial oxygens atoms that made were originating the structure change to $P6_3/mmc$ space group, according to the results detailed above in section 3.1.

Figure 38. HT-XRD patterns of $Y_{0.9}Zr_{0.1}MnO_{3+\delta}$ recorded in air from RT to 850°C. The characteristic peak corresponding to the *P*6$_3$*cm* space group (from T~350°C) is highlighted in a red rectangle.

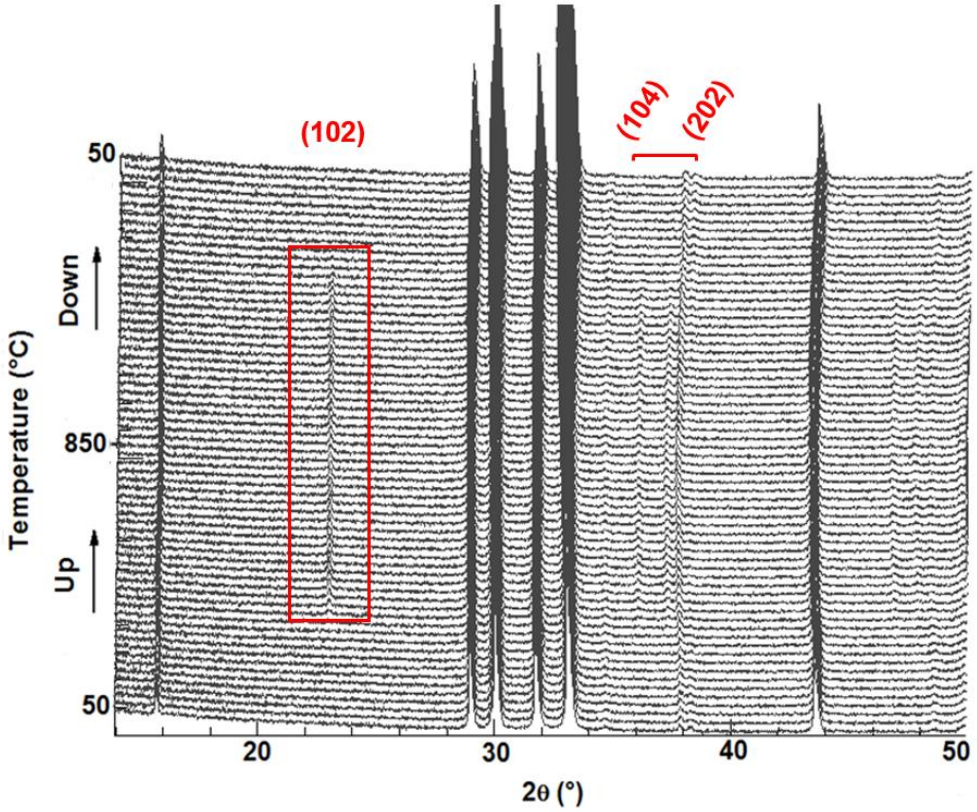

To continue with our analysis, it is necessary to carry out a cyclic structure refinement using the diffraction patterns collected by HT-XRD. The obtained lattice parameters are shown in Figure 39. From RT to T~250°C, the patterns can all be indexed with a *P*6$_3$/*mmc* arrangement and each lattice parameter increases linearly due to thermal dilation. Near 250°C, the linear trend is lost because of oxygen uptake, similarly to that happens in the non-doped manganite. The *P*6$_3$/*mmc* arrangement prevails up to 350°C when the material begins to desorb the oxygen excess (see Figure 27 in section 3.1). Finally, the phase transition to *P*6$_3$*cm* seems to be complete at T~500°C when the material raises its stoichiometric oxygen content $Y_{0.9}Zr_{0.1}MnO_{3.05}$ and from the linear behavior is recovered. Likewise, it is worth noting that the compound

returns to its initial arrangement since, as can be observed in Figure 27, the absorbs/desorbs of oxygen are a reversible process.

Figure 39. Temperature dependence in air of the lattice parameters for $Y_{0.9}Zr_{0.1}MnO_{3+\delta}$. Colored symbols indicate the evolution during heating and black symbols during cooling.

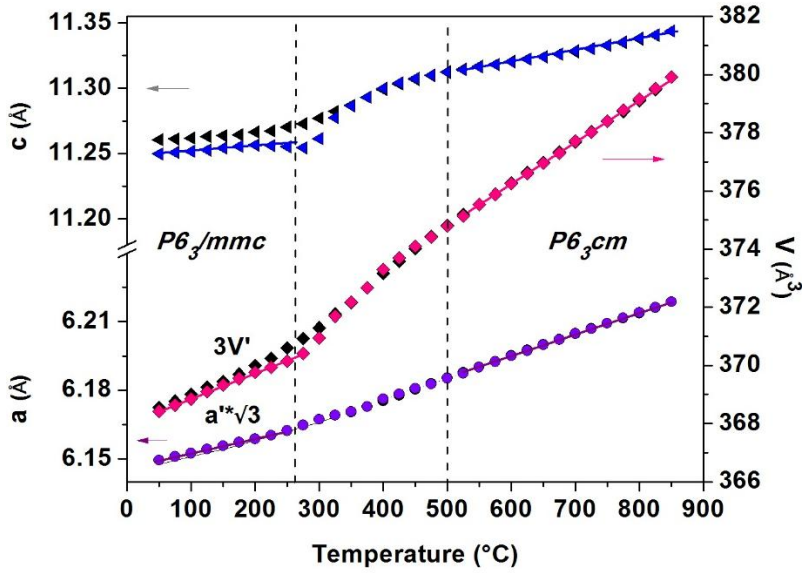

Moreover, we can also appreciated that, at the difference of $YMnO_3$, for the Zr-doped material, *c* parameter remains constant (or increases very smoothly) in the temperature range 50-250°C, then increases more rapidly (and not in a linear way) due to the material stoichiometry (and symmetry) changes (250-500°C) and finally, increases but more slowly for T>500°C. Concerning the two extreme ranges (*i.e.* T<250°C and T>500°C), the behavior of *c* can be clearly understood considering that for $Y_{0.9}Zr_{0.1}MnO_{3+\delta}$, the size of the A site diminishes in comparison to the $YMnO_3$ due to Zr^{4+} presence (r_{Y3+}=1.014 Å and r_{Zr4+}=0.84 Å)[189] and, as in the case of Y^{3+} respect to Sc^{3+}, *c* tends to be constant or to increase with temperature when the size of A cation is small [187]. The latter means that A size influence seems to be the same for both *P*6$_3$*cm* or *P*6$_3$*/mmc* space groups, but more important, the dilatation

lattice in these ranges are only by thermal effects. Therefore, the coefficient of thermal expansion (TEC) can be calculated for $Y_{0.9}Zr_{0.1}MnO_{3+\delta}$ in a similar way as for the non-doped manganite only for the two extreme ranges T<250°C and T>500°C. Specifically, we can obtain one TEC_1 for the low-temperature structure ($P6_3/mmc$) and another for the high non-centrosymmetrical one (TEC_2). The obtained results are summarized in Table 10.

Table 10. TEC values for low and high temperature $Y_{0.9}Zr_{0.1}MnO_{3+\delta}$

Temperature (°C)	**Space group**	α_a **(x10^{-6} K^{-1})**	α_c **(x10^{-6} K^{-1})**	β **(x10^{-6} K^{-1})**
50-250	$P6_3/mmc$	10.49	2.40	23.38
500-850	$P6_3cm$	15.46	7.97	38.90

The low (respectively high) temperature volumetric TEC values have a markedly difference of 30% (resp. 15%) with the coefficient of volumetric thermal expansion of 8YSZ electrolyte (β~31-33x10^{-6}K^{-1}), especially in the range 50-250°C [199]. Similar to the case in the non-doped $YMnO_3$, such difference could be problematic, especially at low temperature in this case. Nevertheless, given the good chemical compatibility of Zr-doped manganite and 8YSZ electrolyte, we can consider the possibility of using (Y,Zr)MnO_3/YSZ mixtures for the electrode instead of a pure phase.

The nonlinear expansion in the intermediate temperatures region (250-500°C) seems to be a product not only of temperature increase but also due to the stoichiometry change accompanied by the progressive transition to the $P6_3cm$ structure, which promote a gradual increase in the tilting of the MnO_5 polyhedra and the buckling of Y^{3+}/Zr^{4+} layers [201]. In this temperature range, the TEC is the sum of a thermal expansion (TE) and a chemical expansion (CE), where the TE is caused by expansion of bond lengths due to thermal energy; whereas the CE is a

consequence of changes in composition [126]. Taking into account that, the Zr-doped compound absorbs/desorbs high oxygen amount in this temperature range, it is not surprising to think that there is a part of CE in the total expansion evidenced for this material. In general, this contribution is estimated assuming that $(\Delta L/L_0)\%$ is a linear function of the oxygen nonstoichiometry variations ($\Delta\delta$) under isothermal conditions while controlling pO_2 [202], [203]. The above is possible because the change in composition of the materials occur slowly over a wide range of temperatures and the constant temperatures and different pO_2 allows to separate the CE effect [126]. However, considering that our experiments were made by classical HT-XRD at fixed pO_2, *i.e.* in agreement with the application itself, we proposed the estimation of the chemical expansion contribution by the following relation:

$$CE = \frac{1}{\Delta\delta}\left(\frac{\Delta V}{V_0}\right) \qquad (55)$$

Where,

ΔV is the volume difference between the HT experimental data (where TEC_2 is calculated, *i.e.* for T>500°C) and the extrapolated data if TEC_1 would have been the only TEC value in the whole range of temperature.

and $\Delta\delta$ is the absolute change in oxygen content between LT and HT region in which the material stoichiometry is $Y_{0.9}Zr_{0.1}MnO_{3.05}$, measured from TG experiment, considering that such stoichiometry is still valid at T=500°C during cooling.

Thus, CE value was carried out using the same HT-XRD measurements during cooling and in air atmosphere. In Figure 40 is depicted the way we used for such calculation.

Figure 40. Calculation procedure for the Chemical Expansion Coefficient of $Y_{0.9}Zr_{0.1}MnO_{3+\delta}$ (250-500°C) from the volume evolution against T calculated using HT-XRD during cooling in air. The oxygen content of the material is plotted in the inset graph.

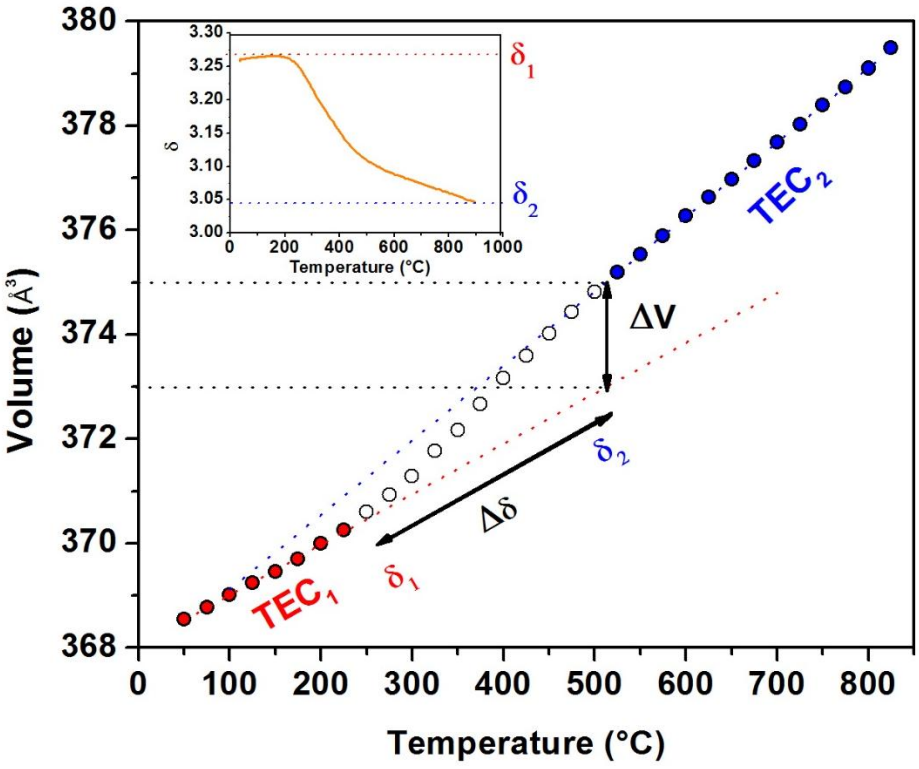

On the graph that represents the experimental evolution of cell volume against T during cooling, red circles represent experimental data in the low temperature range, where the TEC_1 was calculated. Additionally, we plotted the volume change assuming no compositional or phase transition (red dot line), *i.e.* a straight line of TEC_1 slope from the highest temperature with $Y_{0.9}Zr_{0.1}MnO_{3+\delta 1}$ stoichiometry (T~230°C). In Figure 40, the blue circles, correspond to the experimental points in the high temperature region in which TEC_2 has been determined (T>520°C for which we assume the constant $Y_{0.9}Zr_{0.1}MnO_{3+\delta 2}$ stoichiometry) and we also represent, as a guideline for the eyes, the extrapolated volume values until low temperature (blue

dot line). Then, ΔV is estimated as the difference between the two straight lines at the temperature of 520°C and $\Delta\delta=\delta_1-\delta_2$ is the change of oxygen content between the low and the high temperature regions, determined from the TGA measurements (see inset in Figure 40). Due to experimental differences between TG and HT-XRD measurements, we assumed a $\delta_2=0.05$ value at T=520°C, *i.e.* the lowest value obtained from TG curve.

In the temperature range of ~250-500°C, CE=0.026 and CE=0.015 were obtained, for Zr- doped and pure $YMnO_3$ respectively by the same procedure. In previous researches CE values for some electrode materials had been reported: $La_{0.6}Sr_{0.4}Co_{0.2}Fe_{0.8}O_{3-\delta}$ (CE=0.1) in air or doped $CeO_{2-\delta}$ (CE=0.21) under anodic operating conditions [204]. In comparison, the chemical expansion values of doped $CeO_{2-\delta}$ and $La_{0.6}Sr_{0.4}Co_{0.2}Fe_{0.8}O_{3-\delta}$ are considered as large and in some cases mechanical stresses lead to fracture and delamination at electrode/electrolyte interface cells using such materials [31], [202], [205]. In our case, the calculated CE is ~70-90% smaller than for those materials, and we expect that yttrium manganite's will not be prone to such mechanical failure due to chemical expansion.

3.4 DETERMINATION OF THE TRANSPORT PROPERTIES OF THE MATERIALS

3.4.1 Sintering procedure. The determination of the sintering temperature is one of the most important aspects in the study of electrode compounds, since for the measurement accuracy of the electrical conduction properties; one of the requirement is to reach the highest sample density. Then, to establish the best sintering conditions, the dimensional change of $YMnO_3$ and $Y_{0.9}Zr_{0.1}MnO_3$ pressed cylindrical samples (Diameter 5 mm x Height 8 mm) has been measured using dilatometry. The results are shown in Figure 41.

Figure 41. Dilatometric curves of $YMnO_3$ and $Y_{0.9}Zr_{0.1}MnO_3$ measured in air.

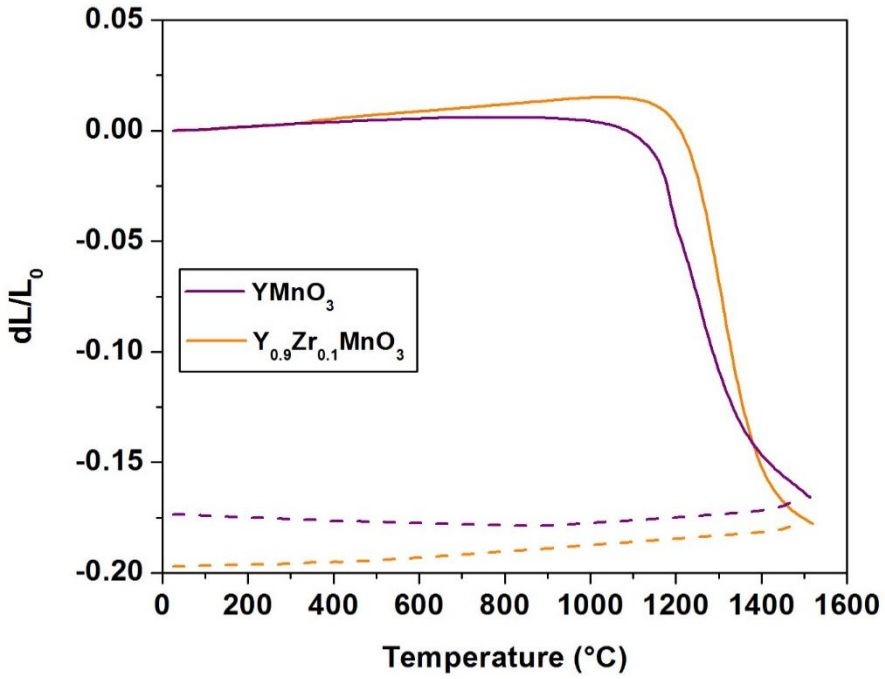

Comparing the two curves, it can be noticed that the behavior of both compounds is quite similar, and no special anomaly can be observed. Additionally, it is observed that the two samples linearly dilate up to the high temperatures (T~1000°C), although $Y_{0.9}Zr_{0.1}MnO_3$ does it largely, especially for T>500°C at which we know that the coefficient of thermal expansion of the material is higher than for the non-doped manganite (see section 3.3). Then, the samples present a strong contraction from T~1100°C, which is characteristic of the ceramic sintering. However, the most interesting place in the curves is found at around 1200-1300°C, where the highest sintering speed can be derived. For that reason, other temperatures close to this point are tested to determine in which compacity (or relative density) is achieved. For this purpose, pellets of diameter 5 mmx height 4-5 mm were thermally treated at chosen temperatures during 2 hours (ramps of heating and cooling of 5°C min^{-1}) The obtained compacity at each sintering temperature are given in the Table 11.

Table 11. Compacity of $YMnO_3$ and $Y_{0.9}Zr_{0.1}MnO_3$ at different temperatures.

Sample	Temperature (°C)	Density (g/cm^3)		Compacity (%)
		Theoretical	Experimental	
$YMnO_3$	1200	5.1349	4.2529	82.82
	1250		4.1992	81.78
	1300		4.4197	86.07
	1350		4.5137	87.90
	1400		4.2908	83.56
$Y_{0.9}Zr_{0.1}MnO_3$	1300	5.1940	4.8036	92.48
	1350		5.0198	96.64
	1400		4.7777	91.99
	1450		4.8627	93.62
	1500		4.8434	93.25

For both materials, we can confirm that the conductivity can be measured with good accuracy using the 4-point probes method, since all the obtained compacity values are greater than 80%. The highest compacity is obtained at sintering temperature of T=1350°C. The corresponding samples have been examined by Scanning Electron Microscopy (SEM) in order to observe the microstructure of the sintered materials (Figure 42).

Figure 42. SEM Micrographs of the a).$YMnO_3$ and b).$Y_{0.9}Zr_{0.1}MnO_3$ samples sintered in air at T=1350°C.

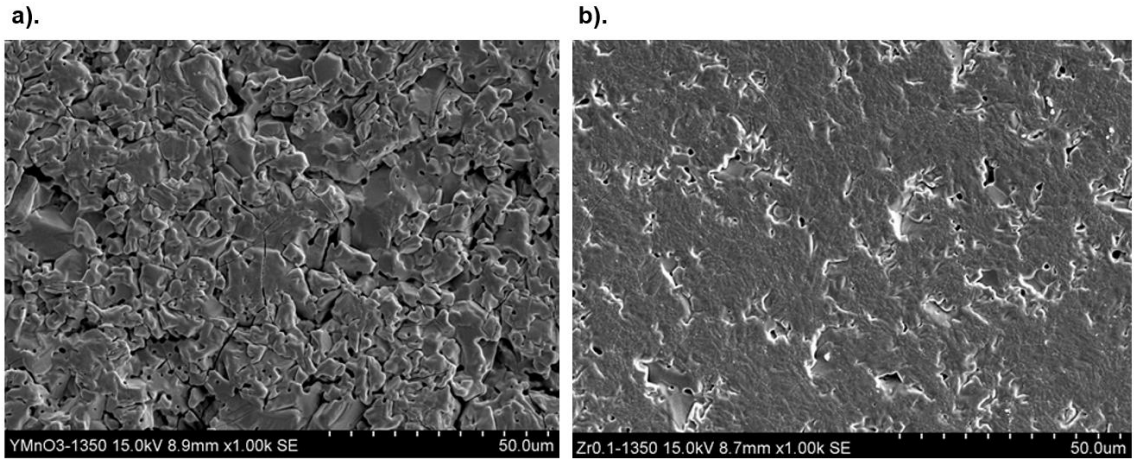

In these micrographs, it can be noticed on the one hand that at the optimum temperature of sintering, $YMnO_3$ microstructure still presents small grains, some cracks, and high level of porosity, in agreement with the compacity value. The latter, can be possibly attributed to the phase transition that has been reported at T~980°C in this material as well as the anisotropic expansion of lattice parameters that can generate residual stresses during the cooling from the sintering temperature. These facts have been previously reported, and our results are quite in agreement [206]. On the other hand, the introduction of zirconium doping seems to improve the way in which the material sinters, since it seems to favor the growth of the grains and therefore, the decrease of porosity. However, the cracks are not totally eliminated because $Y_{0.9}Zr_{0.1}MnO_3$ also undergoes a phase transition as has been discussed before.

3.4.2 Determination of the electrical resistivity of the compounds. Based on the aforementioned results, samples of similar dimensions 5 x 10 mm (diameter x height) were thermally treated at the best sintering temperatures for 2 hours (ramps of

heating and cooling of 5°C min^{-1}) and were subsequently measured by the 4-points probe technique. The results of experimental density and compacity of the corresponding materials are found in Table 12 (the theoretical density Zr-doped material was calculated taking into account their measured oxygen content as detailed in the first section of the present chapter) and are coherent with the preliminary experiments on optimum sintering conditions, even if better compacity were now obtained.

Table 12. Density and compacity of the $YMnO_3$ and $Y_{0.9}Zr_{0.1}MnO_{3.05}$ sintered samples prepared for conductivity measurements.

Sample	Experimental density (g/cm^3)	Compacity (%)
$YMnO_3$	4.624	90.05
$Y_{0.9}Zr_{0.1}MnO_{3.05}$	4.920	94.58

The resistivity of each sample was measured by the 4-points probe technique at different temperatures and in air. From the measured values, the electrical conductivity was determined according to the description made in the experimental chapter, and the corresponding curves are shown in Figure 43. For both materials, the conductivity increases in a similar way when the temperature raises, exhibiting a semiconducting behavior [84] but the Zr-doped sample shows much higher conductivity level than the pure yttrium manganite, what will be discussed below. It is worth noting that other authors have studied the behavior of $YMnO_3$ compound previously and their results are summarized in Table 13.

Figure 43. Evolution with the temperature of the electrical conductivity of $YMnO_3$ and $Y_{0.9}Zr_{0.1}MnO_{3+\delta}$ compounds in air.

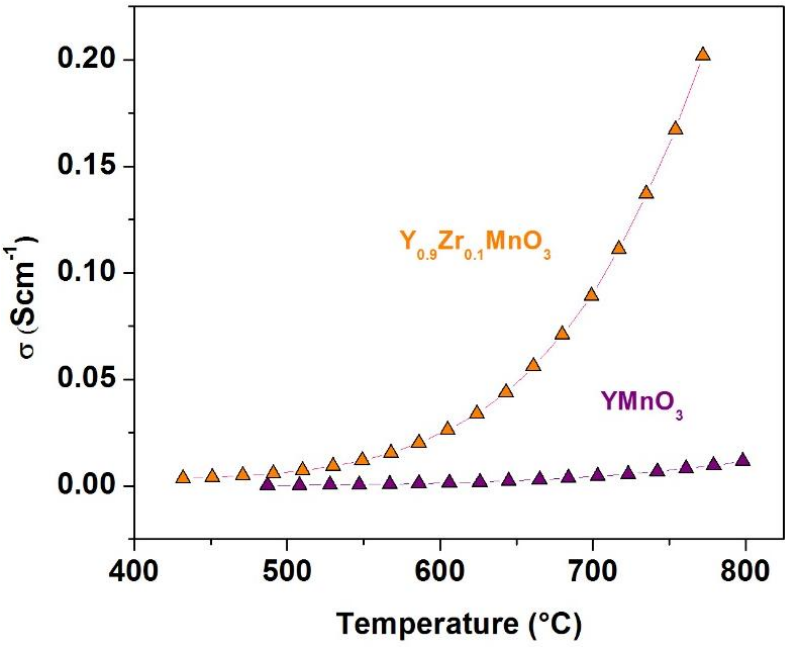

Table 13. Reported electrical conductivity values for $YMnO_3$ at 750°C in air.

Reference	σ (S cm^{-1})
Remsen *et al.* [126]	2x10^{-3}
Jeuvrey *et al.* [146]	3.5x10^{-3}
Ismailzade *et al.* [207]	3.16x10^{-3}
This work	7.4x10^{-3}

As can be seen, although our measurements show slightly higher electrical conductivity than the reported values for $YMnO_3$, it is in the same order of magnitude. For that reason, it is important to highlight that in our case, not only the prepared samples were almost completely dense but also compacity (or porosity) corrections

were applied to the measured data, which take into account the deviation to completely dense sample measurements. Such kind of corrections are no reported in the previously mentioned articles [126], [146], [207] and suggest the possible low density obtained by those authors, as a result of the high synthesis temperatures and the corresponding difficult to densify the materials. Despite those discrepancies, $YMnO_3$ has been described effectively as a semiconductor; more specifically a p-type conductor [84], [132], [133], as other hexagonal manganites with small rare-earth cations at the A-site (Er, Tm, Yb, Lu and Y) [132]. In those materials, the conductivity is mainly due to the partial oxidation of Mn^{3+} to Mn^{4+}, which corresponds to the formation of electron holes [116], [208]. Particularly, in the studied materials this could be related to the extra interstitial oxygen (as described in first section of this chapter). The above because a fraction of occupied Mn *d* states closest to the Fermi energy is lifted above E_F on inclusion of O_i as electron density is donated from Mn 3*d* (Mn^{4+} $d_{x^2y^2}$) to O 2*p* ($2p_x$ and $2p_y$) and, although the charge transfer is not complete, this is regarded as the oxidation of Mn^{3+} to Mn^{4+} [192]. Therefore, holes are created in the valence band and p-type conductivity is carried out. The conduction process consists in small polarons formation and their movement between the Mn^{3+} and Mn^{4+} sites according to a hopping mechanism [84], [132], [133], [146]. It is worth remembering that a small polaron is a fictitious particle formed by a hole (or electron) and its respective crystal framework polarization, that carries an electrical charge and displaces it below an electric field [209]. Most of the metal transition oxides of perovskite structure (ABO_3) conduct electricity by such kind of mechanism, given that the radius of the particle is comparable to the interatomic distances of the oxide [209]; therefore, even if the crystal structure is not the same, it is not surprising that hexagonal $YMnO_3$, presents the same behavior. In addition, the reported low drift mobility of the positive carriers (μ=3 x 10^{-6} cm^2/V.s at 500°C), that is characteristic of holes which move along localized levels, and the positive sign of Seebeck coefficient (p-type electronic conduction) [192], [210] support those previous statements. As a consequence, the conduction in those materials can be modeled with the following expression [126], [146]:

$$\sigma = \frac{A}{T} e^{\frac{-E_a}{kT}} \quad (56)$$

With

A, a constant characteristic of the material,

T, the temperature,

k, the Boltzman constant,

and E_a, the activation energy for polaron hopping.

In Figure 44, the Arrhenius plot that corresponds to ln (σT) vs 1000/T is represented in order to calculate the activation energy of the process.

Figure 44. Arrhenius plot of the electrical conductivity evolution with the temperature for $YMnO_3$ (purple triangles) and $Y_{0.9}Zr_{0.1}MnO_{3+\delta}$ (orange triangles) in air.

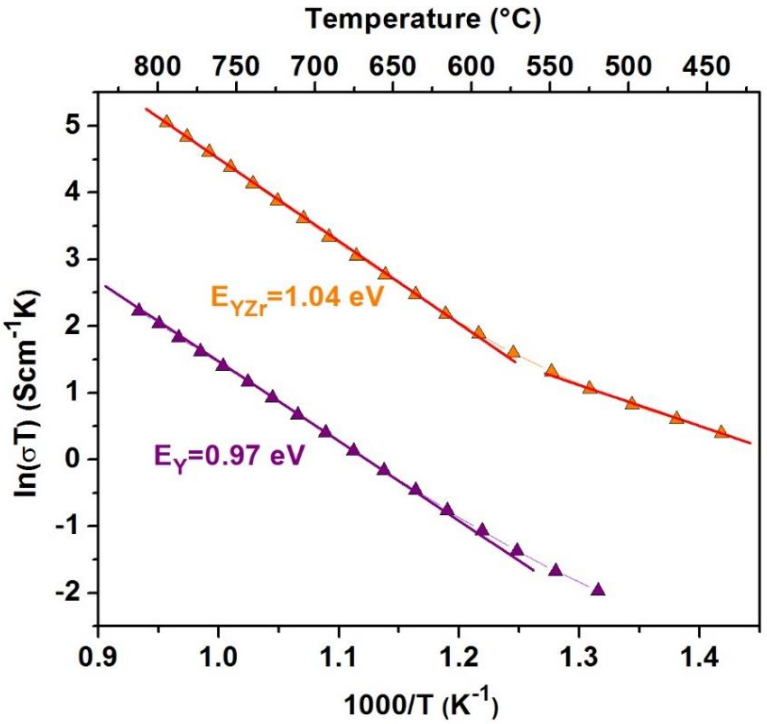

As can be seen in Figure 43, the values fit very well to this linearization, confirming that the materials are narrow band semiconductor where the small polarons move [132]. Additionally, we can observe that for both materials, the conductivity exhibits a change of slope around T=550°C, *i.e.* there are two different activation energy values, at low (LT) and high temperature (HT), respectively. The calculated activation energies for each compound in both temperature regions are shown in Table 14.

Table 14. Activation energy of the electrical conduction process for $YMnO_3$ and $Y_{0.9}Zr_{0.1}MnO_{3+\delta}$ in air

Sample	**Temperature (°C)**	**Activation energy**		
		(eV)	**(kJ/mol)**	**R^2**
$YMnO_3$	490-550	0.7680(3)	74.10(3)	0.9968
	550-800	0.9664(4)	93.24(4)	0.9996
$Y_{0.9}Zr_{0.1}MnO_3$	430-570	0.6282(2)	60.61(2)	0.9916
	570-770	1.0396(9)	100.31(9)	0.9998

Some values of activation energy of $YMnO_3$ compound have been previously reported for the HT region and they are in agreement with what we calculated in this work for the yttrium manganite (E_a=109.99 kJ/mol at 700-900°C [126], 90 kJ/mol at 600-1000°C [84] or 93.31 kJ/mol at T>500°C [208]). It is worth highlighting that the HT values are similar for the two studied compounds, so it is possible to think that the same process governs the conductivity in the undoped and doped materials. At low temperature, *i.e.* below 550°C, the activation energies are significantly lower than in the HT region; and are more different between non-doped and Zr-doped samples.

Such break in the slope in $YMnO_3$ material has been attributed to a ferroelectric-paraelectric transition that experience these kind of compounds around 660°C (T_c, curie temperature) [133], [210]. However, the aforementioned ability of these materials for storing/releasing oxygen seems also to play an important role in the conductivity process change because if oxygen content is modified structural, occupancy and spin state as well as exchange interaction modifications are expected [126]. Thus, it is possible to think that in the LT range, the presence of Mn^{3+}-Mn^{4+} charge carriers is responsible for the electrical conduction of both materials. In fact, it could also explain why the LT activation energy of Zr-doped compound be lesser than that of $YMnO_3$, because the former can absorbs more extra oxygen than the pure manganite and a higher amount of carriers participate in the conduction [211]. Now, the electrical conductivity process in the high-temperature ranges is more difficult to understand given the compounds lose the oxygen excess, and Mn is not far to be purely Mn^{3+}, in both compounds. Then, it is possible affirm that the density of Mn^{4+} carriers (holes) strongly decreases in the HT ranges. In such case, the possibility has been described in literature that the theoretical single valence Mn^{3+} of the compounds exhibits a disproportionation. This reaction is common in TM oxides and consists in the simultaneous oxidation and reduction of the transition metal (Mn in our case) as follows [212]–[214]:

$$2Mn^{3+} = Mn^{2+} + Mn^{4+} \qquad (57)$$

If this happens, Mn^{2+} and Mn^{4+} turn in the new charge carriers of the arrangement [215] with the aim to stabilize the ordering structure [216]. In this case, the activation energy necessary to carried out the disproportionation of Mn^{3+} (Eq. 55) has to paid in addition to the existing activation energy to carry out the hopping mechanism, what could be explained the difference of behavior for both materials between HT and LT.

Another important aspect that needs to be discussed is why Zr-doped material exhibits higher conductivity in the entire measured range (1.6 x 10^{-1} S cm^{-1} at 750°C) in comparison with the non-doped material with σ=7.4 x10^{-3} S cm^{-1} at 750°C (Figure 43). In order to find an explanation, the structural parameters of the corresponding materials should be analyzed. It is important to remember that $Y_{0.9}Zr_{0.1}MnO_3$ present *P*6_3*/mmc* arrangement after synthesis, while $YMnO_3$ crystallizes in a *P*6_3*cm* space group. Whereby it is possible to think that due to the fact that, in *P*6_3*cm* structure, the MnO_5 bipyramids are tilted (Mn-O4-Mn basal angles are 119.373°, 119.358° and 119.387°, and Mn-O3-Mn basal angle is 117.141° in $YMnO_3$), it could be hinder the movement of carriers. On the contrary, the more symmetrical *P*6_3*/mmc* (Mn-O2-Mn basal angles of 120°) should enhance the electrical conduction, as reported for some perovskites in which the Mn-O-Mn angles, generally close to their ideal value (180°), raises better electrical conductivity values [217]. However, as demonstrate previously with the HT- X Ray probes, the Zr-doped compound adopts the same *P*6_3*cm* structure at higher temperatures contradicting the previous hypothesis. Additionally, it is worth noting that the Mn-Mn distance in $YMnO_3$ at HT (average ~3.5518 Å) is very similar to that in $Y_{0.9}Zr_{0.1}MnO_{3.05}$ at HT (average ~3.5292 Å) with only ~0.6% of difference; for that reason, it is possible to affirm the carrier mobility or the hopping distance are approximately the same for both structures. In conclusion, the structural changes seem not be responsible for the conductivity properties. As no structural considerations can really explain the difference between both compounds, we can conclude that the best behavior of $Y_{0.9}Zr_{0.1}MnO_{3.05}$ can be due to the fact that a large part of the electrical conductivity is not electronical in those materials, but ionic (*i.e.* by oxide ions). Indeed, the main difference between $YMnO_3$ and $Y_{0.9}Zr_{0.1}MnO_{3.05}$ is the naturally higher oxygen content.

As a final aspect to analyze, more in scope with the application itself, the conductivity of both compounds is low, compared to perovskite materials that are commonly used as SOFC cathodes: LSM (σ~180 Scm^{-1}), LSCF (σ~300-400 Scm^{-1}), BSCF (σ~30 Scm^{-1}) [218] or LBC (σ~300 Scm^{-1}) [44] and in fact, the materials studied as

electrodes usually exhibits higher conductivity in air. In contrast, in anodic atmosphere the compounds hardly reach a minimum of conductivity of 1 S cm^{-1} and this electrochemical performance is poor, but not because these materials are bad electrocatalysts but bad conductors [219]. For that reason, Gorte *et al.* proposed a strategy to get good anode performance despite the low conductivity values of the electrode material. It consists in building one electrode in two parts: the first, generally thin (10-20 μm), is called functional layer and is only responsible of the electrocatalysis; the second layer, generally thicker and on the top of the functional layer, is in-charge of the current collection. In this kind of electrode configuration, the functional layer requires a minimal conductivity value of only σ~0.01 S cm^{-1}, meanwhile, for the second layer we can use any porous material (cermets, oxides or metals) with enough conductivity electrical (electronical indeed) but chemical compatible with the functional layer material [90], [219], [220]. The possible application of such methodology resulted important in cases like the $La_xSr_{1-x}TiO_{3-\delta}$ lamellar anode. For this, the LST3D compound (x=0.33) exhibits a conductivity of two orders of magnitude higher (σ=8.0 S cm^{-1} at 800°C in reducing atmosphere) than its familiar LST2D (x=0.8) which exhibits only σ=2.3x10^{-2} S cm^{-1} at 800°C in anodic conditions [221]. However, the electrochemical performance of the LST2D material is seven times higher than of the LST3D in reducing atmosphere, when these materials operate as functional layer and a current collecting layer made of a nickel deposited on the top of the titanate [90]. Taking into account these considerations, it is possible to study the electrochemical behavior of the proposed $Y_{1-x}Zr_xMnO_3$ materials if a suitable current collector layer is chosen, as will be discussed in the next section.

3.5 ELECTROCHEMICAL MEASUREMENTS

In this section, the mechanisms of oxygen reduction reaction using symmetrical cells is described, considering $YMnO_3$ and $Y_{0.9}Zr_{0.1}MnO_3$ as potential cathodes materials.

3.5.1 Preliminary EIS measurements. In the first attempts to study the electrochemical behavior of $YMnO_3$, a cell arrangement including a Pt (metallic) current collector was built. Specifically, the configuration used was $Pt/YMnO_3/YSZ/YMnO_3/Pt$, where the $YMnO_3$ electrode (4 layers, ~20 μm) was deposited over the densified electrolyte YSZ via spin coating and sintered at 1000°C for 1 h, then a Pt layer was applied by the sputtering method. The electrochemical impedance spectra of the cell were measured in air ($pO_2 \approx 0.20$ atm) using 2 thermal cycles between 500 and 800°C. The corresponding results are shown in Figure 45.

Figure 45. (a) Arrhenius plot of ASR vs temperature for $Pt/YMnO_3/YSZ/YMnO_3/Pt$ symmetrical cells and (b) Example of impedance response (at 550°C during second cooling and at 600°C during heating).

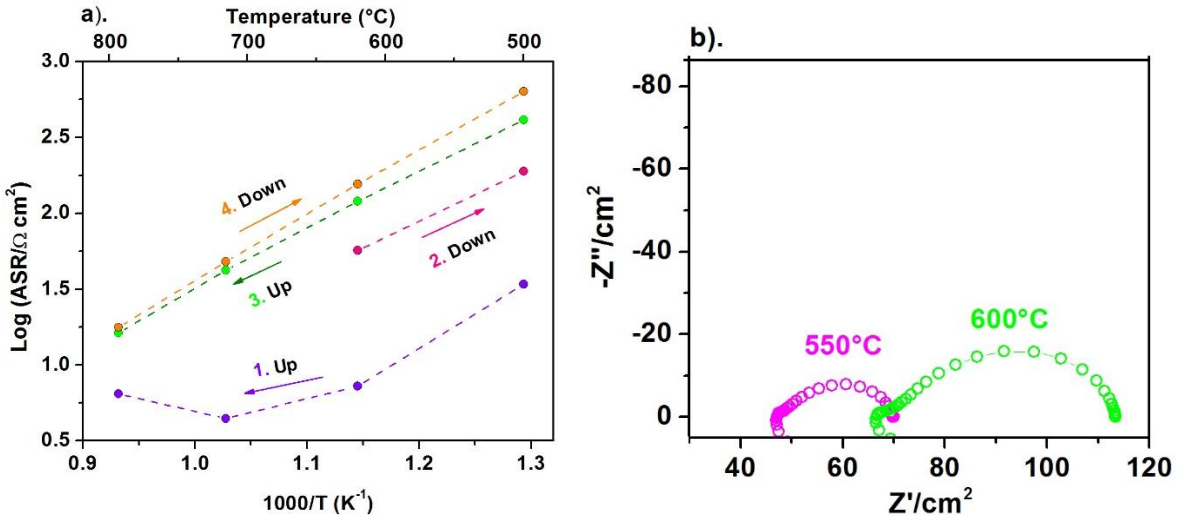

The plot of ASR values as a function of temperature (in Arrhenius coordinates) and during the 2 cycles is shown in Figure 45(a). We can notice that during the first cycle (*i.e.* increasing the temperature from 500 to 800°C, cycle 1.Up), the logarithm of the total Area Specific Resistance (ASR) initially diminishes as temperature increases, as expected. However, the behavior deviates from linearity and ASR begins to increase for T>700°C. Additionally, we observe that during the first cooling (2.Down),

log(ASR) continues to raise and do not show the same values as during the first heating. Similarly, during the second heating (3.Up), the value of log(ASR) increases again and such unstable behavior repeats again during the last thermal cycle. In Figure 45(b), two examples of impedance spectrum are shown, that have been obtained in different conditions (at 550°C during cooling and at 600°C during second heating); it can be appreciated that the shape of the spectra are similar and this is indeed the case during the whole experiment. Now, in order to understand the reason of such behavior, the sample was analyzed by Scanning Electron Microscopy (SEM) (Figure 46(a)).

Figure 46. SEM Micrograph of (a) the Pt/$YMnO_3$/YSZ/$YMnO_3$/Pt cell, after EIS measurements, and (b) YSZ electrolyte with a layer of Pt deposited by sputtering (after treatment at 800°C).

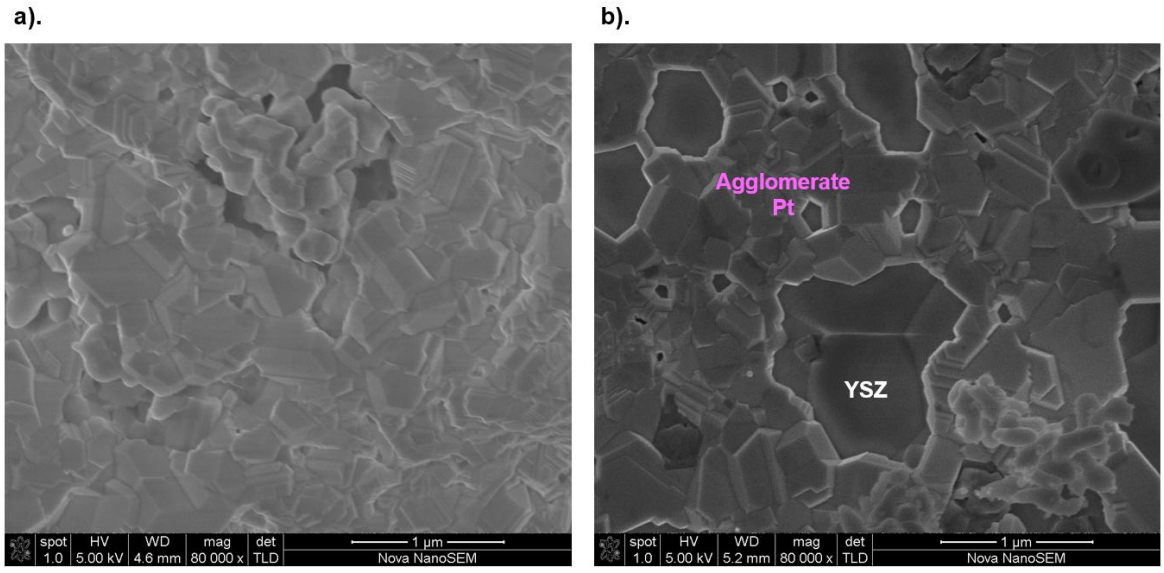

In Figure 46(a), a top view of one face of the symmetric cell is presented, after EIS measurements. Here, a layer of almost square-shaped crystallites can be observed. This particular microstructure belongs to the Pt layer that covers the substrate; as

shown in Figure 46(b), in the case of a dense YSZ pellet directly coated with platinum (after a heat treatment at 800°C, during 12 h), Pt agglomerates in the form of square-shaped plates. When this occurs, some regions remains uncovered by platinum and hence the specific resistance increases, maybe due to the fact that current collection is less effective, what is especially an issue for electrodes with low electrical conductivity, as this is the case for $YMnO_3$. However, the most important consequence of the microstructure change after thermal treatment can also be observed in Figure 46(a). On the top of the sample, there is no detectable porosity, *i.e.* agglomerated platinum seems to prevent the necessary gas diffusion and oxygen access to the electrode, causing also the resistance increase. In view of the above, a replacement of the metal for a thermally stable ceramic current collector was considered. Specifically, the electronic conductor LSM ($La_{0.2}Sr_{0.8}MnO_3$) was chosen. In this case, when we carry out electrochemical measurements using LSM/$YMnO_3$/YSZ/$YMnO_3$/LSM symmetric cell, the resistance values completely overlap during heating and cooling, as shown in Figure 47. It is also worth noting that the polarization resistance values are lower when using LSM, what suggests a more effective current collection with the second material. For that reason, LSM was chosen as a current collector for all the tests in cathodic conditions. The symmetrical cells were built with the following arrangement: LSM/$YMnO_3$/YSZ/$YMnO_3$/LSM, and subsequently the conditions to minimize ASR values were optimized. First, the influence of the sintering temperature on the transport properties was studied. For this, the number of layers of the LSM current collector (2 layers, ~10 µm) and of the electrode (4 layers, ~20 µm) was set. The samples were submitted to sintering heat-treatment at different temperatures (from 1000 to 1250°C, every 50°C) and their impedance data were measured (pO_2≈0.20 atm, 500-800°C).

Figure 47. Arrhenius plot of ASR as a function of temperature for an LSM/$YMnO_3$/YSZ/$YMnO_3$/LSM cell (pO_2≈0.20 atm).

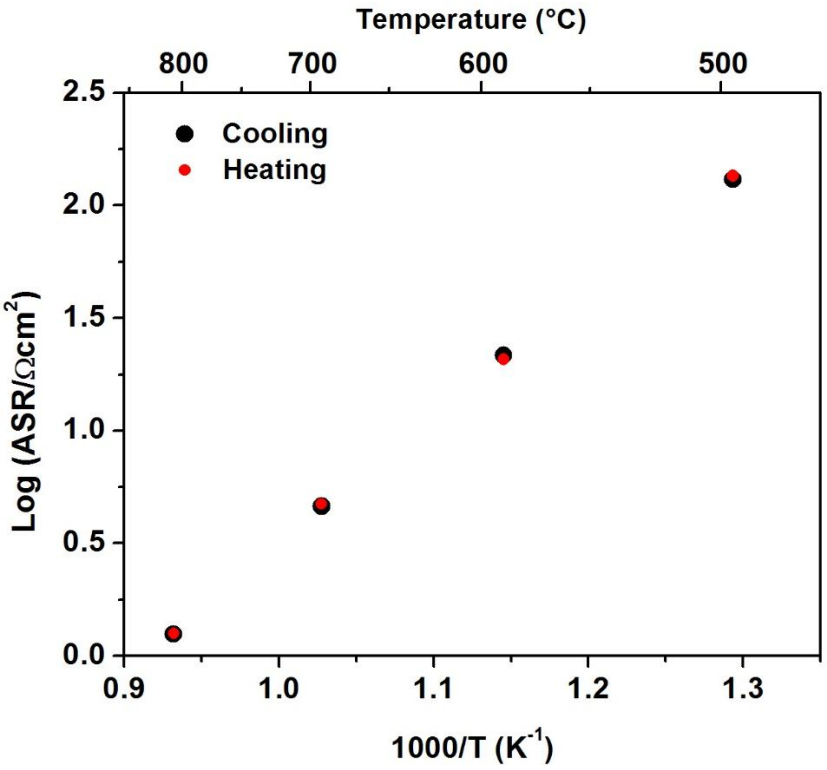

The curves corresponding to log(ASR) as a function of temperature for the different sintering conditions, are depicted in Figure 48. We observe that in the interval from 1000 to 1150°C the resistance decreases with the sintering temperature. However, from 1200°C, the resistance starts increasing again. Then, a temperature of 1150°C is considered as an optimal point and is highlighted with a dashed oval in the same Figure 48.

Figure 48. Arrhenius plot of ASR as a function of temperature in air ($pO_2 \approx 0.20$ atm) for symmetric cells including $YMnO_3$ cathode prepared at different sintering temperatures. Enclosed in an oval is the optimal condition for T=1150°C.

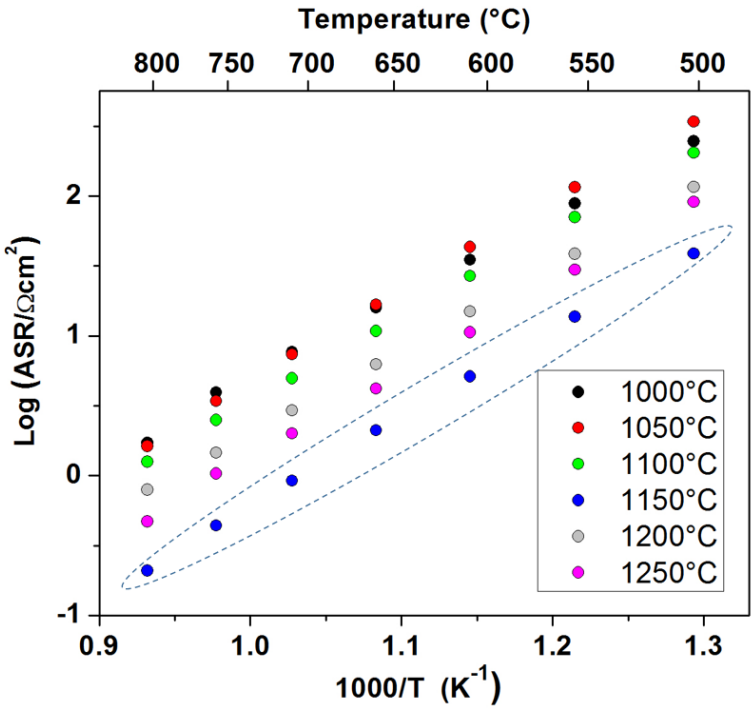

It is worth noting that the resistance values are different for every temperature because the cathode microstructure varies (grain size and porosity) and hence the interaction with reactive gas is changing. In order to examine such variation, SEM images of the different cells are shown in Figure 49.

Figure 49. SEM images of the $YMnO_3$ electrode microstructure when subjected to different sintering treatments: (a) 1100°C, (b) 1150°C and (c) 1250°C.

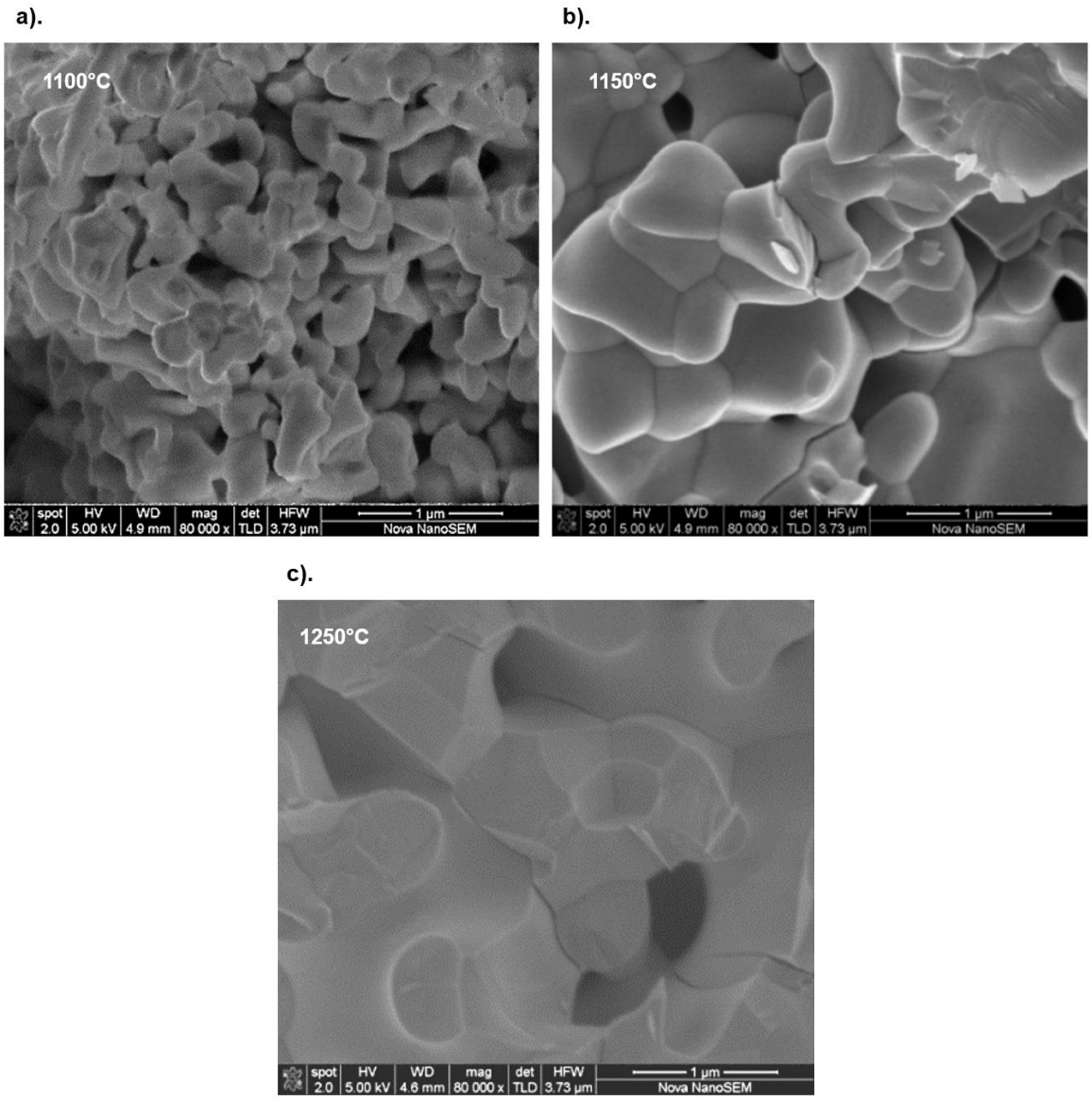

We observe that, at 1100°C (Figure 49(a)), the material is constituted of small grains which that increase the specific surface for O_2 reduction reaction; nevertheless, this temperature does not correspond to the best condition due to the fact that the same grains have poor contact between them and with the YSZ electrolyte. The latter could

be detrimental for the charge transfer of electroactive species within the cathode material and therefore resistance is high [222]. Likewise, cells that have been heat-treated at 1250°C (Figure 49(c)) present huge specific resistance values. In this case, the reason is that electrode grains have grown, agglomerated and finally the material is almost sintered. Therefore, such cathode material does not exhibit sufficient specific area and porosity for the diffusion of reactive gases; therefore, the cathode reaction is blocked. As a consequence, the sintering temperature of 1150°C (Figure 49(b)) seems to maintain a balance between porosity and connection between $YMnO_3$ grains.

Another factor affected by the sintering temperature is the adhesion of the cathode compound on the dense electrolyte. Then, the electrode-electrolyte interface of the same cells was observed by SEM (Figure 50). By comparing the three micrographs, it is possible to notice that at 1000°C (Figure 50(a)), the electrode material is not properly joined to the electrolyte. As a consequence, electroactive species cannot move through the interface and the cathode mechanism can not occur in a proper way. For the two higher temperatures, a good contact electrode-electrolyte is achieved (Figure 50(b) and 50(c)). Nonetheless, as already said, the best comprise is obtained for the cell prepared at 1150°C, which shows the lowest resistance in the whole studied temperature range, due to its good microstructure and its appropriate adhesion.

Figure 50. SEM micrographs of the electrode-electrolyte interface for $YMnO_3$/YSZ/$YMnO_3$ cells prepared at different sintering temperatures: (a) 1100°C, (b) 1150°C and (c) 1250°C.

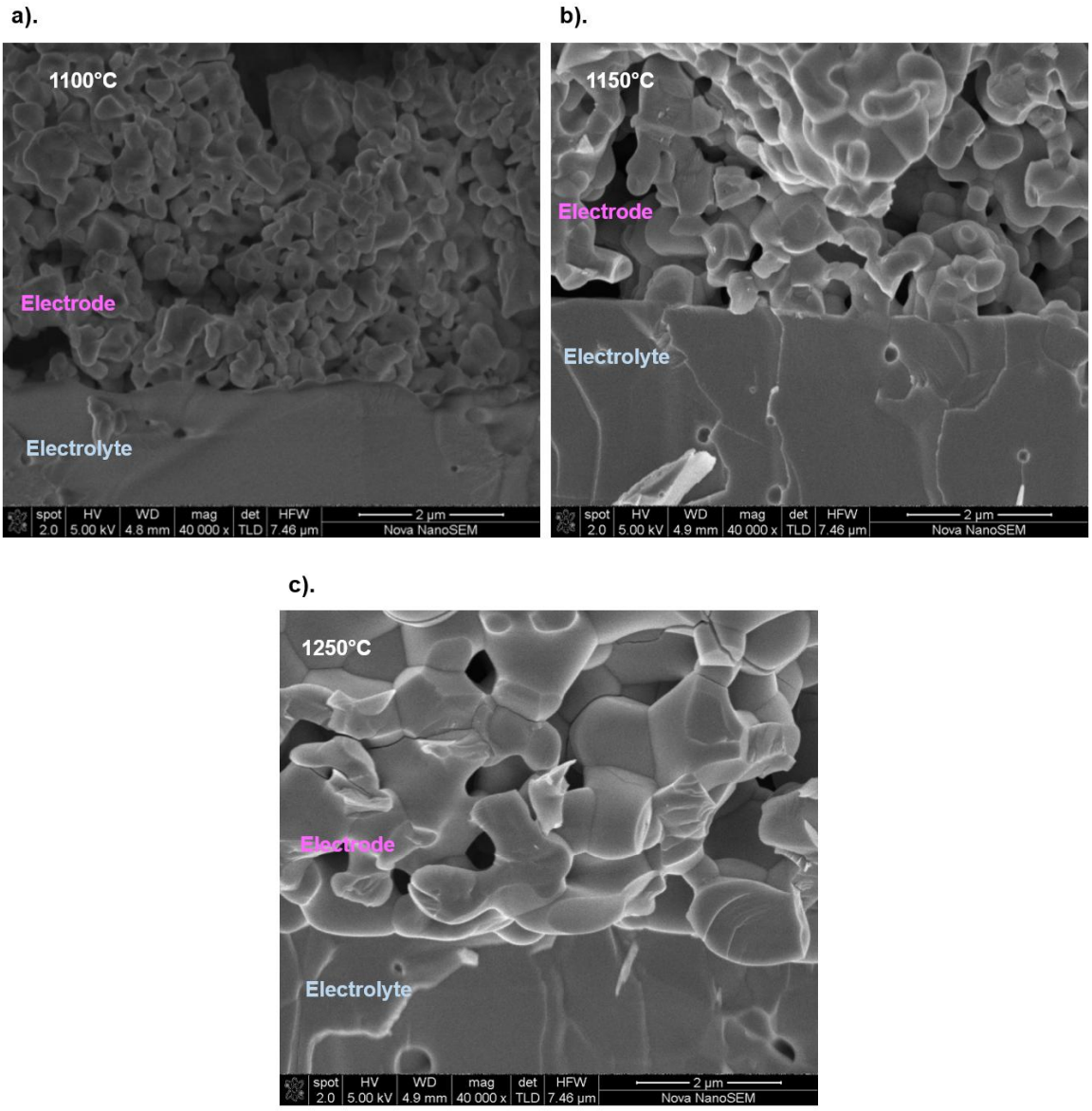

Considering the linear behavior observed in Figure 48, an apparent activation energy can be calculated at each sintering temperature, summarized in Table 15. All values are very similar, and it is possible to affirm that limiting reaction mechanisms are

probably the same; however, considering that the best choice is for a sintering temperature of 1150°C, such study will be examined and discussed into details later, after performing EIS measurements in different oxygen partial pressures; it will be the object of the next section.

Table 15. ASR apparent activation energy of LSM/$YMnO_3$/YSZ/$YMnO_3$/LSM symmetric cells for the different sintering temperatures.

Sintering temperature (°C)	Activation energy (eV)
1000	1.15(9)
1050	1.27(9)
1100	1.20(3)
1150	1.24(8)
1200	1.19(1)
1250	1.24(7)

The second variable we considered was the number of electrode layers applied to the electrolyte, *i.e.* the cathode thickness. For that, LSM/$YMnO_3$/YSZ/$YMnO_3$/LSM symmetric cells were prepared with 2, 4 or 6 layers of the $YMnO_3$ compound and were heat-treated at the optimal temperature previously determined (T=1150°C) for 3 hours. In the same way, a fixed amount of LSM (2 layers) was deposited on the top of the active layer. Sectional views of the cells were observed using SEM technique, with the aim of determining the electrode thickness. As can be observed in Figure 51 (a-c), the cathode thickness of 2, 4 and 6 layers corresponds to 12, 24 and 42 µm, respectively.

Figure 51. SEM micrographs of LSM/$YMnO_3$/YSZ/$YMnO_3$/LSM symmetric cells showing the thickness of the active layer made of: (a) 2 layers, (b) 4 layers and (c) 6 layers.

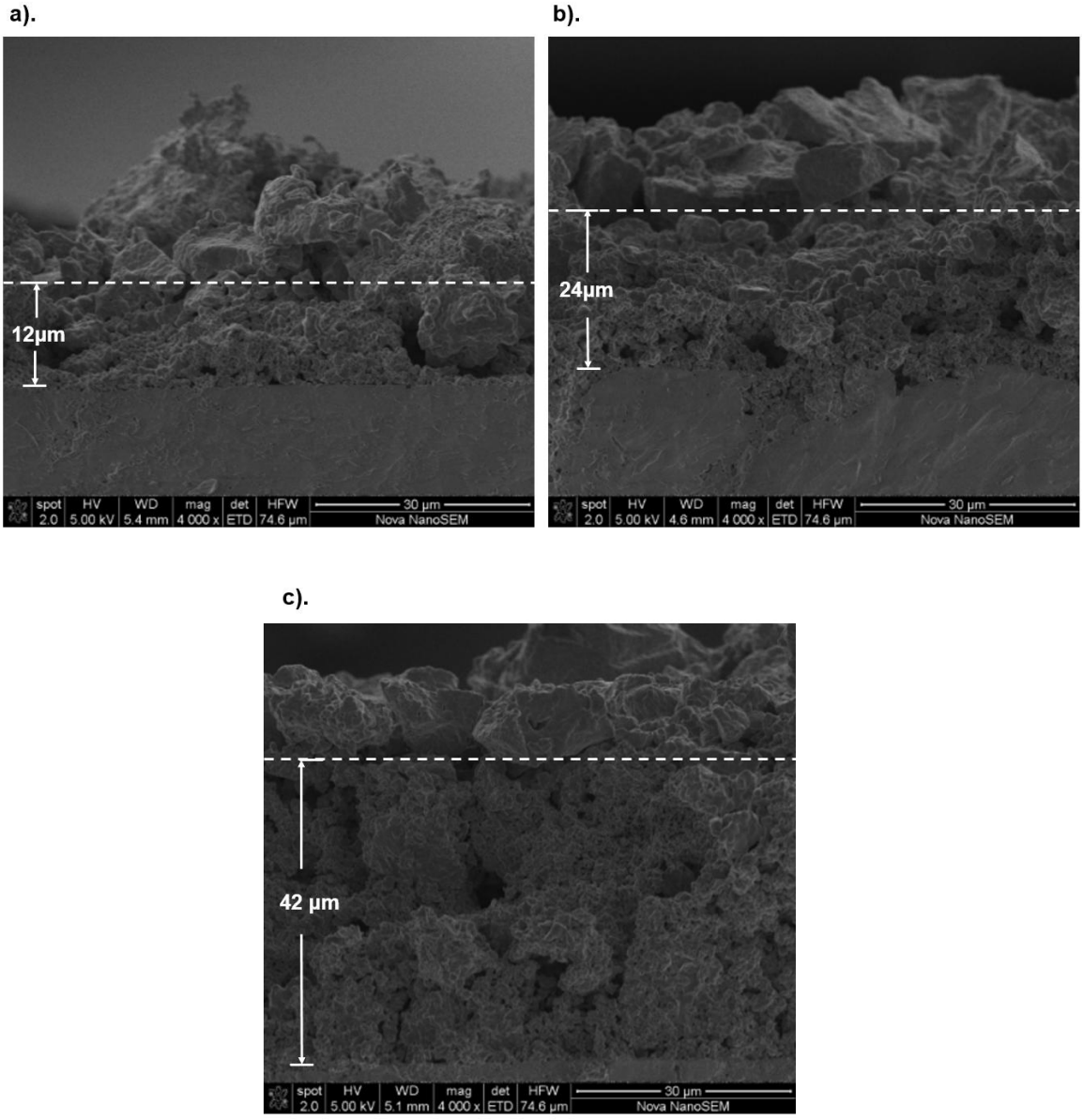

The impedance spectra of the cells were measured in order to determine the best conditions concerning the active layer thickness. A visual analysis of the impedance spectra and bode representation of the three cells allows to appreciate a similar

shape (Figure 52(a) and 52(b)). Then, it seems that, regardless of the layer thickness, the processes carried out are similar but with different magnitude.

Figure 52. Comparison of (a) Impedance response in air and at 800°C for LSM/$YMnO_3$/YSZ/$YMnO_3$/YSZ symmetric cells with different thickness of electroactive layer (The numbers indicate the frequency logarithms), (b) Bode representation and (c) the Arrhenius plot of ASR vs measurement temperature.

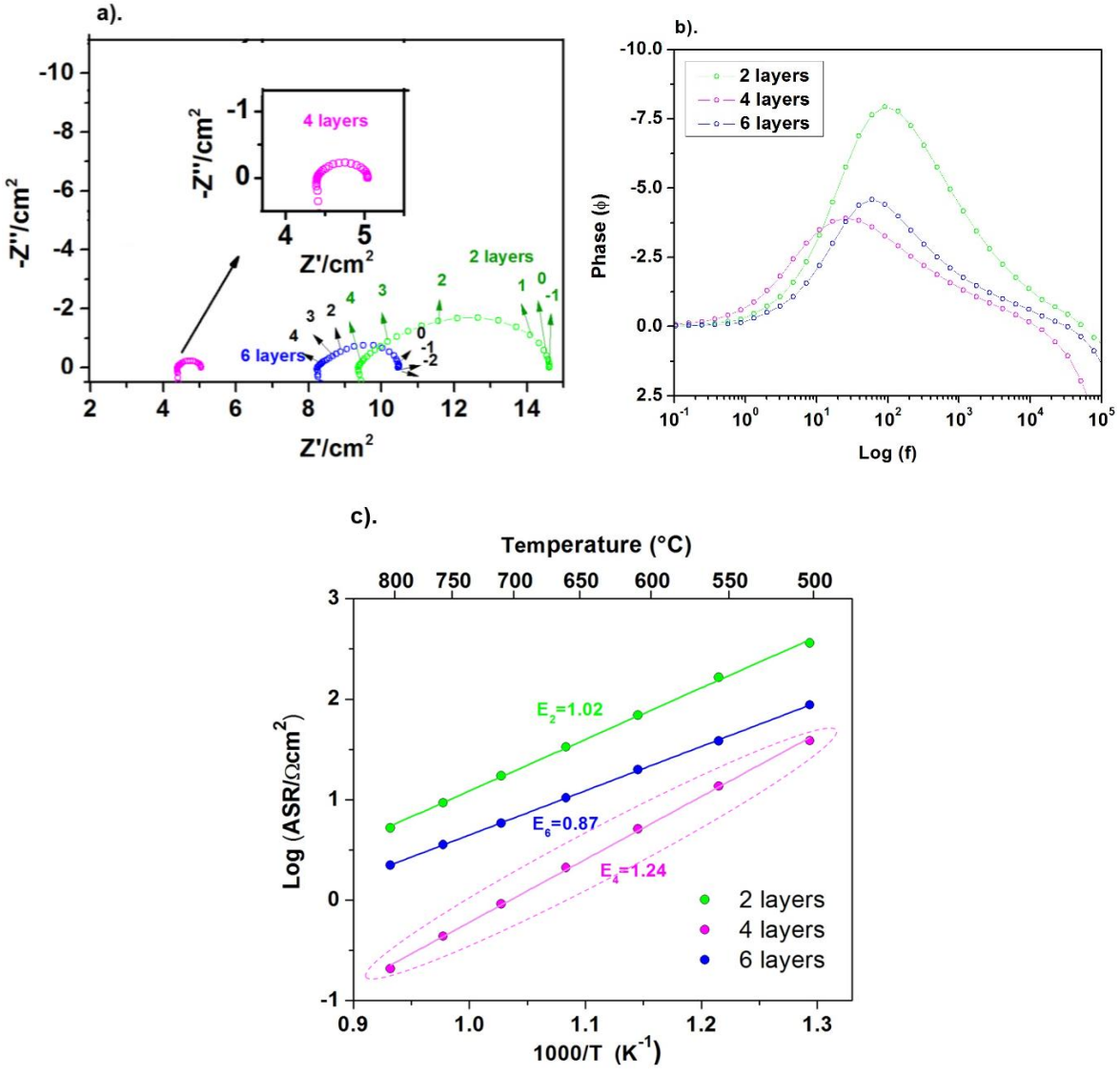

On the other hand, from Figure 52 it seems clear that the symmetric cell made of 2 layers of active material exhibit a higher total ASR than in the other cases. The above could be consequence of the increment of active sites for electrochemical reaction [223]. Additionally, given that $YMnO_3$ material exhibits low conductivity, a poor cross conductivity is expected in a thinner electroactive layer of the compound. Therefore, an increase in the thickness of the layer could mean an increment in the fraction of the material used to the conduction process. However, when the number of layers increments from 4 to 6, the specific resistance raises again. One possible reason is that although there are more sites, only those which are close to the gas-electrode interface actively participate in cathode reaction [222]. Hence, in previous research, it has been demonstrated that the loss in electrode performance is almost entirely caused by an increase in ohmic resistance in the cells with thicker functional layers [220]. Therefore, the thin active layer of 24 μm is considered as optimal maybe due to negligible ohmic resistance.

Similarly, symmetrical cells with a configuration $LSM/Y_{0.9}Zr_{0.1}MnO_3/YSZ/Y_{0.9}Zr_{0.1}MnO_3/LSM$ were built with the aim to study the influence of Zr-doping on the electrochemical properties. In this case, the number of layers of the LSM current collector (2 layers) and the electrode (4 layers) were set, and only the influence of the sintering temperature was analyzed. Thus, cells were heat-treated in a range of 1000-1250°C and, subsequently, their impedance were measured. In Figure 53, we can appreciate that the total resistance visibly decreases from 1000°C to 1100-1150°C. Nevertheless, for higher temperatures, the ASR increases again.

Figure 53. Arrhenius plot of ASR as a function of temperature in air for LSM/$Y_{0.9}Zr_{0.1}MnO_3$/YSZ/$Y_{0.9}Zr_{0.1}MnO_3$/LSM symmetric cells prepared with different sintering temperatures of the active layer.

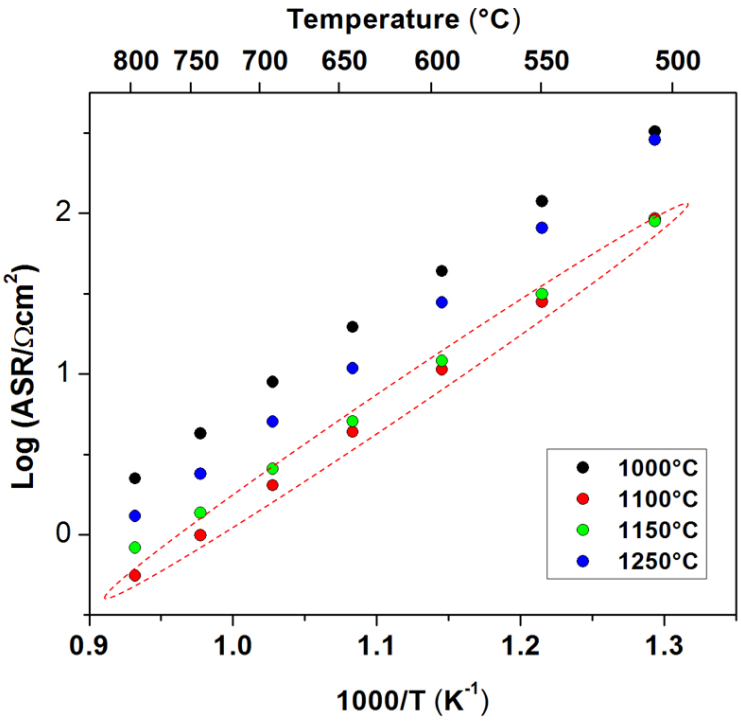

In view of the above, it is possible to say that an active layer sintering temperature of T=1100 or 1150°C (for which the ASR values almost overlap) are optimal conditions. In order to understand such behavior, the corresponding cells were examined by SEM. The micrographs are shown in Figure 54.

Figure 54. SEM images of the electrode microstructure for LSM/$Y_{0.9}Zr_{0.1}MnO_3$/YSZ/$Y_{0.9}Zr_{0.1}MnO_3$/LSM symmetric cells prepared with different heat treatments: (a) 1000°C, (b) 1100°C and (c) 1250°C.

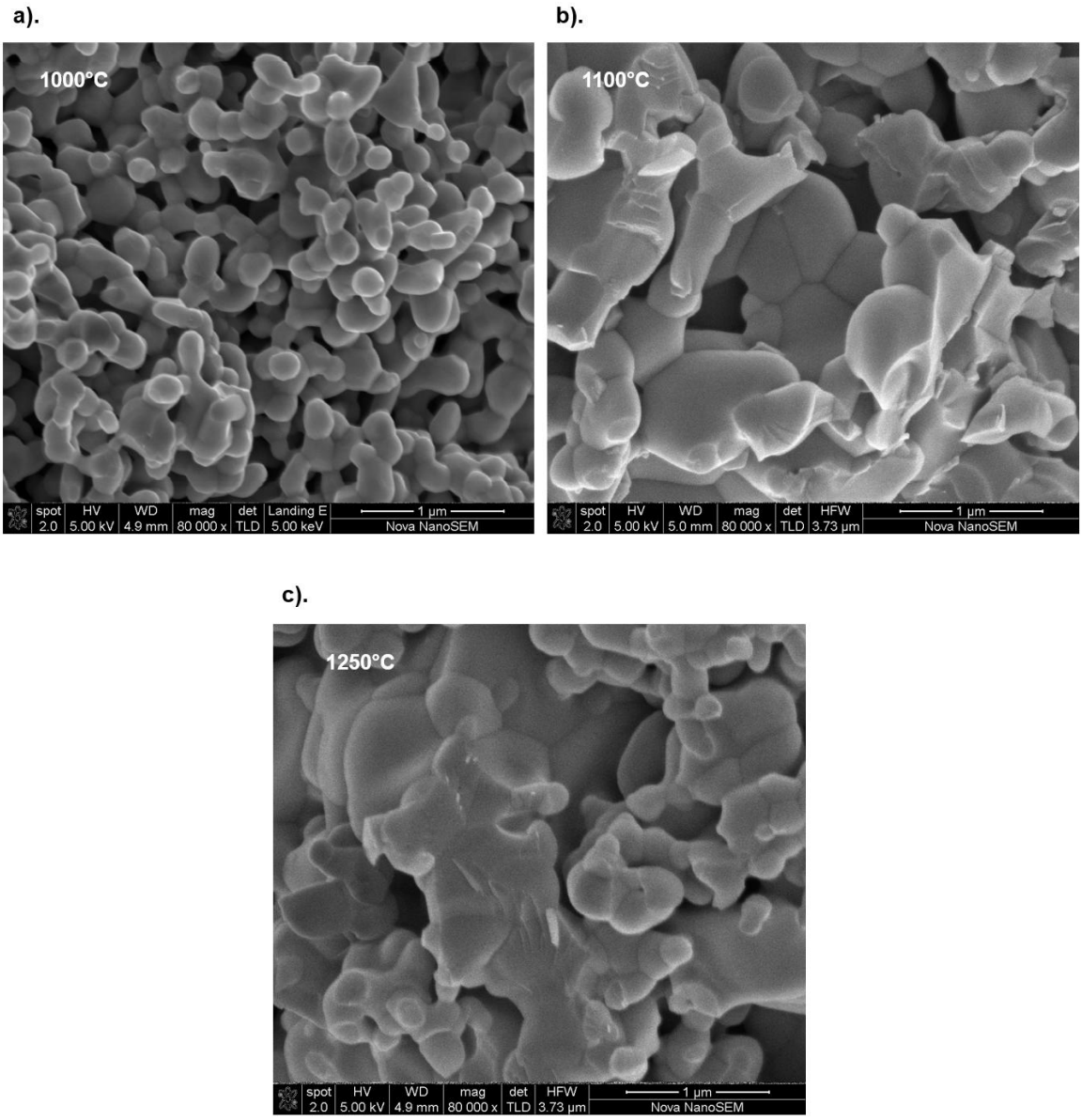

First, a good distribution of grains can be observed at 1000°C (Figure 54(a)); nonetheless, particles are widely separated. As a result of the low grain contact, the conduction in the bulk of the electrode is also limited. At higher temperatures (Figure

54(b) and 54(c), the material particles grow in size and the porosity decreases; nonetheless, a higher performance is observed for the cell prepared at 1100°C because of a good balance between a low grain size and sufficient porosity vs a better contact between the manganite grains. Finally, the activation energies of each set of data have been determined and are reported in Table 16. These values are relatively close and, therefore, the cells exhibit possibly the same limiting reaction mechanisms at all temperatures of sintering.

Table 16. ASR apparent activation energy of LSM/$Y_{0.9}Zr_{0.1}MnO_3$/YSZ/$Y_{0.9}Zr_{0.1}MnO_3$/LSM symmetric cells for the different sintering temperatures.

Sintering temperature (°C)	Activation energy (eV)
1000	1.18(1)
1100	1.22(1)
1150	1.12(1)
1250	1.28(1)

As a summary of this section, the evolution with temperature of the impedance data corresponding to the optimal cells prepared with $YMnO_3$ (sintered at 1150°C) and 10%Zr-doped $YMnO_3$ (sintered at 1100°C) are exhibited in Figure 55 and 56, respectively. Impedance values were normalized considering the electrode area in a symmetric cell and the cell geometry ($Z_{Normalized}=Z_{Measured}$*Electrode geometric area/2). Thus, for both the LSM/$YMnO_3$/YSZ/$YMnO_3$/LSM and LSM/$Y_{0.9}Zr_{0.1}MnO_3$/YSZ/$Y_{0.9}Zr_{0.1}MnO_3$/LSM cells, the spectra present two well distinguished arcs. Nonetheless, the high frequency contribution (frequency higher than 10^1 Hz) disappears from 600°C; therefore, this arc seems to belong to the

electrolyte impedance [169]. In this form, only the low frequency contribution can be associated with the Oxygen Reduction Reaction at the electrode.

Figure 55. Impedance spectra of LSM/$YMnO_3$/YSZ/$YMnO_3$/LSM cell (sintered at 1150°C) at different temperatures, in air.

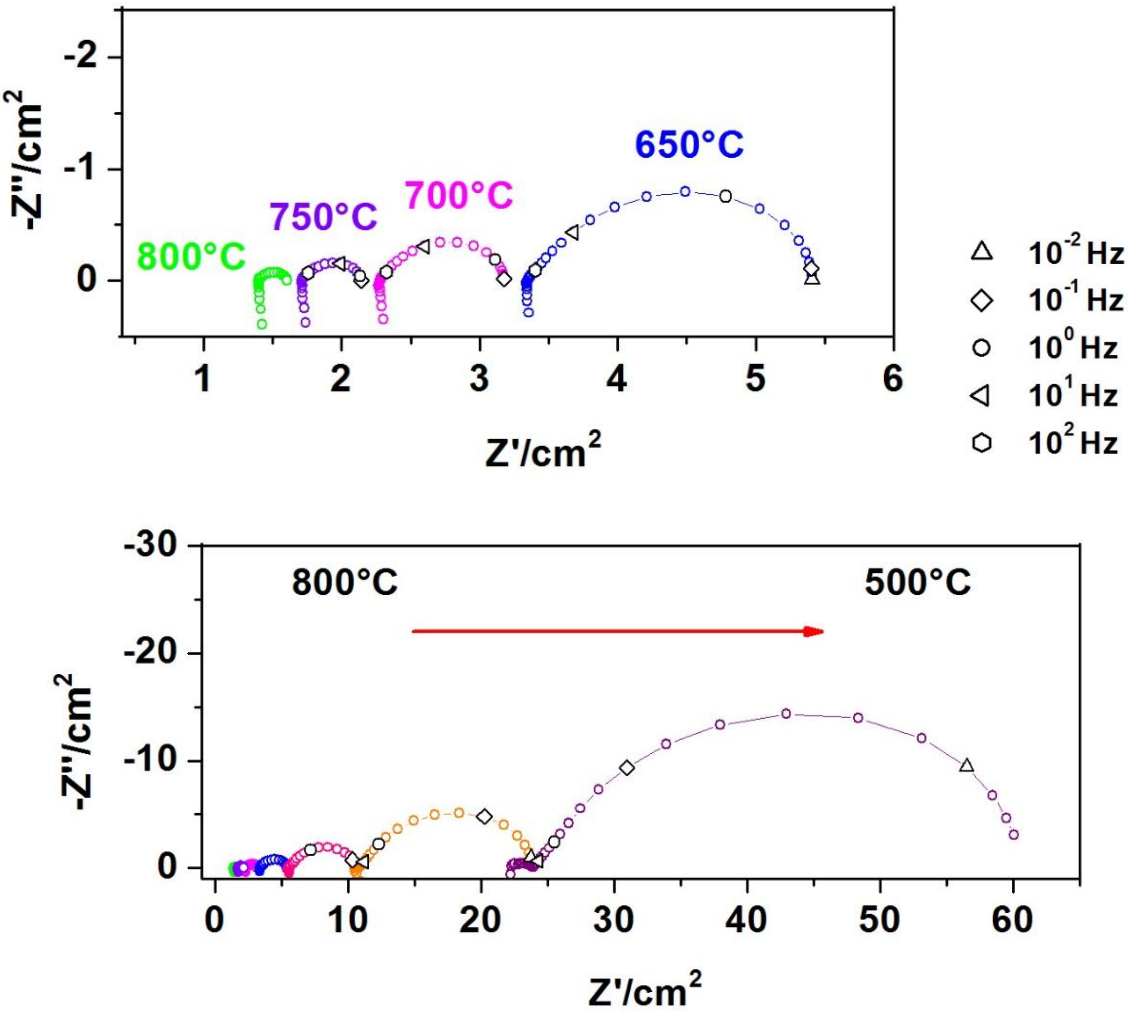

On the other hand, the shape of the spectra for the cells including the Zr-doped manganite are different from the cells with $YMnO_3$, what must be related to different limiting processes. In each case, such difference will be deeply studied in the next

section, but, from Figures 55 and 56, it is already possible to conclude that the resistances for LSM/$YMnO_3$/YSZ/$YMnO_3$/LSM cell are lower than for LSM/$Y_{0.9}Zr_{0.1}MnO_3$/YSZ/$Y_{0.9}Zr_{0.1}MnO_3$/LSM cells at every temperature of measurement.

Figure 56. Impedance spectra of LSM/$Y_{0.9}Zr_{0.1}MnO_3$/YSZ/$Y_{0.9}Zr_{0.1}MnO_3$/LSM cell (sintered at 1100°C) measured in air at different temperatures.

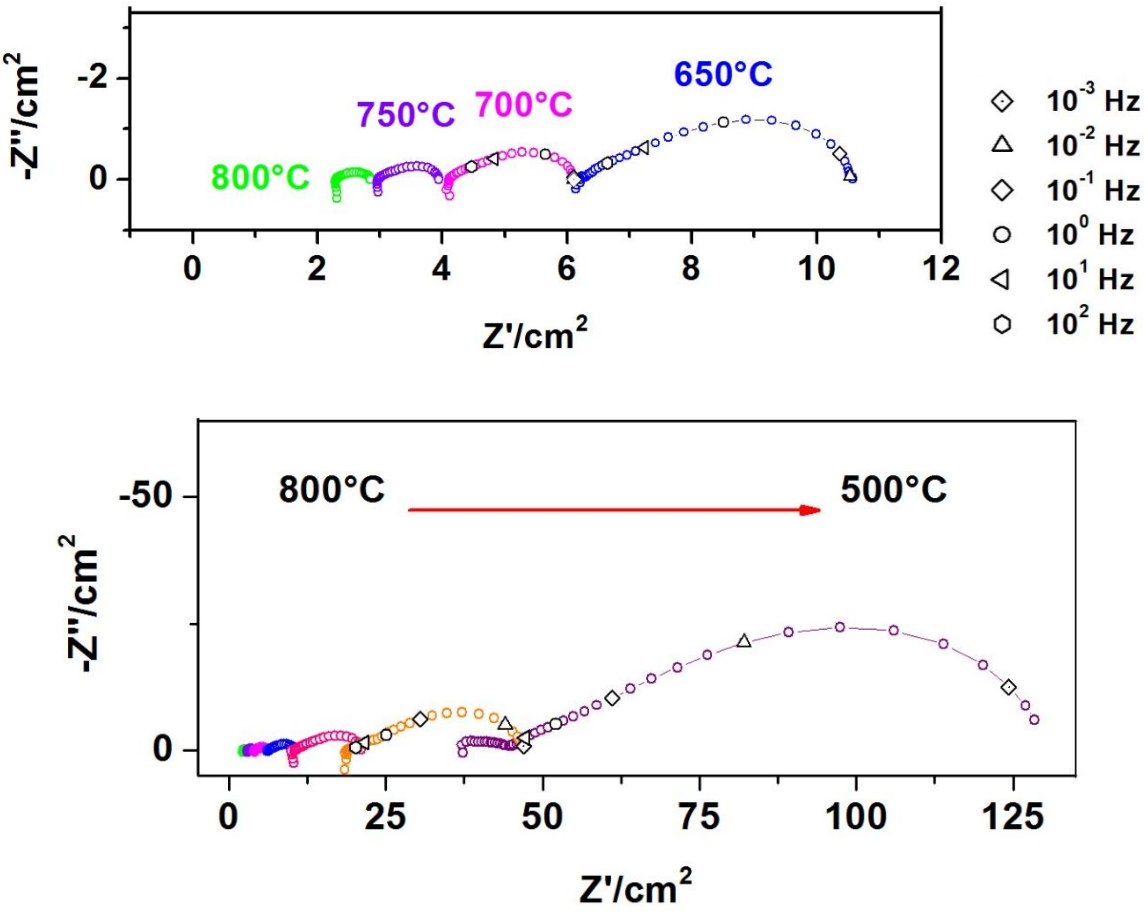

A comparison of the Arrhenius plot of the ASR vs temperature evolution for each optimal cells using $YMnO_3$ (sintered at 1150°C) or 10%Zr-doped (sintered at 1100°C) electrode is given in Figure 57. It emphasizes the best performance of the $YMnO_3$-based cell (R_P=0.209 Ω cm^2 at 800°C), although it is important to highlight

that both sets of values can be considered as high for cathodes (R_P=0.555 Ω cm^2 at 800°C $Y_{0.9}Zr_{0.1}MnO_3$-based cell). For example, the layered cobaltites $NdBaCo_2O_{6-\delta}$ or $SmBaCo_2O_{6-\delta}$ exhibit values of more than one order of magnitude lower for the polarization resistance at 700°C (R_P=0.035 and 0.08 Ω cm^2, respectively). However, our values for the new manganites are lower than the reported for the state of art cathode LSM (R_p<1 Ω cm^2 at 1000°C) or the Ruddlesden Popper ferrites $Sr_3FeMO_{6+\delta}$ (M= Fe, Co, Ni) (R_P≈1.25-4 Ω cm^2 at 800°C) [47]. Our polarization resistance values are comparable with those of LSM/YSZ composites 60:40 and 40:60 (0.49 Ω cm^2 and 6.53 Ω cm^2 at 700°C, respectively) [224]. Therefore, being the first reported study on the subject, we can conclude that the electrode proposed in the current work are promising also from the electrochemical point of view

Figure 57. Log ASR values vs temperature for symmetrical cells containig $YMnO_3$ and $Y_{0.9}Zr_{0.1}MnO_3$ compound is its optimal conditions.

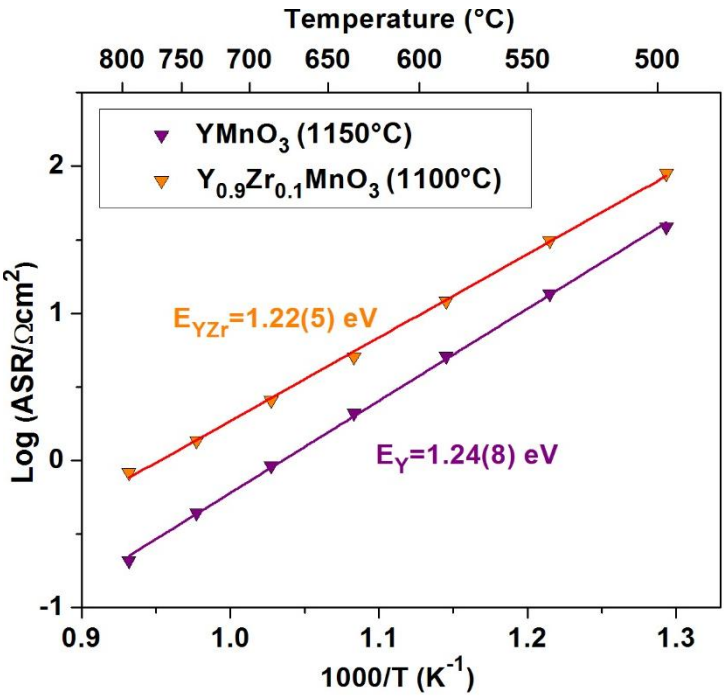

3.5.2 Study of EIS vs pO_2 at different temperatures. In order to determine what processes are involved in the oxygen reduction reaction of the potential electrode materials, the optimized symmetrical cells were measured at different oxygen partial pressures ($10^{-4} \leq pO_2 \leq 1$ atm) and at one constant temperature (T= 600, 700 or 800°C). In Figure 58, an example of EIS spectrum of each of the cells LSM/$Y_{1-x}Zr_xMnO_3$/YSZ/$Y_xZr_{1-x}MnO_3$/LSM (x= 0, 0.1) is depicted. It is clear that $Y_{0.9}Zr_{0.1}MnO_3$ cell exhibits higher resistances than $YMnO_3$ cell and such behavior is repeated at every temperature, whatever the oxygen partial pressure.

Figure 58. EIS spectra of LSM/$Y_{1-x}Zr_xMnO_3$/YSZ/$Y_xZr_{1-x}MnO_3$/LSM (x=0, 0.1) cells measured at T=800°C and pO_2=0.20 atm.

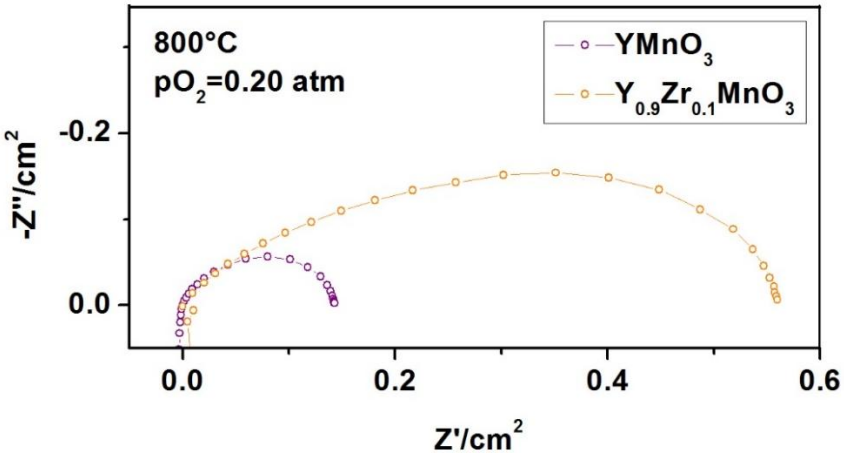

However, the most important information obtained from these measurements is the phenomena individualization through the calculation of oxygen reaction order γ ($R_i \alpha pO_2^{\gamma}$) and capacitances C (the latter increases as the process dimension increases, from interface to electrode bulk) [225]. For this, all the spectra were fitted with equivalent circuits built from the analysis of impedance data and taking into account the shape; subsequently, one element is attributed to one physic process according to its dependance with pO_2, capacitance value and frequency range [44].

3.5.2.1 Identification of limiting steps for LSM/$YMnO_3$/YSZ/$YMnO_3$/LSM cell. First, the spectra in Nyquist representation of LSM/$YMnO_3$/YSZ/$YMnO_3$/LSM cell measured at **600°C** under different pO_2 are shown in Figure 59. The impedance grows as pO_2 value decreases, as expected. Likewise, the shape of the spectra does not exhibit any substantial change along the pO_2 range; as a consequence, all the spectra can be fitted using the same model.

Figure 59. Electrochemical impedance spectra of LSM/$YMnO_3$/YSZ/$YMnO_3$/LSM at T=600°C for different pO_2 values.

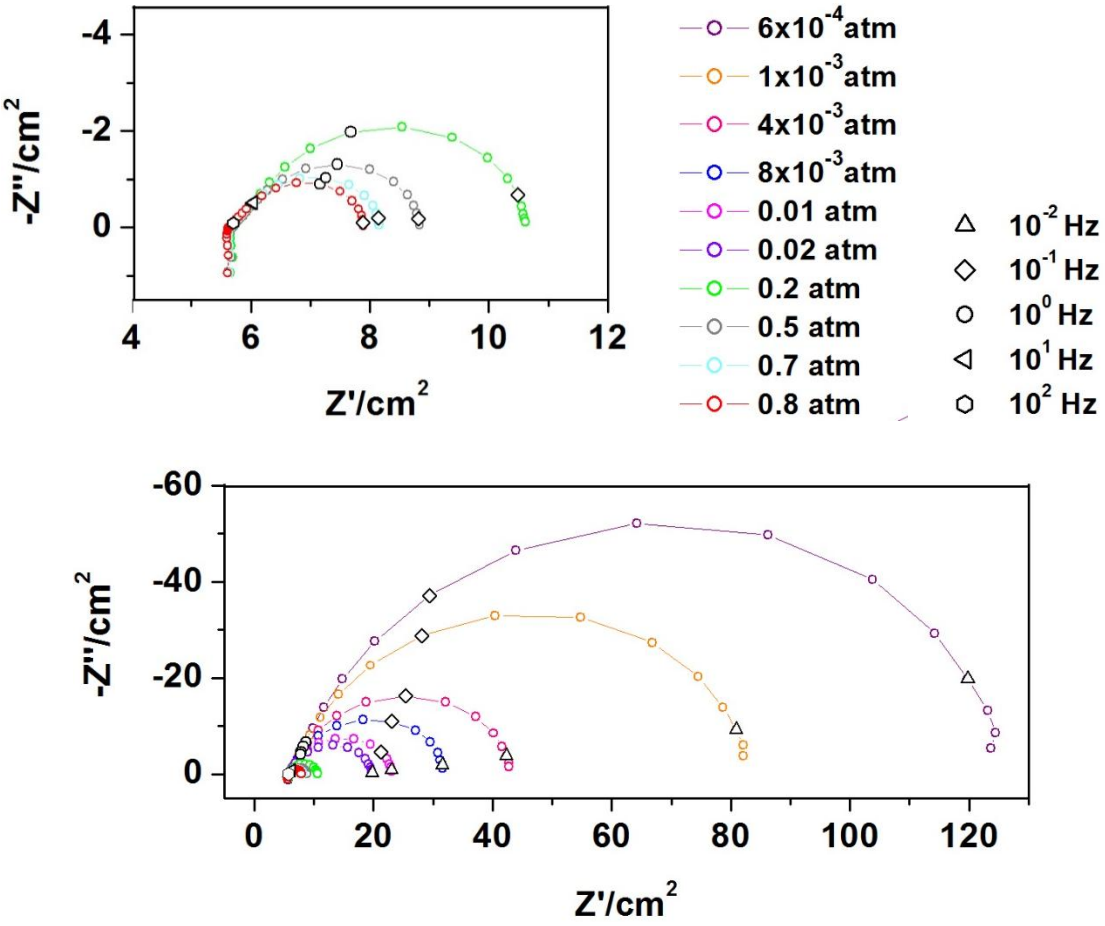

Additionally, all the curves in the Bode plot (Figure 60) show only one maximum of relaxation frequency; therefore, it is possible to suppose there is mainly an unique contribution or limiting step in the entire pO_2 range.

Figure 60. EIS spectra in Bode representation for LSM/$YMnO_3$/YSZ/$YMnO_3$/LSM cell at T=600°C for different pO_2 values.

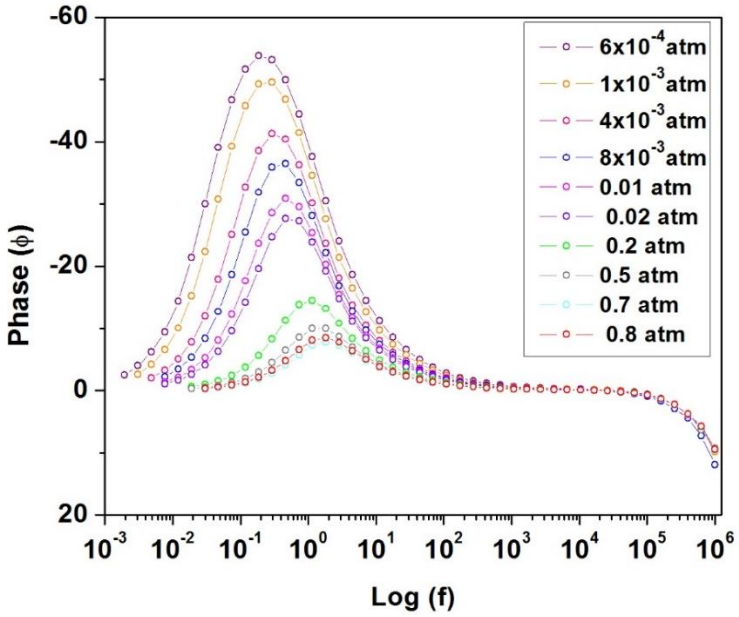

In this sense, the impedance response has been modeled initially with one equivalent circuit consisting of (i) an inductive element (L_1) due to the inductance of the wires, (ii) an ohmic resistance (R_1) that corresponds mainly to the electrolyte resistance and (iii) a parallel combination of one resistance and one constant phase element (R/CPE). The result of the fit for the highest pO_2 is graphed in Figure 61(a). As can be observed, the model is not satisfactory to explain the spectrum shape. For that reason, a second circuit with a Gerischer-type impedance (R_G), instead an the R/CPE element, was also tested. However, this model neither explains effectively the experimental data as shown in Figure 61(b).

Figure 61. Experimental EIS spectrum of LSM/$YMnO_3$/YSZ/$YMnO_3$/LSM cell at T=600°C and pO_2≈0.8 atm, compared to the calculated spectrum corresponding to (a) a R/CPE element and (b) Gerischer element.

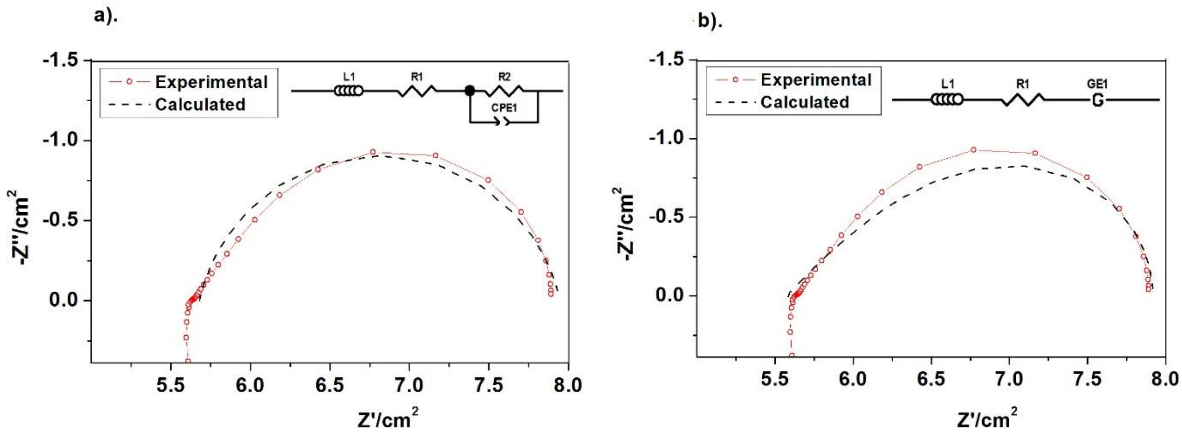

Considering those first results, and in particular that, in the Bode plot, several limiting phenomena are probably overlapping because they correspond to similar relaxation times or because the influence of one element is too small compared to the other, a new equivalent circuit with both a R/CPE and a Gerischer element has been tested. Additionally, a small (R/CPE) contribution has been added at high frequencies, that was not taken into account at the beginning in the equivalent circuit. As shown in Figure 62(a,b), the impedance response is now successfully modeled using such complex equivalent circuit.

Figure 62. (a) Impedance spectrum adjustment of LSM/$YMnO_3$/YSZ/$YMnO_3$/LSM cell (T=600°C and pO_2≈0.8 atm) indicating the three limiting contributions to the equivalent circuit and (b) Bode representation with the same deconvolution.

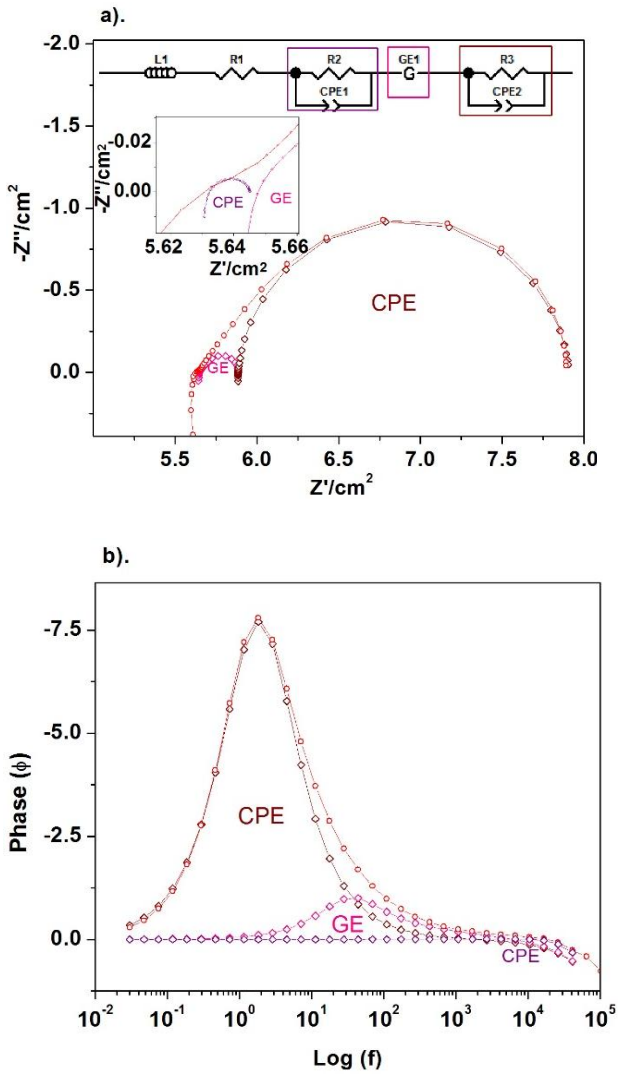

At this point, it is worth highlighting that the spectra in the entire pO_2 range were all well adjusted with the same circuit and all ontributions increase as the oxygen partial pressure (pO_2) decreases, but the R/CPE of the lowest frequency is the most affected contribution (see Annex D). Using the results of the adjustments, a log-log plot of resistances vs pO_2 values can be obtained (Figure 63), with the aim of

characterizing the nature of the limiting steps, the latter because the aforementioned reaction order (γ) represents the calculated slope for each curve using such kind of graph.

Figure 63. Dependence with oxygen partial pressure of the ASR for each limiting process in the case of an LSM/$YMnO_3$/YSZ/$YMnO_3$/LSM cell at T=600°C. The reaction order (γ) of each step is also included.

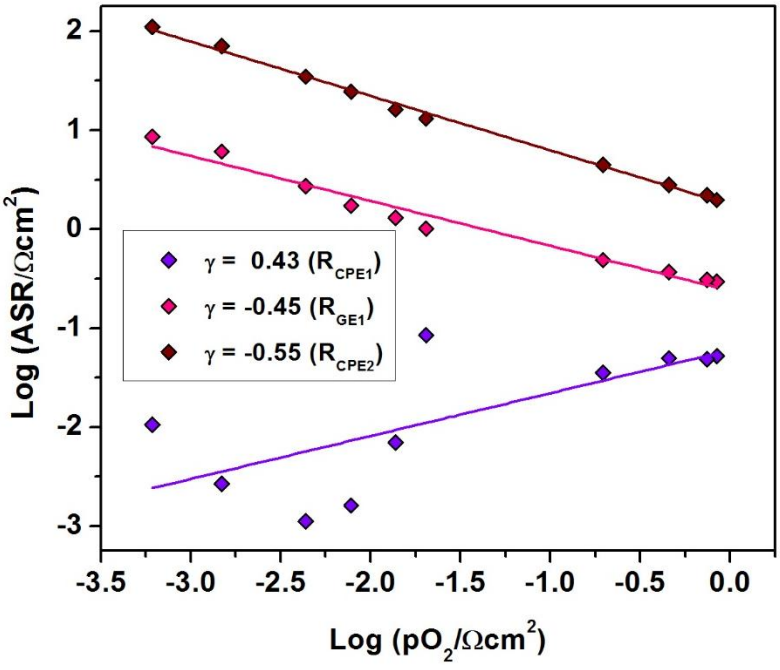

At 600°C, the R_2/CPE_1 contribution exhibits a dependence of R α $pO_2^{0.43}$ and capacitances of C~10^{-5} F/cm^2, which can be associated with a process of ionic transfer to the electrode or to the TPB. However, it must be clarified that such element explains the very small semicircle at higher frequencies, but this does not fit easily and is only present at such low temperature. Therefore, the contribution can be attributed with greater certainty to the ionic intergranular resistances of the electrolyte, due to the fact that YSZ electrolyte exhibits low ionic conductivity values at T≤ 600°C. Given that the YSZ conductivity increases with temperature, such

contribution disappears at higher temperatures and, is not usually taken into account for analysis [47], [226].

The second contribution is a Gerischer element (R_G) and it shows a dependence of $R \alpha pO_2^{-0.45}$ and capacitances of $C \sim 10^{-2}$-10^{-1} F/cm^2. This impedance element arises from solving the diffusion equation for a finite medium in which occurs surface oxygen exchange [44]; thus, it can be described more accurately as a co-limiting process between the oxygen exchange at the electrode/gas surface and the oxygen diffusion in the bulk [227]–[229]. In principle, the Gerischer model was developed for a porous single-phase MIEC and depends on the concentration and diffusivity of vacancies within the electrode bulk [230]. Then, Gerischer impedance has been found in mixed conducting electrodes even with poor electronic conductivity as those made of lanthanum chromite/titanate. Therefore, it is not surprising to find this element in cells with $YMnO_3$ compound, which also exhibits a low electric conductivity but maybe a high ionic conductivity. On the other hand, it is important to mention that usually a γ close to -0.25 is expected for cathode materials; however, a lower γ value could suggest a higher contribution of the oxygen exchange to the co-limiting process [44]. In addition, it is necessary to point out that the Gerischer model starts with the fact that the oxygen reduction reaction is carried out within a penetration depth (*d*) in the MIEC material. The *d* value is interpreted as the length of the reaction zone beyond the triple phase boundary (TPB), and in some compounds is much larger than the average grain size and the entire electrode grain participates in the reaction [215], [230]. In the cases in which *d* is higher than the electrode thickness (penetration depth approaching the size of the particles at higher frequencies or approaching the total thickness of the cathode) [231], [232], the high-frequency slope in the spectra exhibits some deviation from the expected 45° slope and the chemical capacitance is large in comparison to the other impedance elements [230]. These facts are observed in the tested cell as shown in Nyquist plot (Figure 64) and capacitances raise a value of ~0.5 F/cm^2 [230].

Figure 64. The experimental EIS spectra of LSM/$YMnO_3$/YSZ/$YMnO_3$/LSM cell at T=600°C and pO_2≈0.8 atm. A comparison with the 45° slope expected for Gerischer impedance is also shown.

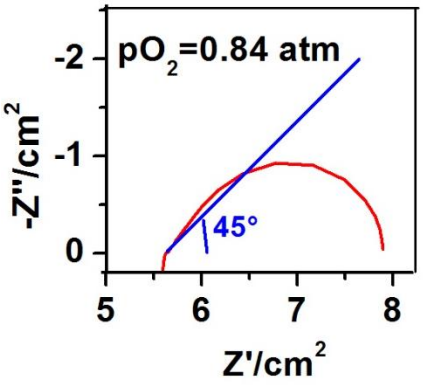

For its part, the third contribution is a R_3/CPE_2 element with a dependence of R α $pO_2^{-0.55}$ and capacitances of C~0.05 F/cm^2. The γ value and the fact that such impedance appears at low frequency allows associating it with an oxygen dissociative adsorption process on electrode surface [225], [233]. This is also in agreement with the intermediate calculated capacitances characteristic of superficial processes [225]. It is worth taking into account that, in general, the presence of an adsorption limiting step depends on the number of active sites for oxygen adsorption. About this, some authors affirm that, in perovskite and Ruddlesden-Popper phases the adsorption is carried out by the transition metal; nonetheless, the resistances are higher in the second kind of materials. The reason is that the number of available sites for adsorption per surface unit[2] is lower for the Ruddlesden-Popper (Γ~10^{-6} mol cm^{-2} for $Sr_3FeBO_{6+\delta}$ with B=Fe, Co and Ni against Γ~10^{-5} mol cm^{-2} for $La_{0.6}Sr_{0.4}Co_{0.8}Fe_{0.2}O_3$ perovskite) [47]. For its part, the studied $YMnO_3$ material exhibits even higher polarization resistance of adsorption compared to both mentioned materials. Therefore, it is easy to think that the number of available sites

[2] Maximal number of adsorption sites, $\Gamma = \frac{Metal-moles}{Unit\ cell\ area}\ [=]\frac{mol}{cm^2}$

for adsorption is lower in the case of $YMnO_3$ electrode. Although, to compare the Γ values, the materials microstructure must be similar [227], a maximal number of absorption sites can be estimated for the studied case. The calculated value is in the same magnitude order of the Ruddlesden-Popper compound ($\Gamma \sim 10^{-6}$ mol cm^{-2}). Then, it seems that the Mn in these non-isotropic arrangements interacts with the oxygen in a different way and adsorption becomes slow. In the same way, it is important to notice that this type of limiting step could be better understood if porosity, tortuosity and superficial area would be known [234] because the dissociative adsorption usually appears in the impedance diagram as grain size decreases or when the thickness is small enough so that ionic conductivity does not control the reaction [47]. However, such aspects of the microstructure was not studied in this work although, as it was discussed above, the particles in this electrode seem not too large in comparison with the active reaction zone.

In the case of the measurements carried out at **700°C** ($10^{-4} \leq pO_2 \leq 1$ atm) on an LSM/$YMnO_3$/YSZ/$YMnO_3$/LSM cell, it is possible to observe lower resistance values in comparison with those measured at 600°C. However, these resistances also grow as pO_2 value decreases, as shown in the Nyquist representation of Figure 65. It is worth noting that the spectra have similar shape as for T=600°C; hence, it is likely that the same model can be used.

Figure 65. Electrochemical impedance spectra of LSM/$YMnO_3$/YSZ/$YMnO_3$/LSM cell at T=700°C for different pO_2 values.

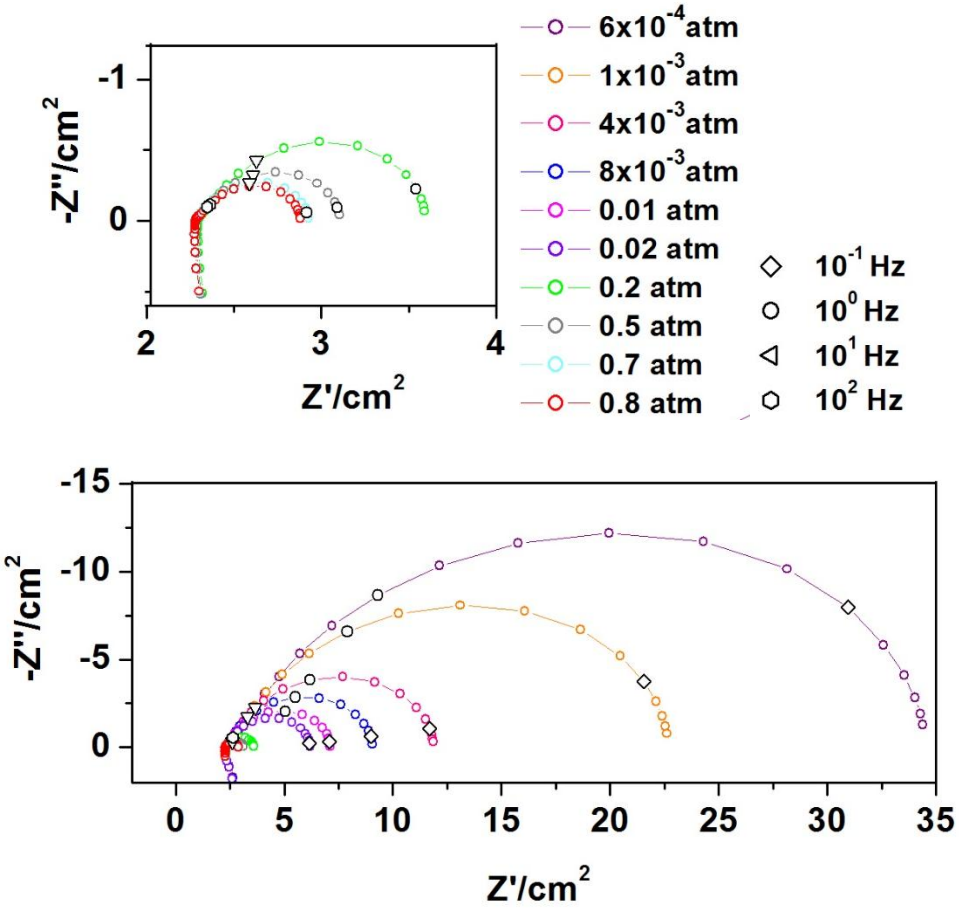

Using Bode plot of the data (Figure 66) we observed that the curves have one maximum of relaxation frequency. Nevertheless, as in the previous case, there are indeed two main contributions but with similar relaxation times. Thus, the proposed equivalent circuit includes (i) an inductive element (L_1) due to the inductance of the wires, (ii) an ohmic resistance (R_1) that is mainly due to the electrolyte resistance, (iii) a Gerischer-type element (R_G) and, finally, (iv). a parallel combination of one resistance and one constant phase element (R/CPE). This model fits experimental data appropriately in the entire range of measurements (Annex E). An example is graphed in Figure 67.

Figure 66. EIS spectra in Bode representation for LSM/$YMnO_3$/YSZ/$YMnO_3$/LSM cell at T=700°C for different pO_2.

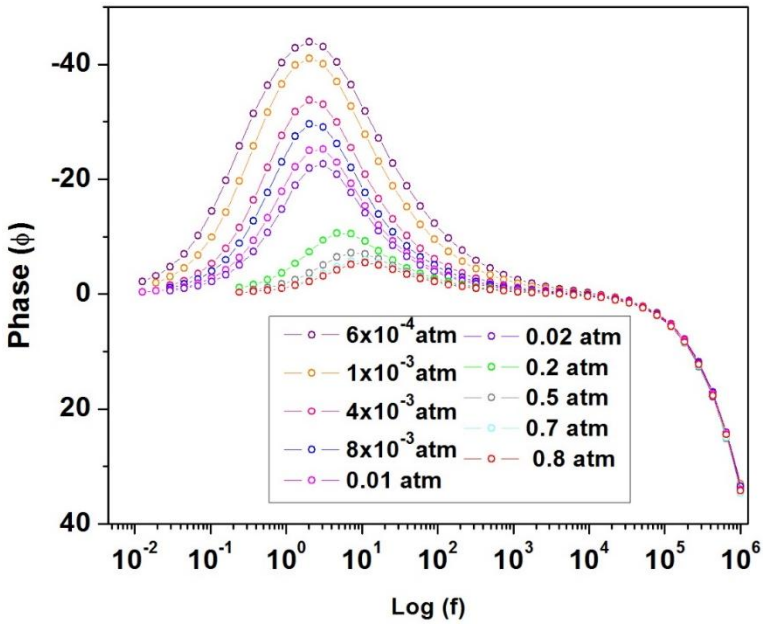

Figure 67. (a) Impedance spectrum adjustment of LSM/$YMnO_3$/YSZ/$YMnO_3$/LSM cell (T=700°C and $pO_2 \approx 6x10^{-4}$ atm) indicating the different contributions of the equivalent circuit (b) Bode representation with the same deconvolution.

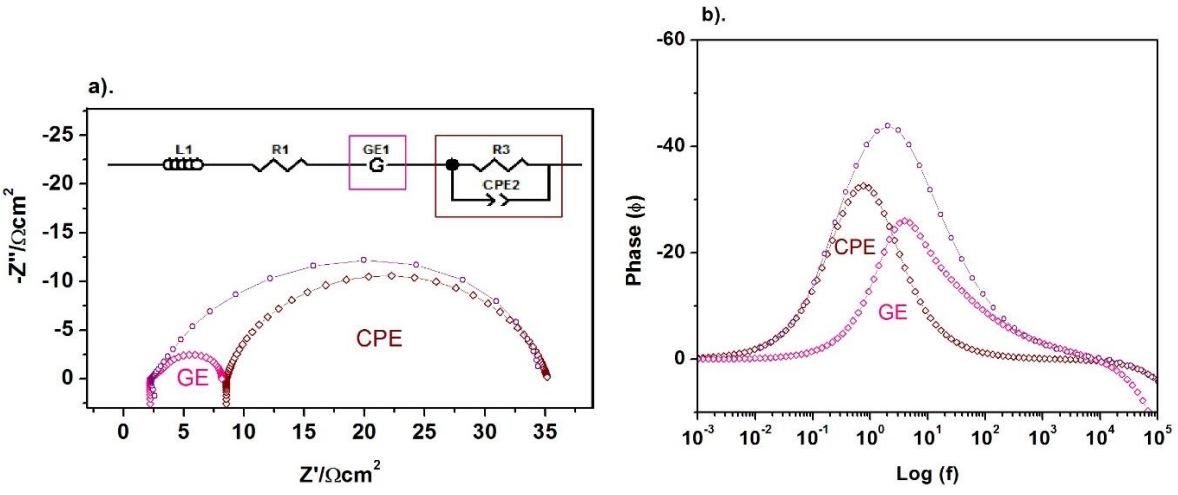

It can also be observed that the R/CPE element at low frequency predominates in the entire pO_2 range. Now, using the results of the adjustments, a log-log plot of resistances vs pO_2 is built (Figure 68), in order to state the processes carried out in these conditions.

Figure 68. Dependence of ASR of each limiting process versus oxygen partial pressure for LSM/$YMnO_3$/YSZ/$YMnO_3$/LSM cell at T=700°C. The reaction order (γ) of each step is also included.

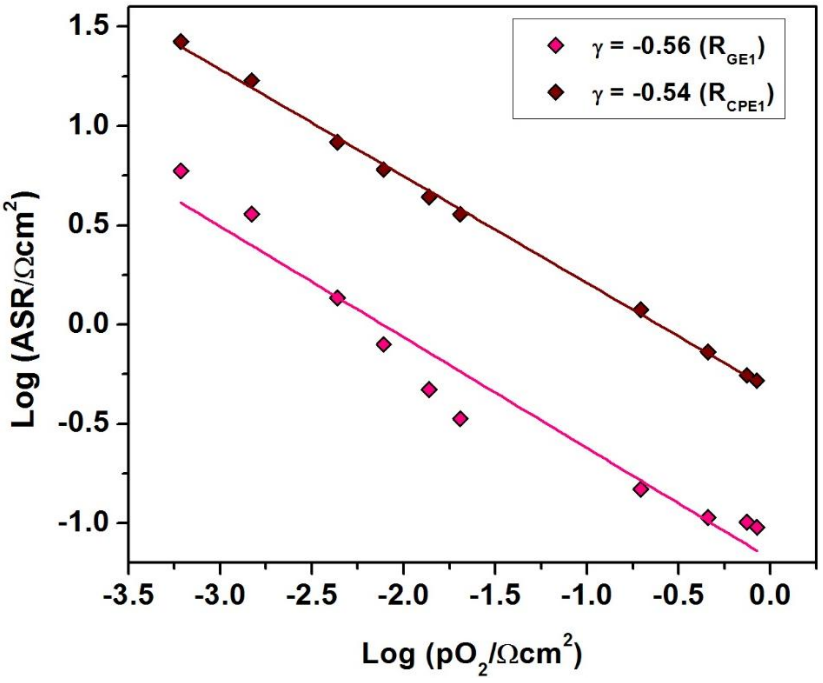

At 700°C, the limiting steps are similar to those found at 600°C. There is also a Gerischer impedance element (R_G) in approximately the same frequency range and capacitance values (C~10^{-2} F/cm^2). Specifically, it corresponds to the same co-limiting process between the oxygen exchange at the electrode/gas surface and the oxygen diffusion in the bulk. Likewise, the dependence with the partial oxygen pressure slightly decreases (R α $pO_2^{-0.56}$) at this temperature, what could be

associated with a higher contribution of the exchange of oxygen on the surface [44]. Nevertheless, the shape of the spectra is another interesting change at 700°C, since we can observe that the high-frequency slope diminishes and is almost exactly 45° (Figure 69). The deviation from the expected slope was previously associated with the electrode microstructure, made of small grains due to the sintering temperature used. Therefore, the decrease in the angle could be related to the (slight) grains growth due to the higher temperature of the measurements, increasing the resistance of oxide ion charge transfer [47], [231].

Figure 69. The experimental EIS spectra of LSM/$YMnO_3$/YSZ/$YMnO_3$/LSM cell at T=700°C and pO_2≈0.8 atm. A comparison with the slope expected for ideal Gerischer impedance is also shown.

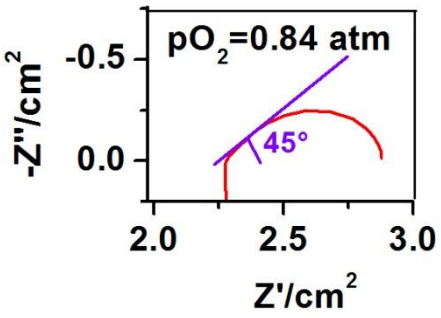

For its part, the second contribution is a R_3/CPE_2 element. At this temperature, the pO_2 dependence and capacitances values remain the same as for T=600°C (R α $pO_2^{-0.54}$ and capacitances of C~10^{-2} F/cm^2). Thus, it is possible to affirm that the same oxygen dissociative adsorption process on the electrode surface is carried out. This reflects the fact that such process is dominant in the LSM/$YMnO_3$/YSZ/$YMnO_3$/LSM cell.

Finally, the measurements were carried out at **800°C** (10^{-4} ≤ pO_2 ≤ 1 atm) for the same LSM/$YMnO_3$/YSZ/$YMnO_3$/LSM cell. In these conditions, the lowest resistance

values of the three experiments are obtained and, as in the case of the other two temperatures, the resistance grows as pO_2 value decreases. In Figure 70, the Nyquist representation of the EIS data is shown. Here, it can be appreciated that the spectra change of shape with the oxygen partial pressure value.

Figure 70. Electrochemical impedance spectra of LSM/$YMnO_3$/YSZ/$YMnO_3$/LSM at T=800°C for different pO_2 values.

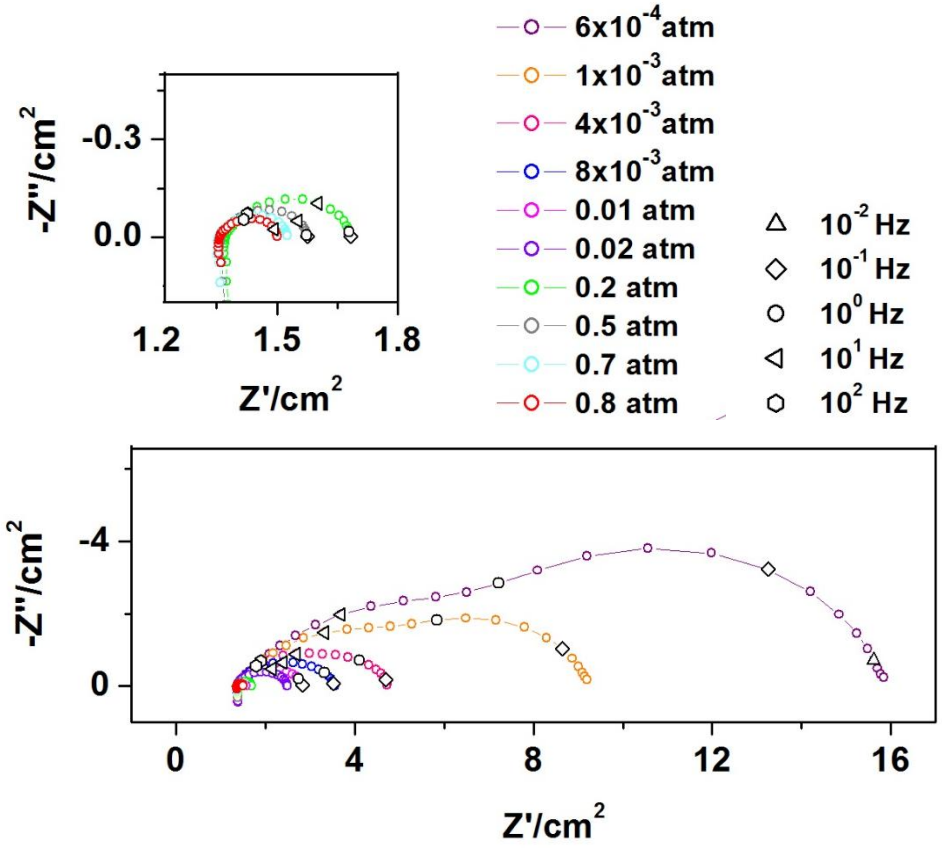

The Bode representation of EIS data (Figure 71) allows observing that at high pO_2 there is only a maximum of relaxation frequency, but at lower oxygen partial pressures we clearly identify two contributions.

Figure 71. EIS spectra in Bode representation for LSM/$YMnO_3$/YSZ/$YMnO_3$/LSM cell at T=800°C for different pO_2 values.

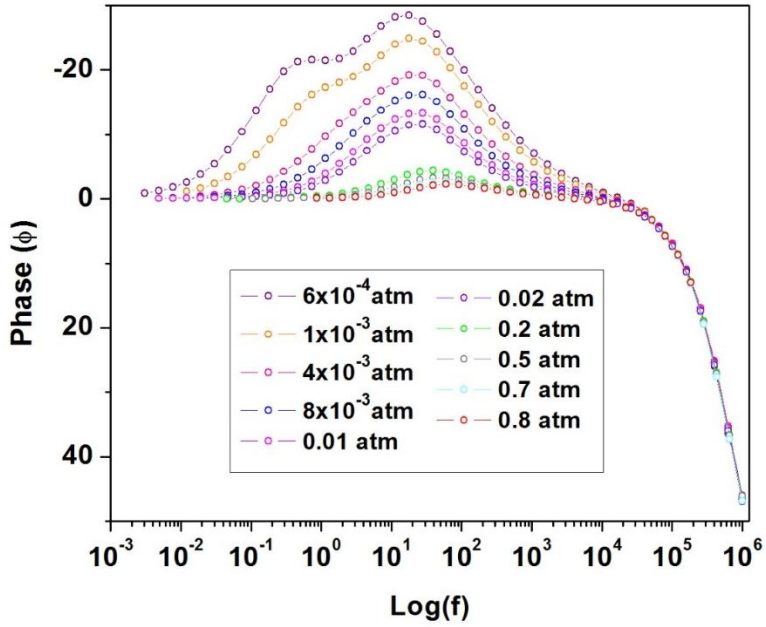

Therefore, the impedance response at 800°C has been modeled with two circuits depending on the pO_2 value. At high oxygen partial pressures the equivalent circuit includes (i) an inductive element (L_1) due to the inductance of the wires, (ii) an ohmic resistance (R_1) that corresponds mainly to the electrolyte resistance, and (iii) a Gerischer-type element (R_G). A good fit is obtained for the spectrum at the highest oxygen partial pressure measured (pO_2≈0.8 atm) with such model, as can be seen in Figure 72.

Figure 72. Experimental EIS spectrum of the LSM/$YMnO_3$/YSZ/$YMnO_3$/LSM cell at T=800°C and pO_2≈0.8 atm, with calculated curve corresponding to an equivalent circuit including a Gerischer element.

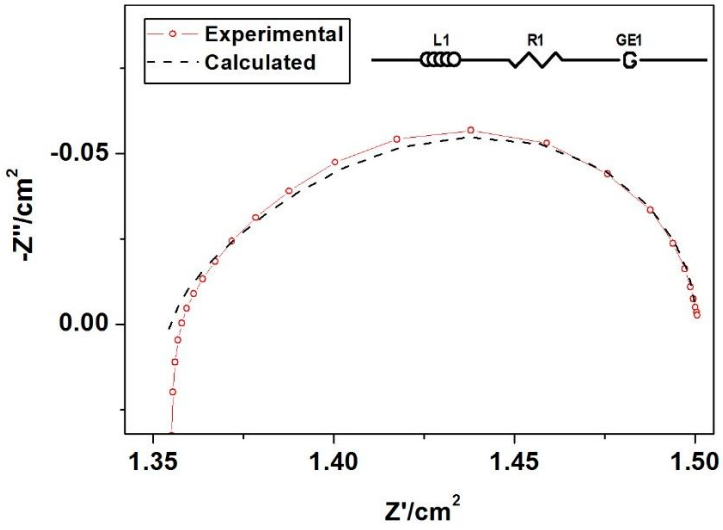

Figure 73. (a) Impedance spectrum adjustment of LSM/$YMnO_3$/YSZ/$YMnO_3$/LSM cell (T=800°C and pO_2≈6x10^{-4} atm) indicating the contributions of the equivalent circuit, (b) Bode representation with the same deconvolution.

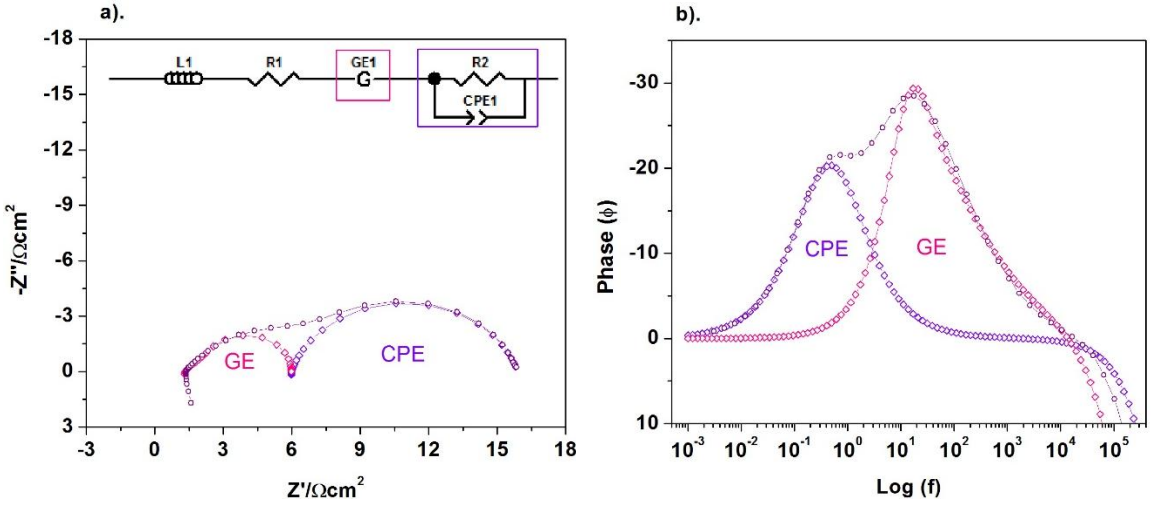

From a pO_2 of ~0.02 atm, the circuit is completed with (iv) a parallel combination of one resistance and one constant phase element (R/CPE), to model an additional limiting step at low frequency. This model works appropriately for the remaining spectra at low oxygen partial pressure (Annex F). The fit for the lowest pO_2 values is depicted in Figure 73. Using such representation, it can be seen that both elements (Gerischer and R_2/CPE_1) are relevant, although R_2/CPE_1 seems to be predominant.

The results of the all adjustments are shown in a log-log plot of resistances vs pO_2 (Figure 74), in order to attribute the limiting processes carried out in these conditions.

Figure 74. Dependence of the ASR of each limiting process versus oxygen partial pressure for LSM/$YMnO_3$/YSZ/$YMnO_3$/LSM cell at T=800°C. The reaction order (γ) of each step is also included.

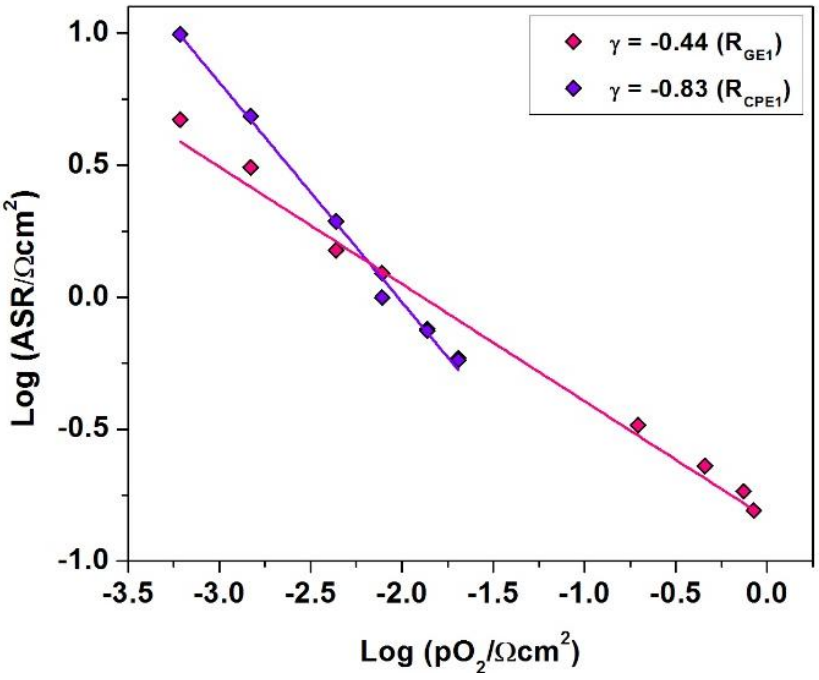

At 800°C, the limiting steps are similar to those found at lower temperatures; nevertheless, the dependence with pO_2 exhibits more variation. First, the Gerischer impedance element (R_G) presents a dependence of $R \alpha pO_2^{-0.44}$ and large capacitances of $C \sim 10^2$ F/cm^2, which means that a co-limiting process between the oxygen exchange at the electrode/gas surface and the oxygen diffusion in the bulk is again present. This behavior suggests a large contribution of oxygen surface exchange, as said previously. On the other hand, the R/CPE_1 contribution shows a dependence $R \alpha pO_2^{-0.83}$ and capacitances values are in the same order of magnitud *i.e.* $C \sim 10^{-2}$ F/cm^2. The capacitances and the intermediate γ value (between -0.5 and -1) indicate that this limiting step is also a dissociative adsorption process but combined with gas phase difusion, *i.e.* both mechanisms are comparable and therefore simultaneously participate to the cathode reaction [65], [225]. In addition, this value closer to -1 also means that gas diffusion is more dominant and dissociative adsorption is less limitant at high temperature [44]. This is not surprising because usually higher temperatures hinder the gas diffusion and, on the other hand, the dissociative adsorption element, which is a thermally activated phenomenon, decreases and becomes comparable to gas phase diffusion at 800°C.

3.5.2.2 Identification of the limiting steps for the LSM/$Y_{0.9}Zr_{0.1}MnO_3$/YSZ/$Y_{0.9}Zr_{0.1}MnO_3$/LSM cell. In previous sections we observed that $Y_{0.9}Zr_{0.1}MnO_3$ material shows higher electrical conductivity than $YMnO_3$; then, a better impedance response could have been expected for the doped compound. Nevertheless, the LSM/$Y_{0.9}Zr_{0.1}MnO_3$/YSZ/$Y_{0.9}Zr_{0.1}MnO_3$/LSM cell exhibits higher resistances than for $YMnO_3$ electrode. For some cobaltite materials (*e.g.* BSCF or LSCF) the reason for that is the TEC mismatch between the electrode and electrolyte that can cause adherence issues or electrode delamination [235]. These problems have not been observed for Zr-doped $YMnO_3$ cell even with the TEC difference with YSZ electrolyte already discussed at the beginning of the chapter. A microstructural difference could also originate the loss of performance given that the impedance

limiting steps strongly depends on it [234], a point that was not completely optimized in this work. Nonetheless, both electrodes were prepared in similar conditions and, therefore, a similar microstructure is expected. Despite the above discussion, it is worth noting that LSM/$Y_{0.9}Zr_{0.1}MnO_3$/YSZ/$Y_{0.9}Zr_{0.1}MnO_3$/LSM cell exhibits the same impedance contributions of LSM/$YMnO_3$/YSZ/$YMnO_3$/LSM cell, as shown in Figure 75. Here, we can distinguish the evolution of the bode curves at the three temperatures under the same oxygen partial pressure ($pO_2 \approx 6x10^{-4}$ atm). At T=600°C, the R/CPE (at low frequencies) and the Gerisher-element (at high frequencies) are overlapping, but as temperature increases, the two contributions clearly separate.

Figure 75. EIS spectra in Bode representation showing the evolution of impedance elements for LSM/$Y_{0.9}Zr_{0.1}MnO_3$/YSZ/$Y_{0.9}Zr_{0.1}MnO_3$/LSM cell at T=600, 700 and 800°C and $pO_2 \approx 6x10^{-4}$ atm.

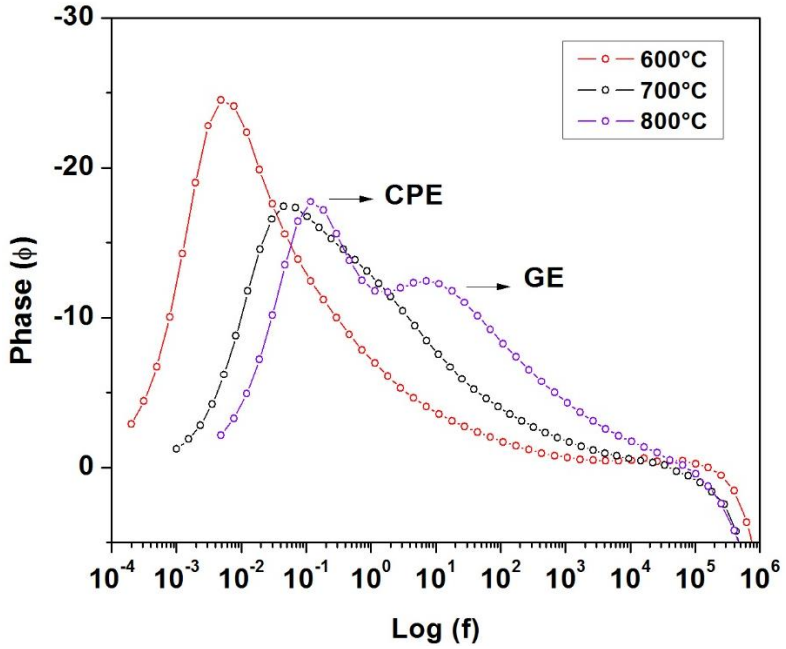

Specifically, the EIS data in Nyquist representation of LSM/$Y_{0.9}Zr_{0.1}MnO_3$/YSZ/$Y_{0.9}Zr_{0.1}MnO_3$/LSM cell measured at **600°C** under different pO_2 are shown in Figure 76. In the graph, we observe that the impedance grows as pO_2 value decreases, as expected. Likewise, the shape of the spectrum changes in the pO_2 range.

Figure 76. Electrochemical impedance spectra of LSM/$Y_{0.9}Zr_{0.1}MnO_3$/YSZ/$Y_{0.9}Zr_{0.1}MnO_3$/LSM cell at T=600°C for different pO_2 values.

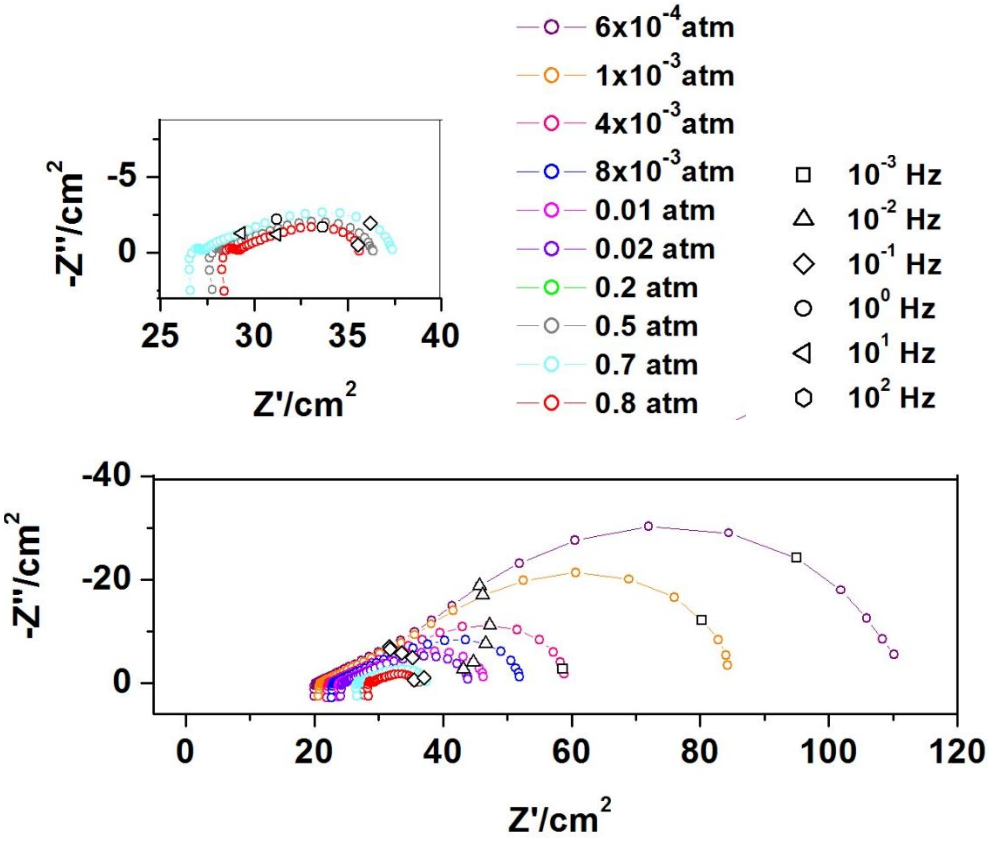

In addition, all the curves in the Bode plot (Figure 77) show only one clear maximum of relaxation frequency, but one shoulder grows when the pO_2 value decreases. As a consequence, the impedance response was modeled with two circuits depending

on the pO_2 values. At high oxygen partial pressures, the equivalent circuit includes (i) an inductive element (L_1) due to the inductance of the wires, (ii) an ohmic resistance (R_1) that corresponds mainly to the electrolyte resistance, (iii) a parallel combination of one resistance and one constant phase element (R/CPE) and (iv) a Gerischer-type element (R_G).

Figure 77. EIS spectra in Bode representation for LSM/$Y_{0.9}Zr_{0.1}MnO_3$/YSZ/$Y_{0.9}Zr_{0.1}MnO_3$/LSM cell at T=600°C for different pO_2 values.

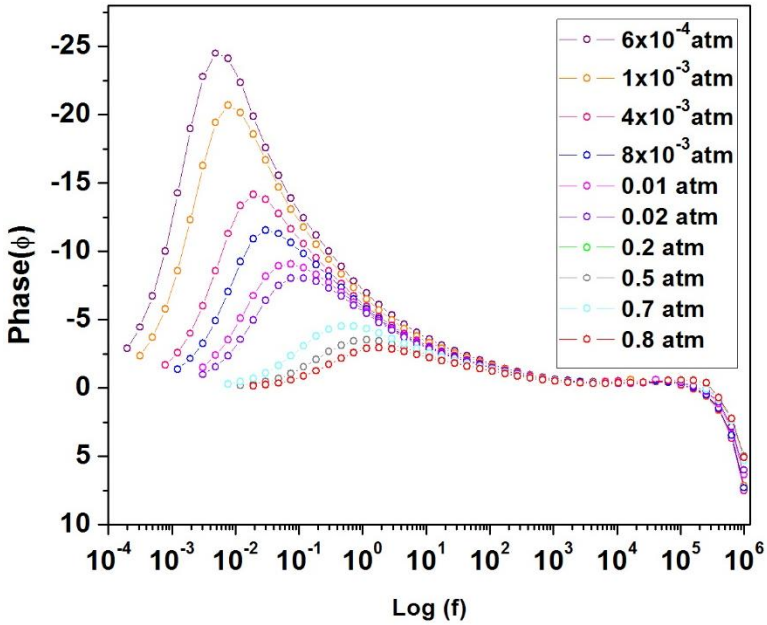

A good adjusment is obtained for the spectrum at the highest oxygen partial pressure measured (pO_2≈0.8 atm), as can be seen in Figure 78. From a pO_2 of ~0.02 atm, the circuit requires an extra element to model the spectra, *i.e* (v) a parallel combination of one resistance and one constant phase element (R/CPE). This model fits appropriately the spectra at low oxygen partial pressures (Annex G). In Figure 79, the adjustments for the lowest pO_2 values are depicted.

Figure 78. Impedance spectrum adjustment and corresponding equivalent circuit for LSM/$Y_{0.9}Zr_{0.1}MnO_3$/YSZ/$Y_{0.9}Zr_{0.1}MnO_3$/LSM cell (T=600°C and pO_2≈0.8 atm).

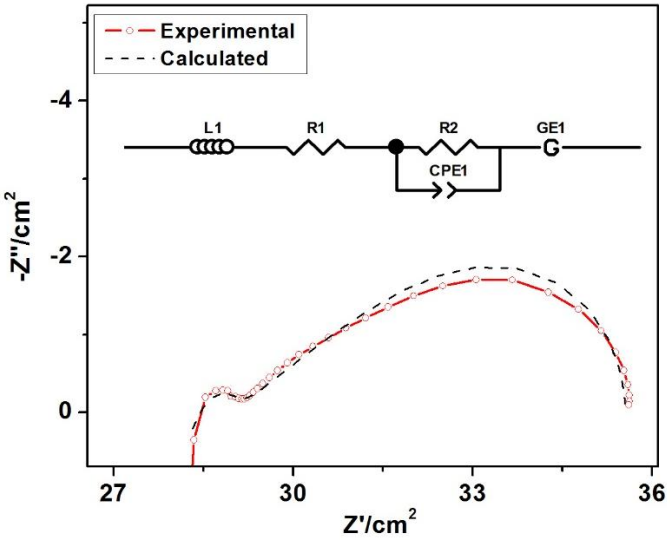

Figure 79. (a) Impedance spectrum adjustment for LSM/$Y_{0.9}Zr_{0.1}MnO_3$/YSZ/$Y_{0.9}Zr_{0.1}MnO_3$/LSM cell (T=600°C and pO_2≈$6x10^{-4}$ atm) indicating the contributions of the equivalent circuit, (b) Bode representation with the same deconvolution.

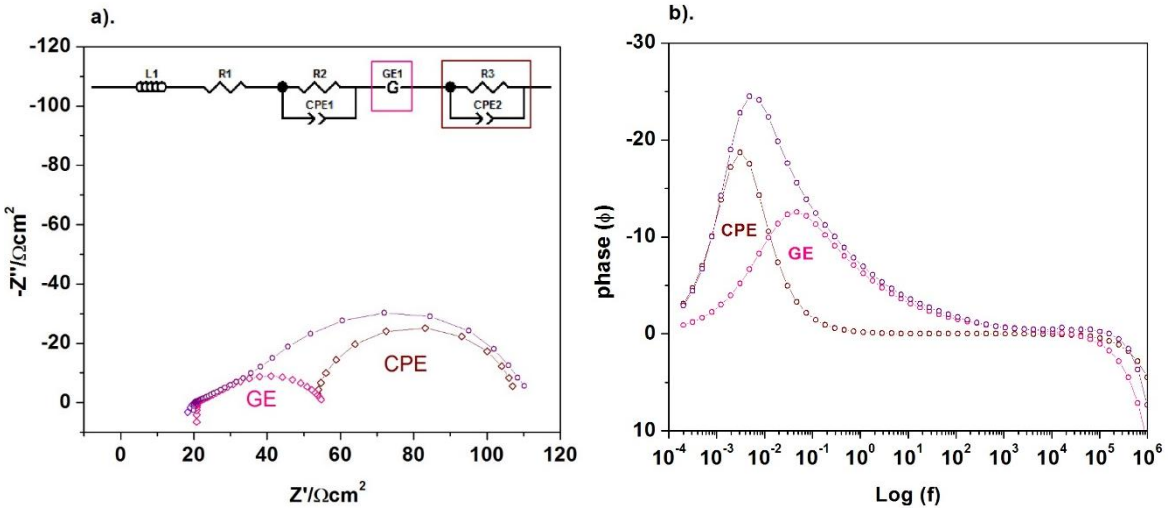

In this representation, it can be seen that both elements (Gerischer and R/CPE) are relevant, although R_2/CPE_1 seems to be predominant. The results of the all fits are shown in a log-log plot of resistances vs pO_2 values (Figure 80), in order to define the limiting processes carried out at 600°C.

Figure 80. Dependence of ASR of each limiting process versus oxygen partial pressure for LSM/$Y_{0.9}Zr_{0.1}MnO_3$/YSZ/$Y_{0.9}Zr_{0.1}MnO_3$/LSM cell at T=600°C. The reaction order (γ) of each step is also included.

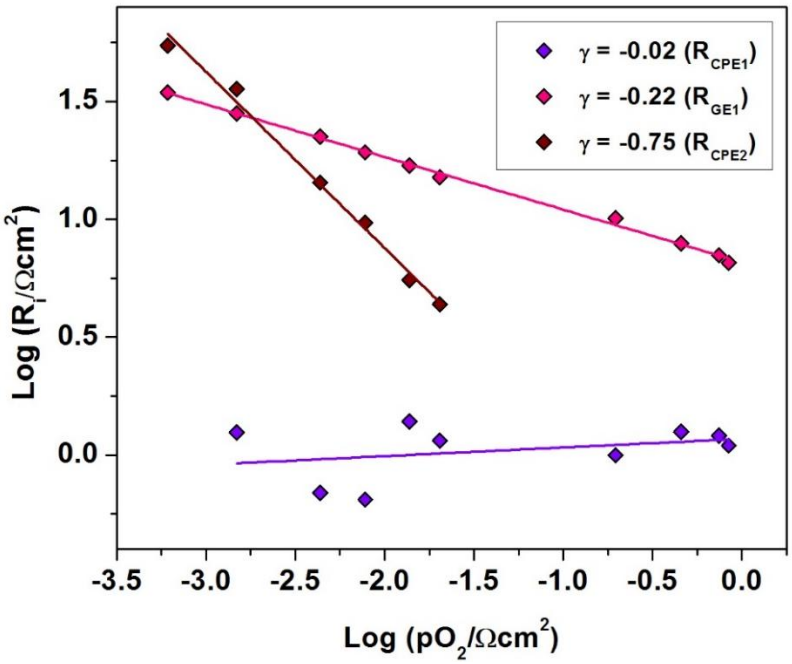

The first impedance element at 600°C is a R/CPE, which models the small contribution at higher frequencies. The dependence with oxygen partial pressure is $R \alpha pO_2^{-0.02}$ and the capacitances are $C \sim 10^{-7}$-10^{-9} F/cm^2, *i.e.* the change in the dependence is almost negligible. Nonetheless, as in the case of a cell including $YMnO_3$, this contribution can be attributed to the ionic intergranular resistances of the electrolyte (due to the low ionic conductivity of YSZ at T ≤ 600°C). Such a contribution disappears at higher temperatures [47], [226]. A second phenomenon

was attributed to a Gerischer element (R_G) with a dependence of R α $pO_2^{-0.22}$ and capacitances of C~10^{-2}-10^{-1} F/cm^2. These values of γ and capacitances are associated with the co-limiting process between the oxygen exchange at the electrode/gas surface and the oxygen diffusion in the bulk [227]–[229]. The great difference between the Gerischer response of LSM/$Y_{0.9}Zr_{0.1}MnO_3$/YSZ/$Y_{0.9}Zr_{0.1}MnO_3$/LSM and LSM/$YMnO_3$/YSZ/$YMnO_3$/LSM cells is that, for the Zr-doped electrode, the high frequency slope is quite lower than the expected angle of 45° in Nyquist plot (Figure 81).

Figure 81. The experimental EIS spectrum for LSM/$Y_{0.9}Zr_{0.1}MnO_3$/YSZ/$Y_{0.9}Zr_{0.1}MnO_3$/LSM cell at T=600°C and pO_2≈0.8 atm. A comparison with the slope expected for an ideal Gerischer impedance is also shown.

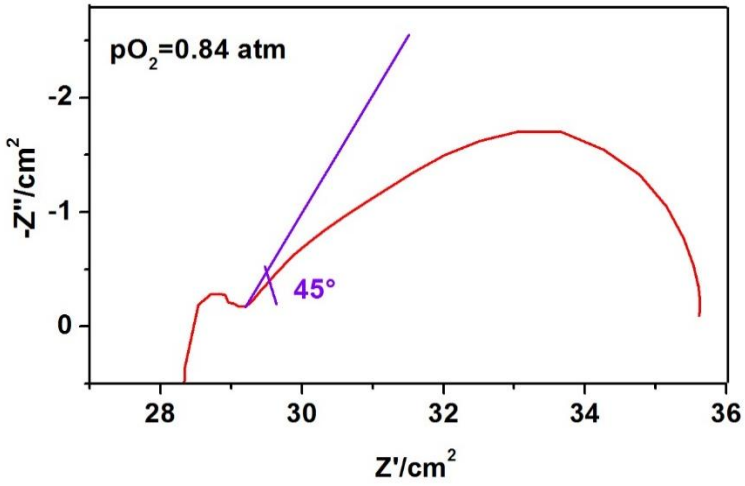

This kind of response has been observed in electrodes with fine particles [231], what could reflect that actually the microstructure of the different studied cells presents some differences. Finally, the third contribution is a R/CPE element with a dependence of R α $pO_2^{-0.75}$ and capacitances of C~1 F/cm^2. The intermediate γ value indicates a combined contribution between dissociative adsorption and gas oxygen diffusion [65]; in addition, the capacitances values allow to distinguish the process

as being diffusive. This is not surprising taking into account this co-limiting process is frequently found in porous electrodes of small grains analyzed at low temperatures [169].

Now, if the experiment is carried out at **700°C** ($10^{-4} \leq pO_2 \leq 1$ atm) for a LSM/$Y_{0.9}Zr_{0.1}MnO_3$/YSZ/$Y_{0.9}Zr_{0.1}MnO_3$/LSM cell, we can observe lower resistance values in comparison with those measured at 600°C. Additionally, these resistances increase as pO_2 value decreases as shown in the Nyquist representation of Figure 82.

Figure 82. Electrochemical impedance spectra for LSM/$Y_{0.9}Zr_{0.1}MnO_3$/YSZ/$Y_{0.9}Zr_{0.1}MnO_3$/LSM cell at T=700°C for different pO_2 values.

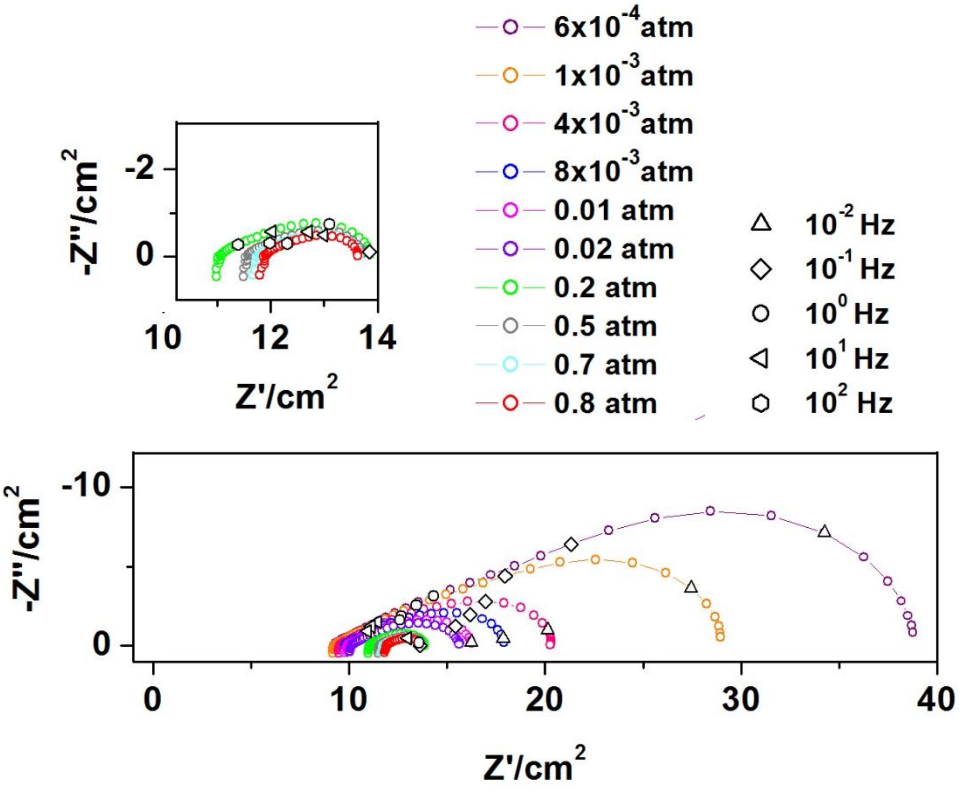

It is worth noting that the shape of the spectra changes with pO_2 as for the previous temperature; hence, two equivalent circuits are also necessary to model the behavior at 700°C. Likewise, using the Bode plot representation (Figure 83), we can also notice the change in the shape of the curves. In this way, at high oxygen partial pressures, there is one maximum of relaxation frequency; however, one shoulder grows at low frequencies as pO_2 value decreases.

Figure 83. EIS data in Bode representation for LSM/$Y_{0.9}Zr_{0.1}MnO_3$/YSZ/$Y_{0.9}Zr_{0.1}MnO_3$/LSM cell at T=700°C for different pO_2 values.

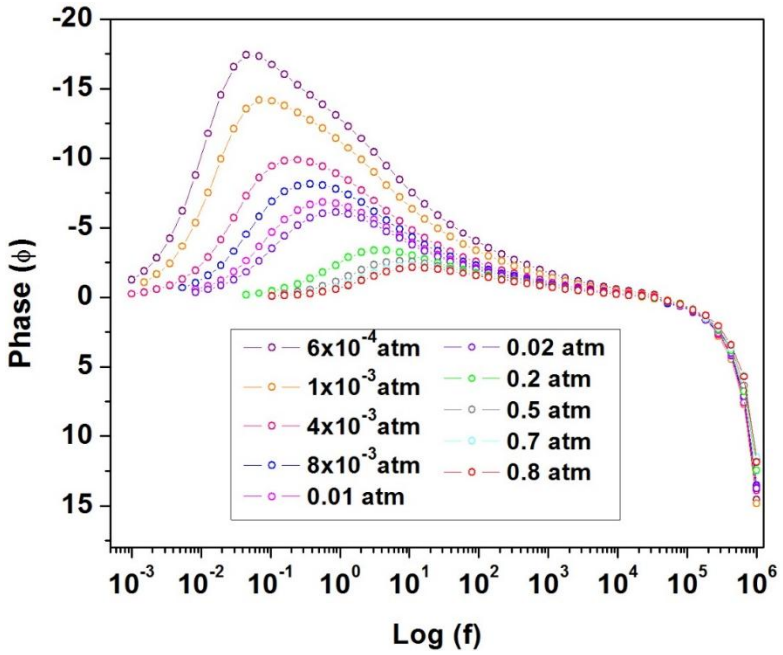

Thus, the impedance response can be correctly fitted with two equivalent circuits which include (i) an inductive element (L_1) due to the inductance of the wires, (ii) an ohmic resistance (R_1) that is mainly the electrolyte resistance and (iii) a Gerischer-type element (R_G). Such model adjusts well to the experimental data in the range of high pO_2 values (Annex H). An example is graphed in Figure 84.

Figure 84. Impedance spectrum adjustment of LSM/$Y_{0.9}Zr_{0.1}MnO_3$/YSZ/$Y_{0.9}Zr_{0.1}MnO_3$/LSM cell (T=700°C and pO_2≈0.8 atm) indicating the equivalent circuit.

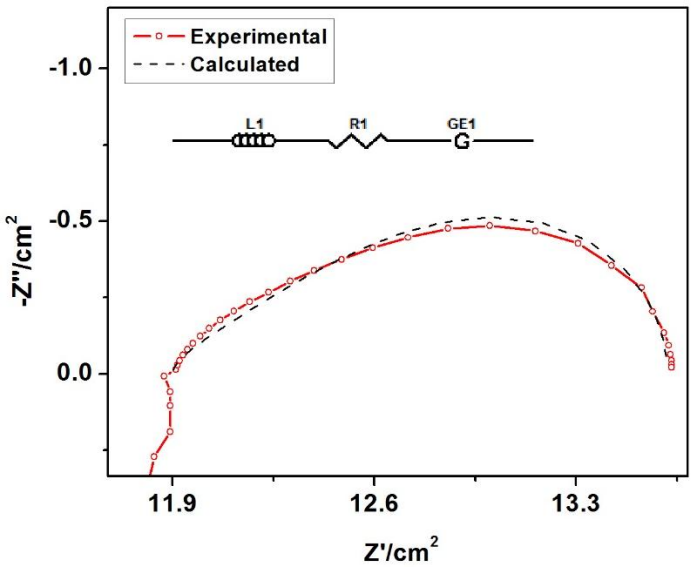

From a pO_2 of ~0.02 atm, the circuit is completed with (iv) a parallel combination of one resistance and one constant phase element (R/CPE), to model the additional contribution observed at low frequency. The obtained fit for the lowest pO_2 values is depicted in Figure 85. In this Figure, we can appreciate that both elements (Gerischer and R/CPE) contribute in an important way to the impedance response, but R_3/CPE_2 seems to be predominant.

Now, using the results of the adjustments a log-log plot of resistances vs pO_2 values can be graphed (Figure 86), with the aim of characterizing the nature of the limiting steps.

Figure 85. (a) Impedance spectrum adjustment for LSM/$Y_{0.9}Zr_{0.1}MnO_3$/YSZ/$Y_{0.9}Zr_{0.1}MnO_3$/LSM cell (T=700°C and $pO_2 \approx 6x10^{-4}$ atm) indicating the contributions of the equivalent circuit, (b) Bode representation with the same deconvolution.

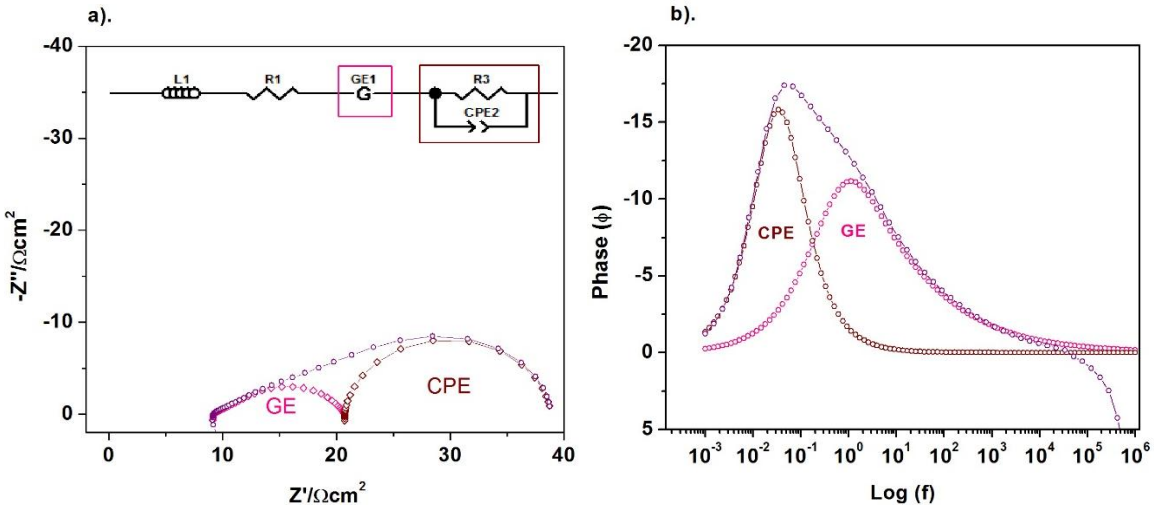

Figure 86. Dependence of the ASR of each limiting process versus oxygen partial pressure for LSM/$Y_{0.9}Zr_{0.1}MnO_3$/YSZ/$Y_{0.9}Zr_{0.1}MnO_3$/LSM cell at T=700°C. The reaction order (γ) of each step is also included.

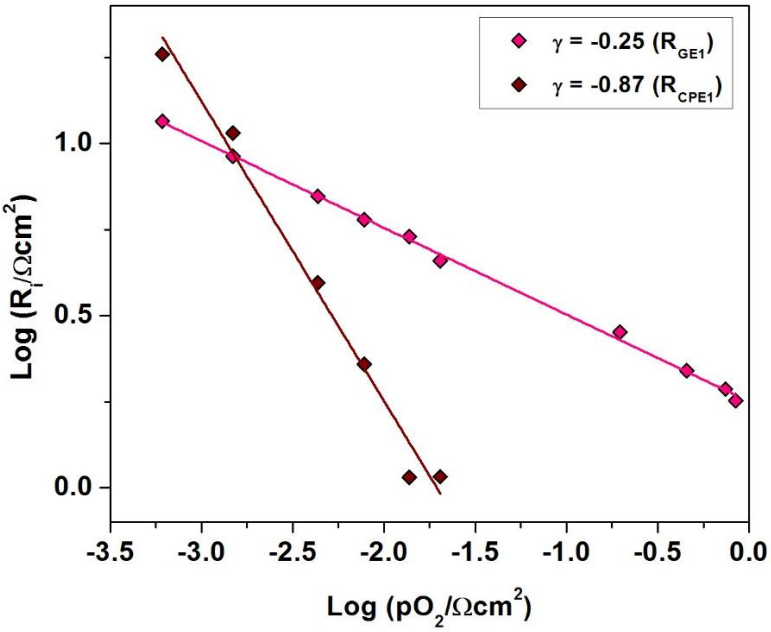

Thus, at 700°C there is a Gerischer impedance element (R_G) at high frequencies. In these conditions, the element shows a slight decrease in the pO_2 a dependence ($R \alpha pO_2^{-0.25}$) and the capacitances remain in the same range of $C \sim 10^{-2}$ F/cm^2, what means that there is no change in the rate limiting step. Then, the same combined process seems to exist, that corresponds to the oxygen exchange at the electrode/gas surface and the oxygen diffusion in the bulk [227]–[229] and it is related with to fact that the penetration depth (*d*) is much larger than the electrode thickness or average particle size [230], [236]. The latter is in agreement with what has been discussed at T= 600°C.

The second contribution is an R/CPE element with a pO_2 dependence of $R \alpha pO_2^{-0.85}$ and capacitances of $C \sim 10^{-1}$-1 F/cm^2. It means that at low frequency there is a colimiting step between oxygen dissociative adsorption process on electrode surface and gas oxygen diffusion [225]; however, the higher γ value, in comparison with what we observed at 600°C, could indicate a decrease of the contribution of dissociative the adsorption resistance with temperature [169].

Finally, the measurements have been carried out at **800°C** ($10^{-4} \leq pO_2 \leq 1$ atm) for the same LSM/$Y_{0.9}Zr_{0.1}MnO_3$/YSZ/$Y_{0.9}Zr_{0.1}MnO_3$/LSM cell. In these conditions, the lowest resistance values of the three experiments are obtained. As in the case of the other two temperatures, the resistance grows as pO_2 value decreases, as shown in the Nyquist representation (Figure 87). In this Figure, it can be appreciated that the spectra change their shape with the oxygen partial pressure value.

Figure 87. Electrochemical impedance spectra for LSM/$Y_{0.9}Zr_{0.1}MnO_3$/YSZ/$Y_{0.9}Zr_{0.1}MnO_3$/LSM cell at T=800°C for different pO_2 values.

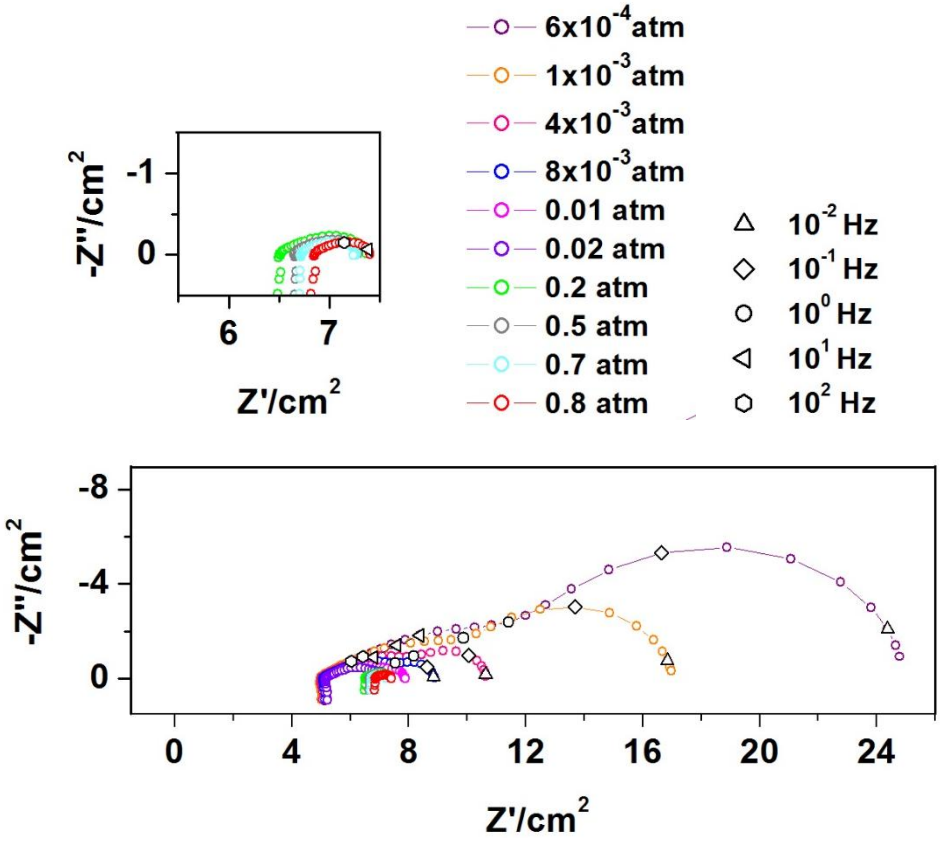

The Bode representation of the EIS data in Figure 88 allows observing that at high pO_2 there is only one maximum of relaxation frequency; however, at lower oxygen partial pressures, two well differentiated contributions exist. In this way, the impedance response at 800°C has been modeled with two circuits depending on the pO_2 value. At high oxygen partial pressures the equivalent circuit includes (i) an inductive element (L_1) due to the inductance of the wires, (ii) an ohmic resistance (R_1) that is mainly the electrolyte resistance, and (iii) a Gerischer-type element (R_G). A well adjusted fit is obtained for the spectrum at the highest oxygen partial pressure (pO_2≈0.8 atm) using such model, as can be seen in Figure 89.

Figure 88. EIS data in Bode representation for LSM/$Y_{0.9}Zr_{0.1}MnO_3$/YSZ/$Y_{0.9}Zr_{0.1}MnO_3$/LSM cell at T=800°C and different pO_2 values.

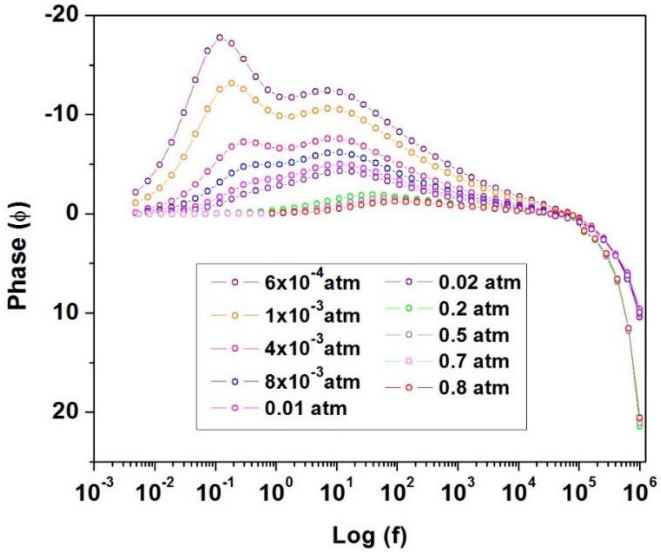

Figure 89. Impedance spectrum adjustment for LSM/$Y_{0.9}Zr_{0.1}MnO_3$/YSZ/$Y_{0.9}Zr_{0.1}MnO_3$/LSM cell (T=800°C and pO_2≈0.8 atm) indicating the equivalent circuit.

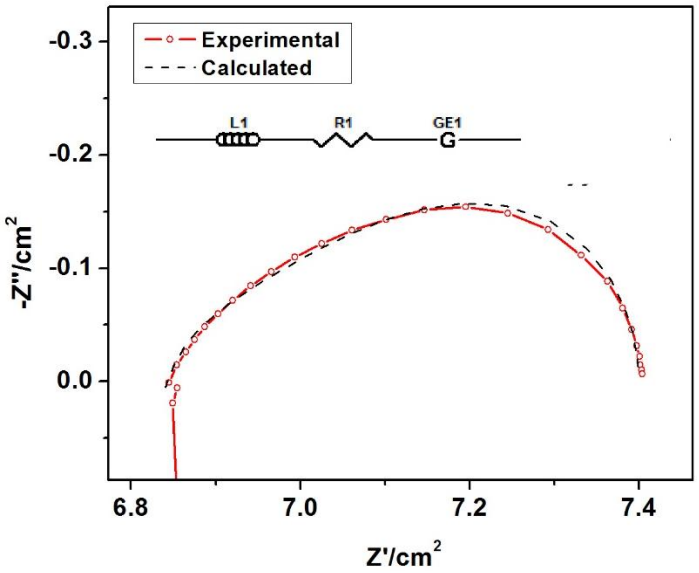

From a pO_2 of ~0.02 atm, the circuit is completed with (iv) a parallel combination of one resistance and one constant phase element (R/CPE), to model the resistance at low frequency. Such model fits the experimental data appropriately in the entire interval of measurements (Annex I). The adjustment for the lowest pO_2 values is depicted in Figure 90. In this representation, we can observe that both elements (Gerischer and R_2/CPE_1) are relevant, although the R/CPE contribution is again predominant.

Figure 90. (a) Impedance spectrum adjustment for LSM/$Y_{0.9}Zr_{0.1}MnO_3$/YSZ/$Y_{0.9}Zr_{0.1}MnO_3$/LSM cell (T=800°C and $pO_2 \approx 6x10^{-4}$ atm) indicating the contributions of the equivalent circuit, (b) Bode representation with the same deconvolution.

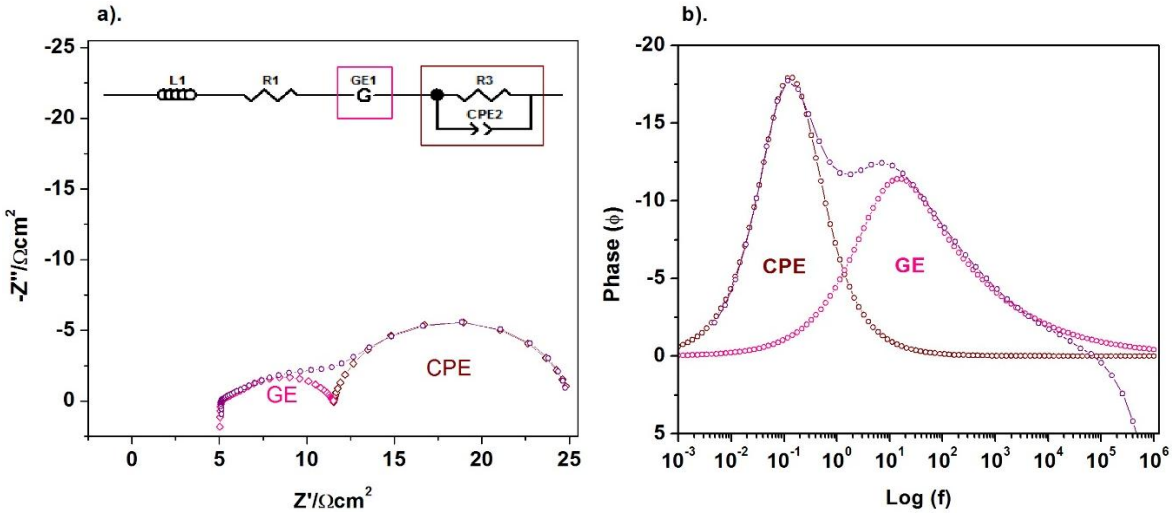

The results of all the adjustments are summarized in a log-log plot of resistances vs pO_2 (Figure 91), in order to define the origin of each limiting process observed in these conditions.

Figure 91. Dependence of the ASR of each limiting process versus oxygen partial pressure for LSM/$Y_{0.9}Zr_{0.1}MnO_3$/YSZ/$Y_{0.9}Zr_{0.1}MnO_3$/LSM cell at T=800°C. The reaction order (γ) of each step is also included.

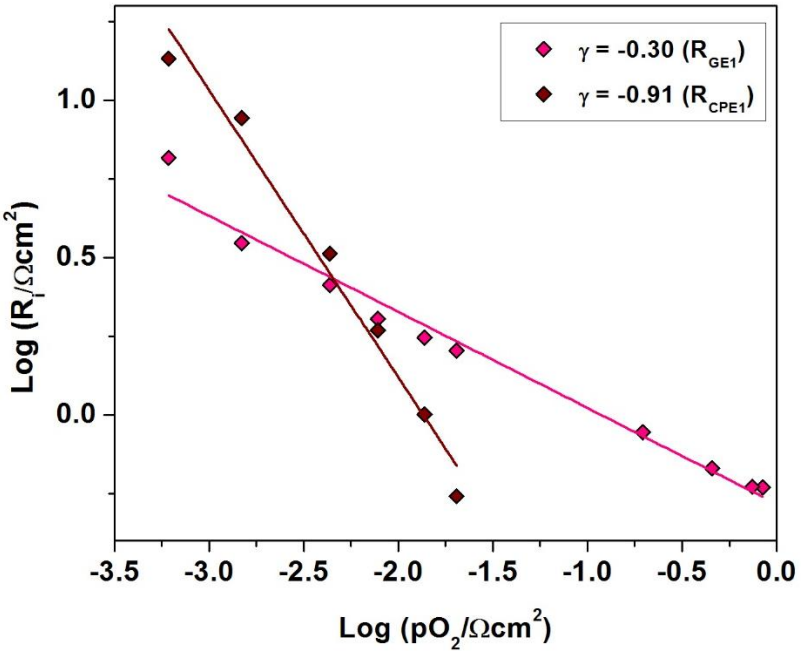

In this case, the Gerischer impedance at high frequencies shows a dependence of R α $pO_2^{-0.30}$ and capacitances of C~10^{-3}-10^{-2} F/cm^2. It means the dependence also decreases at 800°C, but the co-limiting step between oxygen exchange at the electrode/gas surface and the oxygen diffusion in the bulk is still present [227]–[229]. However, the decrease in capacitance seems to indicate a higher contribution of the superficial resistance [47].

The second contribution is a R/CPE element with a dependence of R α $pO_2^{-0.91}$ and capacitances of C~10^{-1} F/cm^2. The γ value close to -1 can be related to the oxygen gas phase diffusion within the electrode pores, *i.e.* the contribution of dissociative adsorption resistance disappears completely at high temperatures [65], [225]. The decrease in the magnitud of the capacitance value in agreement with such assumption [169].

Finally, given that both studied cell show the same electrochemical processes: the co-limiting step between oxygen exchange at the electrode/gas surface and the oxygen diffusion in the bulk (Gerischer) and the combination of gas phase diffusion and dissociative adsorption (R/CPE), an Arrhenius graph was built with the resistances calculated for each impedance element at the different measured temperatures (Figure 92).

Figure 92. Activation energy of impedance elements identified (a) in the LSM/$YMnO_3$/YSZ/$YMnO_3$/LSM cell and (b) in the LSM/$Y_{0.9}Zr_{0.1}MnO_3$/YSZ/$Y_{0.9}Zr_{0.1}MnO_3$/LSM cell. The ASR values showed are of measured at $pO_2 \approx 6x10^{-4}$ atm and T=600, 700 and 800°C.

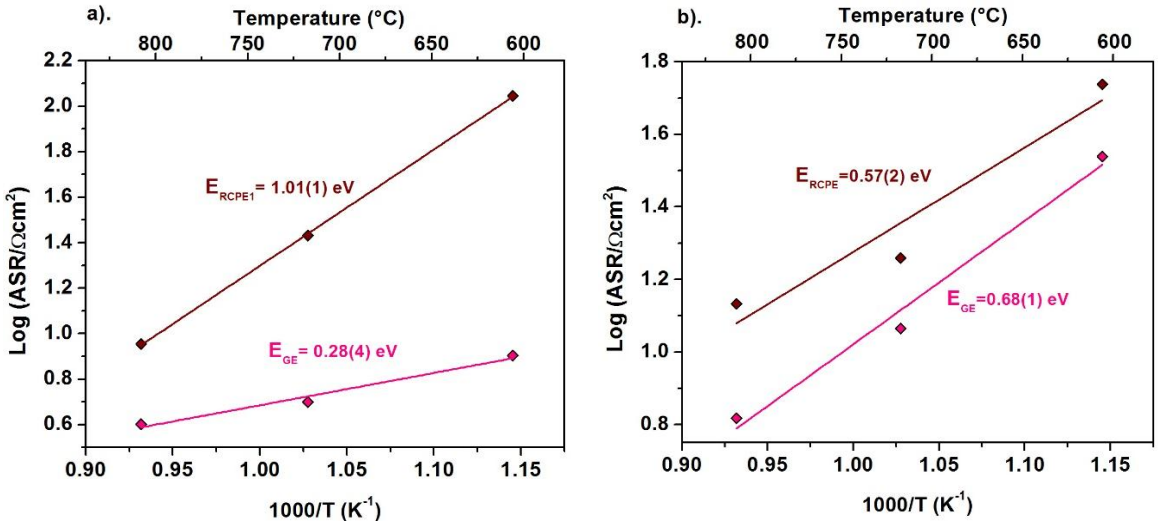

By such comparison, it is possible to observe that even when both cells exhibit the same elements, their respective activation energies are different. Specifically, the R/CPE is almost two times higher for LSM/$YMnO_3$/YSZ/$YMnO_3$/LSM cell in comparison with cell built on Zr-doped $YMnO_3$, while the Gerischer is two times lower. Particularly, the processes represented by the Gerischer depends on the number of adsorption sites, and the electronical and ionical conductivity [237]. For

that reason, it is easy to think that in the sample with $Y_{0.9}Zr_{0.1}MnO_3$, the oxygen diffusion in the bulk contribution in the process of the Gerischer element be low.The above taking into account $Y_{0.9}Zr_{0.1}MnO_3$ exhibits higher electrical conductivity (maybe due to a higher ionic conductivity). Nonetheless, the key role of the microstructure cannot be ignored in the electrochemical behaviour of these materials. In that way, It is possible to suggest that even when both cathode materials in these cells exhibit relatively small grains, the microstructure seems finer in LSM/$YMnO_3$/YSZ/$YMnO_3$/LSM cells. The latter is in accordance with the showed in previous sections of this chapter, in which it could be observed that the pellets of $YMnO_3$ material reaches a low sinterization level in comparison with that made of $Y_{0.9}Zr_{0.1}MnO_3$. As a consequence, a higher surface area is found for the sample with $YMnO_3$; hence, the microstructure facilitates the oxygen surface exchange in the co-limiting process of Gerischer [44]. In contrast, Zr doping in $YMnO_3$ seems to favor the grain growth and sinterization process. For that reason, the oxygen diffusion in the bulk is probably very high in the process of the Gerischer element and the activation energy is finally higher for the LSM/$Y_{0.9}Zr_{0.1}MnO_3$/YSZ/$Y_{0.9}Zr_{0.1}MnO_3$/LSM cell. In the case of the second element (R/CPE), a higher activation energy for the LSM/$YMnO_3$/YSZ/$YMnO_3$/LSM cell is observed. The reason of that the aforementioned finer grain microstructure of $YMnO_3$ favor the dissociative adsorption and maybe the influence of this process is much higher than in the case of LSM/$Y_{0.9}Zr_{0.1}MnO_3$/YSZ/$Y_{0.9}Zr_{0.1}MnO_3$/LSM cell [47]

Conclusions of the chapter

In this first chapter, we could observe that $Y_{1-x}Zr_xMnO_{3+\delta}$ lamellar materials exhibit interesting structural properties as the capability to absorb interstitial oxygen excess and the facility to adopt different space groups ($P6_3cm$ or $P6_3/mmc$), depending on the temperature and the atmosphere. The latter characteristics directly affect the properties expected for SOFC electrodes since they determine the conductivity mechanism (and maybe the conductivity level) and influence the thermomechanical

behavior (*i.e.* the TEC values). However, the chemical compatibility of these materials with YSZ electrolyte is perfect, independently of those structural changes, what was one of the main objectives of our study. Those materials can be considered as promising new cathodes due to their already good electrochemical behavior in air, probed in symmetrical cell configuration elaborated by classical ceramic techniques. Apart from the particular properties of each compound, the electrochemical behavior is subject to the thickness of the active electrode layer, the microstructure and, in our case, of an adequate current collector, aspects that generally influence the global properties of the material and that we could roughly optimized. Nevertheless, it is worth noting that such optimization are preliminary and that the cathodic properties of these new materials can be still improved using advanced electrode elaboration techniques that enable finer electrode microstructure and better electrode-electrolyte interphase, *e.g.* impregnation of a YSZ scaffold that generally gives better electrode performance with respect to classical techniques.

4. STABILIZATION OF $YMnO_3$ IN REDUCING ATMOSPHERE FOR USE AS SOFC ANODE MATERIAL

4.1 SYNTHESIS AND STRUCTURAL CHARACTERIZATION OF $YMn_xTi_yO_{3+\delta}$ (y=0.1, 0.2, 0.3 and x+y=0.85, 0.9, 0.95) COMPOUNDS

In the previous chapter, we could observe that pure and Zr-doped manganites present interesting electrode properties, in particular good chemical and thermomechanical compatibility with YSZ electrolyte, thermal stability in air (at operating SOFC temperatures) and acceptable cathodic performance. Unfortunately, those materials decompose in reducing atmosphere at high temperature (T>700°C) precluding their use as an SOFC anode. For that reason, the present section is devoted to the stabilization of $YMnO_3$ structure in reducing atmosphere.

The strategy that we used to increase the stability was inspired from one of the most relevant advances in the field of SOFC anodes: the $La_{0.75}Sr_{0.25}Cr_{0.5}Mn_{0.5}O_3$ (LSCM) perovskite [99]. Such material is the result of the replacement of Cr for Mn at the B-site of $La_{0.2}Sr_{0.8}MnO_3$ (LSM), the state of the art cathode, turning the material stable under reducing atmosphere and leading to performance comparable to Ni/YSZ anode [99], [238]. In our work, Ti^{4+} was substituted for Mn^{3+} at the B site of $YMnO_3$, due to the fact that titanium is a particularly stable element in reducing atmosphere, *i.e.* Ti^{4+} is more difficult to reduce to Ti^{3+} than Mn^{3+} to Mn^{2+}, the origin of $YMnO_3$ instability. The choice of an adequate stoichiometry was based on literature. Indeed, some authors reported the synthesis of $YMn_{1-x}Ti_xO_3$ compounds with Ti contents of $0.05 \leq x \leq 0.4$. They observed that at concentrations of $x<0.15$, the materials crystallize in the same space group as pure $YMnO_3$ ($P6_3cm$) [239]. When the substitution reaches $x \approx 0.175$, the material exhibits a phase transition [163]. Around $x \approx 0.20$, new peaks grow alongside the $P6_3cm$ arrangement (or $P6_3/mmc$ [239]). These reflections belong to an additional phase of $R\text{-}3c$ space group, which coexists with the $YMnO_3$-type phase [125], [137]. The amount of the new phase continues to increase as the

concentration of doping element raises; however, the biphasic system is reported until x=0.4 [240]. Considering such information, the narrow range in which a single-phase can be obtained is probably not enough to obtain significant results and stabilize $YMnO_3$ in anode conditions. For that reason, sub-stoichiometric materials have been proposed as a solution. Indeed, three $YMn_xTi_yO_{3+\delta}$ compositions have been previously reported in literature, that correspond to: y=0.10-x=0.80, y=0.20-x=0.73, and y=0.30-x=0.60; all have been prepared as single-phases [164]. Analyzing those particular stoichiometries, it is worth noting that they all correspond to x+y~0.90. It seems to indicate that this is the clue to obtain single-phases of Ti-doped materials when y value exceeds 0.1.

In order to analyze what is the situation besides such conditions, we also decided to prepare not only the materials corresponding to the aforementioned compositions but also of compounds with x+y values being 0.85 and 0.95 for y=0.2 and 0.3. In this way, we synthesized the eight materials shown in Table 17, using the Pechini's method and synthesis temperatures of 1100-1200°C.

Table 17. Summary of the $YMn_xTi_yO_{3\pm\delta}$ compositions prepared in this work. References to literature concerning some of the successfully prepared stoichiometries is given for information.

y	x	x+y	Reference
0.10	0.80	0.90	Peng [164]
0.20	0.65	0.85	-
	0.70	0.90	-
	0.73	0.93	Peng [164]
	0.75	0.95	-

y	x	x+y	Reference
0.30	0.55	0.85	-
	0.60	0.90	Peng [164]
	0.65	0.95	-

X-Ray diffraction patterns of the synthesized compounds are depicted in Figure 93. The analysis of the diffractograms allows to observe that independently of y value, the materials with x+y=0.85 and 0.9 are single-phases and exhibit a hexagonal lamellar structure like $YMnO_3$. Nevertheless, for higher values of x+y (*i.e.* x+y=0.95), there is a mixture of phases: an hexagonal lamellar material of the $YMnO_3$-type and another that belongs to asuperstructure (*R*-3*c* space group), as aforementioned for the $YMn_{1-x}Ti_xO_3$ compositions (x≥0.2) [116]. The appearance of such rhombohedral phase has been observed in $AMnO_3$ A=Y, Yb, Dy, Ho, Er systems with oxygen excess [117], [118]. In general, this superstructure is related to the *P*6$_3$*cm* in this form:

a lattice parameter (*P*6$_3$*cm*):

$$a=a'' \text{ [=] Å} \qquad (58)$$

c lattice parameter (*P*6$_3$*cm*):

$$c=c''/3 \text{ [=] Å} \qquad (59)$$

Volume (*P*6$_3$*cm*):

$$V=V''/3 \text{ [=] Å}^3 \qquad (60)$$

Figure 93. X-Ray diffraction patterns of sub-stoichiometric $YMn_xTi_yO_{3+\delta}$ materials (a). comparison between y=0 and y=0.10 for x+y=0.90; (b). y=0.20 for x+y=0.85, 0.9 and 0.95; (c). y=0.3 for x+y=0.85, 0.9 and 0.95.

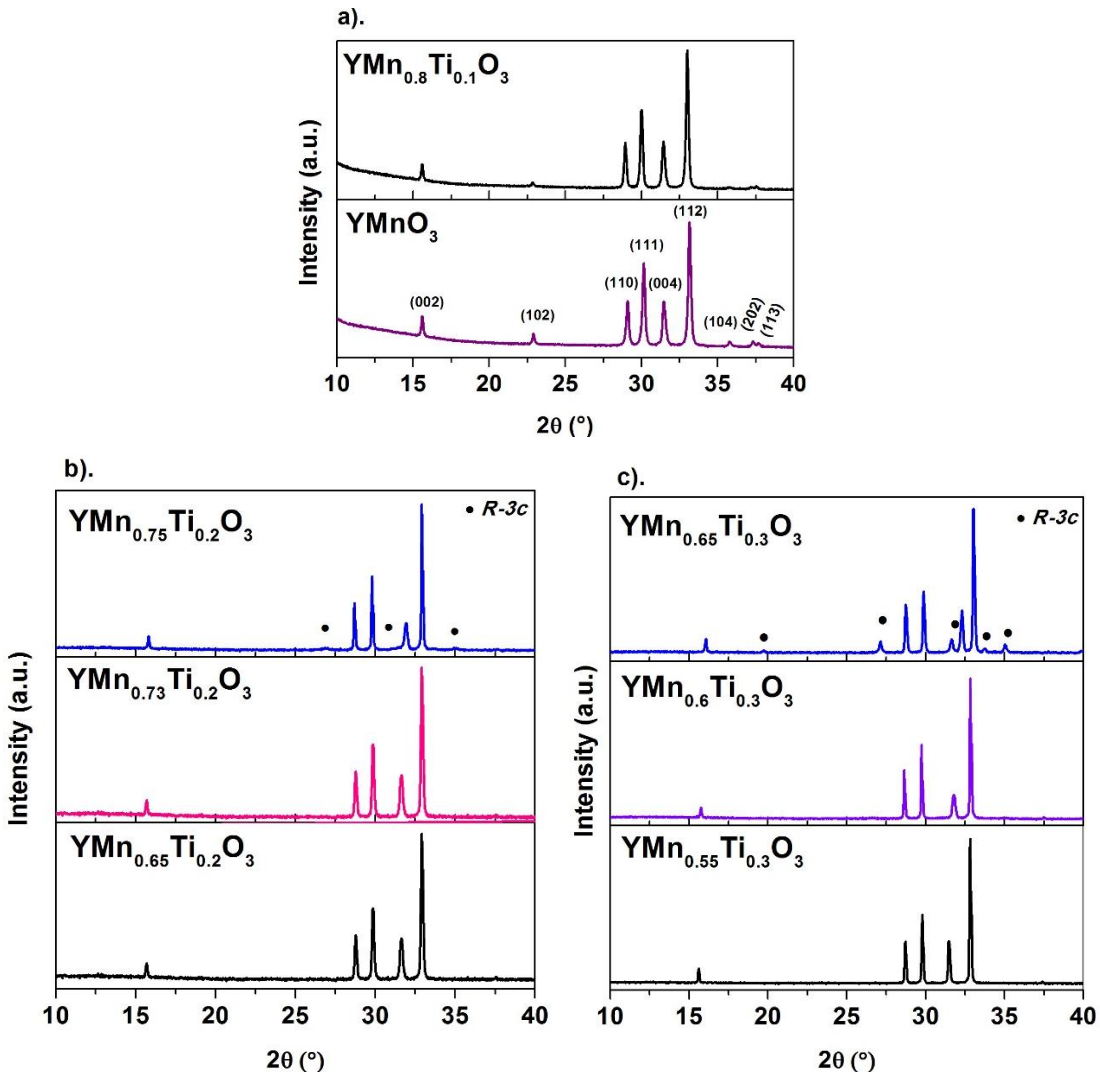

Where a'', c'' and V'' are the values for the *R*-3*c* superstructure lattice. Asaka *et al.* [125] proposed a model for such structure which is a stacking reorganization of *P*6$_3$*cm*, that reduces the strain energy of the crystal. Two types of layers made of $(Mn,Ti)O_5$ polyhedra exist along *c*-axis, namely A_1 in z=0 and B_1 rotated by 60° (z=1/2) (Figure 94).

Figure 94. Stacking of hexagonal lamellar Y(Mn,Ti)O_3 (*P*6$_3$*cm*).

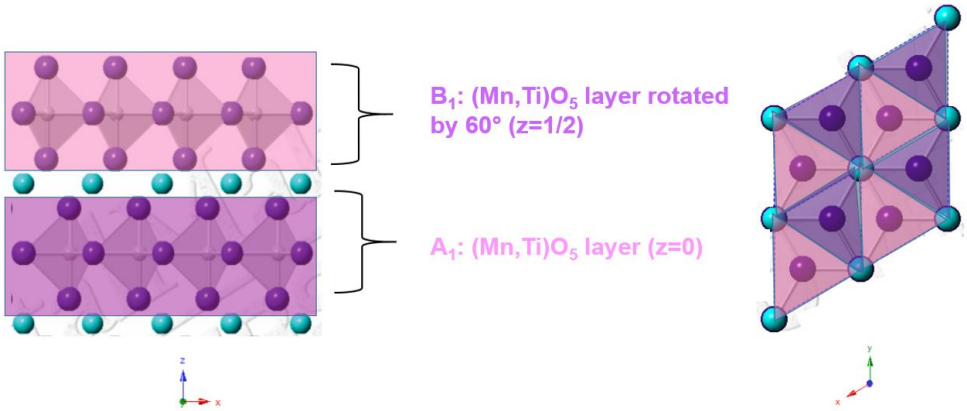

However, the superstructure exhiits several A and B layers, but shifted by $\frac{2}{3}\frac{1}{3}c_h/2$ making the sequence being A_1-B_2-A_3-B_1-A_2-B_3-A_1-B_2... and the vectors for the oxygen atom that join three (Mn,Ti)O_5 being indeed 00z, $\frac{2}{3}\frac{1}{3}z$ and $\frac{1}{3}\frac{2}{3}z$. Nonetheless, Abughayada *et al.* [191] affirmed that the new stack sequence for the superstructures in compounds with oxygen excess is a consequence of the oxidation of Mn^{+3} to Mn^{4+} and the successive appearance of extra oxygen within the interstitial sites (*18b*) of the material.

Back to our compositions, the $YMn_{0.8}Ti_{0.1}O_3$ compound crystallizes in a *P*6$_3$*cm* space group, although a decrease of the intensity of the *(102)* peak at 2θ~23° with respect to the pure $YMnO_3$ material can be noticed. For its part, $YMn_{0.65}Ti_{0.2}O_3$, $YMn_{0.73}Ti_{0.2}O_3$, $YMn_{0.55}Ti_{0.3}O_3$ and $YMn_{0.6}Ti_{0.3}O_3$ materials clearly exhibit a *P*6$_3$*/mmc* space group. Similar to the Zr doping of the previous chapter, this fact is evidenced by the disappearance of reflections at 2θ~23° and 2θ~35-38°. The structure change was also reported in Peng's works [164] and, as in the case of Zr-doped materials, could be related to the increase of oxygen content, with respect to $YMnO_3$, especially considering that the appearance of the aforementioned rhombohedral phase is also related to oxygen excess when titanium content is high (*i.e.* the cation substoichiometry is low). Indeed, in the case of $YMn_{0.875}Ti_{0.125}O_3$, when oxygen

content decreases, a phase transition from *P*6$_3$/*mmc* to *P*6$_3$*cm* has been described [116]. Thus, the fact that Ti-doped compounds can be indexed in *P*6$_3$/*mmc* is possibly the result of higher oxygen content in the structure with respect to the stoichiometry ABO_3, but the situation has to be examined carefully and will be detailed below. A final general remark concerning the X-Ray patterns is the displacement and decrease of the intensity of the *(004)* peak as the amount of Ti increases. Then, it is possible to infer that the substitution promotes an atomic reorganization. As expected, the structural change directly influences the lattice parameters. Those values were calculated using the FPM method, and the results for pure compositions are presented in Table 18.

Table 18. Structural parameters of the $YMn_xTi_yO_{3+\delta}$ materials after synthesis, as obtained from FPM refinement using XRD data.

Sample	a (Å)	c(Å)	V(Å^3)	Reliability factors
$YMnO_3$				
*P*6$_3$*cm*	6.1452(2)	11.3752(3)	372.029(1)	R_p(%)=2.32 GOF=1.41 R_{wp}(%)=3.01
$YMn_{0.8}Ti_{0.1}O_3$				
*P*6$_3$*cm*	6.1777(5)	11.3895(7)	376.44(5)	R_p(%)=3.10 GOF=1.45 R_{wp}(%)=4.02
$YMn_{0.65}Ti_{0.2}O_3$				
*P*6$_3$/*mmc*	6.2121(9)	11.3631(2)	379.779(9)	R_p(%)=6.14 GOF=1.58 R_{wp}(%)= 8.07
*P*6$_3$*cm*	3.5866(5)	11.3631(2)	126.593(3)	
$YMn_{0.7}Ti_{0.2}O_3$				
*P*6$_3$/*mmc*	6.2133(7)	11.3296(2)	378.807(9)	R_p(%)=6.22 GOF=1.42 R_{wp}(%)=8.11
*P*6$_3$*cm*	3.5873(4)	11.3296(2)	126.269(3)	
$YMn_{0.73}Ti_{0.2}O_3$				
*P*6$_3$/*mmc*	3.5904(3)	11,2615(4)	125.727(8)	R_p(%)= 3.26 GOF=1.41

Sample	a (Å)	c(Å)	V(Å^3)	Reliability factors
*P*6$_3$*cm*	6.2188(5)	11.2615(4)	377.181(1)	R_{wp}(%)=4.43
$YMn_{0.55}Ti_{0.3}O_3$				
*P*6$_3$/*mmc*	3.5945(2)	11.3835(9)	127.372(2)	R_p(%)=6.17 GOF=1.56
*P*6$_3$*cm*	6.2258(3)	11.3835(9)	382.116(6)	R_{wp}(%)=7.81
$YMn_{0.6}Ti_{0.3}O_3$				
*P*6$_3$/*mmc*	3.5992(7)	11.3070(8)	126.85(1)	R_p(%)=3.17 GOF=1.53
*P*6$_3$*cm*	6.2339	11.3070(8)	380.55(3)	R_{wp}(%)=4.50
R_p: profile factor R_{wp}: weighted-profile factor GOF: goodness of fit				

As for Zr-doped series, two sets of lattice parameters were included in case the structure is centrosymmetrical (*P*6$_3$/*mmc* space group), in order to enable the comparison between the materials of both structure type. Globally, Ti substitution seems to induce the growth of cell volume because of increase of *a* parameter but such evolution seems neither really clear nor easy to analyze, considering that the cation stoichiometry changes.

On the other hand, graphing the evolution of lattice parameters as a function of Ti content y, for example at a constant transition metal content x+y=0.9, we obtain the Figure 95. The $YMnO_3$ cell parameters have been plotted for comparison even if the composition does not fulfill the same x+y=0.9 condition. We observe that when Ti content increases, *a* parameter and V increases, meanwhile *c* slightly decreases. A similar tendency can be observed in the case of x+y=0.85. Although we do not know the oxygen content in each case, such phenomenon is tentatively associated to the decreasing oxidation state of Mn^{4+} to Mn^{3+} along the series as trivalent manganese (r_{Mn3+}=0.58 Å) is bigger in size than tetravalent (r_{Mn4+}=0.465 Å); additionally, with r_{Ti4+}=0.51 Å, Ti^{4+} is also bigger in size than Mn^{4+} cation [189]. It seems to signify that a higher amount of Ti in the structure means a reduction of manganese in the structure. Another explanation would be to consider that the Mn^{4+}/Mn^{3+} balance remains constant along the series and that the oxygen content increases when Ti

substitutes Mn due to higher coordination of both transition metals. A discussion concerning the oxygen stoichiometry in the series will be given below within the study of stability in reducing conditions.

Figure 95. Evolution as a function of Ti content y of cell parameters *a*, *c* and volume V in the $YMn_xTi_yO_{3+\delta}$ series with x+y=0.9.

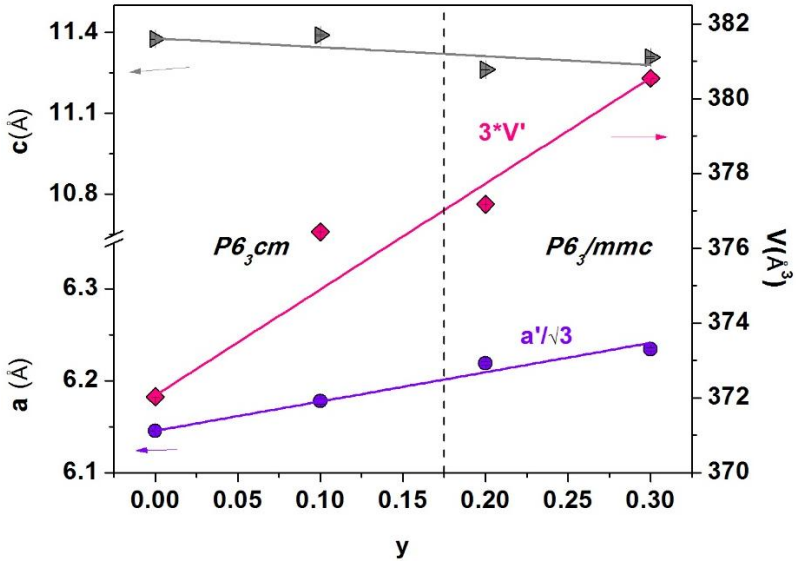

To conclude our analysis of the synthesis conditions to obtain Ti-doped yttrium manganese oxides as pure hexagonal phases and with possibly high content of (interstitial) oxygen, the following stoichiometries can be viewed as particularly interesting $YMn_{0.8}Ti_{0.1}O_{3+\delta}$, $YMn_{0.73}Ti_{0.2}O_{3+\delta}$ and $YMn_{0.6}Ti_{0.3}O_{3+\delta}$. As a consequence, our study have been focused from this point on those three compositions.

4.2 ANALYSIS OF THE MATERIALS' REDOX STABILITY

In order to analyse the stability of the $YMn_xTi_yO_3$ series in anodic environment, $YMn_{0.8}Ti_{0.1}O_3$ and $YMn_{0.73}Ti_{0.2}O_3$ compounds were first exposed to a moist 3%H_2/N_2 (pH_2O~0.03 atm) during 6 hours at high temperature (800°C), those conditions can

be qualified of mild reducing conditions as the corresponding pO_2 is not really low in comparison, for example, to wet H_2. The results of those tests are given in Figure 96.

Figure 96. X-Ray diffraction patterns of (a) $YMn_{0.8}Ti_{0.1}O_3$ and (b) $YMn_{0.73}Ti_{0.2}O_3$ before and after a heat treatment at T=800°C under mild reducing atmosphere of moist 3%H_2/N_2 (pH_2O~0.03 atm).

a). **b).**

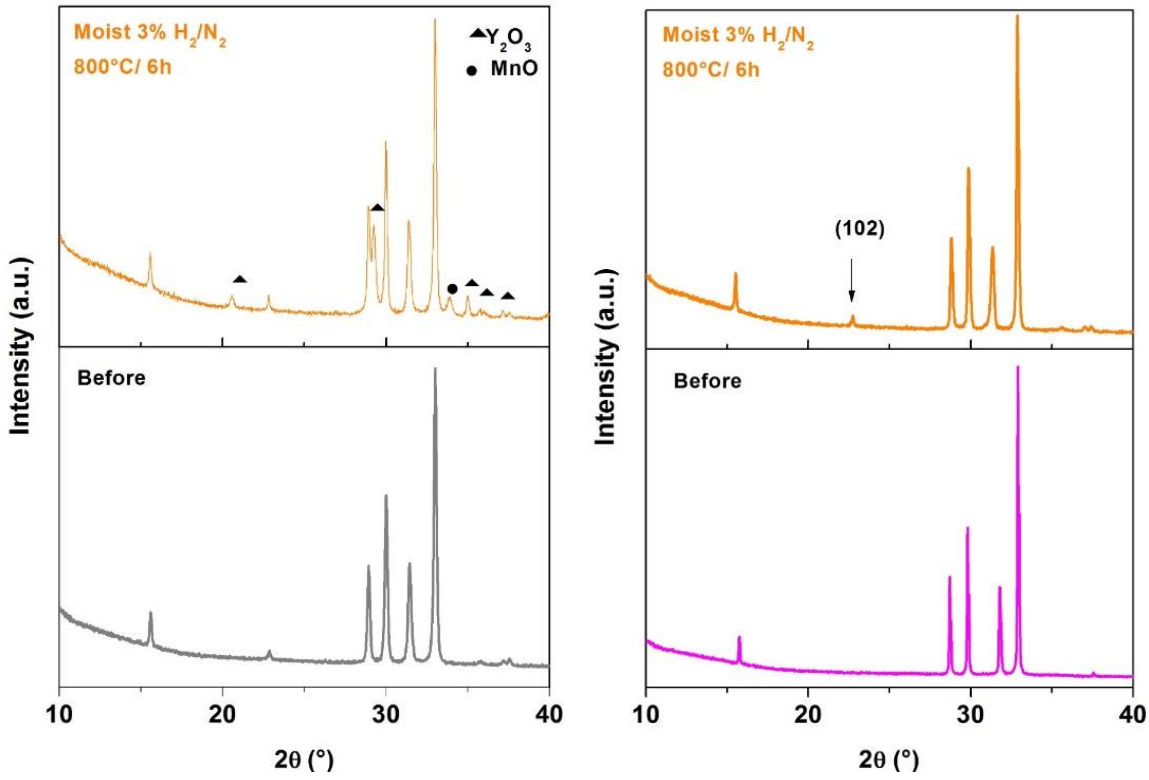

In these same conditions, the pure matrix $YMnO_3$ (and Zr-doped) is completely decomposed (see the previous chapter); however, the $YMn_{0.8}Ti_{0.1}O_3$ material is only partially decomposed into its reactants Y_2O_3 and MnO and a hexagonal lamellar structure (*P*6$_3$*cm*) remains present. Therefore, we can conclude that, at even such low Ti content, the presence of Ti^{4+} already stabilizes the material in reducing conditions, what is remarkable. The reason for that is that Ti^{4+} is a hardly reducible

cation in comparison to Mn^{3+}, what is related to its particularly stable electronic configuration [Ar]$3d^2 4s^2$. Thus, those results open the possibility to use the Ti-doped yttrium manganites as both electrode (anode and cathode), even if the present $YMn_{0.8}Ti_{0.1}O_3$ stoichiometry is perhaps not completely optimized yet (the material begins to decompose in mild reducing conditions). In the case of higher titanium concentration, specifically $YMn_{0.73}Ti_{0.2}O_3$ composition, the material remains as a single-phase after the same heat-treatment at high temperature. Nevertheless, a *(102)* peak appears at 2θ~23° which indicates that the material changes of structural arrangement to the non-centrosymmetrical phase $P6_3cm$. It could be the same case as Zr-doped compound in which a more symmetrical structure ($P6_3/mmc$) is observed when the compound presents extra oxygen atoms; in reducing atmosphere, when material losses the absorbed oxygen, it turns into the lower symmetry $P6_3cm$ space group. To probe the same material in a more realistic SOFC anode conditions, the material was placed during higher duration (16 h) under dry and moist reducing atmosphere. The diffractograms after the corresponding treatments are shown in Figure 97. Here, it can be observed that after a heat treatment in moist atmosphere, the peak at 2θ~23° related to the phase transition to $P6_3/mmc$ appears again. Likewise, additional peaks can be identified. They are attributed to the presence of MnO and a pyrochlore-type $Y_2Ti_2O_7$ phase. Thus, in comparison with the short duration test, for longer exposure to mild reducing conditions, the y=0.2 Ti-containing material begins to decompose. Now, under harsher dry reducing atmosphere (*i.e.* lower pO_2 conditions) the decomposition is much more severe, showing indeed the limits of the compound for anodic application.

Figure 97. X-Ray diffraction patterns of $YMn_{0.73}Ti_{0.2}O_3$ before and after a long heat treatment at T=800°C in mild or severe reducing conditions.

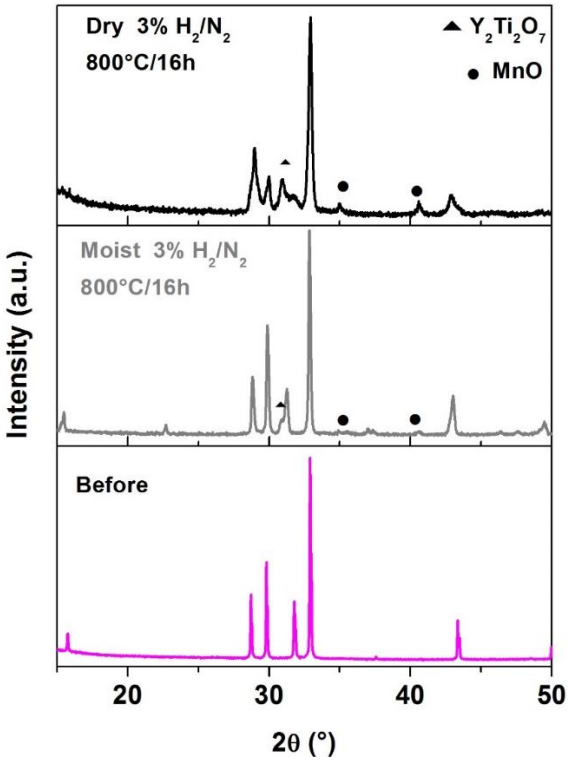

By contrast, the same tests (16 h under moist and dry reducing atmosphere) were carried out for $YMn_{0.6}Ti_{0.3}O_3$ composition. The XRD patterns of the resulting samples are presented in Figure 98. With no additional peaks, $YMn_{0.6}Ti_{0.3}O_3$ remains as single-phase under the moist 3%H_2/N_2 conditions and it can be indexed in the same initial hexagonal $P6_3/mmc$ symmetry. Such behavior could mean that such composition presents a higher quantity of oxygen in comparison with materials with less Ti concentration, impeding the phase transition to the non-centrosymmetrical arrangement, although it is related to some kind of disorder related to Ti/Mn substitution. It is worth noting, indeed, that the peak around 2θ= 31°, indexed as *(004)*, becomes wider, what may be due to the increasing content of oxygen defects in the solid. For its part, in dry reducing atmosphere, the presence of a small impurity is again observed that corresponds to the same oxide $Y_2Ti_2O_7$ reported for y=0.2.

Being very small and considering that the anode conditions are indeed not so reducing in the real application, especially under operation, this composition can be considered as sufficiently stable to probe it for anodic application. Consequently, $YMn_{0.6}Ti_{0.3}O_3$ will be the only composition to be further studied in the forthcoming sections.

Figure 98. X-Ray diffraction patterns of $YMn_{0.6}Ti_{0.3}O_3$ before and after exposure to reducing atmosphere in mild (wet) conditions and severe (dry) conditions for 16 h.

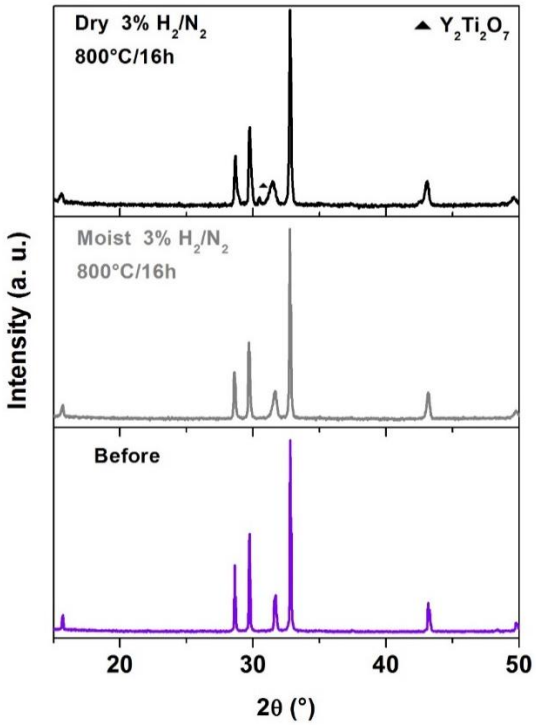

Finally, an inspection of the lattice parameters after exposure allows to observe that the volume slightly increases. This is possibly due to the manganese reduction (Mn^{4+} to Mn^{3+} or Mn^{3+} to Mn^{2+}), as will be further studied in the next section.

Table 19. Comparison of $YMn_{0.6}Ti_{0.3}O_3$ lattice parameters before and after the exposure to reducing atmosphere.

Atmosphere	**Before**	**Moist 3% H_2/N_2**	**Dry 3% H_2/N_2**	
Compound	$YMn_{06}Ti_{0.3}O_3$	$YMn_{0.6}Ti_{0.3}O_3$	$YMn_{0.6}Ti_{0.3}O_3$	$Y_2Ti_2O_3$
Space group	*P*6$_3$/*mmc*	*P*6$_3$/*mmc*	*P*6$_3$/*mmc*	*Fd-3m*
Lattice parameters				
a (Å)	3.5992(7)	3.603(2)	3.599(3)	10.10 (1)
c (Å)	11.307(3)	11.316(8)	11.39(1)	-
V (Å^3)	126.85(5)	127.23(1)	127.28(2)	1032(1.0)

4.2 STUDY OF ELECTRODE-ELECTROLYTE COMPATIBILITY IN AIR AND REDUCING ATMOSPHERE

4.2.1 Determination of chemical compatibility. The X-Ray diffractograms corresponding to a mixture of $YMn_{0.6}Ti_{0.3}O_{3+\delta}$ and YSZ electrolyte, before and after a heat treatment at 1350°C in air (8 hours) followed by a similar test in dry reducing atmosphere at 800°C (16 h) can be observed in Figure 99. In all cases, no additional phases can be identified, what confirms the huge interest of this kind of family, avoiding the main problem of SOFC electrode materials. However, after reactivity test in oxidizing atmosphere, and as in the case of Zr- doping, most of the peaks of the hexagonal phase and of YSZ are shifted to higher angles. Thus, all the refined lattice parameters, listed in Table 20, decrease in comparison to the original values, suggesting a cross-diffusion phenomenon at the interface between both electrode and electrolyte.

Figure 99. XRD patterns of $YMn_{0.6}Ti_{0.3}O_3$/YSZ mixtures before and after heat treatment in different conditions, (asterisks represent YSZ phase).

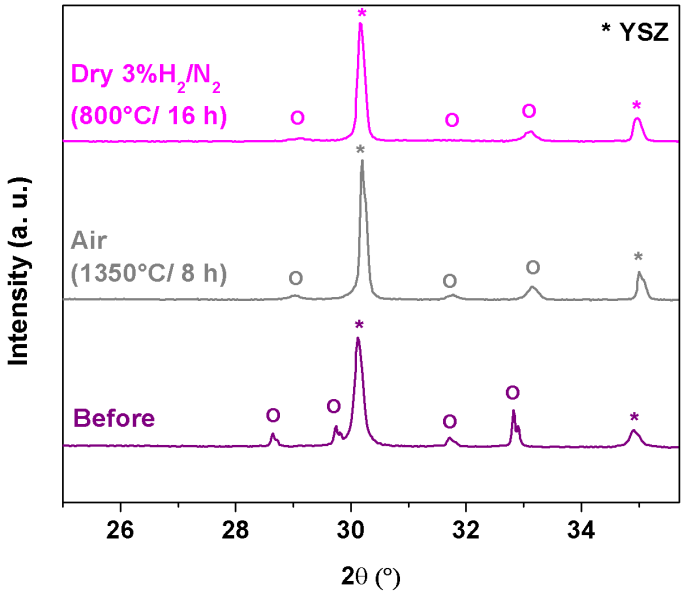

Table 20. Structural parameters of mixtures of$YMn_{0.6}Ti_{0.3}O_3$ and YSZ before and after reactivity tests as obtained from FPM refinement using XRD data.

Atmosphere	Sample	a (Å)	c(Å)	V(Å³)	Reliability factors
Before	**x=0.3**	3.5985(1)	11.2867(5)	126.57(1)	R_p(%)=5.10 GOF=1.62 R_{wp}(%)=6.78
	YSZ	5.1404(2)	-	135.82(1)	
Air	**x=0.3**	3.5557(3)	11.2624(16)	123.31(2)	R_p(%)= 7.10 GOF=2.12 R_{wp}(%)=4.4
	YSZ	5.1217(1)	-	134.35(1)	
Dry 3%H_2/N_2	**x=0.3**	3.5554(7)	11.3603(47)	124.37(6)	R_p(%)=7.76 GOF=2.38

Atmosphere	Sample	a (Å)	c(Å)	V(Å^3)	Reliability factors
	YSZ	5.1341(2)	-	135.33(1)	R_{wp}(%)=4.49
R_p: profile factor R_{wp}: weighted-profile factor GOF: goodness of fit					

First, it is possible to think in a Ti^{4+} diffusion to the electrolyte. In literature, the solubility limit of TiO_2 in the fluorite YSZ is reported to be less than 10 mol% since at higher concentrations, a new $ZrTiO_4$ phase appears [241]–[244]. This is in agreement with the fact that the lattice parameter of YSZ decrease when Ti^{4+} substitute Y^{3+} [242], [245]. Similarly, the decrease of both *a* and *c* parameters of the $YMn_{0.6}Ti_{0.3}O_3$ could be a result of the migration of Mn^{3+} (r_{Mn3+}=0.58 Å) and/or Ti^{4+} (r_{Ti4+}=0.51 Å) cations [189] to the electrolyte, according to their smaller ionic radii with respect to Zr^{4+} (r_{Zr4+}=0.78 Å) and Y^{3+} (r_{Y3+}=1.075 Å) [196]. In addition, Zr from of YSZ could diffuse to the Y site of Ti-doped material, which also induce the lattice parameter decrease. Then, in reducing atmosphere, an increase of the cell volume for the electrode is observed. This fact can be attributed to the partial reduction of Mn^{3+} (r_{Mn3+}=0.58 Å) to Mn^{2+} (r_{Mn2+}=0.75 Å) or Mn^{4+} (r_{Mn4+}=0.49 Å) to Mn^{3+} [189], which implies the ionic radii increases. At the same time, it is important to clarify that an eventual sign of reduction would be difficult to detect due to the decomposition in this conditions is very low and the intensity of YSZ reflections is very high in comparison with those of the Ti-doped $YMnO_3$ compound.

4.2.2 Analysis of the thermo-mechanical compatibility. The structural analysis concerning high temperature stability and the determination of the thermomechanical properties of $YMn_{0.6}Ti_{0.3}O_3$ were studied by means of High Temperature X Ray Diffraction (HT-XRD). This technique allows identifying structural changes while temperature varies, under a special atmosphere. Figure

100 corresponds to the patterns collected first in air, then in a reducing wet 3%H_2/Ar atmosphere and finally, again in air to study the reoxidation process.

Figure 100. Structural evolution of $YMn_{0.6}Ti_{0.3}O_3$ obtained by HT-XRD under different atmospheres: air, wet 3%H_2/Ar and finally air (red arrows: heating, blue arrows: cooling).

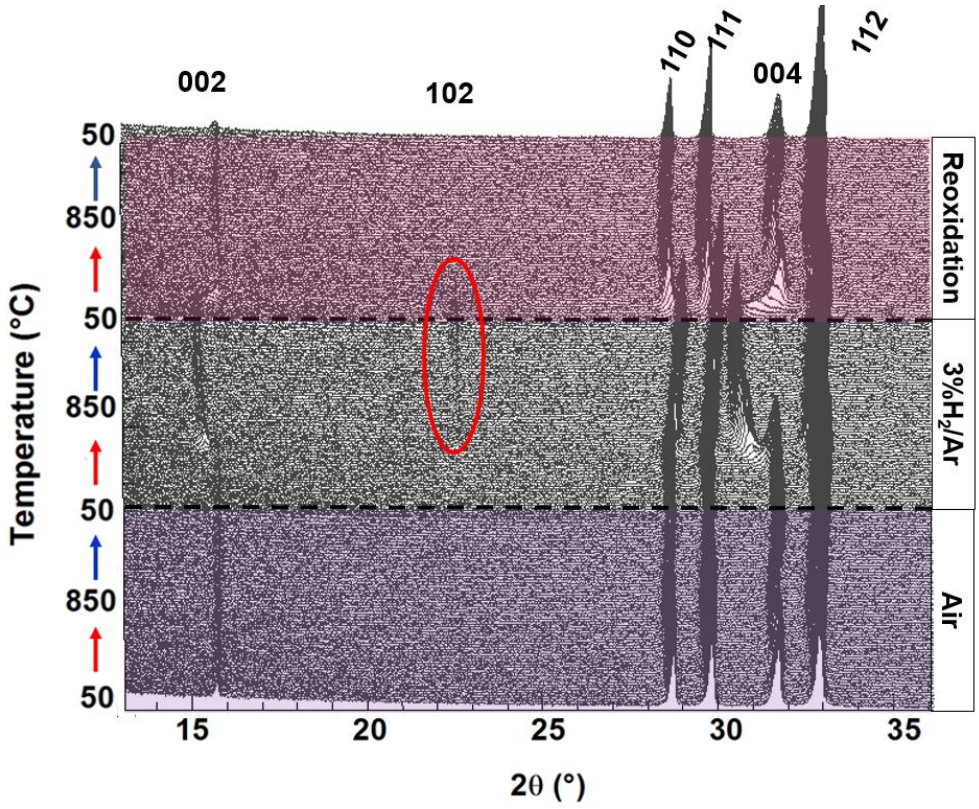

During the first cycle, we can observe that the material retains the initial *P*6$_3$/*mmc* hexagonal structure with in particular, the absence of any diffraction peaks around 2θ~23° that would be characteristic of the change to the non-centrosymmetrical *P*6$_3$*cm* structure. In this same environment, the evolution of refined cell parameters as a function of temperature, shown in Figure 101, allows to appreciate that the *a* lattice parameter increases with the temperature in the whole range and in a relatively linear way. On the other hand, the *c* parameter smoothly increases up to

T~250°C. In the intermediate temperature range of ~250-400°C and more marked to what occurs in the Zr- doped $YMnO_3$ material (described in last chapter), *c* shows a deviation to the linear evolution with a global decrease. At higher temperatures (T=400-600°C), *c* parameter seems to increase faster and in a linear way similar to the low temperature behavior. For the case of $Y_{0.9}Zr_{0.1}MnO_3$, the non-linear behavior was attributed to the oxygen absorption/desorption at intermediate temperatures and it is more than probable that the observed behavior for Ti-doped manganite stems from the same phenomenon.

Figure 101. Temperature dependence in air of $YMn_{0.6}Ti_{0.3}O_{3+\delta}$ (a) *a* and *c* lattice parameters and (b) cell Volume. Colorful and black symbols indicate heating and cooling conditions, respectively. (α is the symbol of the *P*6$_3$/*mmc* phase).

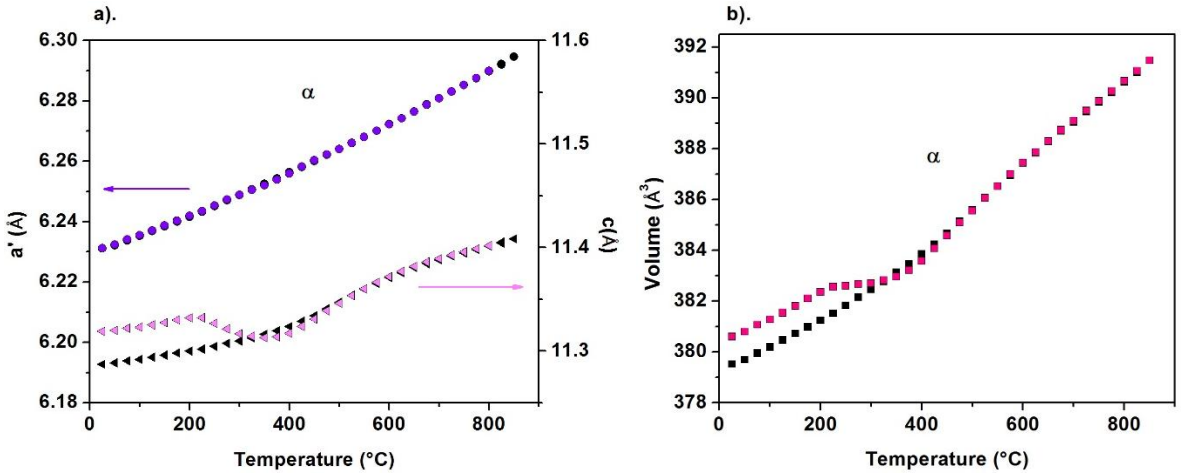

In order to confirm such assumption, the thermogravimetrical analysis of the material has been carried out in air and is depicted in Figure 102.

Figure 102. Thermogravimetrical analysis (TGA) measurements of $YMn_{0.6}Ti_{0.3}O_{3+\delta}$ in air (heating and cooling rates = 1°C/min)

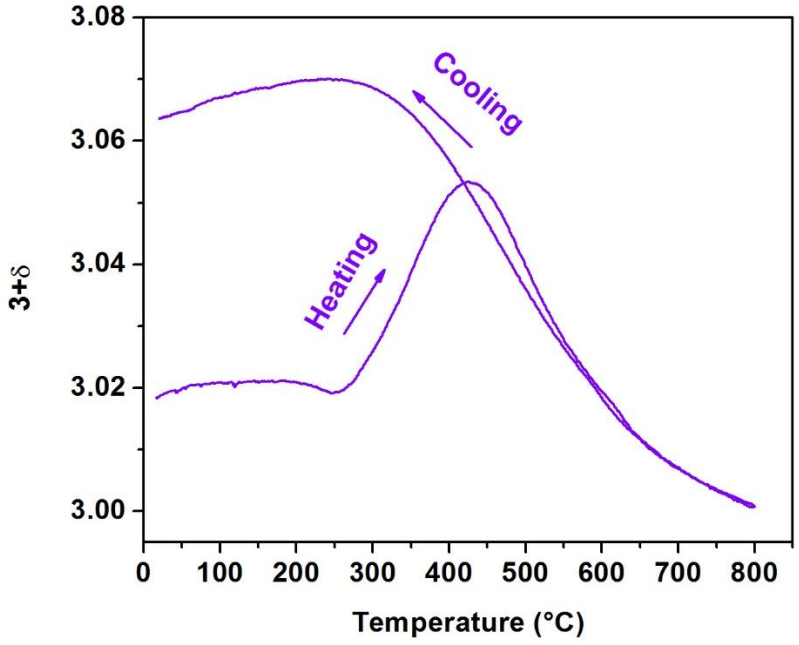

Here, it can be appreciated that, as occurs in most of the hexagonal $AMnO_3$ compounds as $YMnO_3$, $Y_{0.9}Zr_{0.1}MnO_{3.05}$ and including the reported stoichiometry $YMn_{0.875}Ti_{0.125}O_3$ [116], $YMn_{0.6}Ti_{0.3}O_{3+\delta}$ also exhibits a weight uptake from T~250°C up to 400°C, which is the same temperature in which the first accident in *c* and V evolution is evidenced. The oxygen excess is then released between 400 and 600°C explaining the second part of the *c* parameter change with T. As a conclusion, both phenomena are strongly related and based on the previous study concerning pure and Zr-doped $YMnO_3$, the variation of oxygen stoichiometry in the intermediate temperature range can explain the deviation of thermal dilatation from the classically observed linear expansion with T. Contrary to what happens for $Y_{0.9}Zr_{0.1}MnO_{3.05}$ material, *c* clearly decreases in the intermediate temperature range for the Ti-doped manganite, *i.e.* the effect of oxygen uptake seems much more important in case of Ti-substituted material. We could indeed think that the latter behavior is a consequence of a stronger oxidation to the smaller cation Mn^{4+} (r_{Mn4+}=0.46 Å) in the

structure due to the oxygen incorporation [189]. Nevertheless, according to Figure 102 in comparison to Figure 27 for the case of $Y_{0.9}Zr_{0.1}MnO_{3+\delta}$, the maximum oxygen amount in the Zr-manganite exceeds widely the case of $YMn_{0.6}Ti_{0.3}O_{3+\delta}$ ($3+\delta=3.21$ and $3+\delta=3.05$, respectively). Similarly, the maximum oxygen uptake after a heating-cooling cycle is higher for the Zr-doped $YMnO_3$ ($3+\delta\sim3.25$) than the value that is reached for $YMn_{0.6}Ti_{0.3}O_{3+\delta}$ ($3+\delta\sim3.07$). So, it seems the absolute value for oxygen uptake is not very important to explain the difference of behavior.

Another explanation is perhaps related to the phase transition from *P*6$_3$/*mmc* to *P*6$_3$*cm* structure that some Ti-doped manganites seems to exhibit according to literature. As can be seen in Figure 103, $YMn_{0.875}Ti_{0.125}O_{3+\delta}$, with similar stoichiometry to our case, presents such kind of phase transition around T~300°C, the same temperature range in which a *c* anomaly is observed. However, such phase transition is not evidenced at all by XRD in our Ti-doped compound that remains apparently with the same symmetry in the whole temperature range. However, such phase transition is not present in the Ti-doped compound that remains with the same *P*6$_3$/*mmc* symmetry in the whole temperature range; we think this case is perhaps not so trivial and suggest a deeper structural study should be carried out using Neutron and/or Electron Diffraction in order to elucidate possible analogies between $YMn_{0.6}Ti_{0.3}O_{3+\delta}$ and $YMn_{0.875}Ti_{0.125}O_{3+\delta}$.

Figure 103. Literature data for (a) HT-XRD collected in air and (b) Temperature dependence of the lattice parameters derived using XRD (heating in air in red and in helium in blue) for $YMn_{0.875}Ti_{0.125}O_{3+\delta}$ material (after [116])

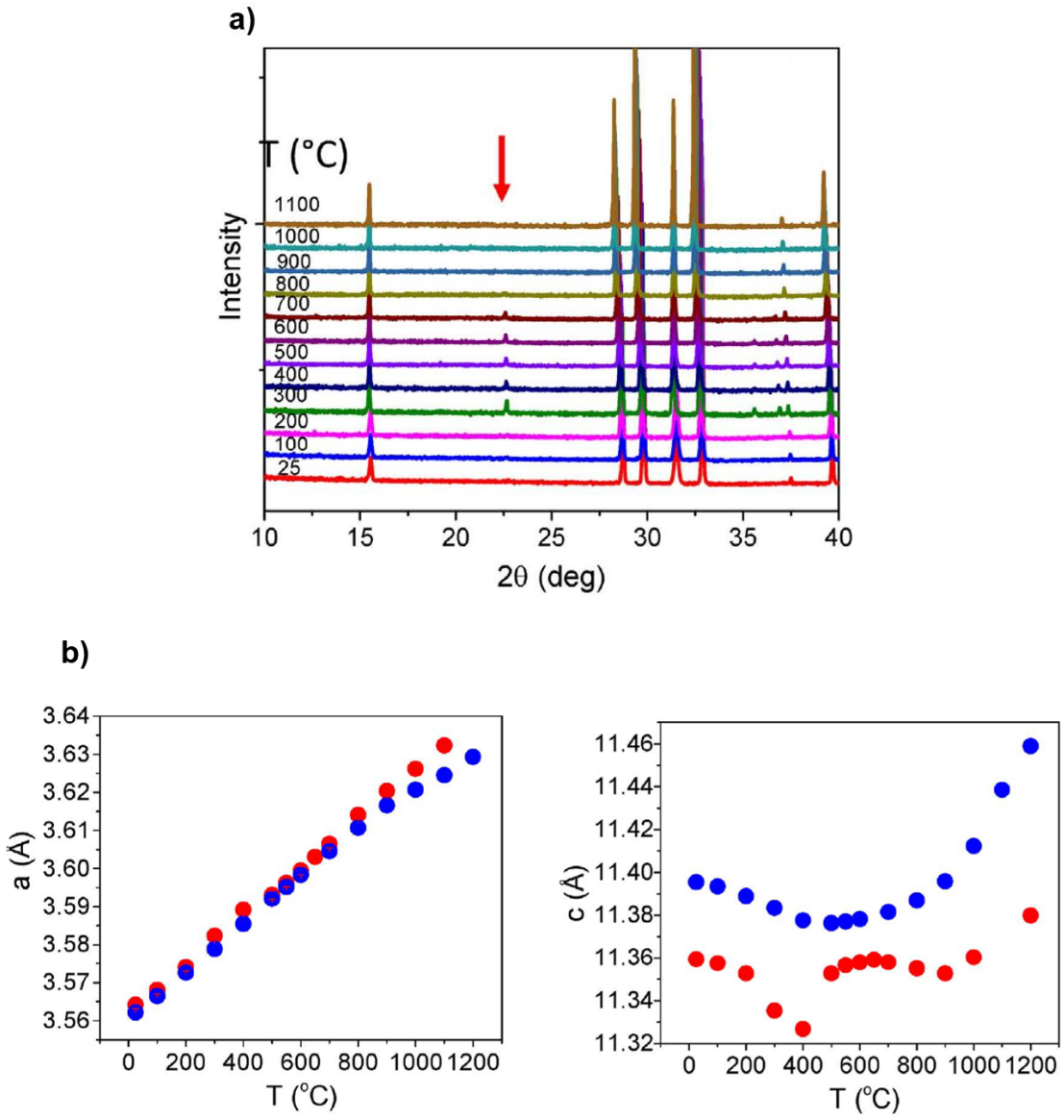

On the other hand, during the reduction cycle in wet diluted H_2, a phase transition from *P*6$_3$/*mmc* to *P*6$_3$*cm* space group is clearly observed during heating, as indicated in Figure 100. Such structure change is again evidenced with the appearance of

peak located around 2θ≈23° for T≥650°C, but at lower temperature, the growing of the *(004)* peak of *P*6$_3$*cm* at 2θ≈30.9° and the decrease of the *(004)* peak intensity for *P*6$_3$/*mmc* structure at 2θ≈31.48° are earlier changes of the XRD that indicate that phase transition, as evidenced in the zoom 2θ=13-45° region (Figure 104). At higher temperatures, the *P*6$_3$*cm* phase keeps on growing and coexists with the initial *P*6$_3$/*mmc* structure. The transition to *P*6$_3$*cm* ends at T~675°C, when the *(102)* peak at 2θ~23° clearly appears.

Figure 104. Structural evolution of $YMn_{0.6}Ti_{0.3}O_{3+\delta}$ obtained by HT-XRD under wet 3%H_2/Ar showing the phase transition from *P*6$_3$/*mmc* (α) to *P*6$_3$*cm* (γ) in the temperature range 575°C<T<675°C.

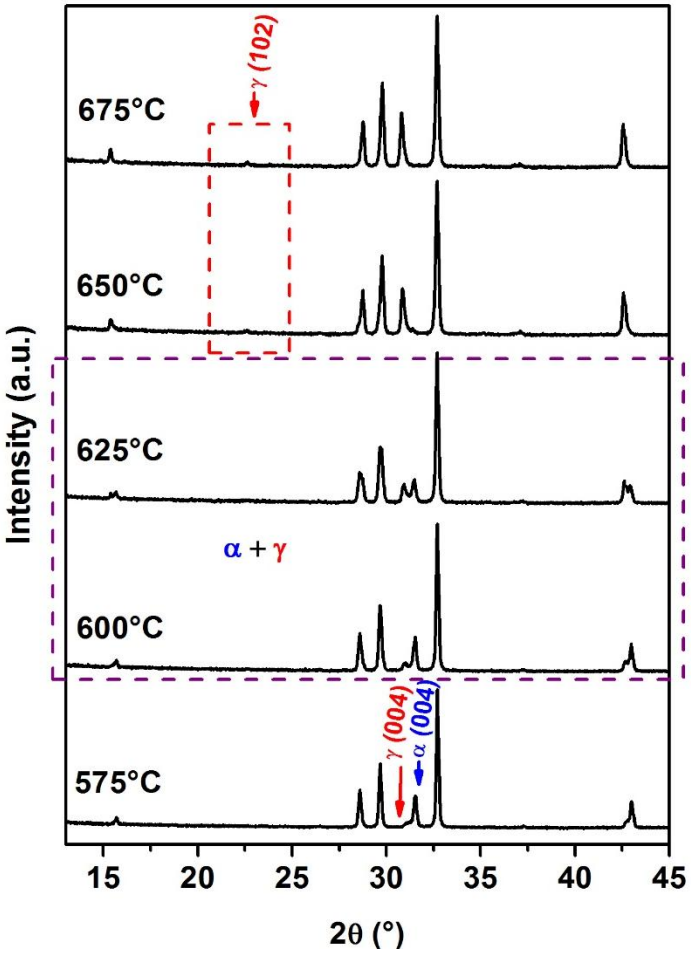

Meanwhile, the new structure is retained up to the maximum temperature of the test and during cooling in the same reducing atmosphere. The evolution of the lattice parameters and volume is shown in Figure 105.

Figure 105. Temperature dependence of (a) *a* and (b) *c* lattice parameters and (c) cell Volume for $YMn_{0.6}Ti_{0.3}O_{3+\delta}$ in wet 3%H_2/Ar. Colorful and black symbols indicate heating and cooling conditions, respectively. α and γ are the symbols of *P*6$_3$/*mmc* and *P*6$_3$*cm* structures, respectively.

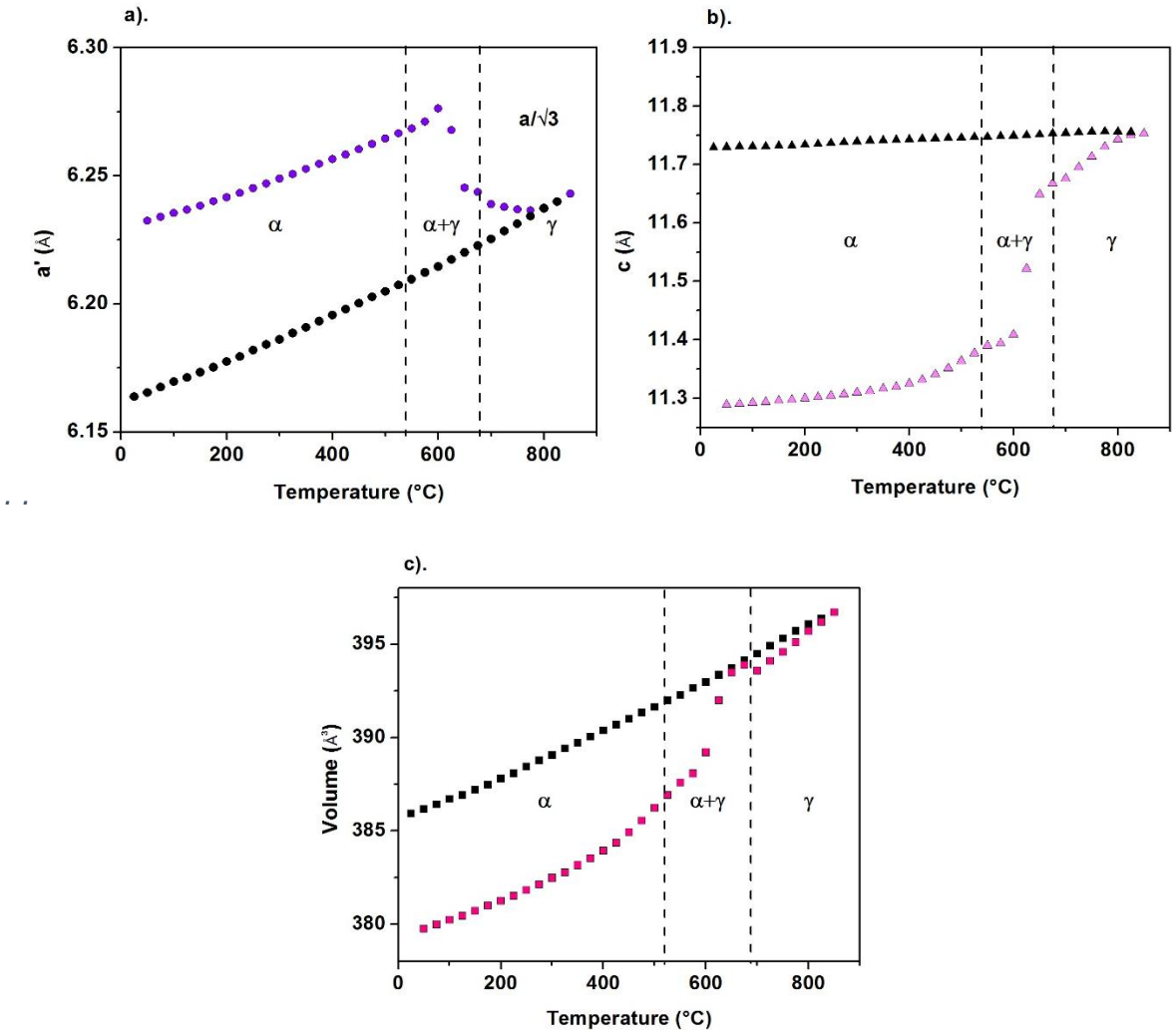

Thus, during heating in reducing atmosphere, both *a* and *c* parameters, and hence the unit-cell volume, increase in the $P6_3/mmc$ region (T<550°C). A thermogravimetrical analysis of the compound in reducing atmosphere demonstrate that such behavior corresponds to classical thermal dilatation because there is no weight change up to at least 400°C (Figure 106). However, at intermediate temperatures when the phase transition is evidenced by XRD, a weight loss is observed in TGA curve, which is related to the oxygen loss; in view of the temperature range similar to what we observed for $YMnO_3$, the weight loss is, with high probability, associated to the reduction of Mn^{4+} to Mn^{3+}, the global abrupt increase of cell volume being explained by the bigger ionic radius of Mn^{3+} cation (r_{Mn3+}=0.58 Å) in comparison to Mn^{4+} (r_{Mn4+}=0.46 Å) [189]. The difference between the beginning of the weight loss (T~400°C) and the structure change temperature (T~550°C) means that the materials can begin to lose interstitial oxygen atoms without atomic reorganization to $P6_3cm$ symmetry; nevertheless, a structure change due to chemical modification (oxygen loss) is already observed for T>400°C as indicates the deviation from linearity observed on the *c* parameter and unit-cell volume evolution (Figure 106). Now, it is worth noting that during cooling, the evolution of *a* and *c* parameters, and therefore of the unit-cell volume, is almost linear and is thus related to thermal contraction, as the material has been already reduced and should not present any additional change of oxygen content or symmetry. By careful analysis of the cooling curve for V, we can observe indeed a very slight change of slope that allows to define 3 ranges of temperature in which the behavior is perfectly linear: T<375°C, 400°C<T<525°C and T>675 °C. The origin of such slight variation in the expansion behavior of the material has not been understood yet and could require the use of heaviest characterization techniques like Neutron Diffraction.

Figure 106. Thermogravimetrical analysis (TGA) measurements of $YMn_{0.6}Ti_{0.3}O_{3+\delta}$ as a function of temperature in inert and reducing atmosphere (heating and cooling rates = 1°C/min).

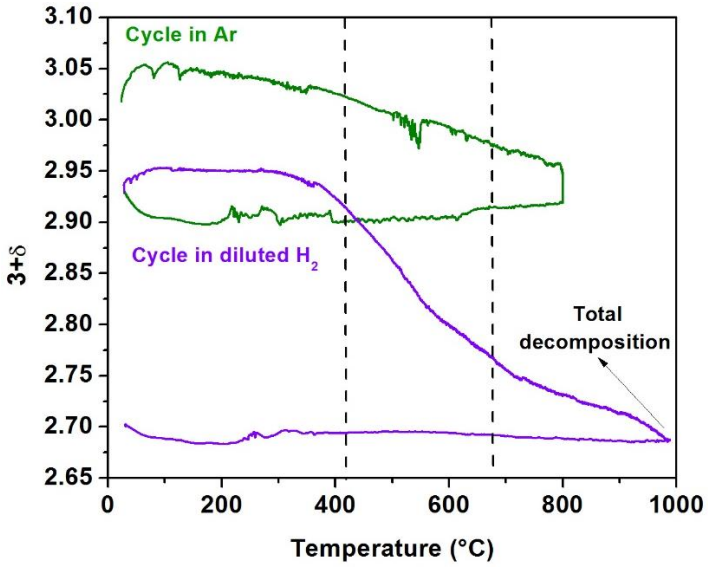

A consequence is that it is possible to calculate the thermal expansion coefficients (TECs) in both environments during cooling, according to the procedure described in the previous Chapter. The results are given in Table 21 with two ranges of temperatures for the behavior in air (high and low temperatures) and three sections in reducing atmosphere. In this table, we can observe that in both atmospheres, at low temperatures, the calculated β have 2-8% difference with the volumetric coefficient thermal expansion of 8YSZ electrolyte (β ~ 31-33x10^{-6} K^{-1}) [199]. Meanwhile, at high temperatures the difference increases to almost 30%. However, it is worth to mention that LSF ($La_{1-x}Sr_xFeO_3$) electrode reaches β = 42x10^{-6} K^{-1} [246] and LSM-based cathodes with β = 33.3-38.4x10^{-6} K^{-1} [46] are considered thermo-mechanically compatible with 8YSZ. And again, it is worth remembering that $YMnO_3$-based materials are perfectly compatible with YSZ on the chemical point of view, contrary to La/Sr perovskites.

Table 21. TEC values deduced from HT-XRD analysis (during cooling) of $YMn_{0.6}Ti_{0.3}O_{3+\delta}$ in air and wet 3%H_2/N_2.

Atmosphere	Range of temperature (°C)	Space group	β (x10^{-6} K^{-1})
dry air	50-300	*P6₃/mmc*	28.83
	550-850		42.36
wet 3%H_2/N_2	50-375	*P6₃/mmc*	30.96
	400-525	*P6₃/mmc*	32.47
	675-850	*P6₃cm*	37.26

On the other hand, the non-linear expansion observed at intermediate temperatures in both atmospheres during heating or during cooling in air, is the product of a contribution of chemical expansion (CE) to the global thermal expansion coefficient. For that reason, a calculation of the CE was also realized for the compound in oxidizing and reducing environments in the same way as in the previous chapter. Thus, in Figure 107 are depicted the linear volume evolution measured in the low temperatures range (red circles) and in which a TEC_1 can be calculated.

Figure 107. Estimation of Chemical Expansion Coefficient for $YMn_{0.6}Ti_{0.3}O_{3+\delta}$ from volume evolution obtained by HT-XRD: (a) during cooling in air and (b) during heating in reducing atmosphere. Oxygen content with temperature are given in the inset graph.

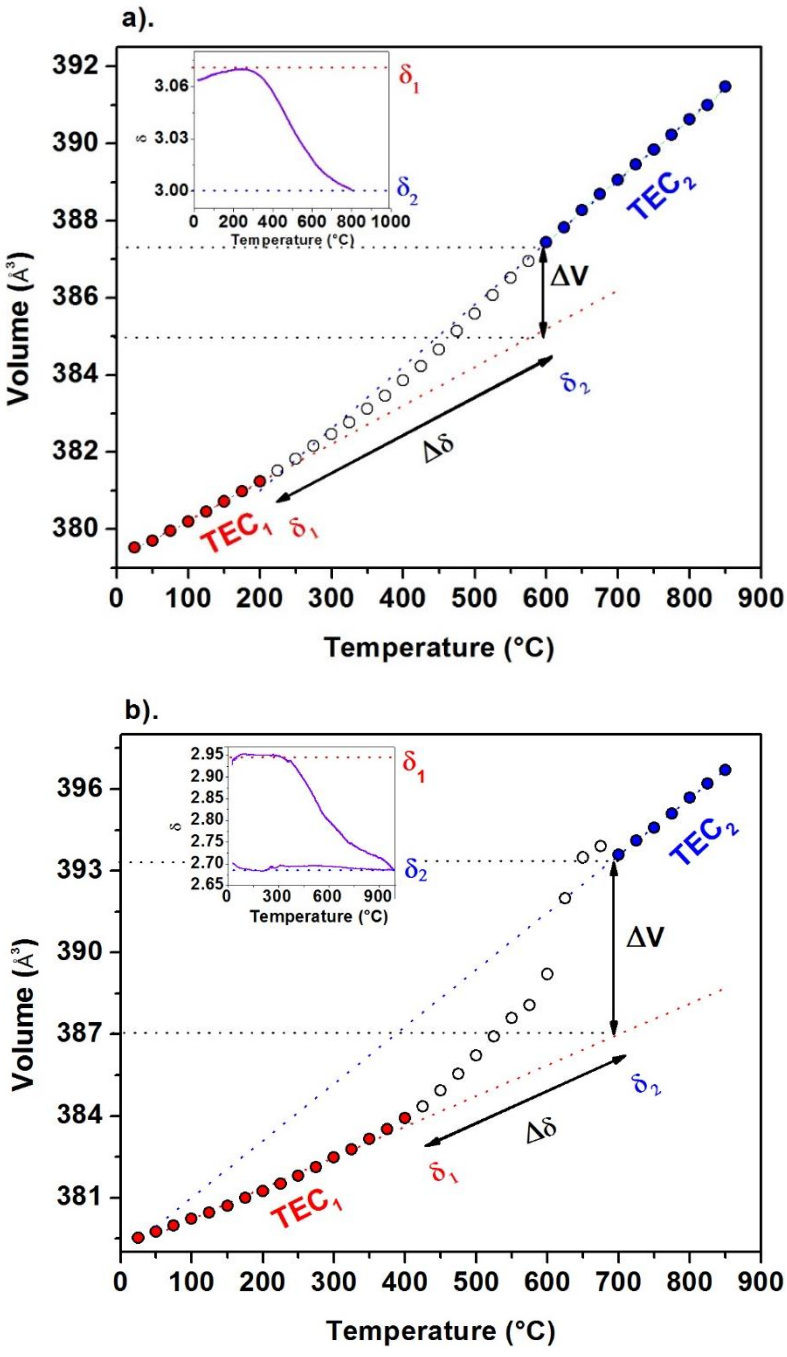

Additionally, in the graph appears the values that the cell volume would have had if no compositional change would have happened (red dot line). Similarly, the volume values measured in the high temperatures range (blue circles) and the extrapolated volume values until low temperature (blue dot line) are also represented in both figures. Then, the volume variation due to chemical composition change, ΔV, is estimated as the difference between the two right lines for the corresponding $\Delta\delta$ value, *i.e.* the change of oxygen content in the considered temperature deduced from TGA measurements

In the temperature range ~200-600°C in air, a value of CE=0.09 is obtained for Ti-doped compound; such value is higher than for $YMnO_3$ and $Y_{0.9}Zr_{0.1}MnO_3$ (CE= 0.015 and 0.026, respectively) in the same atmosphere. Meanwhile, in reducing atmosphere the CE value reaches a value of 0.05 (~400-700°C). In general, both values are considered high and are comparable with that of doped $CeO_{2-\delta}$ (CE=0.21) and $La_{0.6}Sr_{0.4}Co_{0.2}Fe_{0.8}O_{3-\delta}$ (CE=0.1) [204]. Therefore, an electrode made of $YMn_{0.6}Ti_{0.3}O_{3+\delta}$ could present some risks of fracture and delamination at the electrode/electrolyte interface cells [31], [202], [205]. Nonetheless, in case such issue would be evidenced in the future, the good chemical compatibility of this compound with YSZ would allow preventing thermo- o chemomechanical mismatch during cell elaboration or operation.

4.3 TRANSPORT PROPERTIES

4.3.1 Sintering procedure. With the aim to measure the conductivity of the synthesized Ti-doped compound, a study of ideal sintering conditions was carried out to get the highest sample density. First, the dimensional change of pressed cylindrical samples of $YMn_{0.6}Ti_{0.3}O_3$ (Diameter 5 mm x Height 8 mm) has been measured using dilatometry technique in air. The resulting curve is depicted in Figure 108.

Figure 108. Dilatometric curve of $YMn_{0.6}Ti_{0.3}O_3$ measured in air. Inset: zoom at low temperature showing two different rates of contraction.

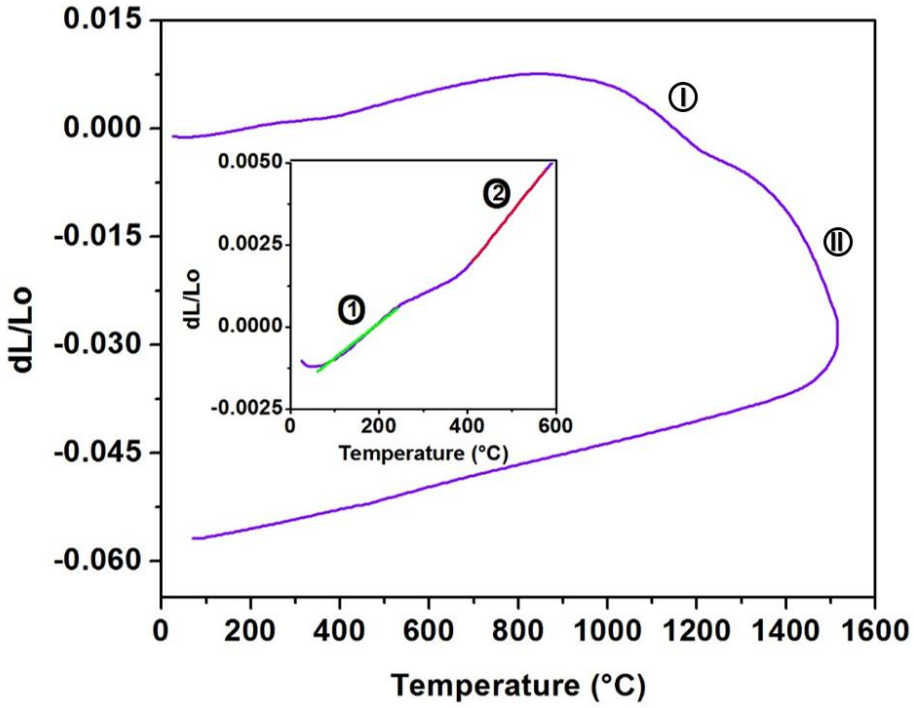

$YMn_{0.6}Ti_{0.3}O_3$ thermally dilates at low temperature (until T~250°C) with a quite linear behavior (number 1 in Figure 108); in this region, a TEC value of 32.41 x 10^{-6} K^{-1} can be calculated, which is slightly higher than what was estimated by HT-XRD (28.83 x 10^{-6} K^{-1}). However, in the intermediate temperature range, the dilatation curve exhibits a small accident in the same temperature range in which the material absorbs oxygen, what can be related to the cell volume decrease that was mentioned before. From T~400°C, the compound begins to dilate thermally again, but with higher slope up to T~950°C (number 2 in Figure 108) with a calculated TEC value of 42.86 x 10^{-6} K^{-1}, very close to the 42.36 x 10^{-6} K^{-1} calculated from HT-XRD datup to 850°C. At higher temperatures, the curve presents a contraction that is characteristic of the material sintering. Nevertheless, it proceeds in two steps (thereafter referred to as I. and II.): one from T~950°C to T~1200°C and the other

for T>1200°C. The actual reason of the observed accident around T=1200°C remains unknown and could be due to a structure change around such temperature, but the impossibility to carry out any HT-XRD analysis for Ti-doped material up to 1300°C cannot allow to confirm such hypothesis; it is worth mentioning that is not observed for $YMnO_3$. Nonetheless, the very fast second sintering stage is clearly a consequence of the grain growth and the decrease of the ceramic porosity. From the dilatometric curve, the temperature with the highest sintering speed can be calculated; in this case, such temperature is found around. T~1400-1450°C, what would be the temperature range to which the ceramic pellet should be ideally densified. A series of experiments was then carried out to determine the exact thermal treatment that must be used to get high enough sample compacity, using a sintering duration of 2 hours and heating/cooling ramps of 5°C/min. The compacity values obtained for each sintering temperature are listed in Table 22.

Table 22. Compacity of $YMn_{0.6}Ti_{0.3}O_{3+\delta}$ pellet as a function of the sintering temperature (the measured oxygen excess was set to ~3.06 for theoretical density calculation).

Temperature (°C)	Density (g/cm^3)		Compacity (%)
	Theoretical	Experimental	
1400	4.8608	3.57	73.44
1450		3.65	75.09
1500		4.03	82.91
1550		4.42	90.93

In this case, the highest compacity can be obtained for a sintering temperature of 1550°C, the corresponding compacity, greater than 80%, enables the use of the 4-

points probe technique to measure the bulk electrical conductivity with sufficient accuracy and apply in particular the aforementioned compacity correction.

4.3.2 Determination of the electrical resistivity of the compounds. Based on the preliminary results of dilatometry, conductivity samples with similar dimensions 5 x 10 mm (diameter x height) were thermally treated in the optimal sintering conditions, as described in the previous section. The experimental density and compacity were found as ρ=4.513 g/cm^3 and 92.70 %, respectively, confirming that these are correct conditions to use the technique. The resistivity of the corresponding samples was measured using the 4-points probe technique in several atmospheres as a function of temperature up to 850°C. The electrical conductivity was calculated from the measured values as described in the methodology chapter, and the corresponding σ=f(T) curve in air of Ti-doped $YMnO_3$ is shown in Figure 109, in comparison to the $Y_{1-x}Zr_xMnO_3$ materials.

Figure 109. Electrical conductivity as a function of temperature in air for $YMnO_3$, $Y_{0.9}Zr_{0.1}MnO_3$ and $YMn_{0.6}Ti_{0.3}O_3$.

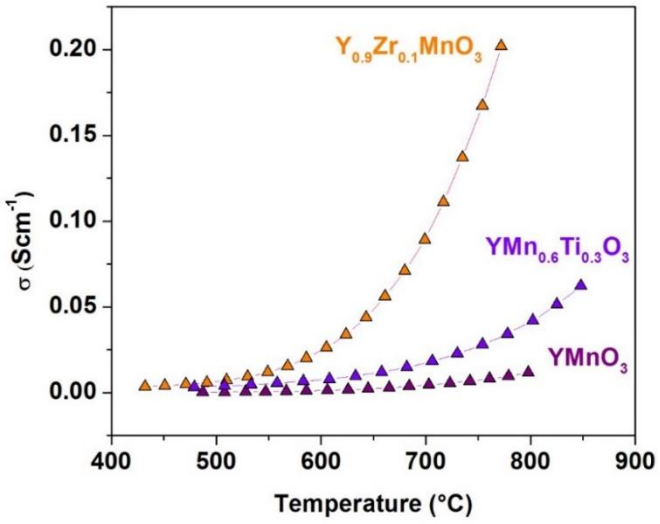

We can observe that the Ti-doped material exhibits in air the same p-type semiconducting electrical behavior of $Y_{1-x}Zr_xMnO_3$ compounds. Consequently, the Arrhenius-type evolution of ln(σT) vs 1000/T was plotted in order to calculate the activation energy of the hopping process (Figure 110).

Figure 110. Arrhenius plot of the electrical conductivity in air for $YMnO_3$, $Y_{0.9}Zr_{0.1}MnO_3$ and $YMn_{0.6}Ti_{0.3}O_3$.

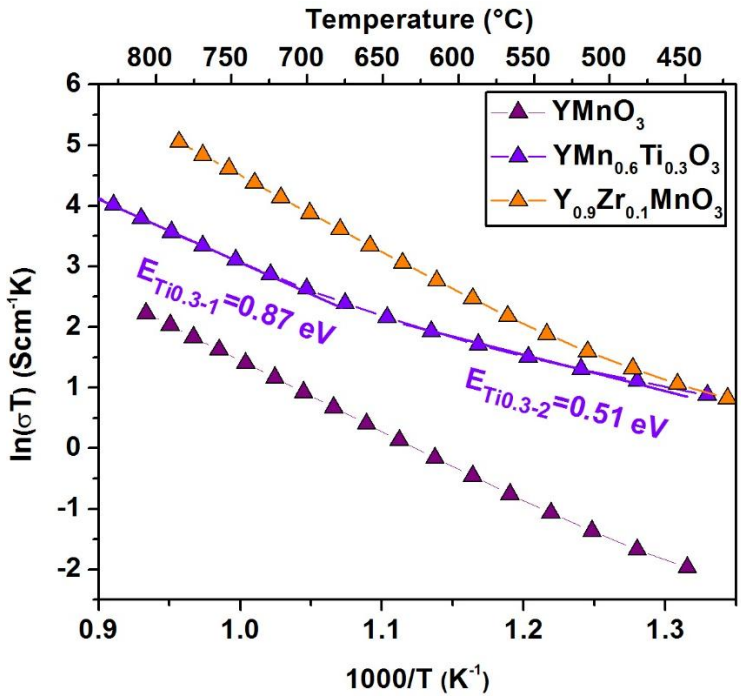

It is worth noting that $YMn_{0.6}Ti_{0.3}O_3$ conductivity curve in Arrhenius coordinates presents a change of slope around 650°C, similar to the case of pure or Zr-doped compound, but very pronounced. The calculated activation energies for the Ti-doped compound in both low (LT) and high (HT), temperature regions are reported in Table 23.

Table 23. Activation energy of the conductivity process in air for the studied compounds.

Sample	Temperature (°C)	Activation energy		
		(eV)	(kJ/mol)	R^2
$YMn_{0.6}Ti_{0.3}O_3$	480-660	0.5070 (2)	48.89	0.9949
	660-850	0.8690 (2)	83.82	0.9955
$YMnO_3$	490-550	0.7680(3)	74.10(3)	0.9968
	550-800	0.9664(4)	93.24(4)	0.9996
$Y_{0.9}Zr_{0.1}MnO_3$	430-570	0.6282(2)	60.61(2)	0.9916
	570-770	1.0396(9)	100.31(9)	0.9998

Both the HT and the LT activation energy values are significantly lower than the values obtained for $Y_{1-x}Zr_xMnO_3$ compounds, especially at low temperature. Now, the fact that Ti-doped materials presents a slope break in conductivity demonstrates that such kind of behavior is intrinsic of substituted $YMnO_3$ materials and the mechanisms would be the same for all of them [210]. Then, the main considerations to understand the conductivity process of $YMn_{0.6}Ti_{0.3}O_3$ are the same discussed in the Chapter 3 for $Y_{1-x}Zr_xMnO_3$ materials. First, at low temperatures the conductivity is related to small polaron phenomenon with hopping along the Mn sites. It is clearly related to oxygen excess (responsible of the presence of Mn^{3+}/Mn^{4+} pairs); nonetheless, in the case of Ti-doped manganite, the release of extra oxygen atoms extends to higher temperature for around 125°C than for $Y_{1-x}Zr_xMnO_{3+\delta}$ compounds and therefore, for $YMn_{0.6}Ti_{0.3}O_{3+\delta}$, the first slope regime prevails up to T~660°C. In addition, Ti-doped compound has a maximum value of oxygen uptake of $3+\delta=3.07$ which is between the value for $YMnO_{3+\delta}$ and $Y_{0.9}Zr_{0.1}MnO_{3+\delta}$ ($3+\delta=$ 3.05 and 3.26, respectively). It seems to explain the intermediate conductivity value at 750°C of

$YMn_{0.6}Ti_{0.3}O_3$ (σ=2.7 x 10^{-2} S cm^{-1} between 7.4 x 10^{-3} and 1.6 x 10^{-1} S cm^{-1} for $YMnO_3$ and $Y_{0.9}Zr_{0.1}MnO_3$, respectively). However, the conductivity of Ti-doped material at LT is closer to the value obtained for the Zr-doped than to the pure $YMnO_3$. At this stage, it is worth remembering that, on one hand, both substituted materials present the same arrangement (*P*6$_3$/*mmc*) in this temperature range, but on the other hand the *a* lattice parameter is higher for $YMn_{0.6}Ti_{0.3}O_3$ (*a*=3.5503 Å) in comparison with the calculated distance for Zr-doped $YMnO_3$ (*a*=3.599 Å), *i.e.* the Mn-Mn bond distances are longer for Ti-doped material, what generally corresponds to lower carrier mobility. Comparing both doped samples, the influence of Mn-Mn distance seems not be as important as the fact that the parent (*i.e.* Mn-O-Mn angles ~120°) and, and, as for perovskites, the effect of structure seems to dominate the electrical behavior, explaining the similar values of conductivity for the two doped materials. Concerning now the change of slope for the conductivity, in the case $Y_{1-x}Zr_xMnO_3$ materials at high temperatures, it has been possibly attributed to the change of carrier's concentration due to the disproportionation of Mn^{3+}, which is the only process that can make create Mn^{4+} species at high temperature. As a consequence, the electrical behavior is characterized by an increases the activation energy. On the other side, for the specific case of $YMn_{0.6}Ti_{0.3}O_3$ material, the concentration of Mn^{3+} cations is expected lower in comparison to $Y_{1-x}Zr_xMnO_3$ due to the material stoichiometry and B-site dilution by Ti (which does probably not participate to the conduction process). The conductivity is consequently lower than for $Y_{0.9}Zr_{0.1}MnO_3$ in the HT interval. In the same way, the fact that Ti-doped material retains its symmetrical *P*6$_3$/*mmc* space group up to the highest temperature makes the conductivity of $YMn_{0.6}Ti_{0.3}O_3$ higher in comparison with $YMnO_3$. Finally, and as proposed to the Zr-doped $YMnO_3$, the titanium manganite may exhibit a higher ionic conductivity contribution in comparison to the pure $YMnO_3$ but, despite our efforts to address this point, we couldn´t characterize the ionic transport in such materials yet. Such aspect has to be examined into more details in the future. In reducing atmosphere, there is no change of slope and the behavior is perfectly linear, what can be understood by the fact that there is not phase transition or structural anomaly

in the measurements under reducing atmosphere (the material's symmetry is *P*6$_3$*cm* in the whole temperature range) (Figure 111). In addition, we can observe that, in these conditions, the conductivity of $YMn_{0.6}Ti_{0.3}O_3$ strongly decreases with a value of σ=2 x10^{-4} S cm^{-1} at 750°C.

Figure 111. Arrhenius plot of the electrical conductivity for $YMn_{0.6}Ti_{0.3}O_3$ in air (closed symbols) and moist reducing atmosphere (open symbols).

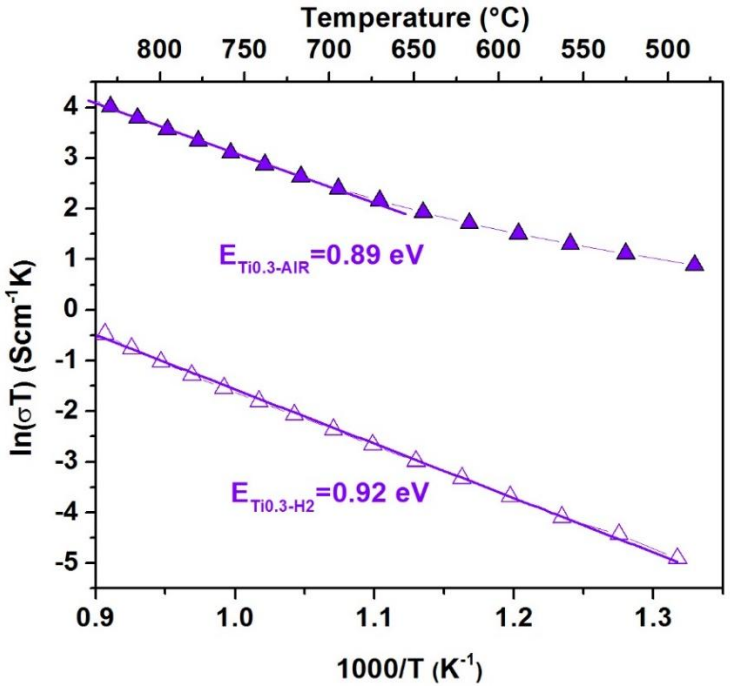

Such phenomenon is not surprising, taking into account that manganese oxides with p-type conductivity show generally much lower electronic conductivity in reducing than in oxidizing atmosphere; this is the case, for example, for $La_{0.4}Sr_{0.6}Ti_{0.6}Mn_{0.6}O_{3-\delta}$ that exhibits 22.6 S cm^{-1} in air and 1.5 S cm^{-1} in wet Ar/4% H_2 at 810°C [193]. Such kind of p-type conductivity is again expected for $YMn_{0.6}Ti_{0.3}O_3$, and would explain the lower conductivity level in reducing atmosphere. In addition, the fact that the activation energy value is very similar for the measurements in both oxidizing (HT

region) and reducing atmosphere (Table 24); seems to confirm that the material experience the same conductivity process in both atmospheres.

Table 24. Activation energy of the conductivity process of $YMn_{0.6}Ti_{0.3}O_3$ compound (air and diluted H_2)

Sample	Atmosphere	Activation energy		
		(eV)	(kJ/mol)	R^2
$YMn_{0.6}Ti_{0.3}O_3$	Air (HT)	0.869(2)	83.82(2)	0.9955
	3%H_2/Ar	0.925(1)	89.21(1)	0.9977

Nevertheless, such analysis is perhaps too fast: as described in the thermogravimetrical study of the previous chapter (Figure 106), in presence of diluted H_2, the $YMn_{0.6}Ti_{0.3}O_{3+\delta}$ totally loses the oxygen excess and Mn^{3+} is partially reduced to Mn^{2+} (going from $Y^{3+}Mn^{2+}_{0.1}Mn^{3+}_{0.5}Ti^{4+}_{0.3}O^{-2}_{2.95}$ to almost $Y^{3+}Mn^{2+}_{0.5}Mn^{3+}_{0.1}Ti^{4+}_{0.3}O^{-2}_{2.75}$ in the conductivity measurement range). It means that, at the difference to what happens in air, the nature of the small polaronic pair in reducing conditions must be indeed Mn^{2+}/Mn^{3+} instead of Mn^{3+}/Mn^{4+}. Additionally, the reduction of $YMn_{0.6}Ti_{0.3}O_3$ material entails an *a* cell parameter increase. It means the Mn-Mn bond distances are longer in reducing atmosphere in the doped manganite and it is reasonable to think that the carrier mobility is lower in these conditions, what is another explanation of the lower conductivity level in reducing conditions. The variation of conductivity between both atmospheres could be consequence of the difference in the nature of the charge carriers in this hexagonal structure. It is worth noting that, as described above, we expect titanium cations retain its +4 oxidation state in all conditions, in presence of more easily reducible Mn^{3+} cations; as a consequence, Ti^{4+} cations is not expected to influence the conductivity process of the material in anodic conditions. As a final point concerning

the conductivity study of Ti-doped manganite, and as discussed previously, the conductivity value itself does no determine the cell efficiency and one material with low conductivity could have a good electrochemical behavior using an adequate current collector. In this case, we also used this strategy to study the electrochemical response of the $YMn_{0.6}Ti_{0.3}O_3$, as will be discussed in the next section.

4.4 ELECTROCHEMICAL MEASUREMENTS

In this section, in a first step, the cathode behavior and identification of the mechanisms of oxygen reduction reaction using LSM/$YMn_{0.6}Ti_{0.3}O_3$/YSZ/$YMn_{0.6}Ti_{0.3}O_3$/LSM symmetrical cells are studied. In a second section, we carried out first measurements concerning the use of the same Ti-doped manganite in SOFC conditions.

4.4.1 Preliminary EIS measurements in air. The symmetric electrochemical cells used to study $YMn_{0.6}Ti_{0.3}O_3$ behavior as an SOFC cathode were built with 2 layers of LSM current collector (~10µm) and 4 layers of electrode (~20µm), since the variables were previously established for the $YMnO_3$ and Zr-doped compounds. Then, the samples were submitted to a sintering heat-treatment at different temperatures (from 1000 to 1400°C, every 100°C) and their impedance data were measured ($pO_2 \approx 0.20$ atm, T=500-800°C). The curves corresponding to log(ASR) as a function of temperature for the different sintering conditions, are depicted in Figure 112. We observe that in the interval from 1000 to 1300°C the resistance decreases when the sintering temperature increases. However, from 1400°C the resistance starts increasing again. Then, the temperature of 1300°C is considered as the optimal condition probably because, at this temperature, a good balance between porosity, grain size and connection between grain is obtained. It is interesting to notice that at low sintering temperatures there are two regimes, similar to what we observed in previous sections due to a change of the material oxygen stoichiometry

which affects the conductivity and the lattice parameters (Figure 112). Therefore, two apparent activation energies can be calculated up to 1200°C.

Figure 112. Arrhenius plot of ASR as a function of temperature in air ($pO_2 \approx 0.20$ atm) for symmetric cells including $YMn_{0.6}Ti_{0.3}O_3$ cathode for different sintering temperatures.

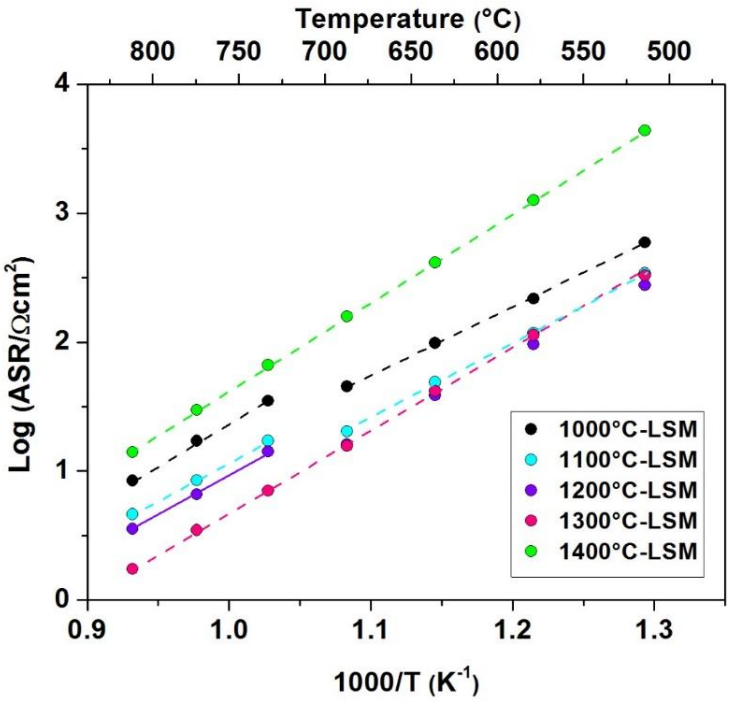

The values are summarized in Table 25. All values (in both ranges) are very similar, and it is possible to affirm that the limiting reaction mechanisms are probably the same; however, considering that the best choice is for a sintering temperature of 1300°C, such study will be examined and discussed into details later, using EIS measurements in different oxygen partial pressures. This will be the object of the next section.

A comparison of the Arrhenius plot of ASR vs temperature for each optimal cells studied in this work is given in Figure 113.

Table 25. ASR apparent activation energy of LSM/$YMnO_3$/YSZ/$YMnO_3$/LSM symmetric cells for the different sintering temperatures.

Sintering temperature (°C)	Activation energy (eV)	
1000	1.28 (2)	1.05 (1)
1100	1.18 (3)	1.15 (1)
1200	1.25 (2)	1.16 (1)
1300	1.25 (1)	-
1400	1.36 (1)	-

Figure 113. Arrhenius plot of ASR as a function of temperature for symmetrical cells containing $YMnO_3$, $Y_{0.9}Zr_{0.1}MnO_3$ and $YMn_{0.6}Ti_{0.3}O_3$ compound in its optimal sintering conditions.

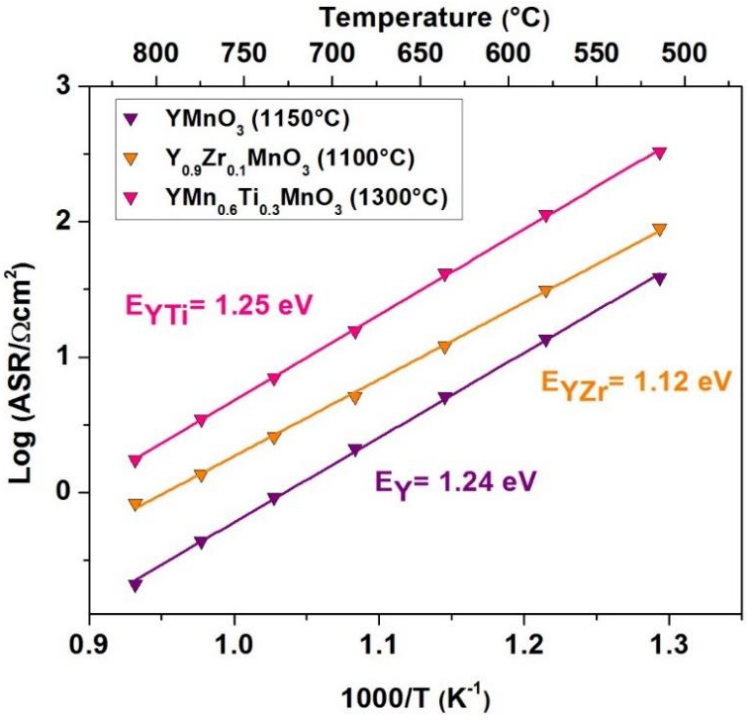

We can appreciate that the best performance is again for the $YMnO_3$-based cell as the cell with the Ti-doped $YMnO_3$ exhibits relatively poor performance. Nonetheless, all values for the new manganites are lower than the reported for the state of art cathode LSM (R_p>100 Ω cm^2 at 800°C) [47] and comparable with those of LSM/YSZ composites 60:40 and 40:60 (0.49 Ω cm^2 and 6.53 Ω cm^2 at 700°C, respectively) [224]. Hence, in principle this cathode are also promising from the electrochemical point of view. In addition, the evolution with temperature of the impedance data corresponding to the optimal cell (sintered at 1300°C) is exhibited in Figure 114. Impedance values were normalized considering the electrode area in a symmetric. The spectra present two well distinguished arcs in the whole temperature range.

Figure 114. Impedance spectra of LSM/$YMn_{0.6}Ti_{0.3}O_3$/YSZ/ $YMn_{0.6}Ti_{0.3}O_3$/LSM cell (sintered at 1300°C) measured in air at different temperatures.

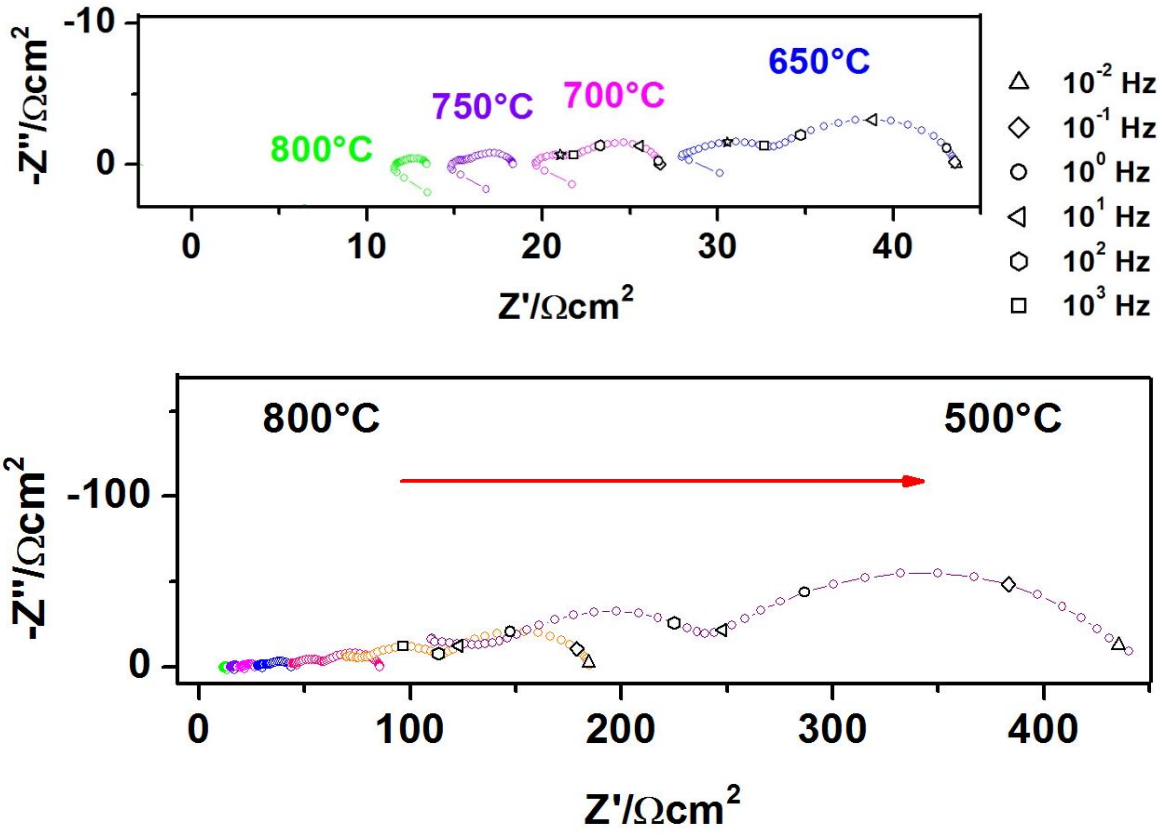

4.4.2 Study of EIS vs pO_2 at different temperatures. In order to determine the processes involved in the oxygen reduction reaction of this potential electrode, the optimized symmetrical cell was measured at different oxygen partial pressures ($10^{-4} \leq pO_2 \leq 1$ atm) and one constant temperature (T= 600, 700 or 800°C). Subsequently, all spectra were fitted with an equivalent circuits built from the analysis of impedance data and taking into account the shape of the spectra. Finally, each element was attributed to one physic process according to its dependance with pO_2, capacitance value and frequency range [44].

4.4.2.1 Identification of limiting steps in air for LSM/$YMn_{0.6}Ti_{0.3}O_3$/YSZ/$YMn_{0.6}Ti_{0.3}O_3$/LSM cell. First, the spectra in Nyquist representation of LSM/$YMn_{0.6}Ti_{0.3}O_3$/YSZ/$YMn_{0.6}Ti_{0.3}O_3$/LSM cell measured at **600°C** under different pO_2 are shown in Figure 115.

Figure 115. Electrochemical impedance spectra of LSM/$YMn_{0.6}Ti_{0.3}O_3$/YSZ/$YMn_{0.6}Ti_{0.3}O_3$/LSM at 600°C and different pO_2 values.

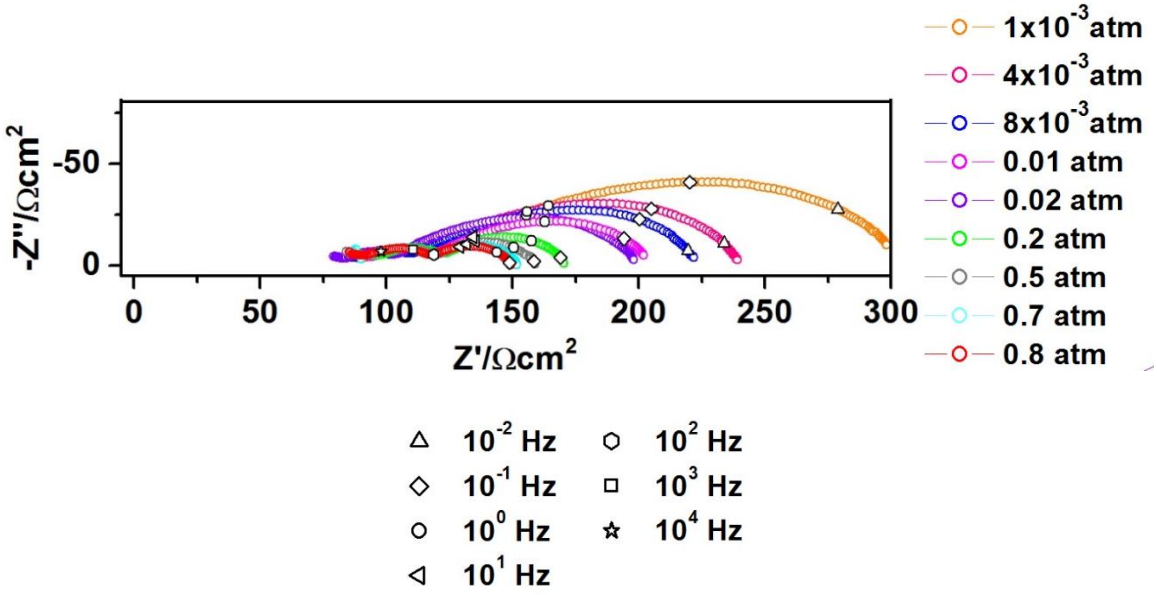

The impedance grows as pO_2 value decreases, as expected, and the spectra does not exhibit any substantial change in shape along the pO_2 range; as a consequence, all the spectra can be fitted using the same model. The curves in the Bode plot (Figure 116) show two maximum of relaxation frequency; therefore, it is possible to suppose there is mainly two limiting steps. However, the impedance response was better modeled in the entire pO_2 range with a more complex equivalent circuit consisting of (i) an inductive element (L_1) due to the inductance of the wires, (ii) a parallel combination of one resistance and one constant phase element (R/CPE_1), (iii) a Gerischer-type impedance (R_{G1}) and (iv) a second parallel combination of one resistance and one constant phase element (R/CPE_2). The detailed results of thosw fits can be observed in Annex J.

Figure 116. EIS spectra in Bode representation for LSM/$YMn_{0.6}Ti_{0.3}O_3$/YSZ/$YMn_{0.6}Ti_{0.3}O_3$/LSM cell at T=600°C for different pO_2 values.

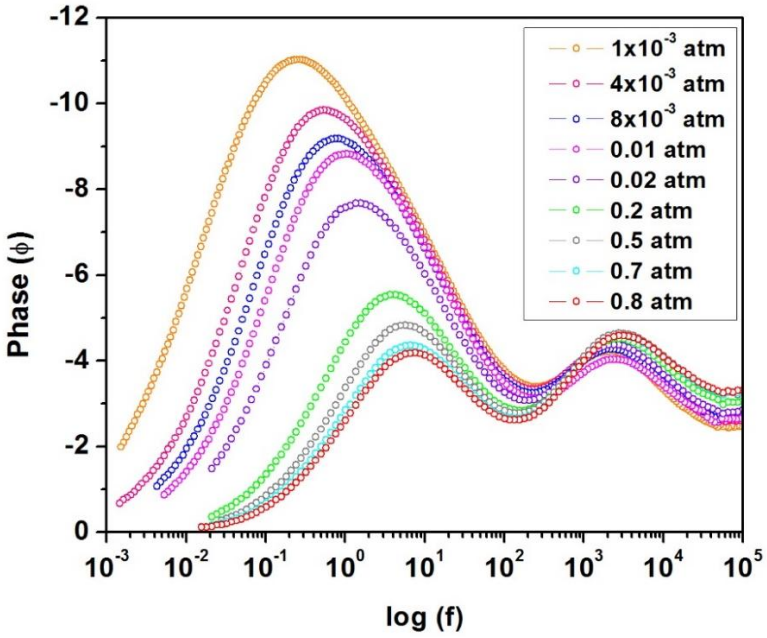

As an example, in Figure 117, we can be observe that the proposed model satisfactorily explains the spectrum shape at $pO_2 \approx 1x10^{-3}$ atm.

Figure 117. (a) Impedance spectrum adjustment of LSM/$YMn_{0.6}Ti_{0.3}O_3$/YSZ/$YMn_{0.6}Ti_{0.3}O_3$/LSM cell (T=600°C and $pO_2 \approx 1x10^{-3}$ atm) indicating three limiting contributions to the equivalent circuit, (b) Bode representation with the same deconvolution.

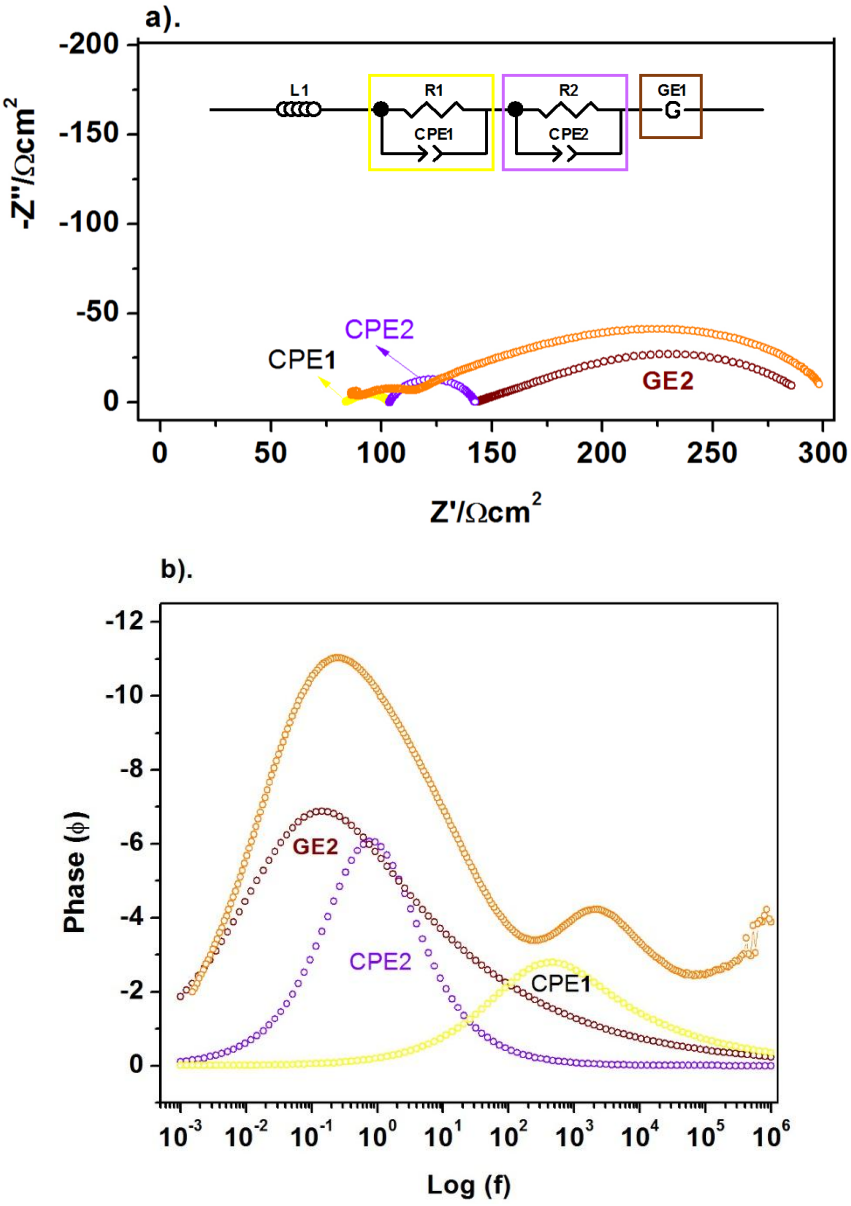

Also, it is important to highlighting that all contributions increase as the oxygen partial pressure (pO_2) decreases, but the Gerischer element (at the lowest frequency) is the most affected contribution. Then, using the results of the adjustments, a log-log plot of resistances vs pO_2 values can be obtained (Figure 118), with the aim of determining the nature of the limiting steps through the reaction order (γ) which is the calculated slope for each curve.

Figure 118. Dependence of the ASR of each limiting process versus oxygen partial pressure for LSM/$YMn_{0.6}Ti_{0.3}O_3$/YSZ/$YMn_{0.6}Ti_{0.3}O_3$/LSM cell at T=600°C. The reaction order (γ) of each step is also included.

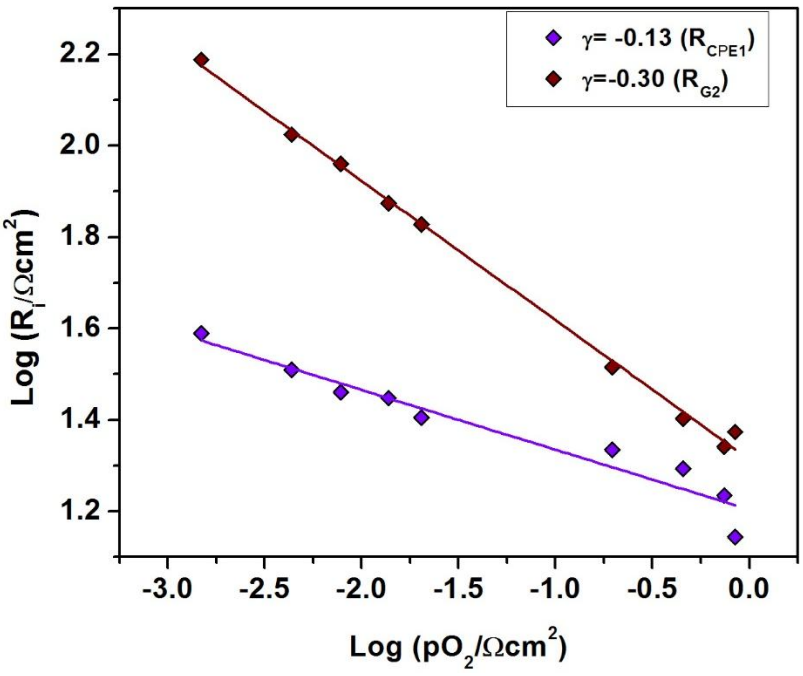

At 600°C, the contribution at highest frequencies was difficult to model and is only present at such low temperature. Therefore, the contribution can be attributed with greater certainty to the ionic intergranular resistances of the electrolyte, due to the fact that YSZ electrolyte exhibits low ionic conductivity values at T≤ 600°C. Given

that the YSZ conductivity increases with temperature, such contribution disappears at higher temperatures and, is not usually taken into account for analysis [47], [226].

The second contribution is a R/CPE and it shows a dependence of R α $pO_2^{-0.13}$ and capacitances of C~10^{-4}-10^{-5} F/cm^2. This very low dependence with pO_2 had been related previously to the electrolyte [44]; however, the fact that the process is also present at higher temperatures of measurements (as will be shown below) and the interval of capacitances suggest a double layer process maybe due to low interconnection which could affect the charge transfer [225]. The micrograph of the cell, in Figure 119, shows that the low interconnection between grains is the actual reason of the poor oxygen diffusion in this specific case.

Figure 119. SEM image of the electrode microstructure in LSM/$YMn_{0.6}Ti_{0.3}O_3$/YSZ/$YMn_{0.6}Ti_{0.3}O_3$/LSM symmetric cell sintered at T=1300°C.

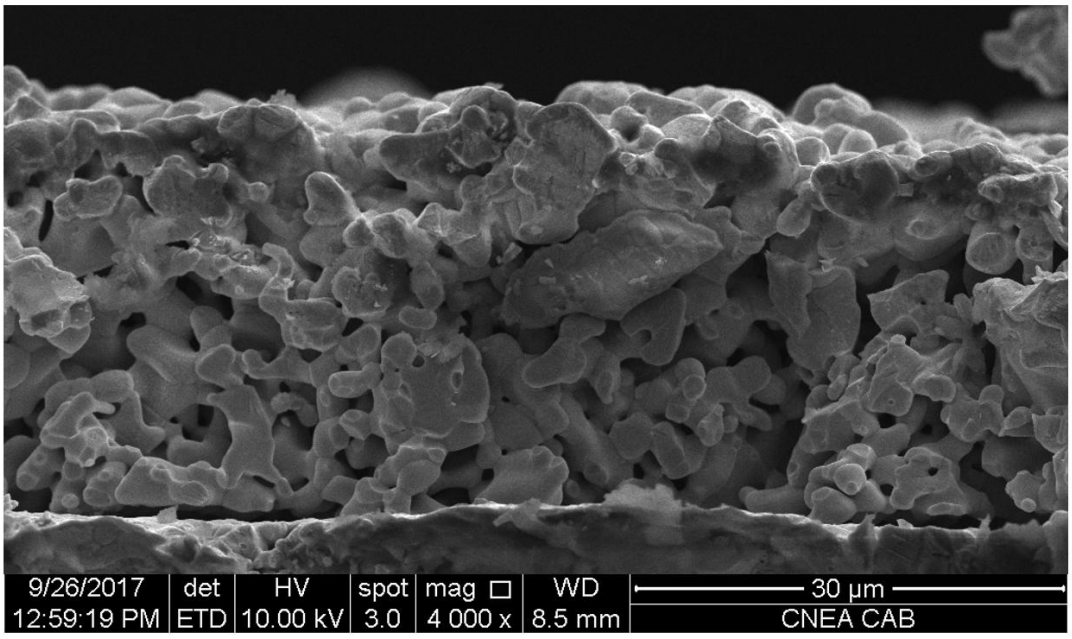

Finally, the third contribution is also a Gerischer impedance (R_{G2}) which presents a dependence of R α $pO_2^{-0.3}$ and capacitances of C~10^{-2}-10^{-3} F/cm^2. Such values are

associated to the co-limiting process between the oxygen exchange at the electrode/gas surface and the oxygen diffusion in the bulk probably because the grains are small and the entire electrode grain participates in the reaction, hence the penetration depth (*d*) approaching the size of the particles of the cathode [231], [232].

In the case of the measurements carried out at **700°C** ($10^{-4} \leq pO_2 \leq 1$ atm) on an LSM/$YMn_{0.6}Ti_{0.3}O_3$/YSZ/$YMn_{0.6}Ti_{0.3}O_3$/LSM cell, it is possible to observe lower resistance values in comparison with those measured at 600°C. However, these resistances also grow as pO_2 value decreases as shown in the Nyquist representation of Figure 120.

Figure 120. Electrochemical impedance spectra of LSM/$YMn_{0.6}Ti_{0.3}O_3$/YSZ/$YMn_{0.6}Ti_{0.3}O_3$/LSM cell at T=700°C for different pO_2 values.

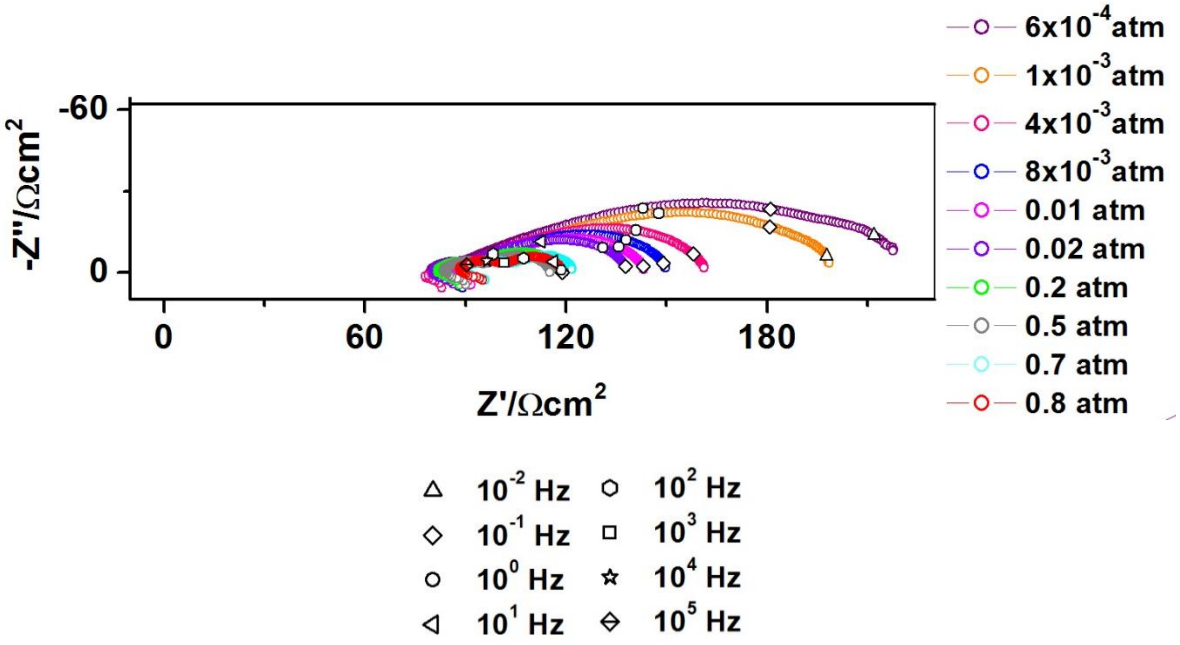

It is worth noting that the spectra change their shape with pO_2 value, since at low pO_2 values appear other impedance contribution. The Bode representation of EIS data (Figure 121) allows observing that at high pO_2 there is two maximum of relaxation frequency, but at lower oxygen partial pressures we clearly identify a new contributions.

Figure 121. EIS spectra in Bode representation for LSM/$YMn_{0.6}Ti_{0.3}O_3$/YSZ/$YMn_{0.6}Ti_{0.3}O_3$/LSM cell at T=800°C and differente pO_2.

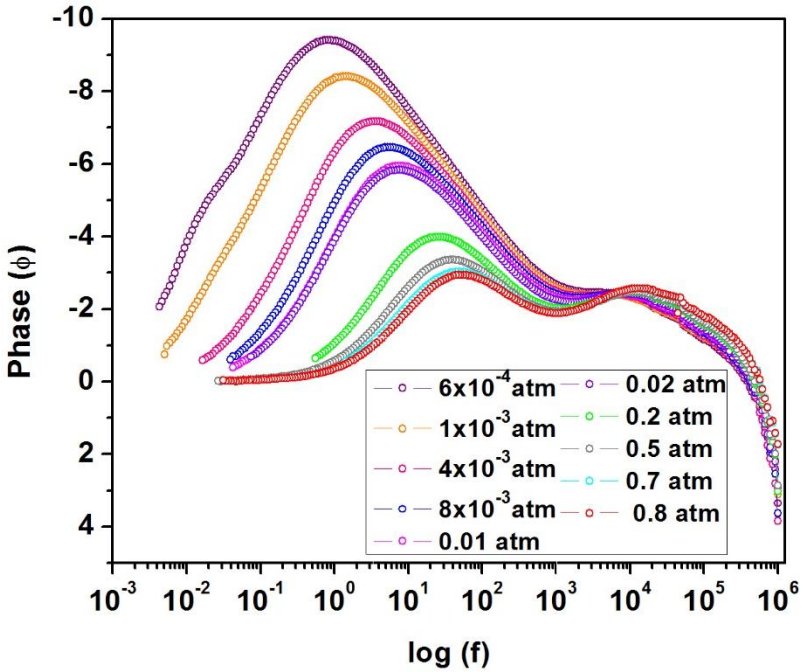

Therefore, the impedance response at 700°C has been modeled with two circuits depending on the pO_2 value. At high oxygen partial pressures the equivalent circuit includes (i) an inductIve element (L_1) due to the inductance of the wires, (ii) an ohmic resistance (R_1) that is mainly the electrolyte resistance, (iii) a parallel combination of one resistance and one constant phase element (R_2/CPE_1) and (iv) a Gerischer-type element (R_G). From a pO_2 of ~0.02 atm, the circuit is completed with another parallel

combination of one resistance and one constant phase element (R_3/CPE_2), to model an additional resistance at low frequency. The fit for the lowest pO_2 value is depicted in Figure 122 and the results for the entire pO_2 interval of measurements are in Annex K.

Figure 122. (a) Impedance spectrum adjustment of LSM/$YMn_{0.6}Ti_{0.3}O_3$/YSZ/$YMn_{0.6}Ti_{0.3}O_3$/LSM cell (T=700°C and $pO_2 \approx 6x10^{-4}$ atm) indicating the contributions of the equivalent circuit, (b) Bode representation with the same deconvolution.

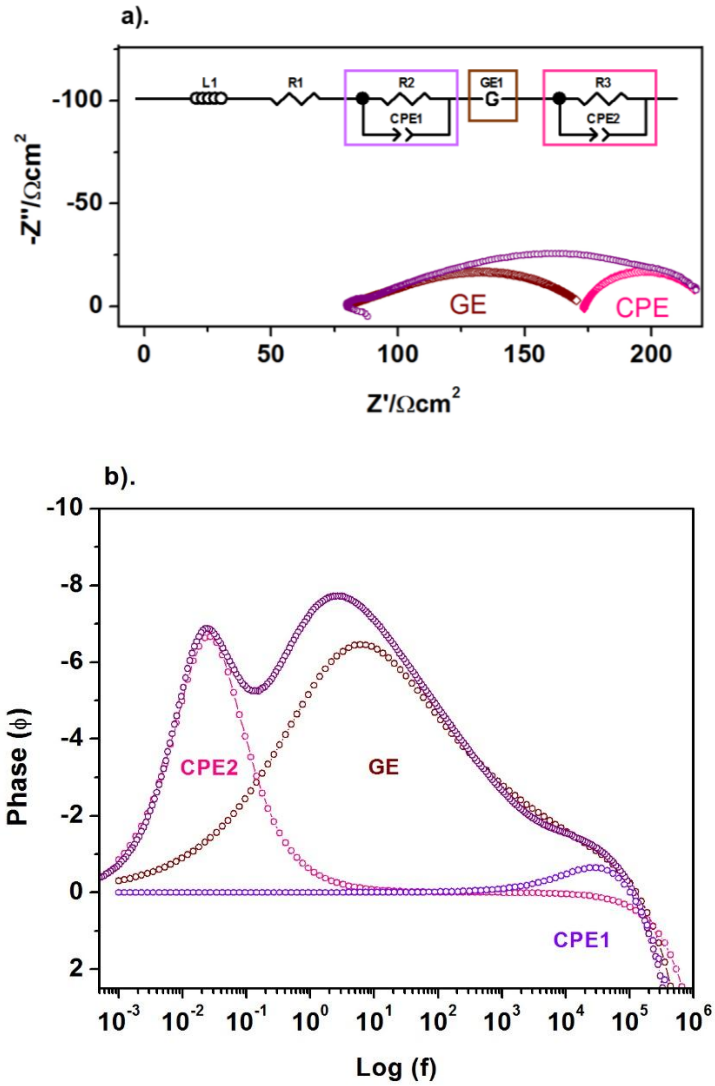

Using such representation, it can be seen that both elements (Gerischer and R_3/CPE_2) are relevant, although the Gerischer seems to be predominant.Using the results of the adjustments, a log-log plot of resistances vs pO_2 values can be obtained (Figure 123), in order to state the process present in these conditions.

Figure 123. Dependence of the ASR of each limiting process versus oxygen partial pressure for LSM/$YMn_{0.6}Ti_{0.3}O_3$/YSZ/$YMn_{0.6}Ti_{0.3}O_3$/LSM cell at T=700°C. The reaction order (γ) of each step is also included.

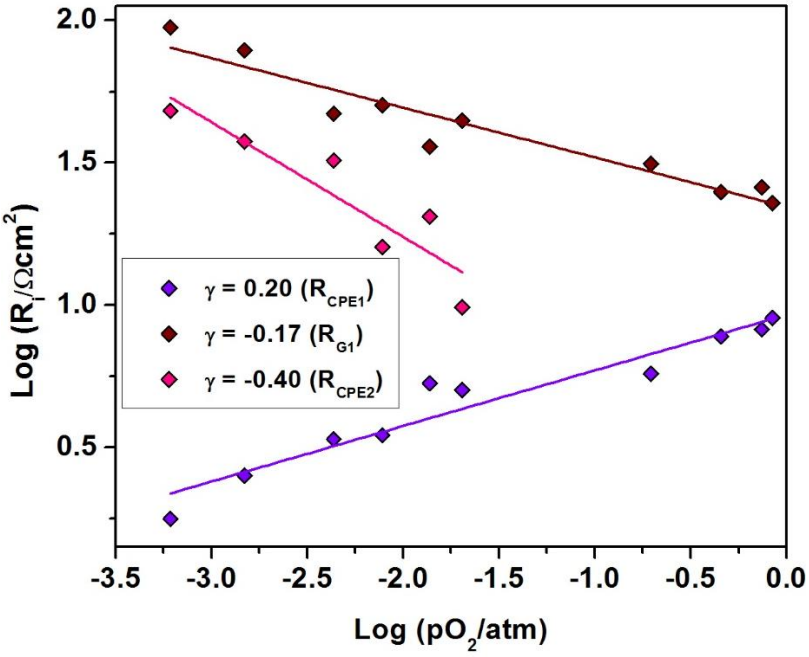

At 700°C, the limiting steps are similar to those found at 600°C. Nevertheless, the first impedance Gerischer element of highest frequencies dissapears maybe due to microstructure evolution with measurement temperature improving the interconnection between electrode grains. Thus, in this case, the highest frequency response is a R/CPE_1 element which exhibits a dependence of $R \alpha pO_2^{0.20}$ and capacitances of $C \sim 10^{-6}$-10^{-7} F/cm^2. Although the value of the dependence is higher

than in the low temperature, both γ and capacitances values are still associated with the same limiting process of ionic transfer at the electrode/electrolyte interface whereby it is inferred that the microstructural change is not pronounced [169], [225]. On the other hand, the second contribution is a Gerischer impedance element (R_G) with a dependence of R α $pO_2^{-0.17}$ and capacitances of C~10^{-3}-10^{-4} F/cm^2, which means that a co-limiting process between the oxygen exchange at the electrode/gas surface and the oxygen diffusion in the bulk is again present. However, the decrease of γ value suggests a higher contribution of oxygen exchange at the electrode/gas surface in accordance with the same grain evolution [44]. In addition, the lowest frequency impedance response, which appears from 700°C, corresponds to a R/CPE element which shows a dependence of R α $pO_2^{-0.40}$ and capacitances of C~10^{-1}-10^{-2} F/cm$^{2.}$. These values suggest a dissociative adsorption process due to possibly to the grain growth with temperature which decreases the superficial area exposed to oxygen molecules [47], [169].

Finally, the measurements were carried out at **800°C** ($10^{-4} \leq pO_2 \leq 1$ atm) using the same LSM/$YMn_{0.6}Ti_{0.3}O_3$/YSZ/$YMn_{0.6}Ti_{0.3}O_3$/LSM cell. In these conditions, the lowest resistance values of the three experiments are obtained and, as in the case of the other two temperatures, the resistance grows as pO_2 value decreases. In Figure 124, the Nyquist representation of the EIS data is shown. Here, it can be appreciated that the spectra's shape is changing with the oxygen partial pressure.

Figure 124. Electrochemical impedance spectra of LSM/$YMn_{0.6}Ti_{0.3}O_3$/YSZ/$YMn_{0.6}Ti_{0.3}O_3$/LSM at T=800°C and different pO_2 values.

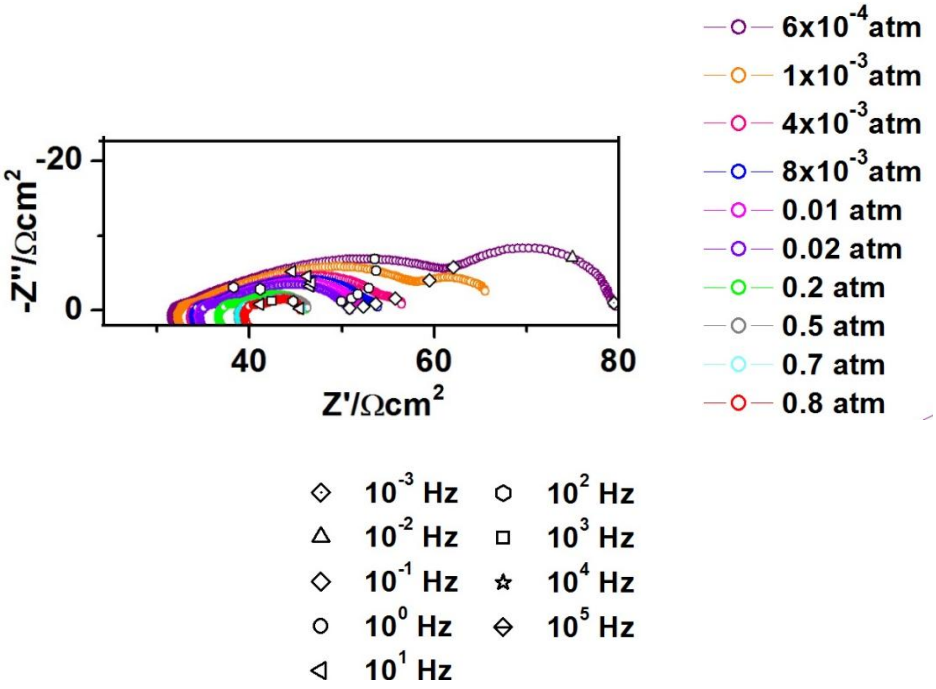

The Bode representation of EIS data (Figure 125) allows observing that at high pO_2 there is only two maximum of relaxation frequency, but at lower oxygen partial pressures we clearly identify an additional contribution. Therefore, the impedance response at 800°C has been modeled with two circuits depending on the pO_2 value. At high oxygen partial pressures the equivalent circuit includes (i) an inductive element (L_1) due to the inductance of the wires, (ii) an ohmic resistance (R_1) that is the electrolyte resistance, (iii) a parallel combination of one resistance and one constant phase element (R/CPE) and (iv) a Gerischer-type element (R_G). From a pO_2 of ~0.2 atm, the circuit is completed with other (v) parallel combination of one resistance and one constant phase element (R/CPE), to model an additional resistance at low frequencies.

Figure 125. EIS spectra in Bode representation for LSM/$YMn_{0.6}Ti_{0.3}O_3$/YSZ/$YMn_{0.6}Ti_{0.3}O_3$/LSM cell at T=800°C and different pO_2.

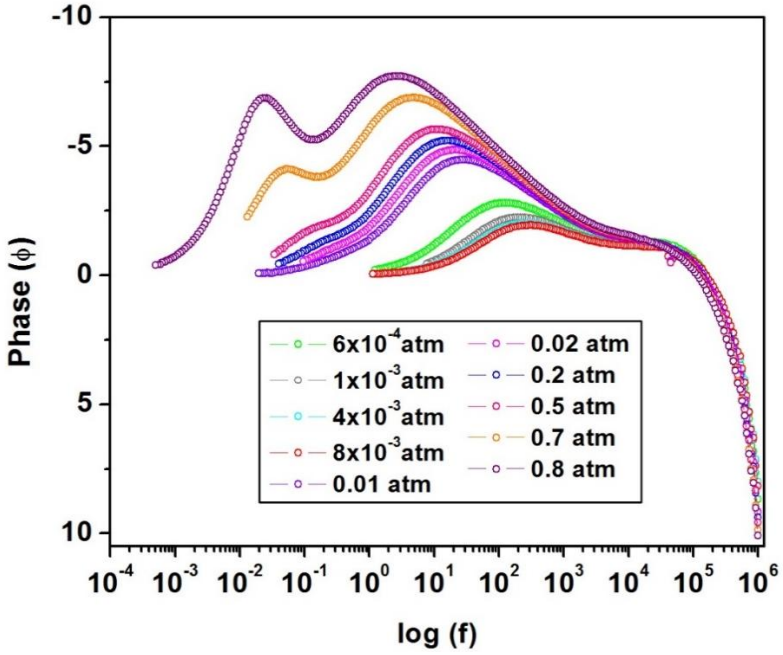

This model seems to explain very well the shape of every spectrum as the example shown in Figure 126. The results of these adjustments can be found in Annex L.

Figure 126. (a) Impedance spectrum adjustment of LSM/$YMn_{0.6}Ti_{0.3}O_3$/YSZ/$YMn_{0.6}Ti_{0.3}O_3$/LSM cell (T=800°C and $pO_2 \approx 6x10^{-4}$ atm) indicating the contributions of the equivalent circuit, (b) Bode representation with the same deconvolution.

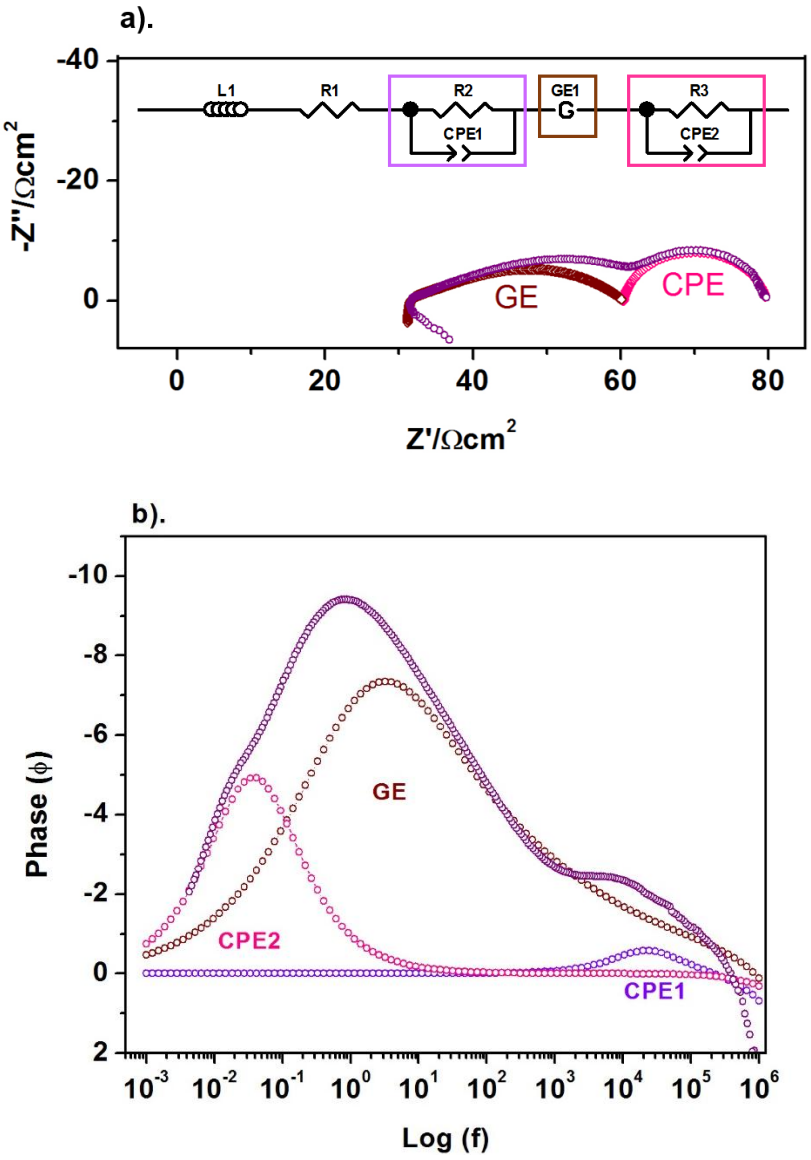

The results of all the adjustments are shown in a log-log plot of resistances vs pO_2 (Figure 127), in order to establish the process carried out in these conditions.

Figure 127. Dependence of the ASR of each limiting process versus oxygen partial pressure for LSM/$YMn_{0.6}Ti_{0.3}O_3$/YSZ/$YMn_{0.6}Ti_{0.3}O_3$/LSM cell at T=800°C. The reaction order (γ) of each step is also included.

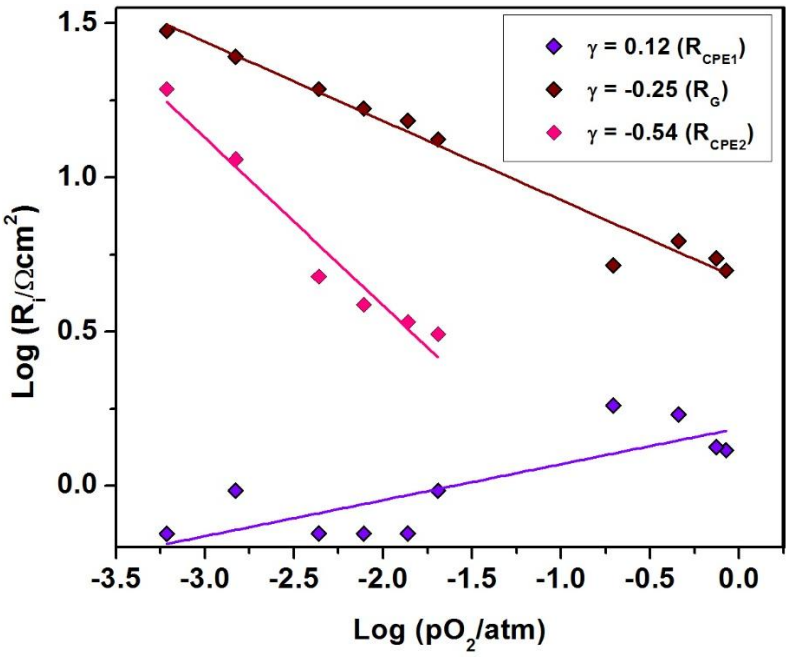

At 800°C, the limiting steps are the same as to those found at 700°C. In first place, we can found a R/CPE contribution which shows a dependence R α $pO_2^{0.12}$ and capacitances of C~10^{-6} -10^{-12} F/cm^2. As can be observed, the value of dependence of this contribution fluctuates in the three temperatures given the difficulty to fit it accurately; however, it can still be related to the ionic transfer at the interface process of the cell [225]. Similarly behavior happens with Gerischer impedance element (R_G) that, at this temperature, presents a dependence of R α $pO_2^{-0.25}$ and capacitances of C~10^{-2} -10^{-4} F/cm^2. This γ value is characteristic of the combined process between the oxygen exchange at the electrode/gas surface and the oxygen diffusion in the bulk. Additionally, a second R/CPE contribution presents a dependence R α $pO_2^{-0.54}$ and capacitances values are C~10^{-3}-10^{-1} F/cm^2. The capacitances and the γ value slightly higher than -0.5 could indicate that this limiting step is also a dissociative

adsorption process but maybe combined with gas phase difusion [65], [225]. This is not surprising because usually higher temperatures hinder the gas diffusion due to activation energy of dissociative adsorption element (higher than the gas phase diffusion process at lower temperatures) decreases and becoming comparable to that of gas phase diffusion at 800°C.

Finally, an Arrhenius graph was built with the resistances calculated for each impedance element at the different measured temperatures (Figure 128) and differentiating the contributions of the electrochemical processes: the ionic transfer at the electrode/TPB (R/CPE_1), the co-limiting step between oxygen exchange at the electrode/gas surface and the oxygen diffusion in the bulk (Gerischer) and the combination of gas phase diffusion and dissociative adsorption (R/CPE_2),

Figure 128. Activation energy of impedance elements identified in LSM/$YMn_{0.6}Ti_{0.3}O_3$/YSZ/$YMn_{0.6}Ti_{0.3}O_3$/LSM cell. The ASR values are those measured at $pO_2 \approx 6x10^{-4}$ atm and at T=600, 700 and 800°C.

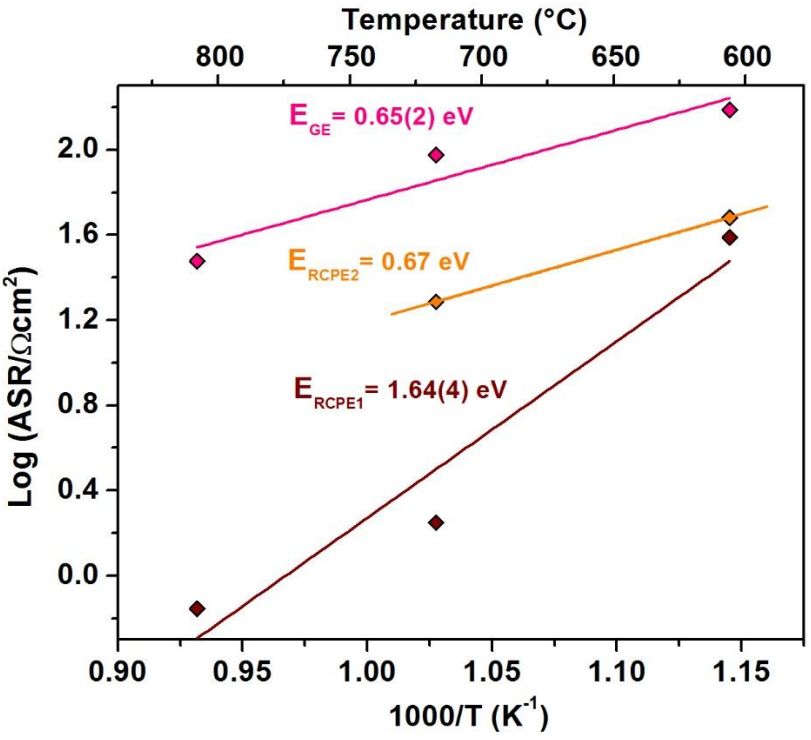

In this case, we can observe that the R/CPE_2 element and the Gerischer impedance show intermediate activation energy values while the R/CPE_1 process exhibits a high value. Now, given that the R/CPE_2 and the Gerischer elements are also present in the case of $Y_{1-x}Zr_xMnO_3$, it is possible to compare the activation energy values. Then, for the Ti-doped material, the oxygen diffusion in the bulk seems to predominate through process described by the Gerischer element, as happens for $Y_{0.9}Zr_{0.1}MnO_3$ electrode, maybe due to the higher ionic conductivity predicted for both compounds. Therefore, a similar activation energies are observed for $Y_{0.9}Zr_{0.1}MnO_3$ and $YMn_{0.6}Ti_{0.3}O_3$. On the other hand, a very high porosity observed for $YMn_{0.6}Ti_{0.3}O_3$ could indicates a low influence of gas phase diffusion, however, the result discussed previosly show that dissociative adsorpion and gas phase diffusion seem to be comparable in this material, explaining also the intermediate activation energy value in comparison with the other two materials which have one predominant contribution for this mixed process. Finally, it is not surprising the very high activation energy necessary to carry out the ionic/charge transfer because the discussed problem of grain interconnection.

4.4.3 Preliminary study $YMn_{0.6}Ti_{0.3}O_3$ performance in SOFC anodic conditions. With the aim to analyze the aptitude of the Ti-doped manganite for the hydrogen oxidation reaction, the symmetrical LBM/$YMn_{0.6}Ti_{0.3}O_3$/YSZ/$YMn_{0.6}Ti_{0.3}O_3$/LBM cell was built with 4 layers of electrode (~20 µm), 2 layers of the LBM ($La_{0.8}Ba_{0.2}MnO_3$) current collector (~10 µm) which contrary to LSM is stable in reducing atmosphere [184] and a dense YSZ electrolyte, sintered at 1300°C. Subsequently, the cell was exposed to a dry 10%H_2/Ar mixture in the 500-800°C temperature range. In a second step, the hydrogen percentage in the reducing atmosphere was varied (10, 20, 50 and 80%H_2/Ar, dry) while the temperature remains constant at 800°C, with the aim to determine the limiting phenomena.

4.4.3.1 Identification of the limiting steps for hydrogen oxidation of LBM/$YMn_{0.6}Ti_{0.3}O_3$/YSZ/$YMn_{0.6}Ti_{0.3}O_3$/LBM cell. The impedance data of the cell were first measured in the temperature range of T=500-800°C and for a gas mixture of 10%H_2/Ar. The curve corresponding to ASR as a function of temperature in Arrhenius representation is depicted in Figure 129.

Figure 129. Arrhenius plot of ASR as a function of temperature for LBM/$YMn_{0.6}Ti_{0.3}O_3$/YSZ/$YMn_{0.6}Ti_{0.3}O_3$/LBM symmetrical cells (10%H_2/Ar, dry) compared to LSM/$YMn_{0.6}Ti_{0.3}O_3$/YSZ/$YMn_{0.6}Ti_{0.3}O_3$/LSM cell measured in air.

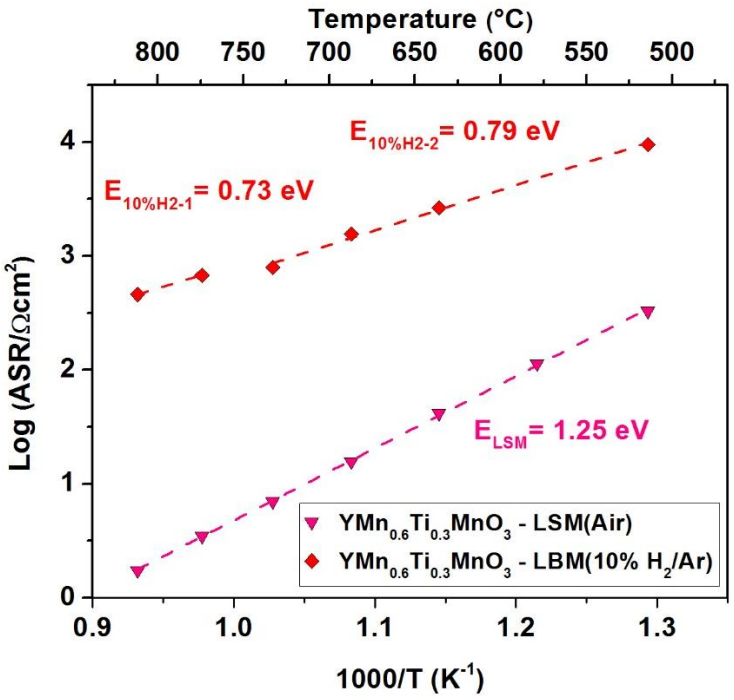

First, we can observe that the resistances almost duplicate their values in reducing atmosphere in comparison with the cell measured in air. As a first explanation could be the lower electrical conductivity of $YMn_{0.6}Ti_{0.3}MnO_3$ in reducing conditions; however, as can be seen in Table 26 the conductivity seems not to be the only decisive variable; indeed, in the case of LSCM symmetrical electrode, the ASR

values are comparable in both air and H_2 atmosphere, even when the electrical conductivity is 10 times lower in anodic environment for this material [19].

Table 26. Conductivity and polarization resistance data in air and hydrogen for the symmetrical electrode materials.

System	T/°C	σ^{air} (S cm^{-1})	σ^{H_2} (S cm^{-1})[a]	Electrolyte	R_p^{air} (Ω cm^2)	$R_p^{H_2}$ (Ω cm^2)
LSCM	900	38	3	YSZ	0.35	0.20
LSCM-YSZ	900	—	—	YSZ	0.29	0.59
LSCM-YSZ	950–850	—	—	YSZ	0.09–0.27	0.18–0.34[c]
$La_{0.75}Sr_{0.25}Cr_{0.5}Al_{0.5}O_{3-\delta}$	950–800	—	—	LSGM	0.18–1.2	0.3–0.45[d]
$La_{0.75}Sr_{0.25}Cr_{0.5}Mn_{0.3}Ni_{0.2}O_{3-\delta}$	800	20	0.5	YSZ	1.6	1
$LaCrO_{3-\delta}$	800	0.96	0.26	—	—	—
$La_{0.7}Ca_{0.3}CrO_{3-\delta}$	800	50.1	1.6	—	—	—
$La_{0.7}Ca_{0.3}Cr_{0.97}O_{3-\delta}$:YSZ (1 : 1)	850	62	3.6	YSZ	0.16	~2
$La_{0.7}Ca_{0.3}CrO_{3-\delta}$:CGO20 (1 : 1)	850	18.6	~1.9	LSGM	—	—
$La_{0.7}Ca_{0.3}Cr_{0.5}Mn_{0.5}O_{3-\delta}$	800	29.9	—	YSZ	0.25	1.4[e]
$Pr_{0.7}Ca_{0.3}Cr_{1-x}Mn_xO_{3-\delta}$	950–800	10	1–0.7	YSZ	0.7–4.0	5–40
$La_{1/3}Sr_{2/3}(Ti_{1-x}Fe_x)O_{3\pm\delta}$	950	0.9	0.1	YSZ	0.6	3
$Sr_2Fe_{1.5}Mo_{0.5}O_{6-\delta}$	780	550	310	LSGM	0.24	0.27
Pt-YSZ	950	—	—	YSZ	0.20	~60[d]
Pt-(YSZ-CeO_2) (1 : 1)	950	—	—	YSZ	0.05	0.45[d]
$La_{0.8}Sr_{0.2}Sc_{0.2}Mn_{0.8}O_3$	850	45	6	ScSZ	6.5[b]	0.35[f]

[19]

Nevertheless, in the case of the symmetrical cells studied here, the electrical conductivity of the current collector used is also different, because LSM and LBM show a conductivity of ~200-300 Scm^{-1} (air) [218], [247] but only 0.06-33 Scm^{-1} from 500 to 800°C in reducing atmosphere [184], respectively. Then, it is possible to infer that this variable could have affected the performance, although the current collector does not influence the electrode behavior in itself but make the whole electrode cannot operate entirely. On the other hand, in the same Figure 128, we can appreciate that the hydrogen oxidation reaction is easier than the oxygen reduction reaction since the activation energy is lower for the cell measured in reducing atmosphere. Additionally, it is worth noting that all the ASR value are relatively high in comparison with other electrodes for SSOFC.

The evolution with temperature of the impedance data corresponding to the LBM/$YMn_{0.6}Ti_{0.3}O_3$/YSZ/$YMn_{0.6}Ti_{0.3}O_3$/LBM cell at different temperatures and dry 10%H_2/Ar are exhibited in Figure 130.

Figure 130. Electrochemical impedance spectra of LBM/$YMn_{0.6}Ti_{0.3}O_3$/YSZ/$YMn_{0.6}Ti_{0.3}O_3$/LBM at different temperatures and dry 10%H_2/Ar (a) Nyquist representation and (b) Bode plot.

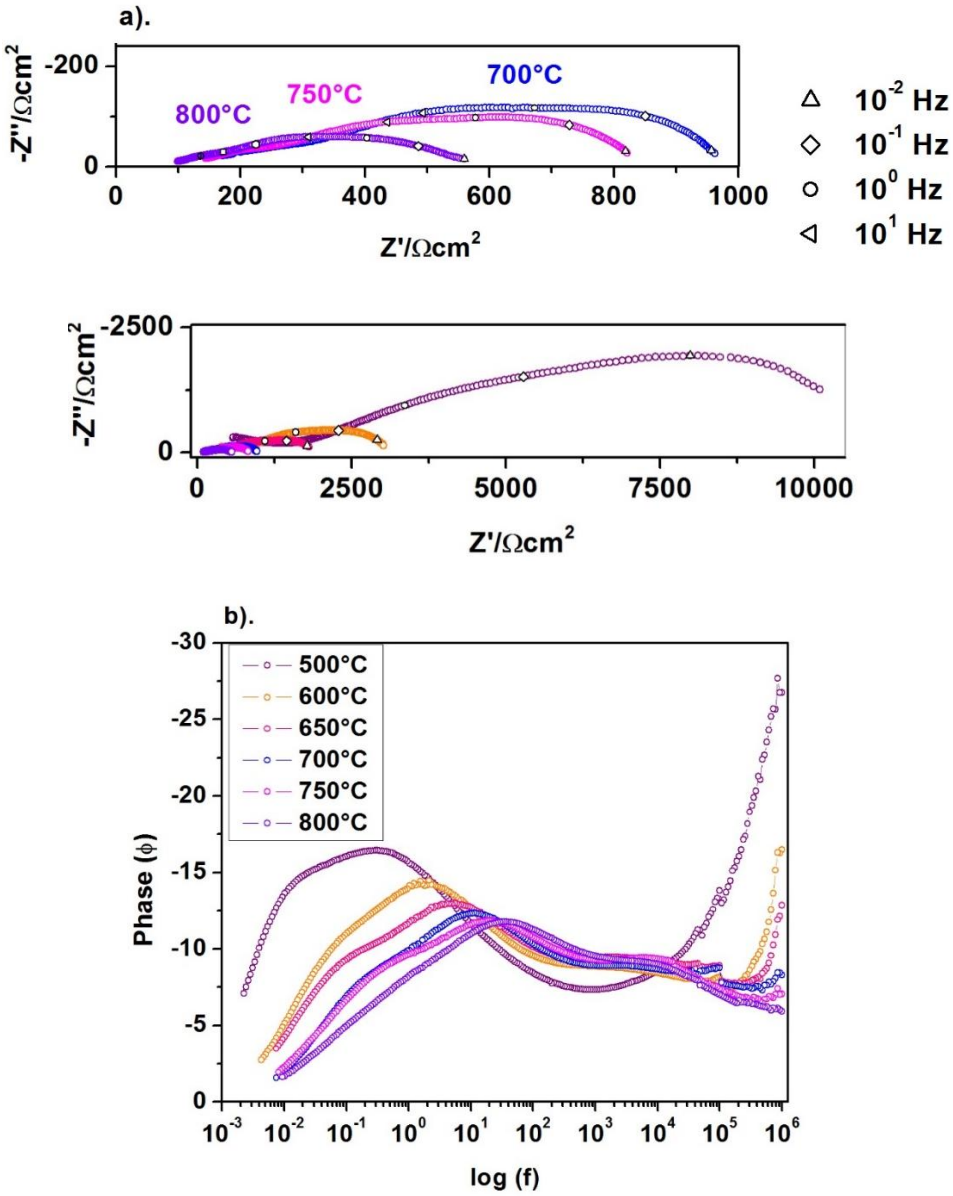

In this Figure, we can see that it is difficult to distinguish arcs or contributions in the Nyquist representation (Figure 130(a)), but based on Bode plot, two (or maybe three) contributions can be two or three contributions can be detected. In this sense, the

impedance response has been satisfactorily modeled with one equivalent circuit consisting of (i) an inductive element (L_1) due to the inductance of the wires, (ii) an ohmic resistance (R_1) that corresponds to the electrolyte resistance, (iii) a Gerischer-type impedance (R_G), (iv) a parallel combination of one resistance and one constant phase element (R/CPE) and finally (v) another parallel combination of one resistance and one constant phase element (R/CPE). As can be observed in Figure 131, all these contributions are thermally activated and exhibit relatively low activation energies.

Figure 131. The Arrhenius plot of ASR vs temperature of each impedance contribution for LBM/$YMn_{0.6}Ti_{0.3}O_3$/YSZ/$YMn_{0.6}Ti_{0.3}O_3$/LBM symmetrical cell measured in 10%H_2/Ar.

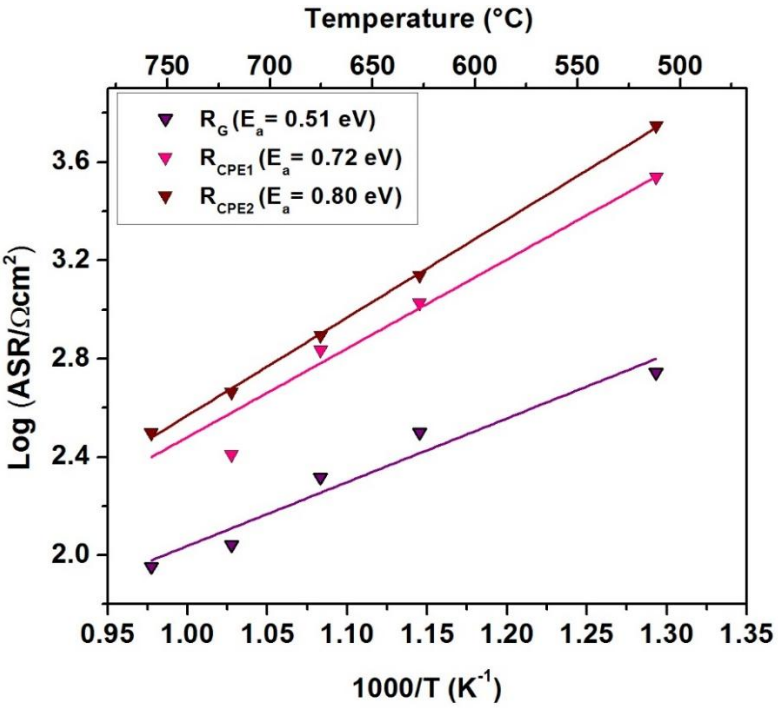

A second experiment under reducing atmosphere was carried out. In this case, the hydrogen content was varied in the Ar mixture (1, 10, 20, 50 and 80%) at constant temperature of 800°C. The results of these measurements are shown in Figure 132.

Figure 132. Dependence of the total ASR with pH_2 for LBM/$YMn_{0.6}Ti_{0.3}O_3$/YSZ/$YMn_{0.6}Ti_{0.3}O_3$/LBM symmetrical cell at T=800°C

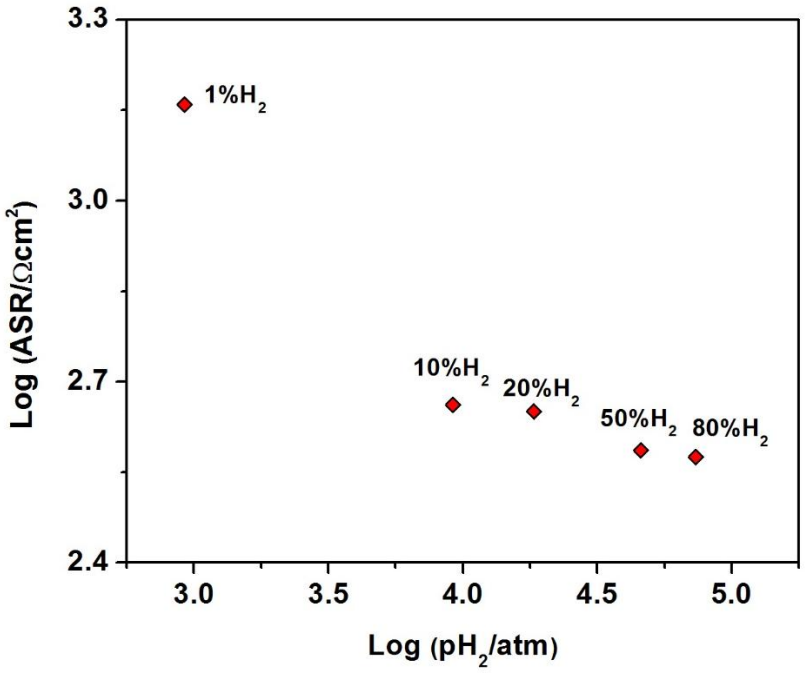

The specific the resistance decrease as the pH_2 value increases in a logarithmic way (Figure 133).

Figure 133. Electrochemical impedance spectra of LBM/$YMn_{0.6}Ti_{0.3}O_3$/YSZ/$YMn_{0.6}Ti_{0.3}O_3$/LBM cell for different H_2 contents (T=800°C)

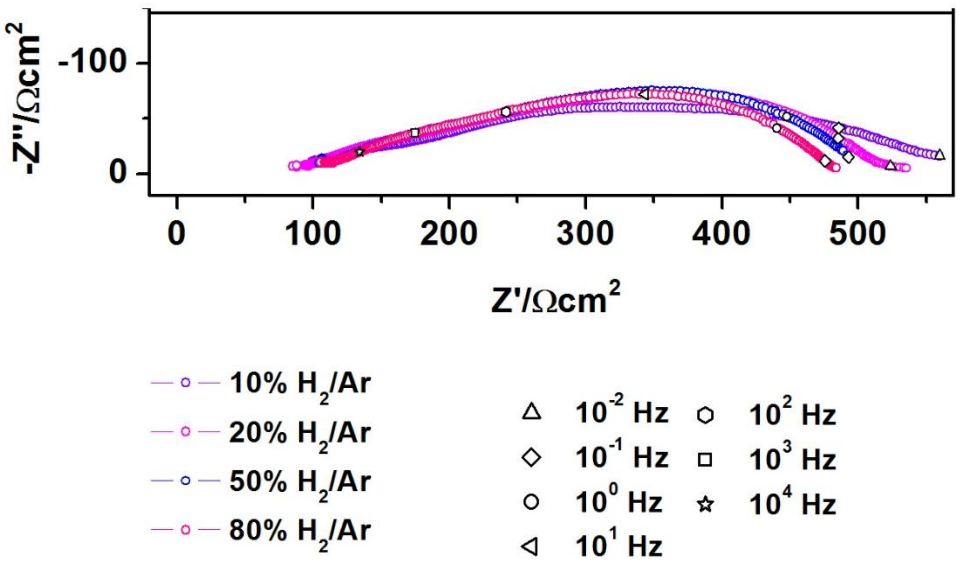

However, the model previously proposed seems to explain the entire experimental data, as can be seen in Figure 134 for 50%H_2/Ar mixture; hence, all the spectra were well adjusted with the same equivalent circuit (Annex M).

Figure 134. (a) Impedance spectrum adjustment for LBM/$YMn_{0.6}Ti_{0.3}O_3$/YSZ/$YMn_{0.6}Ti_{0.3}O_3$/LBM cell measured at T=800°C and for 50%H_2/Ar mixture indicating the contributions of the equivalent circuit, (b) Bode representation with the same deconvolution.

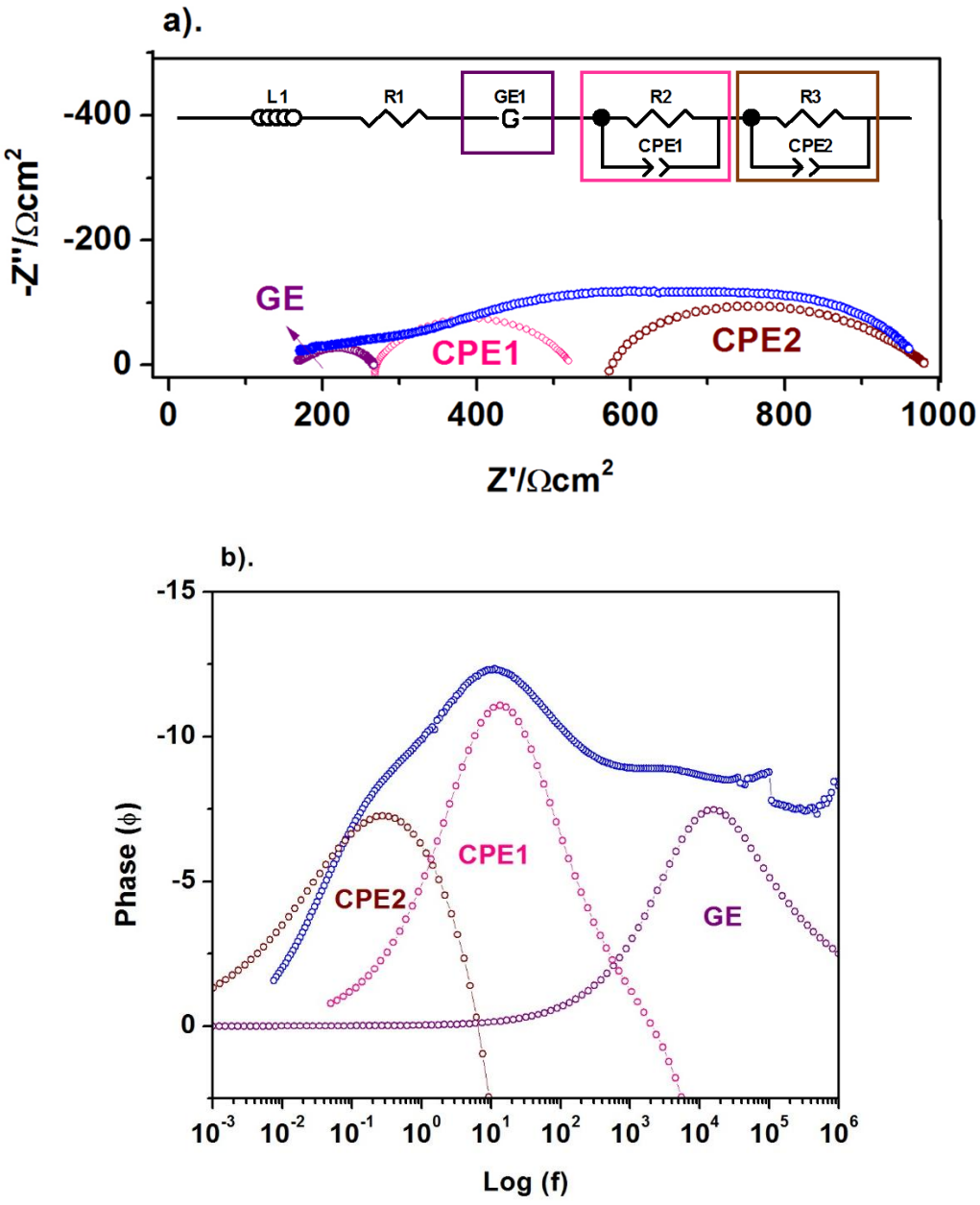

The results of the all these adjustments are shown in a log-log plot of resistances vs pH_2 in Figure 135, in order to propose the origin of the limiting processes in these SOFC anode conditions.

Figure 135. Dependence of the ASR of each limiting process versus hydrogen partial pressure for LBM/$YMn_{0.6}Ti_{0.3}O_3$/YSZ/$YMn_{0.6}Ti_{0.3}O_3$/LBM cell at T=800°C. The reaction order (γ) of each step is also included.

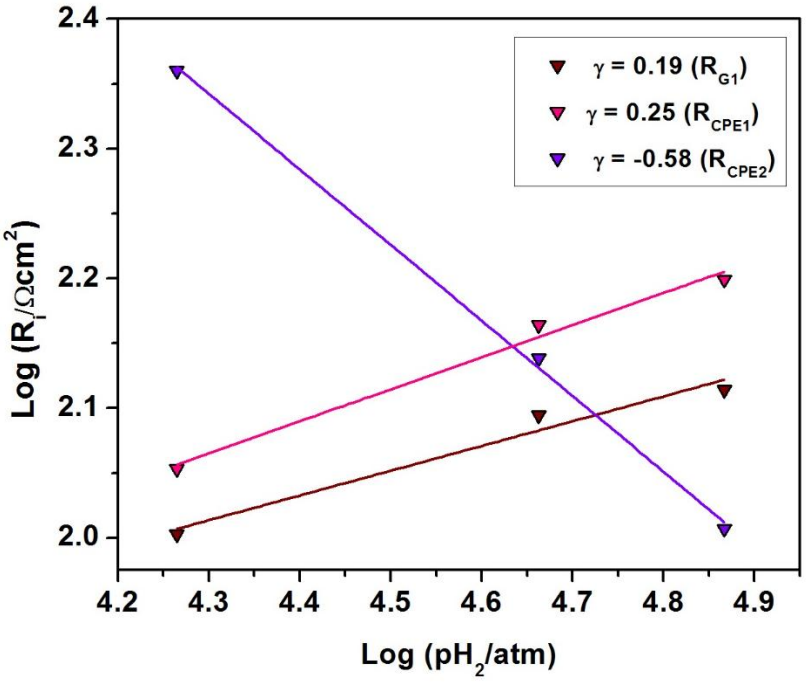

Specifically, at high frequency the impedance is modeled with a Gerischer element. A similar contribution has been observed for other anodes exhibiting poor electronic conductivity, what is the case for $YMn_{0.6}Ti_{0.3}O_3$ (see before), and in some occasions when oxygen exchange/diffusion compete [248]. In addition, an R/CPE_1 element with capacitances of $C \sim 10^{-2}$ F/cm^2 is also contributing to ASR, which could be related to a hydrogen surface diffusion process due to the weak grain connection, as previously discussed [249]. Finally, we identify an additional R/CPE_2 impedance but

with lower capacitances C~10^{-3} F/cm^2. Such limiting step can be related to the adsorption/dissociation of hydrogen. This is not surprising taking into account the intrinsically low catalytic activity of the mixed conductors [248] and is in agreement to the low calculated activation energy value [62].

Conclusions of the chapter

$YMn_xTi_yO_{3+\delta}$ series has been designed and prepared with the objective to use those materials as electrode in symmetrical SOFC, *i.e.* the same electrode material on both side of the cell, what means a double function (and list of requirements) of SOFC aode and cathode. While retaining the good properties of $YMnO_3$ including the chemical compatibility with YSZ electrolyte and electrochemical behavior as a cathode, the presence of sufficient amount of Ti in place of Mn, completely stabilizes the hexagonal structure in a reducing environment, opening the possibility to use the Ti-doped series as and anode. However, the modest results obtained in anode conditions underline the importance of paying special attention to cell fabrication in order to limit the grain coarsening during cell elaboration or operation that decreases the electrochemical active surface area, especially true for those compounds that require higher synthesis temperature.

CONCLUSIONS

Monophasic compounds of stoichiometries $Y_{1-x}Zr_xMnO_3$ ($x \approx 0.1$) and $YMn_xTi_yO_3$ ($x=0.1, 0.2, 0.3$; $x+y=0.85, 0.9, 0.95$) were successfully synthesized in air by solid-state reaction and/or Pechini method. Both doping strategies promote the formation of a phase transition from $P6_3cm$ to more symmetrical $P6_3/mmc$ lamellar hexagonal structure and seem also to improve the absorption kinetic behavior of the pure $YMnO_3$ compound, since a higher and faster oxygen storage is obtained for substituted materials, especially in the case of Zr doping.

$YMnO_3$ and $Y_{0.9}Zr_{0.1}MnO_3$ materials are completely stable in air but only for T<700°C in reducing atmosphere, what precludes their use as anode. However, even a minimal amount of Ti-substitution in $YMnO_3$ matrix inhibits the decomposition of the oxide, as Ti^{4+} cation more easily retains its oxidation state in anodic environment. Specifically, $YMn_{0.6}Ti_{0.3}O_3$ composition demonstrates stability up to 800°C in wet reducing atmosphere enabling to consider its application as electrode for Symmetrical Solid Oxide Fuel Cells (SSOFC).

All the studied compounds are chemically compatible with YSZ electrolyte because they do not react or decompose when they are in contact with this fluorite oxide. A slight cationic diffusion between electrode/electrolyte can be detected, but this is not judged prejudicial at all for the application. In addition, $YMnO_3$ exhibits a coefficient of thermal expansion (TEC) similar to the YSZ electrolyte, for that reason both material can be considered as thermo-mechanically, compatible too. On their side, $Y_{0.9}Zr_{0.1}MnO_3$ and $YMn_{0.6}Ti_{0.3}O_3$ show slightly higher/lower TEC values than the electrolyte material depending on the temperature range. Nevertheless, these differences seem not to have brought any particular problem of electrode delamination and if such issue would be detected in the future, the TEC mismatch could be easily mitigated by the elaboration of a composite electrode with the same electrolyte material. This is indeed one of the major interests of the materials we have developed in this work. To our knowledge, this is the first time those materials are considered for an application as SOFC electrode and, in this sense, our results

demonstrate that their use could probably avoid one of the major issues of high temperature fuel cells, *i.e.* the chemical reactivity at the electrode-electrolyte interphase.

On the electrical point of view, the small polaron process in which Mn^{3+}/Mn^{4+} (respectively Mn^{2+}/Mn^{3+}) pairs are participating to the charge transport, can explain the conductivity behavior for all the studied compounds in cathodic (resp. anodic) conditions. On the other hand, the Zr or Ti- doping strategy seems to induce a favorable increase of the ionic conductivity in the series. In this way, our analysis conducted to the fact that $Y_{0.9}Zr_{0.1}MnO_3$ material exhibits a higher electrical conductivity compared to pure $YMnO_3$ due to it is a higher contribution of ionic conductivity, related to its intrinsic stoichiometry $Y_{0.9}Zr_{0.1}MnO_{3.05}$ characterized by a fixed minimum of oxygen excess in the whole temperature range. On the other hand, $YMn_{0.6}Ti_{0.3}O_3$ exhibits intermediate conductivity values in air ($\sigma_{Zr} > \sigma_{Ti} > \sigma_Y$), what can be attributed not only to the lower amount of Mn cations, in-charge of conduction, which are diluted by Ti on their crystallographic sites, but also to the more symmetrical structure of the doped compound with respect to the pristine manganite. Unfortunately, but as generally the case in manganese-based conduction process, the much lower value of conductivity is obtained for Ti-doped $YMnO_3$ in anodic atmosphere, in part due to the fact that the charge carrier pairs are not the same (Mn^{2+}/Mn^{3+} instead of Mn^{3+}/Mn^{4+}) and structural reasons, *i.e.* longer Mn-Mn distances.

Now, it is worth noting that the electrical conductivity of all the compounds we studied is low, in comparison to perovskite materials that are commonly used as SOFC cathodes. Nevertheless, given that these same materials are chemically compatible with the YSZ electrolyte, the electrochemical behavior in air was studied with the addition of an LSM perovskite-type current collector. The study of $YMnO_3$ and $Y_{0.9}Zr_{0.1}MnO_3$ as a cathode in symmetrical cell configuration with a LSM (or LBM) current collector and YSZ electrolyte, allows to observe that the electrochemical behavior of these compounds are not only subject to their transport properties. Even

when the Zr-doped material exhibits the highest total electrical conductivity, and maybe a higher ionic conductivity, its impedance response is less favorable than that for pure $YMnO_3$. It indicates that, in the case of these materials, which experience the same electrochemical processes, the microstructure obtained is probably more decisive in the electrochemical performance. Specifically, Zr doping seems to favor the grain growth and hence the material sintering, which possibly strongly limits the oxygen diffusion in the bulk. Meanwhile, the finer microstructure obtained for $YMnO_3$ highly promotes the oxygen surface exchange. In agreement with these observations, the same conclusion is found examining the electrochemical behavior of $YMn_{0.6}Ti_{0.3}O_3$ as a cathode material. Large grains are obtained for this compound due to the higher temperature required for its synthesis. Therefore, although the electrochemical cell was built and prepared in a similar way as the others, an additional powder milling step was necessary without which the grains exhibited a very poor connectivity, and the impedance resistance was very high. Unfortunately, the final electrochemical behavior of the Ti-doped manganite is not as better as pure $YMnO_3$, probably due to the aforementioned coarse microstructure resulting from the use of traditional electrode elaboration technique. Preliminary evaluation of $YMn_{0.6}Ti_{0.3}O_3$ in dry reducing atmosphere reveals a poor performance of the material in these conditions, worse than in air, in pair due to the same microstructural issue and maybe as a consequence of the lack of water partial pressure in the working atmosphere.

As a final point of this work, the good electrochemical behavior and the perfect chemical compatibility of $YMnO_3$ and $Y_{0.9}Zr_{0.1}MnO_3$ materials with the YSZ electrolyte allows to affim that these compounds are promising SOFC electrodes. However, their performance is subject to their microstructural characteristics, the chosen current collector and the cell preparation technique. Therefore, it is possible to think that the cathode properties using adequate cell fabrication. For example, a new procedure of electrode deposition, which could be implemented in order to improve the electrochemical activity of those compounds is the impregnation

method. This technique consists in the preparation of a dense electrolyte covered by a porous scaffold of the same material, both being sintered at high temperature. The scaffold is then impregnated with a solution containing the precursors of a mixed oxide electrode, but in this case, a much lower temperature is required to obtain the single-phase electrode. In general, such procedure is used to avoid the high temperatures of solid-state reaction, which promote an excessive grain growth. The result is generally a decrease of the electrode polarization resistance, given that adsorption kinetic of the gas is improved and the TPB length is increased, among others. Additionally, the method enables the construction of very thin electrode layers, avoiding diffusional limitations and issues related to low electrical conducting materials, what is the case of pure or doped $YMnO_3$ [250]–[252].

REFERENCES

[1] I. E. Agency, “Oil Market Report,” 2017. [Online]. Available: https://www.iea.org/. [Accessed: 06-Mar-2017].

[2] O. Singh, Bharat Raj; Singh, “Global Trends of Fossil Fuel Reserves and Climate Change in the 21st Century,” in *World’s largest Science , Technology & Medicine*, S. Khan, Ed. In Tech, 2012, pp. 167–192.

[3] M. Höök and X. Tang, “Depletion of fossil fuels and anthropogenic climate change-A review,” *Energy Policy*, vol. 52, pp. 797–809, 2013.

[4] D. J. Wuebbles and A. K. Jain, “Concerns about climate change and the role of fossil fuel use,” *Fuel Process. Technol.*, vol. 71, no. 1–3, pp. 99–119, 2001.

[5] NASA, “Global Warming,” *Nasa Facts*, pp. 1–4, 1998.

[6] F. R. Posso and J. P. Sánchez, “El desarrollo del Sistema Energético Solar-Hidrógeno en América Latina : Potencialidades , oportunidades y barreras,” *Rev. Semest. la DIUC*, vol. 5, no. 2, pp. 61–79, 2014.

[7] J. Ospina Castillo, “Análisis y evaluación política de Gas natural y el desarrollo de activos de flexibilidad dentro del plan de abastecimiento,” Bogotá, 2017.

[8] A. V. Aldana Urrea and J. M. Grueso Catillo, “Análisis del mercado de gas natural para la generación eléctrica . Retos y perspectivas 2015-2018,” 2016.

[9] A. Martínez, D. Barreneche, D. Bellon, D. Plata, D. Latorre, and A. Porras, “Estudio De Factibilidad De La Economia Del Hidrógeno En Colombia,” *Innov. Res. Eng. Educ. key factor Glob. Compet.*, p. 8, 2013.

[10] D. Higueras, “El camino a la sostenibilidad energética en Colombia,” *Semana Sostenible*, 2016. [Online]. Available: http://sostenibilidad.semana.com/. [Accessed: 28-Apr-2017].

[11] L. Betancurt Alarcón, “Energías renovables ayudarían a evitar apagón: WWF,”

El tiempo, 2016. [Online]. Available: http://www.eltiempo.com/. [Accessed: 28-Apr-2017].

[12] UPME, “Colombia garantiza confiabilidad energética con nuevo plan de expansión,” Bogotá, 2016.

[13] W. Suárez, “El reto de energizar zonas rurales aisladas,” *Semana Sostenible*, 2016. [Online]. Available: http://sostenibilidad.semana.com. [Accessed: 28-Apr-2017].

[14] L. M. Corredor-Rojas, “Pilas de combustible y su desarrollo,” *Ing. y Univ.*, vol. 16, no. 1, pp. 247–263, 2012.

[15] R. Mayén-Mondragón, “Celdas de combustible de Óxido Sólido..... ¿Una de las soluciones al problema energético?,” *Ideas CONCYEG*, vol. 7, no. 72, pp. 647–661, 2011.

[16] T. Hengyong and U. Stimming, “Advances, aging mechanisms and lifetime in solid-oxide fuell cells,” *J. Power Sources*, no. 1–2, pp. 284–293, 2004.

[17] N. B. Rajendra, J. Mukhopadhyay, and S. ABHIJIT DAS, “High Temperature Fuel Cell,” *Proc. Indian Natl. Sci. Acad.*, vol. 81, no. 4, pp. 841–864, 2015.

[18] “Sistema de generación con pila de combustible de óxido sólido,” in *Sistema de generación eléctrica con pila de combustible de óxido sólido alimentado con residuos forestales y su optimización mediante algoritmos basados en nubes de partículas*, pp. 105–140.

[19] J. C. Ruiz-Morales, D. Marrero-López, J. Canales-Vázquez, and J. T. S. Irvine, “Symmetric and reversible solid oxide fuel cells,” *RSC Adv.*, vol. 1, no. 8, p. 1403, 2011.

[20] V. B. Vert Belenguer, “Electrodos avanzados para Pilas De Combustible de Óxido Sólido (SOFCs),” Universitat Politecnica de Valencia, 2011.

[21] Agencia de Noticias de la Universidad Nacional, “Optimizan celdas de

combustible con tecnología colombiana," 2013. [Online]. Available: http://agenciadenoticias.unal.edu.co/. [Accessed: 20-Sep-2017].

[22] J. G. Mejía-Arango and C. A. Acevedo-Álvarez, "Proyección al año 2025 para el uso del hidrógeno en el sector transporte del Valle de Aburrá," *Sci. Tech. Año XVIII*, vol. 18, no. 2, pp. 327–334, 2013.

[23] J. G. Mejía Arango and J. M. Montes Hincapié, "Conveniencia de incorporar las celdas de combustible en el sector del transporte del Valle de Aburrá," *Cienc. Tecnol. Soc.*, no. 5, pp. 74–86, 2011.

[24] H. Carvajal-osorio, J. H. Babativa, and J. A. Alonso, "Estudio sobre producción de H2 con hidroelectricidad para una economía de hidrógeno en Colombia," *Ing. y Competividad*, vol. 12, no. 1, pp. 3–42, 2010.

[25] Caracol Radio, "Gobierno anuncia descubrimiento de gas natural en el Caribe," 2017. [Online]. Available: http://caracol.com.co/. [Accessed: 19-Sep-2017].

[26] Vanguardia, "Descubren uno de los mayores yacimientos de gas natural en Colombia," 2017. [Online]. Available: http://www.vanguardia.com/. [Accessed: 19-Sep-2017].

[27] Xataca Colombia, "Se descubre el pozo de gas natural más grande de Colombia," 2017. [Online]. Available: https://www.xataka.com.co/. [Accessed: 19-Sep-2017].

[28] S. C. Singhal, "Advances in solid oxide fuel cell technology," *Solid State Ionics*, vol. 135, pp. 305–313, 2000.

[29] N. Q. Minh, "Ceramic Fuel Cells," *J. Am. Ceram. Soc.*, vol. 76, no. 3, pp. 563–588, 1993.

[30] D. Z. de Florio, F. C. Fonseca, E. N. S. Muccillo, and R. Muccillo, "Materiais cerâmicos para células a combustível (Ceramic materials for fuel cells),"

Cerâmica, vol. 50, pp. 275–290, 2004.

[31] J. M. Haag, S. A. Barnett, J. W. Richardson, and K. R. Poeppelmeier, “Structural and Chemical Evolution of the SOFC Anode An in Situ Neutron Diffraction Study,” *Chem. Mater.*, vol. 22, pp. 3283–3289, 2010.

[32] M. M. Mench, *Fuel cell engines*. Hoboken, New Jersey: John Wiley & Sons, Inc, 2008.

[33] Bloom energy, “Bloomenergy.” [Online]. Available: www.bloomenergy.com. [Accessed: 17-Apr-2018].

[34] R. H. F. Verhoeven, “Characterisation of La0.75Sr0.25Cr0.50Mn0.50O3-δ (LSCM) redox-stable perovskite anodes for solid oxide fuel cells,” University of Twente, 2006.

[35] P. R. Chandran and T. V Arjunan, “A Review of Materials used for Solid Oxide Fuel Cell,” *Int. J. ChemTech Res.*, vol. 7, no. 1, pp. 974–4290, 2015.

[36] F. Zurlo, I. Natali Sora, V. Felice, I. Luisetto, C. D’Ottavi, S. Licoccia, and E. Di Bartolomeo, “Copper-doped lanthanum ferrites for symmetric SOFCs,” *Acta Mater.*, vol. 112, pp. 77–83, 2016.

[37] P. Asensio, L. A. C. Rodriguez, M. E. G. Sánchez, and Universidad Nacional del Nordeste - Argentina, “Hidrógeno y pila de combustible,” *Fund. la energía la Comunidad Madrid*, p. 16, 2011.

[38] EG&G Technical Services Inc, *Fuel Cell Handbook*, 7 Edition. Morgantown, West Virginia, 2004.

[39] S. M. Haile, “Materials for fuel cells,” *Mater. Today*, pp. 24–29, 2003.

[40] J. E. Vega Castillo, “Estabilidad termodinámica y propiedades eléctricas de los compuestos La2Mo2-xWxO9-D,” Instituto Balseiro, 2013.

[41] E. Flórez Suárez, “Estado Actual del Hidrógeno Índice,” Universidad Nacional Autónoma de México, 2016.

[42] J. T. S. Irvine, “Perovskite oxide anodes for SOFC,” in *Perovskite Oxide for Solid Oxide Fuel Cells*, T. Ishihara, Ed. Springer Science+Bussines Media, 2009, pp. 167–82.

[43] J. Alvarado-Flores and L. Ávalos-Rodríguez, “Materiales para ánodos, cátodos y electrolitos utilizados en celdas de combustible de óxido sólido (SOFC),” *Rev. Mex. Física*, vol. 59, pp. 66–87, 2013.

[44] D. A. Garcés, “Estudio de perovskitas LaBaCo2O6-δ: Propiedades de alta temperatura y su evaluación como potenciales materiales para celdas de combustible o electrolíticas de óxido sólido,” Instituto Balseiro, 2014.

[45] A. Ramirez Hernández, “Las celdas de combustible de óxidos sólidos (SOFC) como fuentes de energía renovable,” 2011. [Online]. Available: http://www.posgradoeinvestigacion.uadec.mx/. [Accessed: 20-Sep-2017].

[46] F. Tietz, “Thermal Expansion of SOFC Materials,” *Ionics (Kiel).*, vol. 5, pp. 129–139, 1999.

[47] L. V. Mogni, “Estudio de nuevos conductores mixtos para aplicaciones electroquímicas de alta temperatura,” Instituto Balseiro, 2007.

[48] K. Chen and S. P. Jiang, “Degradation and durability of electrodes of solid oxide fuel cells.,” in *Materials for High-Temperature Fuel Cells*, 1st ed., S. Ping Jiang and Y. Yan, Eds. Wiley-VCH Verlag GmbH & Co. KGaA, 2013, pp. 245–307.

[49] G. Yang, C. Su, R. Ran, M. O. Tade, and Z. Shao, “Advanced Symmetric Solid Oxide Fuel Cell with an Infiltrated K2NiF4 -Type La2NiO4 Electrode,” *Energy & Fuels*, vol. 28, no. 1, pp. 356–362, 2014.

[50] K. G. Romito, “Synthesis and Characterization of New Ionic and Mixed Ionic / Electronic Conductors,” University of South Carolina, 2013.

[51] J. Kim and A. Manthiram, “Layered LnBaCo2O5+d perovskite cathodes for

solid oxide fuel cells : an overview and perspective," *J. Mater. Chem. A Mater. energy Sustain.*, vol. 3, pp. 24195–24210, 2015.

[52] N. M. Sammes and C. Zhinhong, "Ionic conductivity of ceria/yttria stabilized zirconia electrolyte materials," *Solid State Ionics*, vol. 2738, no. 97, pp. 39–44, 1997.

[53] S. J. Skinner and J. A. Kilner, "Oxygen ion conductors," *Mater. Today*, pp. 30–37, 2003.

[54] T. Wei, P. Singh, Y. Gong, J. B. Goodenough, Y. Huang, and K. Huang, "Sr3-3xNa3xSi3O9-1.5x (x=0.45) as a Superior Solid Oxide-ion Electrolyte for Intermediate-temperature Solid Oxide Fuel Cells," *Energy Environ. Sci.*, pp. 1–15, 2014.

[55] "Chapter 4 Ionic conductivity of GDC electrolyte," pp. 64–88.

[56] C. Pirovano, R. N. Vannier, E. Capoen, G. Nowogrocki, and J. C. Boivin, "Characterisation of the electrode – electrolyte BIMEVOX system for oxygen separation Part I . In situ synchrotron study," *Solid State Ionics*, vol. 159, pp. 167–179, 2003.

[57] J. C. Boivin, C. Pirovano, G. Nowogrocki, G. Mairesse, P. Labrune, and G. Lagrange, "Electrode – electrolyte BIMEVOX system for moderate temperature oxygen separation," *Solid State Ionics*, vol. 115, pp. 639–651, 1998.

[58] E. A. Fortal'nova, V. . V. Murasheva, M. G. Safronenko, N. U. Venskovskii, G. M. Kaleva, and E. D. Politova, "Phase Transitions and Electroconducting Properties of BIMEVOX Solid Electrolytes," *Russ. J. Phys. Chem. A*, vol. 82, no. 10, pp. 1829–1835, 2008.

[59] T. Pfeifer, J. Matyas, P. Balaya, and J. Wei, Eds., *Ceramics for Energy Conversion, Storage, and Distribution Systems*, Volume 155. John Wiley & Sons, Inc, 2016.

[60] H. . Tuller, J. Schoonman, and I. Riess, Eds., *Oxygen Ion and Mixed Conductors and their Technological Applications*, 1st ed. Springer Netherlands, 2000.

[61] P. Holtappels, M. C. Verbraeken, D. H. Blank, and B. A. Boukamp, “The influence of mixed ionic electronic conductivity in the hydrogen electrode reaction in solid state electrochemical cells,” University of Twente.

[62] C. Périllat-merceroz, “Titanates de structures pérovskite et dérivées: Influence des éléments constitutifs et de la dimensionnalité sur les propriétés d’anode SOFC,” Université des Sciences et Technologie de Lille - Lille I, 2009.

[63] H. Takamura, “MIEC Materials,” in *Encyclopedia of Applied Electrochemistry*, G. Kreysa, K. Ota, and R. F. Savinell, Eds. Springer New York, 2014, pp. 1297–1300.

[64] M. Mogensen, T. Lindegaard, and U. R. Hansen, “Physical Properties of Mixed Conductor Solid Oxide Fuel Cell Anodes of Doped CeO2,” *Electrochem. Soc.*, vol. 141, no. 8, pp. 2122–2128, 1994.

[65] N. Grunbaum, “Estudios estructurales y fisicoquímicos de cátodos para celdas combustibles de alta temperatura,” Instituto Balseiro, 2006.

[66] B. de Boer, “SOFC Anode: Hydrogen oxidation at porous nickel and nickel/yttria- stabilised zirconia cermet electrodes,” Universiteit Twente, 1998.

[67] T. Kawada, “Perovskite Oxide for Cathode os SOFCs,” in *Perovskite Oxide for Solid Oxide Fuel Cells*, T. Ishihara, Ed. New York: Springer Science+Bussines Media, 2009, pp. 147–164.

[68] B. Ahmed, S.-B. Lee, R.-H. Song, J.-W. Lee, T.-H. Lim, and S.-J. Park, “Development of Novel LSM/GDC Composite Cathode Material for Cathode-Supported Direct Carbon Fuel Cells,” *ECS Trans.*, vol. 57, no. 1, pp. 2075–2082, 2013.

[69] A. Esquirol, N. P. Brandon, J. A. Kilner, and M. Mogensen, “Cathodes for Intermediate-Temperature SOFCs,” *J. Electrochem. Soc.*, vol. 151, no. 11, pp. 1–10, 2004.

[70] F. Jin, Y. Shen, R. Wang, and T. He, “Double-perovskite PrBaCo2/3Fe2/3Cu2/3O5+d as cathode material for intermediate-temperature solid-oxide fuel cells,” *J. Power Sources*, vol. 234, pp. 244–251, 2013.

[71] L. N. Xia, Z. P. He, X. W. Huang, and Y. Yu, “Synthesis and properties of SmBaCo2-xNixO5+d perovskite oxide for IT-SOFC cathodes,” *Ceram. Int.*, vol. 42, no. 1, pp. 1272–1280, 2016.

[72] J. Kim, J. Shin, H. Y. Jeong, Y. Choi, G. Kim, and M. Liu, “Highly efficient and robust cathode materials for low-temperature solid oxide fuel cells: PrBa0.5Sr0.5Co22xFexO51d,” *Sci. Rep.*, vol. 3, pp. 1–5, 2013.

[73] L. Zhang, G. Yao, Z. Song, B. Niu, W. Long, L. Zhang, Y. Shen, and T. He, “Effects of Pr-deficiency on thermal expansion and electrochemical properties in Pr1-xBaCo2O5+d cathodes for IT-SOFCs,” *Electrochim. Acta*, vol. 212, pp. 522–534, 2016.

[74] J. Xue, Y. Shen, and T. He, “Double-perovskites YBaCo2 − xFexO5+d cathodes for intermediate-temperature solid oxide fuel cells,” *J. Power Sources*, vol. 196, no. 8, pp. 3729–3735, 2011.

[75] S. Takahashi, S. Nishimoto, M. Matsuda, and M. Miyake, “Electrode Properties of the Ruddlesden–Popper Series, Lan+1NinO3n+1 (n=1, 2, and 3), as Intermediate-Temperature Solid Oxide Fuel Cells,” *J. Am. Ceram. Soc.*, vol. 2333, no. 27257, pp. 2329–2333, 2010.

[76] G. Skinner and S. J. Amow, “Recent developments in Ruddlesden – Popper nickelate systems for solid oxide fuel cell cathodes,” *J. Solid State Electrochem.*, pp. 538–546, 2006.

[77] B. Philippeau, F. Mauvy, C. Mazataud, S. Fourcade, and J.-C. Grenier, “Comparative study of electrochemical properties of mixed conducting Ln2NiO4+δ (Ln=La, Pr and Nd) and La0.6Sr0.4Fe0.8Co0.2O3−δ as SOFC cathodes associated to Ce0.9Gd0.1O2−δ, La0.8Sr0.2Ga0.8Mg0.2O3−δ and La9Sr1Si6O26.5 electrolytes,” *Solid State Ionics*, vol. 249–250, pp. 17–25, 2013.

[78] L. Dos Santos-Gómez, L. León-Reina, J. M. Porras-Vázquez, E. R. Losilla, and D. Marrero-López, “Chemical stability and compatibility of double perovskite anode materials for SOFCs,” *Solid State Ionics*, vol. 239, pp. 1–7, 2013.

[79] M. D. Gross, J. M. Vohs, and R. J. Gorte, “A Strategy for Achieving High Performance with SOFC Ceramic Anodes,” pp. 65–69, 2007.

[80] J. J. Alvarado Flores, “Análisis de la estructura perovskita LaxSr1-xCryMn1-yO3-δ con potencial aplicación como ánodo para celdas de combustible de óxido sólido,” *Boletín la Soc. Española Cerámica y Vidr.*, pp. 1–11, 2016.

[81] A. Atkinson, S. Barnett, R. J. Gorte, J. T. . S. Irvine, A. J. McEvoy, M. Mogensen, S. C. Singhal, and J. Vohs, “Advanced anodes for high-temperature fuel cells.,” *Nat. Mater.*, vol. 3, no. 1, pp. 17–27, 2004.

[82] M. Sharma, N. Rakesh, and S. Dasappa, “Solid oxide fuel cell operating with biomass derived producer gas: Status and challenges,” *Renew. Sustain. Energy Rev.*, vol. 60, pp. 450–463, 2016.

[83] R. J. Gorte, J. M. Vohs, and S. Mcintosh, “Recent Developments on Anodes for Direct Fuel Utilization in SOFC Recent Developments on Anodes for Direct Fuel Utilization in SOFC,” *Solid state Ion.*, vol. 175, no. 1–4, pp. 1–6, 2004.

[84] G. Lescano, F. M. Figueiredo, F. M. B. Marques, and J. Schmidt, “Synthesis and electrical conductivity of Y1-xMn1-yO3-d,” *J. Eur. Ceram. Soc.*, vol. 21, no. 10–11, pp. 2037–2040, 2001.

[85] T. Ishihara, “Structure and properties of perovskite Oxides,” in *Perovskite Oxide for Solid Oxide Fuel Cells*, T. Ishihara, Ed. New York: Springer Science+Bussines Media, 2009, pp. 1–15.

[86] O. A. Marina, N. L. Canfield, and J. W. Stevenson, “Thermal, electrical, and electrocatalytical properties of lanthanum-doped strontium titanate,” *Solid State Ionics*, vol. 149, no. 1–2, pp. 21–28, 2002.

[87] A. Ovalle, J. C. Ruiz-Morales, J. Canales-Vázquez, D. Marrero-López, and J. T. S. Irvine, “Mn-substituted titanates as efficient anodes for direct methane SOFCs,” *Solid State Ionics*, vol. 177, pp. 1997–2003, 2006.

[88] S. Hashimoto, L. Kindermann, F. W. Poulsen, and M. Mogensen, “A study on the structural and electrical properties of lanthanum-doped strontium titanate prepared in air,” *J. Alloys Compd.*, vol. 397, no. 1–2, pp. 245–249, 2005.

[89] M. R. Pillai, I. Kim, D. M. Bierschenk, and S. A. Barnett, “Fuel-flexible operation of a solid oxide fuel cell with Sr0.8La0.2TiO3 support,” *J. Power Sources*, vol. 185, no. 2, pp. 1086–1093, 2008.

[90] C. Périllat-Merceroz, P. Roussel, R. N. Vannier, P. Gélin, S. Rosini, and G. Gauthier, “Lamellar titanates: A breakthrough in the search for new solid oxide fuel cell anode materials operating on methane,” *Adv. Energy Mater.*, vol. 1, no. 4, pp. 573–576, 2011.

[91] C. Périllat-Merceroz, G. Gauthier, P. Roussel, M. Huve, P. Gelin, and R. N. Vannier, “Synthesis and Study of a Ce-Doped La / Sr Titanate for Solid Oxide Fuel Cell Anode Operating Directly on Methane edric P,” *Chem. Mater.*, vol. 23, pp. 1539–1550, 2011.

[92] X. Zhou, N. Yan, K. T. Chuang, and J. Luo, “Progress in La-doped $SrTiO_3$ (LST)-based anode materials for solid oxide fuel cells,” *RSC Adv.*, vol. 4, no. 1, pp. 118–131, 2014.

[93] P. Blennow Tullmar, K. Kammer Hansen, L. R. Wallenberg, and M. B.

Mogensen, “Strontium Titanate-based Composite Anodes for Solid Oxide Fuel Cells,” *ECS Trans.*, vol. 13, no. 26, pp. 181–194, 2008.

[94] J. Macías, A. A. Yaremchenko, and J. R. Frade, “Enhanced stability of Perovskite-like SrVO3-based anode materials by donor-type substitutions,” *Mater. Chem. A*, no. 26, 2016.

[95] T. Jardiel, M. T. Caldes, F. Moser, J. Hamon, G. Gauthier, and O. Joubert, “New SOFC electrode materials: The Ni-substituted LSCM-based compounds (La0.75Sr0.25)(Cr0.5Mn0.5-xNi x)O3-d and (La0.75Sr0.25) (Cr0.5-xNixMn0.5)O3-d,” *Solid State Ionics*, vol. 181, no. 19–20, pp. 894–901, 2010.

[96] E. Lay, G. Gauthier, S. Rosini, C. Savaniu, and J. T. S. Irvine, “Ce-substituted LSCM as new anode material for SOFC operating in dry methane,” *Solid State Ionics*, vol. 179, no. 27–32, pp. 1562–1566, 2008.

[97] T. Delahaye, T. Jardiel, O. Joubert, R. Laucournet, G. Gauthier, and M. T. Caldes, “Electrochemical properties of novel SOFC dual electrode La0.75Sr0.25Cr0.5Mn0.3Ni0.2O3-d,” *Solid State Ionics*, vol. 184, no. 1, pp. 39–41, 2011.

[98] E. Lay, G. Gauthier, and L. Dessemond, “Preliminary studies of the new Ce-doped La/Sr chromo-manganite series as potential SOFC anode or SOEC cathode materials,” *Solid State Ionics*, vol. 189, no. 1, pp. 91–99, 2011.

[99] S. Tao and J. T. S. Irvine, “A redox-stable efficient anode for solid-oxide fuel cells.,” *Nat. Mater.*, vol. 2, no. 5, pp. 320–323, 2003.

[100] A. H. Karim, A. Afif, F. Begum, P. I. Petra, and A. K. Azad, “Synthesis and characterization of La0.75Sr 0.25Mn0.5Cr0.2Ti0.3O 3 Anodes for SOFCs,” *IOP Conf. Ser. Mater. Sci. Eng.*, vol. 121, pp. 1–5, 2016.

[101] S. M. Bukhari, S. R. Gamble, D. Neagu, T. Oh, D. N. Miller, R. J. Gorte, J. M. Vohs, and J. T. S. Irvine, “Nano-socketed nickel particles with enhanced coking resistance grown in situ by redox exsolution ´,” *Nat. Commun.*, 2015.

[102] C. Arrivé, T. Delahaye, O. Joubert, and G. Gauthier, “Exsolution of nickel nanoparticles at the surface of a conducting titanate as potential hydrogen electrode material for solid oxide electrochemical cells,” *J. Power Sources*, vol. 223, pp. 341–348, 2013.

[103] O. Kwon, S. Sengodan, K. Kim, G. Kim, H. Y. Jeong, J. Shin, Y. Ju, J. W. Han, and G. Kim, “Exsolution trends and co-segregation aspects of self-grown catalyst nanoparticles in perovskites,” *Nat. Commun.*, vol. 8, no. May, pp. 1–7, 2017.

[104] D. Zhinhong, H. Zhao, S. Yi, Q. Xia, Y. Gong, Y. Zhang, X. Cheng, L. Gu, and K. Świerczek, “High-Performance Anode Material Sr2FeMo0.65Ni0.35O6−δ with In Situ Exsolved Nanoparticle Catalyst,” *ACS Nano*, p. 8660−8669, 2016.

[105] À. Srfeo, J. M. Compana, S. Bruque, E. R. Losilla, and D. Marrero-l, “Symmetric electrodes for solid oxide fuel cells based on Zr-doped,” vol. 279, pp. 419–427, 2015.

[106] S. Y. Istomin, A. P. Ber, N. V Lyskov, and E. V Antipov, “High-Temperature Properties of New Perovskite-Like Oxides,” vol. 62, no. 8, pp. 1021–1025, 2017.

[107] R. Jooris, F. Porcher, P. Roussel, and G. H. Gauthier, “In-depth study of the Ruddlesden-Popper LaxSr2-x MnO4±d family as possible electrode materials for symmetrical SOFC,” *Hydrog. energy*, pp. 1–14, 2017.

[108] J. C. Ruiz-morales, J. Canles-Vázquez, D. López Marrero, and P. Núñez, “On the simultaneous use of La0.75Sr0.25Cr0.5Mn0.5O3−δ as both anode and cathode material with improved microstructure in solid oxide fuel cells,” *Electrochim. Acta*, vol. 52, pp. 278–284, 2006.

[109] Q. X. Fu, F. Tietz, and D. Stöver, “Solid Oxide Fuel Cells,” pp. 74–83, 2006.

[110] Z. Ma, C. Sun, C. Ma, H. Wu, Z. Zhan, and L. Chen, “Ni doped La0.6Sr0.4FeO3-δ symmetrical electrode for solid oxide fuel cells,” *Chinese J.*

Catal., vol. 37, no. 8, pp. 1347–1353, 2016.

[111] R. H. F. Verhoeven, “Symmetric cells of LSCM on a TZ3Y electrolyte,” no. March, 2006.

[112] B. B. van Aken, a Meetsma, and T. T. Palstra, “Hexagonal YMnO(3).,” *Acta Crystallogr. C.*, vol. 57, no. Pt 3, pp. 230–2, 2001.

[113] J. Park, M. Kang, J. Kim, S. Lee, K.-H. Jang, A. Pirogov, J.-G. Park, C. Lee, S.-H. Park, and H. C. Kim, “Doping effects of multiferroic manganites YMn0.9X0.1O (X= Al, Ru, and Zn),” *Phys. Rev. B*, vol. 79, pp. 1–6, 2009.

[114] A. S. Gibbs, K. S. Knight, and P. Lightfoot, “High-temperature phase transitions of hexagonal YMnO3 Alexandra,” *Phys. Rev. B*, vol. 83, no. 9, p. 94111, 2011.

[115] W. Sotero, A. F. Lima, and M. V. Lalic, “Analysis of the Mn–O and Y–O bonds in paraelectric and ferroelectric phase of magnetoelectric YMnO3 from the first principles calculations,” *J. Alloys Compd.*, vol. 649, pp. 285–290, 2015.

[116] I. Levin, V. Krayzman, T. A. Vanderah, M. Tomczyk, H. Wu, M. G. Tucker, H. Y. Playford, J. C. Woicik, C. L. Dennis, and P. M. Vilarinho, “Oxygen-storage behavior and local structure in Ti-substituted YMnO3,” *J. Solid State Chem.*, vol. 246, pp. 29–41, 2017.

[117] C. Abughayada, B. Dabrowski, M. Avdeev, S. Kolesnik, S. Remsen, and O. Chmaissem, “Structural, magnetic, and oxygen storage properties of hexagonal Dy1−xYxMnO3+δ,” *J. Solid State Chem.*, vol. 217, pp. 127–135, 2014.

[118] S. Remsen and B. Dabrowski, “Synthesis and Oxygen Storage Capacities of Hexagonal Dy 1– x Y x MnO 3+δ,” *Chem. Mater.*, vol. 23, no. 17, pp. 3818–3827, 2011.

[119] C. Abughayada, B. Dabrowski, S. Kolesnik, D. Brown, and O. Chmaissem,

"Characterization of Oxygen Storage and Structural Properties of Oxygen-Loaded Hexagonal RMnO3+δ (R = Ho, Er, and Y)," *Chem. Mater.*, vol. 27, no. 18, pp. 6259–6267, 2015.

[120] C. Moure, D. Gutierrez, O. Peña, and P. Duran, "Structural Characterization of YMexMn1−xO3 (Me=Cu, Ni, Co) Perovskites," *J. Solid State Chem.*, vol. 163, no. 2, pp. 377–384, 2002.

[121] P. Ren, H. Fan, and X. Wang, "Bulk conduction and nonlinear behaviour in multiferroic YMnO3 Bulk conduction and nonlinear behaviour in multiferroic YMnO 3," vol. 152905, 2013.

[122] M. Chen, B. Hallstedt, and L. J. Gauckler, "Thermodynamic assessment of the Mn–Y–O system," *J. Alloys Compd.*, vol. 393, no. 1–2, pp. 114–121, 2005.

[123] Q. H. Zhang, X. Shen, Y. Yao, Y. G. Wang, C. Q. Jin, and R. C. Yu, "Oxygen vacancy ordering and its mobility in YMnO3," *J. Alloys Compd.*, vol. 648, pp. 253–257, 2015.

[124] U. Salazar-Kuri, M. E. Mendoza, and J. M. Siqueiros, "Phase transition in multiferroic YMnO3 and its solid solution YMn(0.93)Fe(0.07)O3," *Phys. B Condens. Matter*, vol. 407, no. 17, pp. 3551–3554, 2012.

[125] T. Asaka, K. Nemoto, K. Kimoto, T. Arima, and Y. Matsui, "Crystallographic superstructure of Ti-doped hexagonal YMnO 3," *Phys. Rev. B - Condens. Matter Mater. Phys.*, vol. 71, no. 1, pp. 3–8, 2005.

[126] S. Remsen, "Properties of transition metal oxides for gas separation and oxygen storage applications," 2011.

[127] C. Dubourdieu, G. Huot, I. Gelard, H. Roussel, O. I. Lebedev, and G. Van Tendeloo, "Thin films and superlattices of multiferroic hexagonal rare earth manganites," *Philos. Mag. Lett.*, vol. 87, no. 3–4, pp. 203–210, 2007.

[128] S. G. Barsov, S. I. Vorob'ev, V. P. Koptev, E. N. Komarov, S. a. Kotov, S. M.

Mikirtych'yants, G. V. Shcherbakov, a. E. Pestun, and Y. M. Mukovskiĭ, "Muon investigation of HoMnO3 and YMnO3 hexagonal manganites," *JETP Lett.*, vol. 85, no. 12, pp. 658–661, 2007.

[129] C. M. Jiménez, "Phase transitions induced on hexagonal manganites by the incorporation of aliovalent cations on A or B lattice sites," *Boletín la Soc. …*, vol. 38, no. 5, pp. 417–420, 1999.

[130] J.-W. Bos, B. B. van Aken, and T. T. M. Palstra, "Disorder induced hexagonal-orthorhombic transition in (Y,Gd)MnO3," pp. 1–5, 2008.

[131] A. Veres, J. G. Noudem, S. Fourrez, and G. Bailleul, "The influence of iron substitution to manganese on the physical properties of YMnO3," *Solid State Sci.*, vol. 8, no. 2, pp. 137–141, 2006.

[132] C. Moure, J. F. Fernandez, M. Villegas, and P. Duran, "Non-Ohmic Behaviour and Switching Phenomena in YMnO3-Based Ceramic Materials," *J. Eur. Ceram. Soc.*, vol. 19, no. 1, pp. 131–137, 1999.

[133] M. Tomczyk, P. Maria Vilarinho, A. Moreira, and A. Almeida, "High temperature dielectric properties of YMnO3 ceramics," *J. Appl. Phys.*, vol. 110, no. 6, pp. 6–11, 2011.

[134] S. K. Srivastava, M. Kar, S. Ravi, P. K. Mishra, and P. D. Babu, "Magnetic properties of electron-doped Y1-xCexMnO3 compounds," *J. Magn. Magn. Mater.*, vol. 320, no. 19, pp. 2382–2386, 2008.

[135] A. E. Smith, A. W. Sleight, and M. a. Subramanian, "Synthesis and properties of solid solutions of hexagonal YCu0.5Ti0.5O3 with YMO3 (M=Mn, Cr, Fe, Al, Ga, and In)," *Mater. Res. Bull.*, vol. 46, no. 1, pp. 1–5, 2011.

[136] A. S. Gibbs, K. S. Knight, and P. Lightfoot, "High Temperature Phase Transitions of Hexagonal YMnO3," *Phys. Rev. B*, vol. 83, no. 94111, pp. 1–10, 2010.

[137] M. Tomczyk, a. M. O. R. Senos, I. M. Reaney, and P. M. Vilarinho, “Reduction of microcracking in YMnO3 ceramics by Ti substitution,” *Scr. Mater.*, vol. 67, no. 5, pp. 427–430, 2012.

[138] S. Mori, J. Tokunaga, Y. Horibe, Y. Aikawa, and T. Katsufuji, “Magnetocapacitance effect and related microstrucuture in Ti-doped YMnO3,” *Phys. Rev. B - Condens. Matter Mater. Phys.*, vol. 72, no. 22, pp. 1–5, 2005.

[139] S. Mori, J. Tokunaga, Y. Horibe, Y. Aikawa, and T. Katsufuji, “Structural Phase Transition and Domain Structures in YMn1- xTixO 3,” *Jpn. J. Appl. Phys.*, vol. 44, no. 9B, pp. 7174–7176, 2005.

[140] C. Abughayada, B. Dabrowski, M. Avdeev, S. Kolesnik, S. Remsen, and O. Chmaissem, “Structural, magnetic, and oxygen storage properties of hexagonal Dy 1-xYxMnO3+??,” *J. Solid State Chem.*, vol. 217, pp. 127–135, 2014.

[141] S. Remsen, B. Dabrowski, O. Chmaissem, J. Mais, and a. Szewczyk, “Synthesis and oxygen content dependent properties of hexagonal DyMnO3+δ,” *J. Solid State Chem.*, vol. 184, no. 8, pp. 2306–2314, 2011.

[142] C. Abughayada, B. Dabrowski, S. Kolesnik, D. E. Brown, and O. Chmaissem, “Characterization of Oxygen Storage and Structural Properties of Oxygen-Loaded Hexagonal RMnO3+δ (R = Ho, Er, and Y),” *Chem. Mater.*, vol. 27, no. 18, pp. 6259–6267, 2015.

[143] S. Remsen, B. Dabrowski, O. Chmaissem, J. Mais, and A. Szewczyk, “Synthesis and oxygen content dependent properties of hexagonal DyMnO3+δ,” *J. Solid State Chem.*, vol. 184, no. 8, pp. 2306–2314, 2011.

[144] O. Parkkima, S. Malo, M. Hervieu, and E. Rautama, “Journal of Solid State Chemistry New R MnO 3 þ δ (R ¼ Y , Ho ; δ E 0 . 35) phases with modulated structure,” *J. Solid State Chem.*, vol. 221, pp. 109–115, 2015.

[145] S. Remsen and B. Dabrowski, “Synthesis and oxygen storage capacities of

hexagonal Dy1-x Yx Mn O3+d," *Chem. Mater.*, vol. 23, pp. 3818–3827, 2011.

[146] L. Jeuvrey, O. Peña, a. Moure, and C. Moure, "Synthesis and magnetic properties of hexagonal Y(Mn,Cu)O3 multiferroic materials," *J. Magn. Magn. Mater.*, vol. 324, no. 5, pp. 717–722, 2012.

[147] A. E. Smith, "Functional Transition Metal Oxides: Structure-property Relationships," Oregon state University, 2010.

[148] J. F. Ferna, P. Dura, and O. Pen, "Critical behavior in the perovskite-like system Y (Ni , Mn) O 3," *J. Phys. Chem. Solids*, vol. 61, pp. 2019–2024, 2000.

[149] D. Gutiérrez, O. Peña, K. Ghanimi, P. Durán, and C. Moure, "Electrical and magnetic features in the perovskite-type system Y(Co, Mn)O3," *J. Phys. Chem. Solids*, vol. 63, no. 11, pp. 1975–1982, 2002.

[150] O. Pen, D. Gutie, and P. Dura, "Crystalline structure and electrical properties of YCuxMn1?xO3 solid solutions," *J. Eur. Ceram. Soc. 22*, vol. 22, pp. 2939–2944, 2002.

[151] S. Malo and a. Maignan, "Co-substitution at the Mn-site in YMnO3: Structural stability and physical properties," *Mater. Res. Bull.*, vol. 47, no. 4, pp. 974–979, 2012.

[152] S. Malo, A. Maignan, S. Marinel, M. Hervieu, K. R. Poeppelmeier, and B. Raveau, "Structural and magnetic properties of the solid solution (0<x<1) YMn1−x(Cu3/4Mo1/4)xO3," *Solid State Sci.*, vol. 7, no. 12, pp. 1492–1499, 2005.

[153] I. H. Ismailzade, G. A. Smolenskii, V. I. Nesterenko, and F. A. Agaev, "X-Ray and Electric Investigations of the Systems," *Phys. state solid*, vol. 83, no. 5, pp. 83–89, 1971.

[154] a. M. Zhang, W. H. Zhu, X. S. Wu, and B. Qing, "Effect of Al doping on the

microstructure properties of YMn1−xAlxO3," *J. Cryst. Growth*, vol. 318, no. 1, pp. 912–915, 2011.

[155] A. M. Zhang, W. H. Zhu, X. S. Wu, and B. Qing, "Effect of Al doping on the microstructure properties of YMn1-x AlxO 3," *J. Cryst. Growth*, vol. 318, pp. 912–915, 2011.

[156] U. Salazar-Kuri, M. E. Mendoza, and J. M. Siqueiros, "Phase transition in multiferroic YMnO3 and its solid solution YMn(0.93)Fe(0.07)O3," *Phys. B Condens. Matter*, vol. 407, no. 17, pp. 3551–3554, 2012.

[157] N. Sharma, a. Das, S. K. Mishra, C. L. Prajapat, M. R. Singh, and S. S. Meena, "Magnetic and dielectric behavior in YMn1−xFexO3 ($x \leq 0.5$)," *Journal of Applied Physics*, vol. 115, no. 21. p. 213911, 2014.

[158] S. L. Samal, W. Green, S. E. Lofland, K. V. Ramanujachary, D. Das, and a. K. Ganguli, "Study on the solid solution of YMn1−xFexO3: Structural, magnetic and dielectric properties," *J. Solid State Chem.*, vol. 181, no. 1, pp. 61–66, 2008.

[159] M. Ocaña, J. P. Espinós, and J. B. Carda, "Synthesis, through pyrolysis of aerosols, of YIn1−xMnxO3 blue pigments and their efficiency for colouring glazes," *Dye. Pigment.*, vol. 91, no. 3, pp. 501–507, 2011.

[160] A. E. Smith, H. Mizoguchi, K. Delaney, N. a. Spaldin, A. W. Sleight, and M. a. Subramanian, "Mn3+ in trigonal bipyramidal coordination: A new blue chromophore," *J. Am. Chem. Soc.*, vol. 131, no. 47, pp. 17084–17086, 2009.

[161] T. Asaka, K. Nemoto, K. Kimoto, T. Arima, and Y. Matsui, "Crystallographic superstructure of Ti-doped hexagonal <math display='inline'> <mrow> <mi mathvariant='normal'>Y</mi> <mi mathvariant='normal'>Mn</mi> <msub> <mi mathvariant='normal'>O</mi> <mn>3</mn> </msub> </mrow> </math>," *Phys. Rev. B*, vol. 71, no. 1, p. 14114, 2005.

[162] S. Mori, J. Tokunaga, and Y. Horibe, "Magnetocapacitance effect and related

microstrucuture in Ti-doped YMnO 3," pp. 1–5, 2005.

[163] S. Mori, J. Tokunaga, Y. Horibe, Y. Aikawa, and T. Katsufuji, "Magnetocapacitance effect and related microstrucuture in Ti-doped," *Phys. Rev. B*, vol. 72, no. 22, p. 224434, 2005.

[164] P. Jiang, "Structure-property Relationships of Oxides with Hexagonal AMO3 and Brownmillerite Related Structures," Oregon State University, 2012.

[165] J. Pen, R. J. Chater, S. Fearn, A. V Berenov, S. J. Skinner, and J. A. Kilner, "Anisotropic Oxygen Ion Diffusion in Layered PrBaCo 2 O 5+," *Chem. Mater.*, vol. 24, pp. 613–621, 2012.

[166] A. Chroneos, B. Yildiz, A. Tarancon, D. Parfitt, and J. a. Kilner, "Oxygen diffusion in solid oxide fuel cell cathode and electrolyte materials: mechanistic insights from atomistic simulations," *Energy Environ. Sci.*, vol. 4, pp. 2774–2789, 2011.

[167] S. Sakka, Ed., *Handbook of sol-gel science and technology. Processing, characterization and applications*. Boston/Dordrecht/Londres: Kluwer Academic publishers, 2005.

[168] Grupo Investigación de Materiales Cristalinos, "Difracción de rayos X en muestra policristalina [DRXP]," 2006. [Online]. Available: http://www.ehu.eus/. [Accessed: 29-Sep-2017].

[169] L. Baqué, "Preparación y caracterización de cátodos de alto rendimiento para celdas de combustible de óxido sólido de temperatura intermedia," Instituto Balseiro, 2011.

[170] J. Rodriguez-Carvajal, "Recent advances in magnetic structure determination by neutron powder diffraction," *Phys. B Condens. Matter*, vol. 192, no. 1–2, pp. 55–69, 1993.

[171] J. Rodríguez-Carvajal and R. Thierry, "WinPLOTR: a Windows tool for powder

diffraction patterns analysis Materials Science Forum," *Proc. Seventh Eur. Powder Diffr. Conf. (EPDIC 7)*, pp. 118–123, 2000.

[172] P. Lelann and J. F. Bérar, "ESDs and estimated probable-error obtained in Rietveld refinements with local correlation," *J. Appl. Crystallogr.*, vol. 24, pp. 12–19, 1991.

[173] C. Périillat-Merceroz, P. Roussel, E. Capoen, S. Rosini, P. Géllin, R. N. Vannier, and G. Gauthier, "Synthesis and properties of La0.05Ba0.95Ti1 - xMyO3 (M = Mn, Ce) as anode materials for solid oxide fuel cells," *Solid State Ionics*, vol. 283, pp. 21–29, 2015.

[174] B. S. Instruments, "EC-Lab Software : Techniques and Applications," p. 220, 2011.

[175] B. J. Ford, S. Bradbury, and D. C. Joy, "Scanning electron microscope," 2018. [Online]. Available: https://www.britannica.com. [Accessed: 24-Mar-2018].

[176] J. Vega, "Microscopia Electrónica de Barrido," 2013. [Online]. Available: https://es.slideshare.net. [Accessed: 24-Mar-2018].

[177] Thermo Fisher Scientific, "An Introduction to Electron Microscopy: The Scanning Electron Microscope," 2018. [Online]. Available: https://www.fei.com. [Accessed: 24-Mar-2018].

[178] The complete Microscope Guide: Microscope Master, "Scanning Electron Microscope: Advantages and Disadvantages in ImagingComponents and Applications," 2018. [Online]. Available: https://www.microscopemaster.com. [Accessed: 24-Mar-2018].

[179] D. Johnson, "ZView Version 3.0." Scribner Associates, Inc., p. 2006.

[180] C. Reece, "An Introduction to Electrochemical Impedance Spectroscopy (EIS)." 2005.

[181] S. Tatay, "Solution-processed (Spin) electronics." [Online]. Available:

https://www.slideshare.net/. [Accessed: 27-Sep-2017].

[182] Ossila, “Spin Coating: A Guide to Theory and Techniques.” [Online]. Available: https://www.ossila.com/. [Accessed: 26-Sep-2017].

[183] University of Louisville, “Spin coating theory,” 2013.

[184] S. A. Durán Amaya, “Study of the materials belonging to the system La4BaCu5-xMxO13+d (M: Co, Mn) with potential application as electrode on Solid Oxide Fuel Cells (SOFC),” Universidad Industrial de Santander, 2017.

[185] M. A. Moura de Sousa, “Modelos de circuitos equivalentes para explicar espectros de impedância de dispositivos de efeito de campo,” Universidade de Sao paulo, 2013.

[186] B. B. Van Aken, J.-W. G. Bos, R. A. de Groot, and T. T. M. Palstra, “Asymmetry of electron and hole doping in <math display=‘inline’> <mrow> <msub> <mrow> <mi mathvariant=‘normal’>YMnO</mi> </mrow> <mrow> <mn>3</mn> </mrow> </msub> </mrow> </math>,” *Phys. Rev. B*, vol. 63, no. 12, p. 125127, 2001.

[187] T. Katsufuji, M. Masaki, A. Machida, M. Moritomo, K. Kato, E. Nishibori, M. Takata, M. Sakata, K. Ohoyama, K. Kitazawa, and H. Takagi, “Crystal structure and magnetic properties of hexagonal RMnO3 (R=Y, Lu, and Sc) and the effect of doping T.,” *Phys. Rev. B*, vol. 66, no. 13, p. 134434, 2002.

[188] A. J. Overton, J. L. Best, I. Saratovsky, and M. a. Hayward, “Influence of Topotactic Reduction on the Structure and Magnetism of the Multiferroic $YMnO_3$,” *Chem. Mater.*, vol. 21, no. 20, pp. 4940–4948, 2009.

[189] R. D. Shannon, “Revised effective ionic radii and systematic studies of interatomic distances in halides and chalcogenides,” *Acta Crystallogr. Sect. A*, vol. 32, pp. 751–767, 1976.

[190] C. Zhang, X. Zhang, Y. Sun, and S. Liu, “Atomistic simulation of Y-site

substitution in multiferroic h -YMnO 3," vol. 54104, pp. 1–10, 2011.

[191] C. Abughayada, B. Dabrowski, S. Kolesnik, D. E. Brown, and O. Chmaissem, "Characterization of Oxygen Storage and Structural Properties of Oxygen-Loaded Hexagonal R MnO 3 + δ (R = Ho , Er , and Y)," *Chem. Mater.*, vol. 27, no. 18, pp. 6259–6267, 2015.

[192] S. H. Skjærvø, E. T. Wefring, S. K. Nesdal, N. H. Gaukås, G. H. Olsen, J. Glaum, T. Tybell, and S. M. Selbach, "Interstitial oxygen as a source of p-type conductivity in hexagonal manganites," *Nat. Commun.*, vol. 7, no. 13745, pp. 1–8, 2016.

[193] Q. X. Fu, F. Tietz, and D. Stöver, "La0.4Sr0.6Ti1−xMnxO3−δ Perovskites as Anode Materials for Solid Oxide Fuel Cells," *J. Electrochem. Soc.*, vol. 153, no. 4, pp. D74–D83, 2006.

[194] T. Huang and Y. Huang, "Electrical conductivity and YSZ reactivity of Y 1 − x Sr x MnO 3 as SOFC cathode material," vol. 103, pp. 207–212, 2003.

[195] C. C. Appei, "Zirconia Stabilized by Y and Mn : A Microstructural Characterization," vol. 1, pp. 406–413, 1995.

[196] T. Kawada, N. Sakai, H. Yokokawa, and M. Doklya, "Electrical properties of transition-metal-doped YSZ," *Solid State Ionics*, vol. 56, pp. 418–425, 1992.

[197] T. Atsumi, T. Ohgushi, H. Namikata, and N. Kamegashira, "Oxygen nonstoichiometry of LnMnO 3," vol. 252, pp. 67–70, 1997.

[198] S. C. Singhal and K. Kendal, Eds., *High-temperature Solid Oxide Fuel Cells: Fundamentals, Design and Applications*, 1st Editio. Elsevier Science, 2003.

[199] S. C. Singhal and M. Dokiya, Eds., *Solid Oxide Fuel Cells (SOFC VI): Proceedings of the Sixth International Symposium*. The Electrochemical Society, 1999.

[200] K. Kirsim, A. Heinsaar, G. Nurk, and E. Lust, "Function of Temperature and

Oxygen Partial Pressure , Measured by Electrochemical in Situ High-Temperature XRD Method," vol. 160, no. 9, pp. 1022–1026, 2013.

[201] A. Y. Zuev, V. V Sereda, and D. S. Tsvetkov, "Oxygen Nonstoichiometry , Defect Structure , Thermal and and Double Perovskite GdBaCo 2 O 6 − δ," *J. Electrochem. Soc.*, vol. 161, no. 11, pp. 3032–3038, 2014.

[202] V. V Kharton, A. V Kovalevsky, M. Avdeev, E. V Tsipis, M. V Patrakeev, A. A. Yaremchenko, E. N. Naumovich, and J. R. Frade, "Chemically Induced Expansion of La2NiO4+δ -Based Materials," *Chem. Mater*, vol. 19, pp. 2027–2033, 2007.

[203] S. R. Bishop, "Chemical expansion of solid oxide fuel cell materials : A brief overview," *Acta Mech. Sin.*, vol. 29, pp. 312–317, 2013.

[204] D. Marrocchelli and S. R. Bishop, "Defining chemical expansion : the choice of units for the stoichiometric expansion coefficient," *R. Soc. Chem.*, pp. 9229–9232, 2014.

[205] S. R. Bishop, D. Marrocchelli, C. Chatzichristodoulou, N. H. Perry, M. B. Mogensen, H. L. Tuller, and E. D. Wachsman, "Chemical Expansion : Implications for Electrochemical Energy Storage and Conversion Devices," *Rev. Adv.*, no. February, pp. 1–35, 2014.

[206] M. Tomczyk, A. M. Senos, P. M. Vilarinho, and I. M. Reaney, "Origin of microcracking in YMnO3 ceramics," *Scr. Mater.*, vol. 66, no. 5, pp. 288–291, 2012.

[207] I. H. Ismailzade, G. A. Smolenskii, V. I. Nesterenko, and F. A. Agaev, "X-Ray and electric investigations of the systems Y(Mn1-xBx)03 (B = Fe3+, Cr3+, AL3+)," *Phys. state solid*, vol. 83, no. 5, pp. 83–89, 1971.

[208] P. Ren, H. Fan, and X. Wang, "Bulk conduction and nonlinear behaviour in multiferroic YMnO3," *Appl. Phys. Lett.*, vol. 103, no. 15, 2013.

[209] J. Palma, J. R. Jurado, P. Duran, and C. Pascual, “Química de defectos y mecanismos de conducción en óxidos de estructura perovskita ABO3,” *Bol.Soc.Soc.Esp.Ceram.Vidr.*, vol. 30, no. 6, pp. 472–475, 1991.

[210] G. V. Subba Raao, B. M. Wanklyn, and C. N. R. Rao, “Electrical transport in Rare Earth Ortho-chromites, -manganites and -ferrites,” *J. Phys. Chem. Solids*, vol. 32, pp. 345–358, 1971.

[211] E. Lay, L. Dessemond, and G. Gauthier, “Ba-substituted LSCM anodes for solid oxide fuel cells,” *J. Power Sources*, vol. 221, pp. 149–156, 2013.

[212] S. I. Elkalashy, T. V. Aksenova, A. S. Urusova, and V. A. Cherepanov, “Crystal structure, oxygen nonstoichiometry, thermal expansion and conductivity of (Nd ,Sr)(Fe,Co)O3−δ oxides,” *Solid State Ionics*, vol. 295, pp. 96–103, 2016.

[213] W. T. Fu, “Crystal chemistry of bismuthate-based superconductors: the origin of (local) charge disproportionation,” *Phys. C*, vol. 250, pp. 67–74, 1995.

[214] A. N. Petrov and K. R. Poeppelmeier, “Conductivity and carrier traps in La1-xSrxCo1-zMnzO3-d (x=0.3 ; z=0 and 0.25),” *J. Solid State Chem.*, vol. 172, pp. 296–304, 2003.

[215] M. Kuznecov, P. Otschik, N. Trofimenko, and K. Eichler, “Oxygen Transport in the SOFC Cathode *,” *Russ. J. Phys. Electrochem.*, vol. 40, no. 11, pp. 1162–1169, 2004.

[216] P. Woodware, D. Cox, E. Moshopoulou, and A. Sleight, “CHARGE DISPROPORTIONATION AND MAGNETIC ORDERING IN CaFeO3,” *Res. Highlights*, pp. 38–39, 1990.

[217] E. Lay, L. Dessemond, and G. Gauthier, “Ba-substituted LSCM anodes for solid oxide fuel cells,” *J. Power Sources*, vol. 221, pp. 149–156, 2013.

[218] M. S. Lsm, D. Rembelski, J. Viricelle, M. Rieu, L. Combemale, D. Rembelski, J. Viricelle, M. Rieu, and L. C. Characterization, “Characterization and

Comparison of Different Cathode To cite this version : Characterization and Comparison of Different Cathode Materials for," *Fuel Cells*, vol. 12, no. 2, pp. 256–264, 2012.

[219] M. D. Gross, J. M. Vohs, and R. J. Gorte, "Recent progress in SOFC anodes for direct utilization of hydrocarbons," *J. Mater. Chem.*, vol. 17, pp. 3071–3077, 2007.

[220] M. D. Gross, J. M. Vohs, and R. J. Gorte, "An Examination of SOFC Anode Functional Layers Based on Ceria in YSZ," *J. Electrochem. Soc.*, vol. 154, no. 7, pp. 694–699, 2007.

[221] C. Périllat-merceroz, P. Roussel, M. Huvé, E. Capoen, R. Vannier, and G. Gauthier, "New insights on the structure and reducibility of 3D versus 2D La/Sr titanates for SOFC anodes," *Solid State Ionics*, vol. 247–248, pp. 76–85, 2013.

[222] F. Qiang, K. Sun, N. Zhang, and S. Le, "Optimization on fabrication and performance for SOFC," *J. Solid State Electrochem.*, vol. 13, pp. 455–467, 2009.

[223] S. A. M. Ali, M. Anwar, N. A. Baharuddin, M. R. Somalu, and A. Muchtar, "Enhanced electrochemical performance of LSCF cathode through selection of optimum fabrication parameters," *J. Solid State Electrochem.*, 2017.

[224] B. S. Prakash, S. S. Kumar, and S. T. Aruna, "Effect of composition on the polarization and ohmic resistances of LSM/YSZ composite cathodes in solid oxide fuel cell," *Bull. Mater. Sci*, vol. 40, no. 3, pp. 441–452, 2017.

[225] A. Montenegro-Hernández, "Estudio de reacción de electrodo de compuestos Ln2NiO4+d (Ln: La, Pr Y Nd) y reactividad con diferentes electrolitos," Instituto Balseiro-Universidad Nacional de Cuyo, 2013.

[226] V. V Srdi, R. P. Omorjan, and J. Seydel, "Electrochemical performances of (La , Sr) CoO 3 cathode for zirconia-based solid oxide fuel cells," *Mater. Sci. Eng. B*, vol. 116, pp. 119–124, 2005.

[227] L. V Mogni, “Estudio de nuevos conductores mixtos para aplicaciones electroquímicas de alta temperatura,” *Asoc. Argentina Mater.*, vol. 5, no. 1, pp. 14–23, 2008.

[228] J. Nielsen and J. Hjelm, “Impedance of SOFC electrodes : A review and a comprehensive case study on the impedance of LSM : YSZ cathodes,” *Electrochim. Acta*, vol. 115, pp. 31–45, 2014.

[229] A. Kromp, *Model-based Interpretation of the Performance and Degradation of Reformate*. KIT Scientific Publishing, 2013.

[230] S. B. Adler, J. A. Lane, and B. C. H. Steele, “Electrode Kinetics of Porous Mixed − Conducting Oxygen Electrodes,” *J. Electrochem. Soc.*, vol. 143, no. 11, pp. 3554–3564, 1996.

[231] J. Nielsen, T. Jacobsen, and M. Wandel, “Impedance of porous IT-SOFC LSCF : CGO composite cathodes,” *Electrochim. Acta*, vol. 56, no. 23, pp. 7963–7974, 2011.

[232] Y. Fu, “Theoretical and experimental study of Solid Oxide Fuel Cell (SOFC) using Impedance Spectra,” Massachusetts Institute of technology, 2014.

[233] B. H. Park and G. M. Choi, “Electrochemical performance and stability of La0.2Sr0.8Ti0.9Ni0.1O3-δ and La0.2Sr0.8Ti0.9Ni0.1O3-δ - Gd0.2Ce0.8O2-δ anode with anode interlayer in H2 and CH4,” *Electrochim. Acta*, vol. 182, pp. 39–46, 2015.

[234] N. Grunbaum, L. Dessemond, J. Jouletier, F. Prado, and A. Caneiro, “Electrode reaction of Sr1−x La x Co0.8Fe0.2O3−δ with x = 0 . 1 and 0 . 6 on Ce0.9Gd0.1O1.95 at 600≤T≤800 °C,” *Solid State Ionics*, vol. 177, pp. 907–913, 2006.

[235] C. F. Martínez-Setevich, “propiedades de las perovskitas ABO3 (A=La, Ba y B=Co, Fe) como material de cátodo en celdas de combustible IT-SOFC,” Universidad Nacional del Sur, 2014.

[236] K. Yakal-kremski, L. V Mogni, A. Montenegro-hern, A. Caneiro, S. A. Barnett, and N. D. I. Cient, “Determination of Electrode Oxygen Transport Kinetics Using Electrochemical Impedance Spectroscopy Combined with Three-Dimensional Microstructure Measurement : Application to Nd 2 NiO 4 + δ,” vol. 161, no. 14, pp. 1366–1374, 2014.

[237] J. D. Sirman and J. A. Kilner, “Surface exchange properties of Ce0.9Gd0.1O2 Coated with La1-xSrxFeyCo1 -yO3,” *Electrochem. Soc.*, vol. 143, no. 10, pp. 3–6, 1996.

[238] C. Sun and U. Stimming, “Recent anode advances in solid oxide fuel cells,” *J. Power Sources*, vol. 171, pp. 247–260, 2007.

[239] Y. Aikawa, T. Katsufuji, T. Arima, and K. Kato, “Effect of Mn trimerization on the magnetic and dielectric properties of hexagonal YMnO 3,” *Phys. Rev. B*, vol. 71, no. 184418, pp. 1–5, 2005.

[240] H. Search, C. Journals, A. Contact, M. Iopscience, and I. P. Address, “Structural Phase Transition and Domain Structures in YMn1- x Ti x O3,” vol. 7174, pp. 18–21.

[241] L. S. M. Traqueia, T. Pagnier, and F. M. B. Marques, “Structural and Electrical Characterization of Titania-Doped YSZ,” *J. Eur. Ceram. Soc.*, vol. 17, pp. 1019–1026, 1997.

[242] M. More, Y. Hiei, H. Itoh, G. A. Tompsett, and N. M. Sammes, “Evaluation of Ni and Ti-doped Y2O3 stabilized ZrO2 cermet as an anode in high-temperature solid oxide fuel cells,” *Solid State Ionics*, vol. 160, pp. 1–14, 2003.

[243] A. Kaiser, A. J. Feighery, D. P. Fagg, and J. T. . Irvine, “Electrical Characterization of Highly Titania Doped YSZ,” *Ionics (Kiel).*, vol. 44, pp. 215–219, 1998.

[244] M. T. Colomer and M. Maczka, “Mixed conductivity, structural and microstructural characterization of titania-doped yttria tetragonal zirconia

polycrystalline/titania-doped yttria stabilized zirconia composite anode matrices," *J. Solid State Chem.*, vol. 184, pp. 365–372, 2011.

[245] M. Zhao, X. Ren, and W. Pan, "Effect of Lattice Distortion and Disordering on the Mechanical Properties of Titania-Doped Yttria-Stabilized Zirconia," *J. Am. Ceram. Soc.*, vol. 97, no. 5, pp. 1566–1571, 2014.

[246] A. M. Lassman, "Evaluation of Cathode Materials for Low Temperature (500-700C) Solid Oxide Fuel Cells," University of Conneticut, 2011.

[247] R. Moriche, D. Marrero-López, F. J. Gotor, and M. J. Sayagués, "Chemical and electrical properties of LSM cathodes prepared by mechanosynthesis," *J. Power Sources*, vol. 252, pp. 43–50, 2014.

[248] M. Verbraeken and I. M. Science, "Advanced supporting anodes for Solid Oxide Fuel Cells," no. March, 2005.

[249] L. Sun, M. Rieu, J. Viricelle, C. Pijolat, H. Zhao, L. Sun, M. Rieu, J. Viricelle, C. Pijolat, and H. Zhao, "Fabrication and characterization of anode-supported single chamber solid oxide fuel cell based on cathode," *Int. J. Hydrogen Energy*, vol. 39, no. 2, pp. 1014–1022, 2014.

[250] D. A. Osinkin, N. M. Bogdanovich, S. M. Beresnev, and V. D. Zhuravlev, "High-performance anode-supported solid oxide fuel cell with impregnated electrodes," *J. Power Sources*, vol. 288, pp. 20–25, 2015.

[251] T. Z. Sholklapper, H. Kurokawa, C. P. Jacobson, and S. J. Visco, "Nanostructured Solid Oxide Fuel Cell Electrodes," *Nano Lett.*, vol. 7, no. 7, pp. 2136–2141, 2007.

[252] F. Dogan and P. Kumta, Eds., *Advances in Electronic and Electrochemical Ceramics*. The American Ceramic Society, 2012.

[253] H. Fritzsche, J. Hout, and D. Fruchart, Eds., *Neutron Scattering and Other Nuclear Techniques for Hydrogen in Materials*, 1st ed. Springer International

Publishing, 2016.

[254] International Union of Crystallography, “Online dictionary crystallography,” 2017. [Online]. Available: http://reference.iucr.org/. [Accessed: 17-Nov-2017].

BIBLIOGRAPHY

ABUGHAYADA, C., *et al.* Structural, magnetic, and oxygen storage properties of hexagonal $Dy_{1-x}Y_xMnO_{3+\delta}$. In: J. Solid State Chem., 2014, vol. 217, p. 127–135.

_____, *et al*. Characterization of Oxygen Storage and Structural Properties of Oxygen-Loaded Hexagonal $RMnO_{3+\delta}$ (R = Ho, Er, and Y). In: Chem. Mater., 2015, vol. 27, no. 18, p. 6259–6267.

AGENCIA DE NOTICIAS DE LA UNIVERSIDAD NACIONAL. Optimizan celdas de combustible con tecnología colombiana. 2013. [Online]. Available: http://agenciadenoticias.unal.edu.co/. [Accessed: 20-Sep-2017].

AHMED, B., *et al.* Development of Novel LSM/GDC Composite Cathode Material for Cathode-Supported Direct Carbon Fuel Cells. In: ECS Trans., 2013, vol. 57, no. 1, p. 2075–2082.

ALDANA URREA, A. V. and GRUESO CATILLO, J. M. Análisis del mercado de gas natural para la generación eléctrica. In: Retos y perspectivas 2015-2018, 2016.

ALVARADO-FLORES, J. and ÁVALOS-RODRÍGUEZ, L. Materiales para ánodos, cátodos y electrolitos utilizados en celdas de combustible de óxido sólido (SOFC). In: Rev. Mex. Física, 2013, vol. 59, p. 66–87.

_____.Análisis de la estructura perovskita $La_xSr_{1-x}Cr_yMn_{1-y}O_{3-\delta}$ con potencial aplicación como ánodo para celdas de combustible de óxido sólido. In: Boletín la Soc. Española Cerámica y Vidr., 2016, p. 1–11.

ARRIVÉ, C., *et al.* Exsolution of nickel nanoparticles at the surface of a conducting titanate as potential hydrogen electrode material for solid oxide electrochemical cells. In: J. Power Sources, 2013, vol. 223, p. 341–348.

ASAKA, T., *et al.* Crystallographic superstructure of Ti-doped hexagonal $YMnO_3$. In: Phys. Rev. B - Condens. Matter Mater. Phys., 2005, vol. 71, no. 1, p. 3–8.

ASENSIO, P., RODRIGUEZ, L. A. C and SÁNCHEZ, M. E. G., Hidrógeno y pila de combustible. Universidad Nacional del Nordeste - Argentina, Fund. la energía la Comunidad Madrid, 2011, p. 16.

ATKINSON, A., *et al.* Advanced anodes for high-temperature fuel cells. In: Nat. Mater., 2004, vol. 3, no. 1, p. 17–27.

BARSOV, S. G., *et al.* Muon investigation of $HoMnO_3$ and $YMnO_3$ hexagonal manganites. In: JETP Lett., 2007, vol. 85, no. 12, pp. 658–661.

BETANCURT ALARCÓN, L. Energías renovables ayudarían a evitar apagón: WWF, El tiempo, 2016. [Online]. Available: http://www.eltiempo.com/. [Accessed: 28-Apr-2017].

BLENNOW TULLMAR, P., *et al.* Strontium Titanate-based Composite Anodes for Solid Oxide Fuel Cells. In: ECS Trans., 2008, vol. 13, no. 26, pp. 181–194.

BLOOM ENERGY. Bloomenergy. [Online]. Available: www.bloomenergy.com. [Accessed: 17-Apr-2018].

BOIVIN, J. C., *et al.* Electrode – electrolyte BIMEVOx system for moderate temperature oxygen separation. In: Solid State Ionics, 1998, vol. 115, p. 639–651.

BOS, J.-W.; VAN AKEN, B. B. and PALSTRA, T. T. M. Disorder induced hexagonal-orthorhombic transition in $(Y,Gd)MnO_3$, 2008, p. 1–5.

BUKHARI, S. M., *et al*. Nano-socketed nickel particles with enhanced coking resistance grown in situ by redox exsolution. In: Nat. Commun., 2015.

CARACOL RADIO. Gobierno anuncia descubrimiento de gas natural en el Caribe 2017. [Online]. Available: http://caracol.com.co/. [Accessed: 19-Sep-2017].

CARVAJAL-OSORIO, H.; BABATIVA, J. H. and ALONSO, J. A. Estudio sobre producción de H_2 con hidroelectricidad para una economía de hidrógeno en Colombia. In: Ing. y Competividad, 2010, vol. 12, no. 1, p. 3–42

CHANDRAN, P. R. and ARJUNAN, T. V. A Review of Materials used for Solid Oxide Fuel Cell. In: Int. J. ChemTech Res., 2015, vol. 7, no. 1, p. 974–4290.

Chapter 4 Ionic conductivity of GDC electrolyte [Anonymous], p. 64–88.

CHEN, K. and JIANG, S. P. Degradation and durability of electrodes of solid oxide fuel cells. In: Materials for High-Temperature Fuel Cells, 1st ed., Eds. Wiley-VCH Verlag GmbH & Co. KGaA, 2013, p. 245–307.

CHEN, M.; HALLSTEDT, B. and GAUCKLER, L. J. Thermodynamic assessment of the Mn–Y–O system. In: J. Alloys Compd., 2005, vol. 393, no. 1–2, p. 114–121.

CORREDOR-ROJAS, L. M. Pilas de combustible y su desarrollo. In: Ing. y Univ., 2012, vol. 16, no. 1, p. 247–263.

DE BOER, B. SOFC Anode: Hydrogen oxidation at porous nickel and nickel/yttria-stabilised zirconia cermet electrodes. Universiteit Twente, 1998.

DE FLORIO, D. Z., *et al.* Materiais cerâmicos para células a combustível (Ceramic materials for fuel cells). In: Cerâmica, 2004, vol. 50, p. 275–290.

DELAHAYE, T., *et al.* Electrochemical properties of novel SOFC dual electrode $La_{0.75}Sr_{0.25}Cr_{0.5}Mn_{0.3}Ni_{0.2}O_{3-d}$. In: Solid State Ionics, 2011, vol. 184, no. 1, p. 39–41.

DOS SANTOS-GÓMEZ, L., *et al.* Chemical stability and compatibility of double perovskite anode materials for SOFCs. In: Solid State Ionics, 2013, vol. 239, p. 1–7.

DUBOURDIEU, C., *et al.* Thin films and superlattices of multiferroic hexagonal rare earth manganites. In: Philos. Mag. Lett., 2007, vol. 87, no. 3–4, p. 203–210.

EG&G TECHNICAL SERVICES INC. Fuel Cell Handbook, 7 Edition. Morgantown, West Virginia, 2004.

ESQUIROL, A., *et al.* Cathodes for Intermediate-Temperature SOFCs. In: J. Electrochem. Soc., 2004, vol. 151, no. 11, p. 1–10.

FLÓREZ SUÁREZ, E. Estado Actual del Hidrógeno Índice. Universidad Nacional Autónoma de México, 2016.

FORTAL'NOVA, E. A., *et al.* Phase Transitions and Electroconducting Properties of BIMEVOx Solid Electrolytes. In: Russ. J. Phys. Chem. A, 2008, vol. 82, no. 10, p. 1829–1835.

FU, Q. X., Tietz, F., and Stöver, D. Solid Oxide Fuel Cells, 2006, p. 74–83.

GARCÉS, D. A. Estudio de perovskitas $LaBaCo_2O_{6-\delta}$: Propiedades de alta temperatura y su evaluación como potenciales materiales para celdas de combustible o electrolíticas de óxido sólido. Instituto Balseiro, 2014.

GIBBS, A. S.; KNIGHT, K. S. and LIGHTFOOT, P. High-temperature phase transitions of hexagonal $YMnO_3$. In: Phys. Rev. B, vol. 83, no. 9, p. 94111, 2011.

GORTE, R. J.; Vohs, J. M., and MCINTOSH, S. Recent Developments on Anodes for Direct Fuel Utilization in SOFC Recent Developments on Anodes for Direct Fuel Utilization in SOFC. In: Solid state Ion., 2004, vol. 175, no. 1–4.

GROSS, M. D.; VOHS, J. M. and GORTE, R. J. A Strategy for Achieving High Performance with SOFC Ceramic Anodes, 2007, p. 65–69.

GRUNBAUM, N. Estudios estructurales y fisicoquímicos de cátodos para celdas combustibles de alta temperatura. Instituto Balseiro, 2006.

HAAG, J. M., *et al.* Structural and Chemical Evolution of the SOFC Anode and in Situ Neutron Diffraction Study. In: Chem. Mater., 2010, vol. 22, p. 3283–3289.

HAILE, S. M. Materials for fuel cells. In: Mater. Today, 2003, p. 24–29.

HASHIMOTO, S., *et al.* A study on the structural and electrical properties of lanthanum-doped strontium titanate prepared in air. In: J. Alloys Compd., 2005, vol. 397, no. 1–2, p. 245–249.

HENGYONG, T. and STIMMING, U. Advances, aging mechanisms and lifetime in solid-oxide fuell cells. In: J. Power Sources, 2004, no. 1–2, p. 284–293.

HIGUERAS, D. El camino a la sostenibilidad energética en Colombia. In: Semana Sostenible, 2016. [Online]. Available: http://sostenibilidad.semana.com/. [Accessed: 28-Apr-2017].

HÖÖK, M. and TANG, X. Depletion of fossil fuels and anthropogenic climate change-A review. In: Energy Policy, 2013, vol. 52, p. 797–809.

HOLTAPPELS, P., *et al.* The influence of mixed ionic electronic conductivity in the hydrogen electrode reaction in solid state electrochemical cells. University of Twente.

I. E. Agency, “Oil Market Report,” 2017. [Online]. Available: https://www.iea.org/. [Accessed: 06-Mar-2017].

IRVINE, J. T. S. Perovskite oxide anodes for SOFC. In: Perovskite Oxide for Solid Oxide Fuel Cells. Ed. Springer Science+Bussines Media, 2009, p. 167–82.

TIETZ, F. Thermal Expansion of SOFC Materials. In: Ionics (Kiel*)*, 1999, vol. 5, p. 129–139.

ISHIHARA, T. Structure and properties of perovskite Oxides. In: Perovskite Oxide for Solid Oxide Fuel Cells. Ed. New York: Springer Science+Bussines Media, 2009, p. 1–15.

ISTOMIN, S. Y., *et al.* High-Temperature Properties of New Perovskite-Like Oxides, 2017, vol. 62, no. 8, p. 1021–1025.

JARDIEL, T., *et al*. New SOFC electrode materials: The Ni-substituted LSCM-based compounds $(La_{0.75}Sr_{0.25})(Cr_{0.5}Mn_{0.5-x}Ni_x)O_{3-d}$ and $(La_{0.75}Sr_{0.25})(Cr_{0.5-x}Ni_xMn_{0.5})O_{3-d}$. In: Solid State Ionics, 2010, vol. 181, no. 19–20, p. 894–901.

JIMÉNEZ, C. M. Phase transitions induced on hexagonal manganites by the incorporation of aliovalent cations on A or B lattice sites. In: Boletín la Soc*.,* 1999, vol. 38, no. 5, p. 417–420.

JIN, F., *et al.* Double-perovskite $PrBaCo_{2/3}Fe_{2/3}Cu_{2/3}O_{5+d}$ as cathode material for intermediate- temperature solid-oxide fuel cells. In: J. Power Sources, 2013, vol. 234, p. 244–251.

JOORIS, R., *et al.* In-depth study of the Ruddlesden-Popper $La_xSr_{2-x}MnO_{4\pm d}$ family as possible electrode materials for symmetrical SOFC. In: Hydrog. energy, 2017, p. 1–14.

KARIM, A. H., *et al.* Synthesis and characterization of $La_{0.75}Sr_{0.25}Mn_{0.5}Cr_{0.2}Ti_{0.3}O_3$ Anodes for SOFCs. In: IOP Conf. Ser. Mater. Sci. Eng., 2016, vol. 121, p. 1–5.

KAWADA, T. Perovskite Oxide for Cathode SOFCs. In: Perovskite Oxide for Solid Oxide Fuel CellS. Ed. New York: Springer Science+Bussines Media, 2009, p. 147–164.

KIM, J. and MANTHIRAM, A. Layered $LnBaCo_2O_{5+d}$ perovskite cathodes for solid oxide fuel cells: an overview and perspective. In: J. Mater. Chem. A Mater. energy Sustain., 2015, vol. 3, p. 24195–24210.

_____, *et al.* Highly efficient and robust cathode materials for low-temperature solid oxide fuel cells: $PrBa_{0.5}Sr_{0.5}Co_{22x}Fe_xO_{51d}$. In: Sci. Rep., 2013, vol. 3, p. 1–5.

KWON, O., *et al.* Exsolution trends and co-segregation aspects of self-grown catalyst nanoparticles in perovskites. In: Nat. Commun., 2017, vol. 8, no. May, p. 1–7.

LAY, E., *et al.* Ce-substituted LSCM as new anode material for SOFC operating in dry methane. In: Solid State Ionics, 2008, vol. 179, no. 27–32, p. 1562–1566.

_____; GAUTHIER, G. and DESSEMOND, L. Preliminary studies of the new Ce-doped La/Sr chromo-manganite series as potential SOFC anode or SOEC cathode materials. In: Solid State Ionics, 2011, vol. 189, no. 1, p. 91–99.

LESCANO, G., *et al.* Synthesis and electrical conductivity of $Y_{1-x}Mn_{1-y}O_{3-d}$. In: J. Eur. Ceram. Soc., 2001, vol. 21, no. 10–11, p. 2037–2040.

LEVIN, I., *et al.* Oxygen-storage behavior and local structure in Ti-substituted $YMnO_3$. In: J. Solid State Chem., 2017, vol. 246, p. 29–41.

NASA. Global Warming. In: Nasa Facts, 1998, p. 1–4.

MA, Z., *et al*. Ni doped $La_{0.6}Sr_{0.4}FeO_{3-\delta}$ symmetrical electrode for solid oxide fuel cells. In: Chinese J. Catal., 2016, vol. 37, no. 8, p. 1347–1353.

MACÍAS, J.; YAREMCHENKO, A. A. and FRADE, J. R. Enhanced stability of Perovskite-like $SrVO_3$-based anode materials by donor-type substitutions. In: Mater. Chem. A, no. 26, 2016.

MARINA, O. A.; CANFIELD, N. L., and STEVENSON, J. W. Thermal, electrical, and electrocatalytical properties of lanthanum-doped strontium titanate. In: Solid State Ionics, 2002, vol. 149, no. 1–2, p. 21–28.

MARTÍNEZ, A., *et al.* Estudio de factibilidad de la economia del Hidrógeno en Colombia. In: Innov. Res. Eng. Educ. key factor Glob. Compet., 2013, p. 8.

MAYÉN-MONDRAGÓN, R. Celdas de combustible de Óxido Sólido..... ¿Una de las soluciones al problema energético?. In: Ideas CONCYEG, 2011, vol. 7, no. 72, p. 647–661

MEJÍA-ARANGO, J. G. and ACEVEDO-ÁLVAREZ, C. A. Proyección al año 2025 para el uso del hidrógeno en el sector transporte del Valle de Aburrá. In: Sci. Tech. Año XVIII, 2013, vol. 18, no. 2, p. 327–334.

_____ and MONTES HINCAPIÉ, J. M. Conveniencia de incorporar las celdas de combustible en el sector del transporte del Valle de Aburrá. In: Cienc. Tecnol. Soc., 2011, no. 5, pp. 74–86.

MENCH, M. M. Fuel cell engines. Hoboken, New Jersey: John Wiley & Sons, Inc, 2008.

MINH, N. Q., Ceramic Fuel Cells. In: *J.* Am. Ceram. Soc., 1993, vol. 76, no. 3, p. 563–588.

MOGENSEN, M., LINDEGAARd, T., and HANSEN, U. R. Physical Properties of Mixed Conductor Solid Oxide Fuel Cell Anodes of Doped CeO_2. In: Electrochem. Soc., 1994vol. 141, no. 8, p. 2122–2128.

MOGNI, L. V. Estudio de nuevos conductores mixtos para aplicaciones electroquímicas de alta temperatura. Instituto Balseiro, 2007.

MOURE, C., *et al.* Structural Characterization of $YMe_xMn_{1-x}O_3$ (Me=Cu, Ni, Co) Perovskites. In: J. Solid State Chem., 2002, vol. 163, no. 2, p. 377–384.

OSPINA CASTILLO, J. Análisis y evaluación política de Gas natural y el desarrollo de activos de flexibilidad dentro del plan de abastecimiento. Bogotá, 2017.

OVALLE, A., *et al.* Mn-substituted titanates as efficient anodes for direct methane SOFCs. In: Solid State Ionics, 2006, vol. 177, p. 1997–2003.

PARK, J., *et al.* Doping effects of multiferroic manganites $YMn_{0.9}X_{0.1}O$ (X= Al, Ru, and Zn). In: Phys. Rev. B, 2009, vol. 79, p. 1–6.

PÉRILLAT-MERCEROZ, C. Titanates de structures pérovskite et dérivées: Influence des éléments constitutifs et de la dimensionnalité sur les propriétés d'anode SOFC. Université des Sciences et Technologie de Lille - Lille I, 2009.

_____, *et al.* Lamellar titanates: A breakthrough in the search for new solid oxide fuel cell anode materials operating on methane. In: Adv. Energy Mater., 2011, vol. 1, no. 4, p. 573–576.

_____, *et al.* Synthesis and Study of a Ce-Doped La/Sr Titanate for Solid Oxide Fuel Cell Anode Operating Directly on Methane. In: Chem. Mater., 2011, vol. 23, p. 1539–1550.

PFEIFER, T., *et al.* In: Ceramics for Energy Conversion, Storage, and Distribution Systems, John Wiley & Sons, Inc, 2016, vol. 155.

PHILIPPEAU, B., *et al.* Comparative study of electrochemical properties of mixed conducting $Ln_2NiO_{4+\delta}$ (Ln=La, Pr and Nd) and $La_{0.6}Sr_{0.4}Fe_{0.8}Co_{0.2}O_{3-\delta}$ as SOFC

cathodes associated to $Ce_{0.9}Gd_{0.1}O_{2-\delta}$, $La_{0.8}Sr_{0.2}Ga_{0.8}Mg_{0.2}O_{3-\delta}$ and $La_9Sr_1Si_6O_{26.5}$ electrolytes. In: Solid State Ionics, 2013, vol. 249–250, p. 17–25.

PILLAI, M. R., *et al.* Fuel-flexible operation of a solid oxide fuel cell with $Sr_{0.8}La_{0.2}TiO_3$ support. In: J. Power Sources, 2008, vol. 185, no. 2, p. 1086–1093.

PIROVANO, C., *et al.* Characterisation of the electrode – electrolyte BIMEVOx system for oxygen separation Part I. In situ synchrotron study. In: Solid State Ionics, 2003, vol. 159, p. 167–179.

POSSO, F. R. and SÁNCHEZ, J. P. El desarrollo del Sistema Energético Solar-Hidrógeno en América Latina : Potencialidades , oportunidades y barreras. In: Rev. Semest. la DIUC, 2014, vol. 5, no. 2, p. 61–79.

RAMÍREZ HERNÁNDEZ, A. Las celdas de combustible de óxidos sólidos (SOFC) como fuentes de energía renovable, 2011. [Online]. Available: http://www.posgradoeinvestigacion.uadec.mx/. [Accessed: 20-Sep-2017].

RAJENDRA, N.B.; MUKHOPADHYAY, J. and ABHIJIT DAS, S. High Temperature Fuel Cell. In: Proc. Indian Natl. Sci. Acad., 2015, vol. 81, no. 4, p. 841–864.

REMSEN, S. Remsen. Properties of transition metal oxides for gas separation and oxygen storage applications, 2011.

_____ and DABROWSKI, B. Synthesis and Oxygen Storage Capacities of Hexagonal $Dy_{1-x}Y_xMnO_{3+\delta}$. In: Chem. Mater., 2011, vol. 23, no. 17, p. 3818–3827.

REN, P., FAN, H. and WANG, X. Bulk conduction and nonlinear behaviour in multiferroic $YMnO_3$ Bulk conduction and nonlinear behaviour in multiferroic $YMnO_3$. vol. 152905, 2013.

ROMITO, K. G., Synthesis and Characterization of New Ionic and Mixed Ionic/ Electronic Conductors. University of South Carolina, 2013.

RUIZ-MORALES, J. C, *et al.* Symmetric and reversible solid oxide fuel cells. In: *RSC Adv.*, 2011, vol. 1, no. 8, p. 1403.

_____, *et al.* On the simultaneous use of $La_{0.75}Sr_{0.25}Cr_{0.5}Mn_{0.5}O_{3-\delta}$ as both anode and cathode material with improved microstructure in solid oxide fuel cells. In: *Electrochim. Acta*, 2006, vol. 52, p. 278–284.

SAMMES, N. M. and ZHINHONG, C. Ionic conductivity of ceria/yttria stabilized zirconia electrolyte materials. In: Solid State Ionics, 1997,vol. 2738, no. 97, p. 39–44.

SALAZAR-KURI, U.; MENDOZA, M. E. and SIQUEIROS, J. M. Phase transition in multiferroic $YMnO_3$ and its solid solution $YMn_{(0.93)}Fe_{(0.07)}O_3$. In: Phys. B Condens. Matter, 2012, vol. 407, no. 17, p. 3551–3554.

SHARMA, M.; RAKESH, N. and DASAPPA, S. Solid oxide fuel cell operating with biomass derived producer gas: Status and challenges. In: Renew. Sustain. Energy Rev., 2016, vol. 60, p. 450–463.

SINGH, O. and SINGH, Bharat Raj. Global Trends of Fossil Fuel Reserves and Climate Change in the 21st Century in World's largest Science, Technology & Medicine. S. Khan, Ed. In Tech, 2012, p. 167–192.

SINGHAL, S. C. Advances in solid oxide fuel cell technology. In: Solid State Ionics, 2000, vol. 135, pp. 305–313.

Sistema de generación con pila de combustible de óxido sólido [Anonymous]. In: Sistema de generación eléctrica con pila de combustible de óxido sólido alimentado con residuos forestales y su optimización mediante algoritmos basados en nubes de partículas, p. 105–140.

SKINNER, G. and Amow, S. J. Recent developments in Ruddlesden – Popper nickelate systems for solid oxide fuel cell cathodes. In: J. Solid State Electrochem., 2006, p. 538–546.

SKINNER, S. J. and kilner, J. A. Oxygen ion conductors. In: Mater. Today, 2003, p. 30–37.

SOTERO, W.; LIMA, A. F. Lima and LALIC M. V. Analysis of the Mn–O and Y–O bonds in paraelectric and ferroelectric phase of magnetoelectric $YMnO_3$ from the first principles calculations. In: J. Alloys Compd., 2015, vol. 649, p. 285–290.

SRFEO, À., *et al.* Symmetric electrodes for solid oxide fuel cells based on Zr-doped, 2015, vol. 279, p. 419–427.

SUÁREZ, W. El reto de energizar zonas rurales aisladas. *Semana Sostenible*, 2016. [Online]. Available: http://sostenibilidad.semana.com. [Accessed: 28-Apr-2017].

TAKAHASHI, S., *et al.* Electrode Properties of the Ruddlesden–Popper Series, $La_{n+1}Ni_nO_{3n+1}$ (n=1, 2, and 3), as Intermediate-Temperature Solid Oxide Fuel Cells. In: J. Am. Ceram. Soc., 2010, vol. 2333, no. 27257, p. 2329–2333.

TAKAMURA, H. MIEC Materials. In: Encyclopedia of Applied Electrochemistry, Eds. Springer New York, 2014, p. 1297–1300.

TAO, S. and IRVINE, J. T. S. A redox-stable efficient anode for solid-oxide fuel cells. In: Nat. Mater., 2003, vol. 2, no. 5, p. 320–323.

TIETZ, F. Thermal Expansion of SOFC Materials. In: Ionics (Kiel), 1999, vol. 5, p. 129–139.

TULLER, H.; SCHOONMAN, J. and RIESS, I. Oxygen Ion and Mixed Conductors and their Technological Applications, 1st ed. Springer Netherlands, 2000.

UPME. Colombia garantiza confiabilidad energética con nuevo plan de expansión. Bogotá, 2016.

VAN AKEN, B. B.; MEETSMA, A and PALSTRA, T. T. Hexagonal $YMnO_3$. In: Acta Crystallogr. C., 2001, vol. 57, no. Pt 3, p. 230–2.

VANGUARDIA. Descubren uno de los mayores yacimientos de gas natural en Colombia, 2017. [Online]. Available: http://www.vanguardia.com/. [Accessed: 19-Sep-2017].

VEGA CASTILLO, J. E. Estabilidad termodinámica y propiedades eléctricas de los compuestos $La_2Mo_{2-x}W_xO_{9-D}$. Instituto Balseiro, 2013.

VERHOEVEN, R. H. F. Characterisation of $La_{0.75}Sr_{0.25}Cr_{0.50}Mn_{0.50}O_{3-\delta}$ (LSCM) redox-stable perovskite anodes for solid oxide fuel cells. University of Twente, 2006

_____. Symmetric cells of LSCM on a TZ3Y electrolyte, no. March, 2006.

VERT BELENGUER, V. B. Electrodos avanzados para Pilas De Combustible de Óxido Sólido (SOFCs). Universitat Politecnica de Valencia, 2011.

WEI, T., *et al.* $Sr_{3-3x}Na_{3x}Si_3O_{9-1.5x}$ (x=0.45) as a Superior Solid Oxide-ion Electrolyte for Intermediate-temperature Solid Oxide Fuel Cells. In: Energy Environ. Sci., 2014, p. 1–15.

WUEBBLES, D. J. and JAIN, A. K. Concerns about climate change and the role of fossil fuel use. In: Fuel Process. Technol., 2001, vol. 71, no. 1–3, p. 99–119.

XATACA COLOMBIA. Se descubre el pozo de gas natural más grande de Colombia, 2017. [Online]. Available: https://www.xataka.com.co/. [Accessed: 19-Sep-2017].

XIA, L. N., *et al.* Synthesis and properties of $SmBaCo_{2-x}Ni_xO_{5+d}$ perovskite oxide for IT-SOFC cathodes. In: Ceram. Int., 2016, vol. 42, no. 1, p. 1272–1280.

XUE, J.; Shen, Y., and He, T. Double-perovskites $YBaCo_{2-x}Fe_xO_{5+d}$ cathodes for intermediate-temperature solid oxide fuel cells. In: J. Power Sources, 2011, vol. 196, no. 8, p. 3729–3735.

YANG, G., *et al.* Advanced Symmetric Solid Oxide Fuel Cell with an Infiltrated K_2NiF_4 -Type La_2NiO_4 Electrode. In: Energy & Fuels, 2014, vol. 28, no. 1, p. 356–362.

ZHANG, L., *et al.* Effects of Pr-deficiency on thermal expansion and electrochemical properties in $Pr_{1-x}BaCo_2O_{5+d}$ cathodes for IT-SOFCs. In: Electrochim. Acta, 2016, vol. 212, pp. 522–534.

ZHANG, Q. H., *et al.* Oxygen vacancy ordering and its mobility in $YMnO_3$. In: J. Alloys Compd., 2015, vol. 648, p. 253–257.

ZHINHONG, D., *et al.* High-Performance Anode Material $Sr_2FeMo_{0.65}Ni_{0.35}O_{6-\delta}$ with In Situ Exsolved Nanoparticle Catalyst. In: ACS Nano, 2016, p. 8660−8669.

ZHOU, X., *et al.* Progress in La-doped SrTiO3 (LST)-based anode materials for solid oxide fuel cells. In: RSC Adv., 2014, vol. 4, no. 1, p. 118–131.

ZURLO, F., *et al.* Copper-doped lanthanum ferrites for symmetric SOFCs. In: Acta Mater., 2016, vol. 112, p. 77–83.

ANNEXES

ANNEX A. RIETVELD AND LE BAIL METHODS

The X-ray diffraction technique is well complemented by a structure refinement analysis using the methods of Rietveld or Le Bail that allow extracting structural information from the diffractograms. Based on the diffraction data, both methods allow to refine the structure in a more or less complete from using always a pre-existing model, applying least squares method to minimize the difference between experimental and calculated data [40]:

$$S_y = \sum_i W_i \, (y_i(obs) - y_i(calc))^2$$

Where S_y is the difference function.
y_i *(obs)*, the measured intensity.
y_i *(calc)*, the calculated intensity.
And W_i, the weight of each intensity.

It is important to emphasize that this approximation requires that the starting parameters be close to what is to be obtained. So, the best values for the lattice parameters, the atomic positions of the elements in the compound and their occupation in the phase are calculated. In addition, if required, the Rietveld method makes it possible to quantify the phase amount (in case there is more than one in the sample), and it is possible to know the size of the crystallites and the micro-tensions in them [169].

The refinement of the Le Bail type is simpler and faster than the Rietveld, since it does not include the structural factors. Thus, it only allows the refinement of the

lattice parameters based on the individual analysis of the intensity of the reflections allowed by the symmetry elements of the space group [169].

Both methods are evaluated with four parameters; the lower their value, the better the fit quality [44]. The factors are detailed below [253]:

i) The weighted profile R-factor (R_{wp}): it measures the agreement between the calculated and the experimental patterns. taking into account the different weight (w_i) of each peak

$$R_{w\mathrm{p}} = \sqrt{\frac{\sum_i w_i (y_i - y_{ci})^2}{\sum_i w_i {y_i}^2}}$$

ii) The expected weighted profile R-factor (R_{exp}): it is called expected due to the fact that N-P+C is the desired value for the numerator in R_{wp} factor and it is used to compare the quality of refinements.

$$R_{ex\mathrm{p}} = \sqrt{\frac{N - \mathrm{P} + C}{\sum_i w_i {y_i}^2}}$$

Where N is the number of data points, P the number of fitted parameters and C the number of constraints.

iii) Goodness of fit (GoF): it measures the quality of the fit in terms of chi-square (χ^2). Its value should approach 1.

$$GoF = \sqrt{\chi^2} = \frac{R_{w\mathrm{p}}}{R_{ex\mathrm{p}}}$$

iv) The Bragg R-Factor (R_B): it is used to measure the agreement between the reflection intensities calculated from a crystallographic model and those measured experimentally. This depends on the fit of the structural parameters and not on the profile parameters [254]:

$$R_B = \frac{\sum_{hkl}|I_{hkl}(obs) - I_{hkl}(cal)|}{\sum_{hkl} I_{hkl}(obs)}$$

ANNEX B. REFINED ATOMIC POSITIONS DETERMINED BY RIETVELD REFINEMENT FOR POWDERS OF $YMnO_3$ AND $Y_{0.9}Zr_{0.1}MnO_3$ PREPARED BY SOLID STATE SYNTHESIS

a). $YMnO_3$ (space group: *P*6_3*cm*)

Atom	Wyckoff position	x	y	z	U_{eq}
Y_1	2[a]	0	0	0.2729(5)	0.01481(26)
Y_2	4b	1/3	2/3	0.2323(3)	0.1452(15)
Mn	6c	0.3263	0	0.0005(20)	0.01715(48)
O_1	6c	0.3136	0	0.1604(40)	0.0096(20)
O_2	6c	0.6328	0	0.3389(43)	0.0096
O_3	2[a]	0	0	0.4700(45)	0.0096
O_4	4b	1/3	2/3	0.0150(29)	0.0096

b). $Y_{0.9}Zr_{0.1}MnO_3$ (space group: *P*6_3*cm*)

Atom	Wyckoff position	x	y	z	U_{eq}
Y_1	2[a]	0	0	0.2663(8)	0.0093(42)
Zr_1	2[a]	0	0	0.2663	0.0093
Y_2	4b	1/3	2/3	0.2404(7)	0.0381(44)
Zr_2	4b	1/3	2/3	0.2404	0.0381

Atom	Wyckoff position	x	y	z	U_{eq}
Mn	6c	0.3359(99)	0	-0.0086(23)	0.0187(13)
O_1	6c	0.3085(18)	0	0.1531(10)	0.0404(57)
O_2	6c	0.6566(21)	0	0.3300(90)	0.04040
O_3	2^a	0	0	0.4919(68)	0.04040
O_4	4b	1/3	2/3	0.0269(41)	0.04040

ANNEX C. RESULTS OF RIETVELD REFINEMENT USING NEUTRON DIFFRACTION DATA FOR $Y_{0.9}Zr_{0.1}MnO_{3+\delta}$ PREPARED BY PECHINI METHOD

Neutron diffraction (ND) analysis was carried out for as-synthesized Zr-doped $YMnO_3$. Using only FPM refinement, *i.e.* without including the cell content, the neutron diffraction pattern can be indifferently indexed using either $P6_3cm$ or $P6_3/mmc$ space groups, with quite good R-factors, as shown in (a) and (b):

a). Space group: $P6_3/mmc$; **lattice parameters:** a=3.5517 Å, c=11.2611 Å, **Reliability factors:** GOF=1.55, R_p=2.24, R_{wp}=2.86.

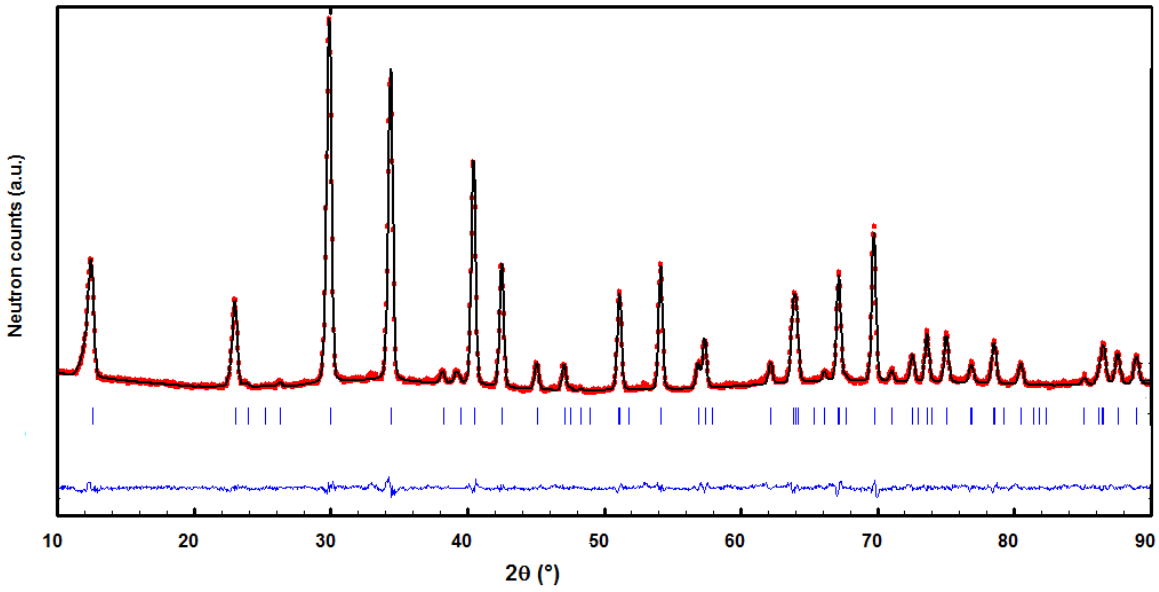

b). Space group: $P6_3cm$; **lattice parameters:** a=6.1518 Å, c=11.2582 Å, **Reliability factors:** GOF=1.43, R_p=2.05, R_{wp}=2.61.

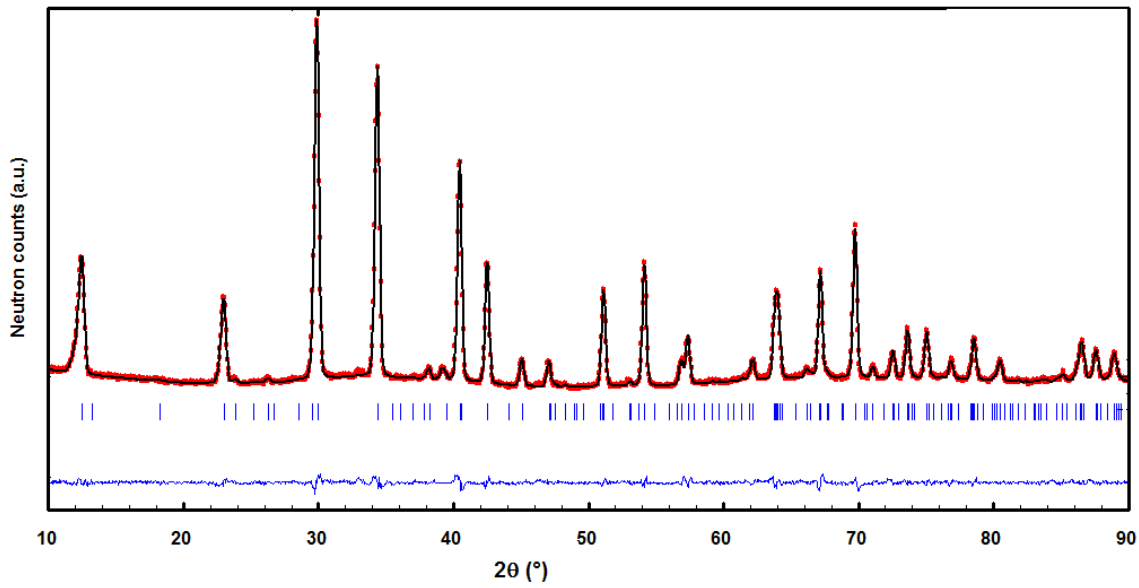

However, the corresponding Rietveld refinements yield high values of reliability factors in both cases (c) and (d):

c). Space group: $P6_3/mmc$; **lattice parameters:** a=3.5517 Å, c=11.2611 Å, **Reliability factors:** GOF=1.72, R_p=3.93, R_{wp}=5.44, R_B=11.98.

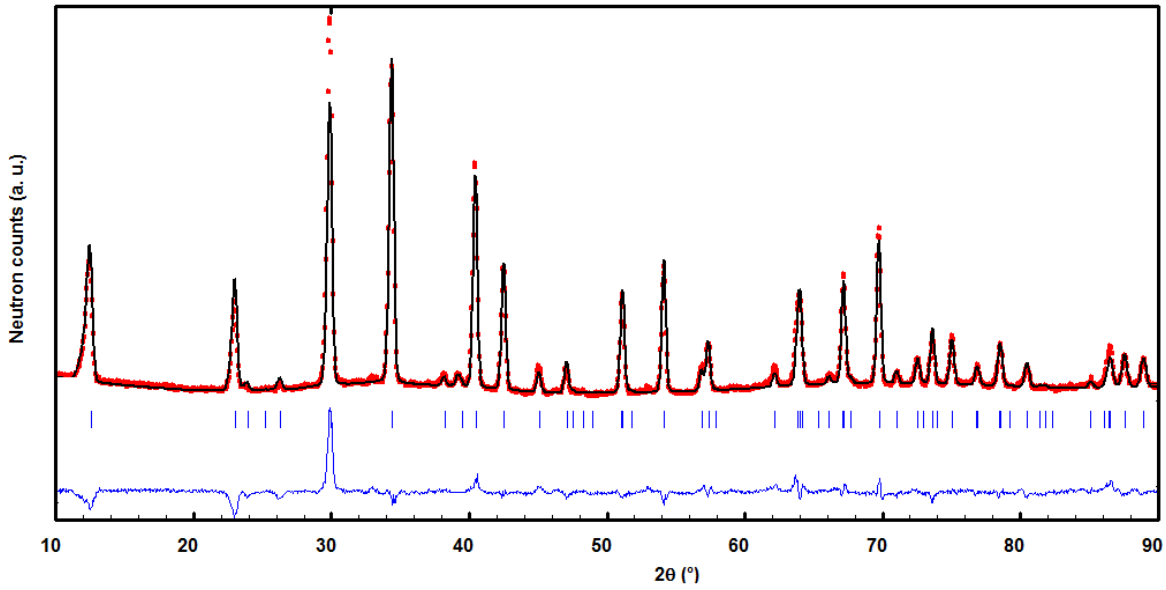

Atom	Wyckoff position	x	y	z	U_{iso}
Y	4e	0	0	-0.0223(2)	0.0122(6)
Zr	4e	0	0	-0.0223	0.0122
Mn	2c	1/3	2/3	1/4	0.0155(4)
O_1	4f	1(3	2/3	0.0850(7)	0.0134(2)
O_2	2b	0	0	1/4	0.0530(5)

d). Space group: *P*6$_3$*cm*; **lattice parameters:** *a*=6.1520 Å, *c*=11.2605 Å, **Reliability factors:** GOF=1.73, R_p=4.03, R_{wp}=5.50, R_B=12.24.

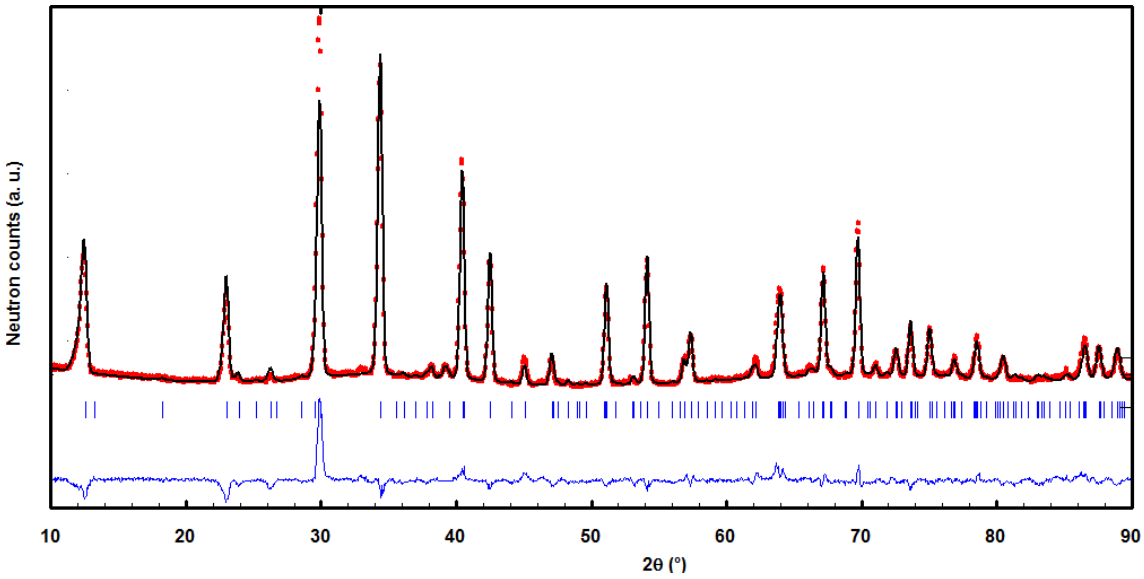

Atom	Wyckoff position	x	y	z	U_{iso}
Y_1	2a	0	0	0.2489(6)	0.0378(2)
Zr_1	2a	0	0	0.2489	0.0378
Y_2	4b	1/3	2/3	0.2377(3)	0.0273(8)
Zr_2	4b	1/3	2/3	0.2377	0.0273
Mn	6c	0.3091(8)	0	0.0020(5)	0.0078(7)
O_1	6c	0.3156(6)	0	0.1679(3)	0.0110(7)
O_2	6c	0.6611(6)	0	0.3400(4)	0.0142(7)
O_3	2a	0	0	0.4869(5)	0.0118(8)
O_4	4b	1/3	2/3	0.0156(5)	0.0687(2)

In addition, we tried to carry out Rietveld refinements using other two models that have been described in literature for oxygen overstoichiometric compounds, *i.e.* with space groups *R*-3*c* (e) and *P*ca2$_1$ (f), respectively [140], [191]. These models had better results than the before space groups, and the difference between them is the additional oxygen atoms positions.

e). Space group: *R*3*c*; **lattice parameters:** *a*=6.1319 Å, *c*=33.6723 Å, **Reliability factors:** GOF=1.36, R_p=2.69, R_{wp}=3.34, R_B=6.92

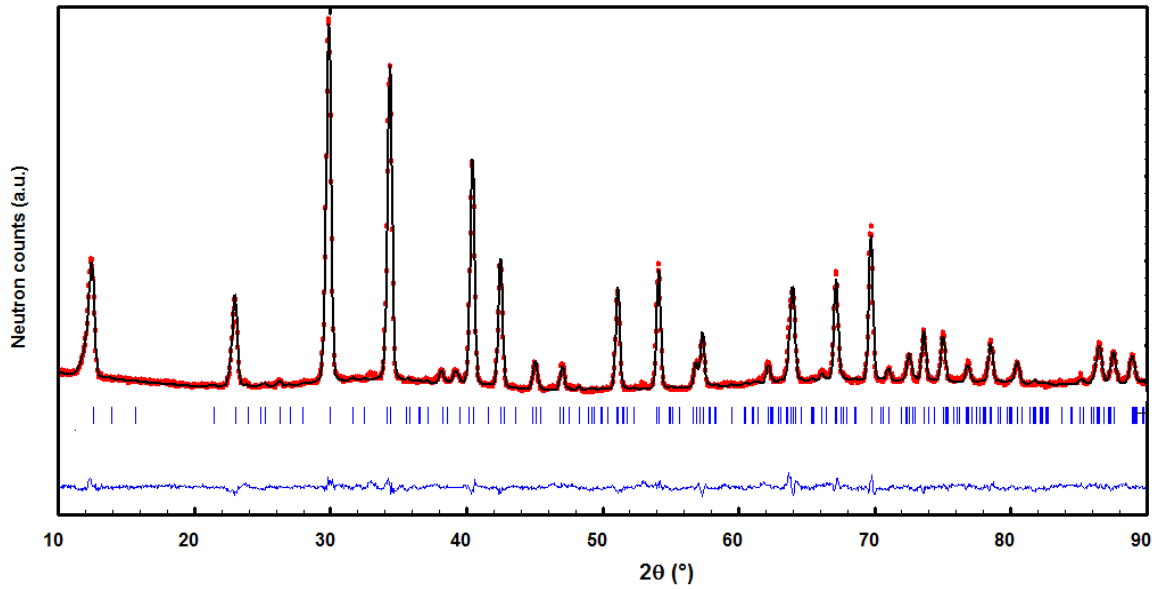

Atom	Wyckoff position	x	y	z	U_{iso}
Y_1	6a	0	0	-0.0835(1)	0.0347(1)
Zr_1	6a	0	0	-0.0835	0.0347
Y_2	6a	0	0	0.0836(2)	0.0297(9)

Atom	Wyckoff position	x	y	z	U_{iso}
Zr_2	6a	0	0	0.0836	0.0297
Y_3	6a	0	0	0.2508(2)	0.0323(1)
Zr_3	6a	0	0	0.2508	0.0323
Mn_1	18b	0.3412(9)	0.0054(1)	0.0031(1)	0.0258(1)
O_1	6a	0	0	0.1688(2)	0.0285(2)
O_2	6a	0	0	1.0045(2)	0.0326(1)
O_3	6a	0	0	0.3437(5)	0.2872(5)
O_4	18b	0.3370(5)	0.0005(6)	0.0592(1)	0.0262(1)
O_5	18b	0.0006(6)	0.3355(5)	0.2828(9)	0.0217(9)
O_6	18b	0.6413(2)	0.0315(4)	0.0013(2)	0.0618(5)

f). Space group: *Pca2$_1$*; **lattice parameters:** *a*=6.1447 Å, *b*=10.6489 Å, *c*=11.2503 Å, **Reliability factors:** GOF=1.43, R_p=2.96, R_{wp}=3.70, R_B=7.73

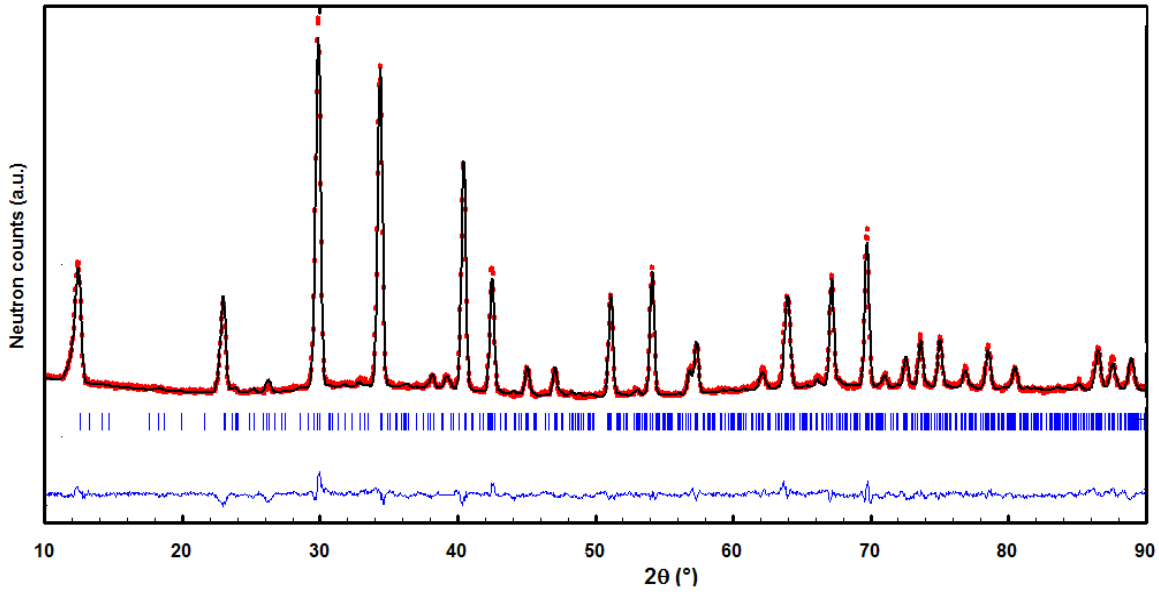

Atom	x	y	z	U_{iso}
Y_1	0.7523(2)	0.7505(4)	0.2408(2)	0.0376(1)
Zr_1	0.7523	0.7505	0.2408	0.0376
Y_2	0.2483(1)	0.9173(4)	0.2494(2)	0.0351(2)
Zr_2	0.2483	0.9173	0.2494	0.0351
Y_3	0.7566(2)	0.4166(6)	0.2444(2)	0.0702(2)
Zr_3	0.7566	0.4166	0.2444	0.0702
Mn_1	0.8954(8)	0.9146(6)	-0.0021(6)	-0.0080(8)
Mn_2	0.4057(1)	0.4121(1)	0.0019(9)	0.0177(2)
Mn_3	0.3903(9)	0.7364(4)	0.0009(7)	-0.0148(8)
O_1	0.9307(1)	0.9181(9)	0.1671(5)	0.0257(2)

Atom	x	y	z	U_{iso}
O_2	0.4272(1)	0.4135(8)	0.704(5)	0.0256
O_3	0.4147(2)	0.7435(8)	0.1699(9)	0.0257
O_4	0.5728(2)	0.5905(8)	0.3348(5)	0.0257
O_5	0.0879(1)	0.0834(8)	0.3394(5)	0.0257
O_6	0.0805(2)	0.7585(7)	0.3386(5)	0.0257
O_7	0.7758(1)	0.7744(5)	0.5378(3)	0.0257
O_8	0.2512(9)	0.9169(9)	0.1348(5)	0.0257
O_9	0.7568(9)	0.4221(9)	0.0140(5)	0.0257
O_{10}	0.6162(2)	0.5792(1)	0.0856(4)	0.0257
O_{11}	0.1408(4)	0.1395(1)	0.0134(8)	0.0257
O_{12}	0.0866(2)	0.7229(8)	0.0105(7)	0.0257

These good results we led to try a model with the *P*6$_3$*cm* and *P*6$_3$*/mmc* space groups but adding one extra oxygen position.

ANNEX D. IMPEDANCE RESPONSE OF $YMnO_3$ COMPOUND AT 600°C

pO_2 (atm)	L (Ωcm^2)	R1 (Ωcm^2)	R_{CPE1} (Ωcm^2)	t	p	R_G (Ωcm^2)	t	p	R_{CPE2} (Ωcm^2)	t	p
0.8449	2.0890E-07	5.5846	0.0522	1.4705E-04	0.9500	0.2957	0.0151	0.5000	1.9749	0.0582	0.9500
0.7426	2.0091E-07	5.6073	0.0485	14087E-04	0.9448	0.3085	0.0155	0.4994	2.2113	0.0564	0.9500
0.4558	1.7430E-07	5.6268	0.0497	11005E-04	0.9427	0.3708	0.0157	0.4999	2.8012	0.0534	0.9500
0.1963	1.5560E-07	5.6412	0.0355	6.1738E-04	0.7924	0.4873	0.0240	0.4762	4.4714	0.0485	0.9498
0.0204	9.6441E-09	5.5650	0.0848	1.3594E-04	0.6903	1.0127	0.0694	0.4364	13.0832	0.0423	0.9500
0.0138	1.3566E-07	5.6339	0.0070	1.8059E-05	0.5014	1.3046	0.1193	0.4082	16.1803	0.0418	0.9500
0.0078	1.7384E-07	5.6442	0.0016	1.1092E-04	0.6704	1.7353	0.1842	0.4063	24.5429	0.0395	0.9500
0.0044	1.1603E-07	5.6537	0.0011	3.4258E-05	0.9500	2.7330	0.4011	0.4080	34.6573	0.0387	0.9500
0.0015	9.7428E-08	5,6636	0.0027	9.6021E-04	0.5148	6.0810	0.8430	0.4698	71.0125	0.0350	0.9500
0.0006	5.1735E-08	5.6812	0.0106	1.2361E-03	0.5823	8.5337	0.9651	0.4981	111.0817	0.0314	0.9500

pO_2 (atm)	Capacitance R_{CPE1} (Fcm^2)	Capacitance R_G (Fcm^2)	Capacitance R_{CPE2} (Fcm^2)
0.8449	7.9116E-05	0.0512	0.0519
0.7426	7.0328E-05	0.0501	0.0506
0.4558	5.2674E-05	0.0424	0.0483
0.1963	3.7105E-05	0.0492	0.0448

pO_2 (atm)	Capacitance R_{CPE1} (Fcm^2)	Capacitance R_G (Fcm^2)	Capacitance R_{CPE2} (Fcm^2)
0.0204	8.2767E-07	0.0685	0.0410
0.0138	2.4916E-12	0.0914	0.0409
0.0078	5.3405E-08	0.1062	0,0394
0.0044	1.3943E-05	0.1468	0.0393
0.0015	5.147E-09	0.1386	0.0368
0.0006	3,8916E-07	0.1131	0.0335

ANNEX E. IMPEDANCE RESPONSE OF $YMnO_3$ COMPOUND AT 700°C

pO_2 (atm)	L (Ωcm^2)	R1 (Ωcm^2)	R_G (Ωcm^2)	t	p	R_{CPE2} (Ωcm^2)	t	p
0.8449	4.9910E-07	2.2655	0.0953	0.0033	0.3907	0.5229	0.0391	0.9499
0.7426	4.8496E-07	2.2742	0.1011	0.0045	0.4968	0.5549	0.0406	0.9497
0.4558	4.0038E-07	2.2757	0.1069	0.0035	0.4757	0.7302	0.0374	0.9500
0.1963	3.1864E-07	2.2755	0.1481	0.0051	0.4234	1.1853	0.0352	0.9488
0.0204	3.7678E-07	2.2839	0.2810	0.0092	0.4999	3.6428	0.0288	0.9455
0.0138	4.2120E-08	2.2928	0.3150	0.0106	0.5000	4.5277	0.0271	0.9421
0.0078	4.3000E-08	2.2889	0.3713	0.0111	0.4996	6.4543	0.0244	0.9289
0.0044	3.6449E-08	2.3025	0.4411	0.0117	0.5000	9.2449	0.0210	0.9117
0.0015	1.1254E-08	2.3354	0.6036	0.0117	0.5000	20.1155	0.0160	0.8648
0.0006	1.3322E-09	2.3645	0.7827	0.0140	0.5000	32.1597	0.0141	0.8285

pO_2 (atm)	Capacitance R_G (Fcm^2)	Capacitance R_{CPE1} (Fcm^2)
0.8449	0.0347	0.0372
0.7426	0.0448	0.0386
0.4558	0.0330	0.0355
0.1963	0.0342	0.0334
0.0204	0.0391	0.0279
0.0138	0.0564	0.0270

pO_2 (atm)	Capacitance R_G (Fcm^2)	Capacitance R_{CPE1} (Fcm^2)
0.0078	0.0587	0.0255
0.0044	0.0517	0.0231
0.0015	0.0359	0.0191
0.0006	0.0282	0.0173

ANNEX F. IMPEDANCE RESPONSE OF $YMnO_3$ COMPOUND AT 800°C

pO_2 (atm)	L (Ωcm^2)	R1 (Ωcm^2)	R_G (Ωcm^2)	t	p	R_{CPE2} (Ωcm^2)	t	p
0.8449	4.3396E-07	1.3445	0.1557	0.0049	0.5000	-	-	-
0.7426	4.7025E-07	1.3412	0.1840	0.0061	0.5000	-	-	-
0.4558	5.0221E-07	1.3443	0.2296	0.0076	0.5000	-	-	-
0.1963	4.5257E-07	1.3524	0.3276	0.0102	0.5000	-	-	-
0.0204	5.2067E-07	1.3325	0.5866	0.0160	0.4986	0.5780	0.0721	0.7773
0.0138	4.0442E-07	1.3230	0.7592	0.0128	0.5000	0.7461	0.0675	0.8301
0.0078	4.7020E-07	1.3102	1.2334	0.0166	0.4982	0.9975	0.0882	0.8125
0.0044	6.7774E-07	1.3020	1.5085	0.0158	0.5000	1.9439	0.0676	0.7832
0.0015	8.9098E-07	1.2773	3.1098	0.0256	0.5000	4.8541	0.0720	0.8035
0.0006	6.7224E-07	1.2704	4.7072	0.0390	0.5000	9.9106	0.0673	0.8179

pO_2 (atm)	Capacitance R_G (Fcm^2)	Capacitance R_{CPE1} (Fcm^2)
0.8449	31.8183	-
0.7426	30.2005	-
0.4558	30.2911	-
0.1963	32.0766	-

0.0204	36.6864	0.0290
0.0138	59.4601	0.0366
0.0078	74.4020	0.0504
0.0044	95.3370	0.0385
0.0015	121.5689	0.0557
0.0006	120.5971	0.0615

ANNEX G. IMPEDANCE RESPONSE OF $Y_{0.9}Zr_{0.1}MnO_3$ COMPOUND AT 600°C

pO_2 (atm)	L (Ωcm^2)	R1 (Ωcm^2)	R_{CPE1} (Ωcm^2)	t	p	R_G (Ωcm^2)	t	p	R_{CPE2} (Ωcm^2)	t	p
0.8449	2.4760E-07	27.9028	1.0961	7.8575E-06	0.8208	6.5493	0.2495	0.3500	-	-	-
0.7426	2.8599E-07	27.5724	1.2066	1.1968E-05	0.7818	7.0462	0.3007	0.3500	-	-	-
0.4558	2.9218E-07	27.0245	1.2542	1.5776E-05	0.7501	7.9172	0.4261	0.3500	-	-	-
0.1963	2.8156E-07	26.1336	0.9973	5.6730E-06	0.8511	10.1046	0.8747	0.3500	-	-	-
0.0204	3.9175E-07	23.5447	1.1496	1.0280E-06	0.9428	15.1086	2.7544	0.3500	4.3541	1.3736	0.9500
0.0138	3.3749E-07	22.8945	1.3870	8.7908E-06	0.7602	16.9067	3.8588	0.3500	5.5304	1.4387	0.9500
0.0078	3.1047E-07	22.6770	0.6472	9.6703E-06	0.8926	19.2577	6.2617	0.3500	9.6797	1.2029	0.9500
0.0044	3.2955E-07	21.9595	0.6919	7.4990E-06	0.9061	22.4334	10.0750	0.3500	14.3285	1.1940	0.9500
0.0015	4.9016E-07	20.1031	1.2444	7.2620E-06	0.8160	28.2000	19.2688	0.3500	35.7964	1.0466	0.9500
0.0006	1.0472E-06	4.7837	15.9389	1.4751E-07	0.7500	34.5885	30.5338	0.3500	54.6749	1.0831	0.9500

pO_2 (atm)	Capacitance R_{CPE1} (Fcm^2)	Capacitance R_G (Fcm^2)	Capacitance R_{CPE2} (Fcm^2)
0.8449	6.1540E-07	0.0381	-
0.7426	5.3357E-07	0.0427	-
0.4558	4.2757E-07	0.0538	-
0.1963	6.8478E-07	0.0866	-

0.0204	4.4887E-07	0.1823	1.5093
0.0138	2.4774E-07	0.2282	1.6047
0.0078	2.2872E-06	0.3252	1.3689
0.0044	2.1233E-06	0.4491	1.3864
0.0015	5.2964E-07	0.6833	1.2666
0.0006	1.9622E-09	0.8828	1.3427

ANNEX H. IMPEDANCE RESPONSE OF $Y_{0.9}Zr_{0.1}MnO_3$ COMPOUND AT 700°C

pO_2 (atm)	L (Ωcm^2)	R1 (Ωcm^2)	R_G (Ωcm^2)	t	p	R_{CPE2} (Ωcm^2)	t	p
0.8449	2.6649E-07	11.8238	1.7908	0.0346	0.3500	-	-	-
0.7426	3.0300E-07	11.7042	1.9348	0.0404	0.3500	-	-	-
0.4558	3.0051E-07	11.4989	2.1906	0.0590	0.3500	-	-	-
0.1963	3.2139E-07	10.9942	2.8271	0.1243	0.3500	-	-	-
0.0204	5.4393E-07	10.0140	4.5571	0.4216	0.3500	1.0769	1.1968	0.9496
0.0138	9.0631E-09	9.8381	5.3645	0.6242	0.3502	1.0715	1.7526	0.9498
0.0078	2.6645E-07	9.6855	6.0000	0.7178	0.3500	2.2875	0.9261	0.9500
0.0044	4.5738E-09	9.4441	7.0204	0.8402	0.3500	3.9441	0.6921	0.9500
0.0015	5.9360E-15	9.1585	9.1890	0.8123	0.3500	10.7252	0.3866	0.9436
0.0006	1.1028E-07	9.1008	11.6100	0.9180	0.3500	18.1589	0.3085	0.9263

pO_2 (atm)	Capacitance R_G (Fcm^2)	Capacitance R_{CPE1} (Fcm^2)
0.8449	0.0193	-
0.7426	0.0209	-
0.4558	0.0269	-
0.1963	0.0440	-

pO_2 (atm)	Capacitance R_G (Fcm^2)	Capacitance R_{CPE1} (Fcm^2)
0.0204	0.0925	1.2131
0.0138	0.1164	1.8119
0.0078	0.1196	0.9634
0.0044	0.1197	0.7297
0.0015	0.0884	0.4210
0.0006	0.0791	0.3538

ANNEX I. IMPEDANCE RESPONSE OF $Y_{0.9}Zr_{0.1}MnO_3$ COMPOUND AT 800°C

pO_2 (atm)	L (Ωcm^2)	R1 (Ωcm^2)	R_G (Ωcm^2)	t	p	R_{CPE2} (Ωcm^2)	t	p
0.8449	1.3110E-07	6.8084	0.5874	0.0042	0.3500	-	-	-
0.7426	1.2437E-07	6.6726	0.5916	0.0048	0.3500	-	-	-
0.4558	1.1256E-07	6.5996	0.6767	0.0072	0.3500	-	-	-
0.1963	1.1674E-07	6.4685	0.8806	0.0131	0.3500	-	-	-
0.0204	2.1122E-07	5.1086	1.6005	0.0308	0.3500	0.5521	0.5279	0.9487
0.0138	6.5208E-08	5.1078	1.7604	0.0278	0.3516	1.0031	0.3379	0.8411
0.0078	6.9883E-08	5.0283	2.0195	0.0239	0.3701	1.8565	0.2258	0.7915
0.0044	2.1639E-07	4.9389	2.5885	0.0289	0.3508	3.2550	0.1787	0.7750
0.0015	2.3648E-08	5.0587	3.5148	0.0231	0.4183	8.7964	0.1085	0.7500
0.0006	2.9733E-07	4.9621	6.5640	0.0699	0.3500	13.5731	0.1275	0.8768

pO_2 (atm)	Capacitance R_G (Fcm^2)	Capacitance R_{CPE1} (Fcm^2)
0.8449	0.0071	-
0.7426	0.0081	-
0.4558	0.0106	-
0.1963	0.0149	-

pO_2 (atm)	Capacitance R_G (Fcm^2)	Capacitance R_{CPE1} (Fcm^2)
0.0204	0.0193	0.4939
0.0138	0.0158	0.2754
0.0078	0.0119	0.1796
0.0044	0.0112	0.1527
0.0015	0.0066	0.1068
0.0006	0.0107	0.1377

ANNEX J. IMPEDANCE RESPONSE OF $YMn_{0.6}Ti_{0.3}O_3$ COMPOUND AT 600°C

pO_2 (atm)	L (Ωcm^2)	R_{CPE2} (Ωcm^2)	t	p	R_{G1} (Ωcm^2)	t	p
0.8449	1.0969E-08	13.9381	0.0033	0.7508	23.6519	0.2243	0.2505
0.7426	1.1281E-11	17.1590	0.0029	0.7500	21.9549	0.2795	0.2500
0.4558	3.6193E-10	19.6370	0.0030	0.7500	25.3062	0.3612	0.2500
0.1963	2.7632E-10	21.6288	0.0033	0.7509	32.7712	0.4606	0.2609
0.0204	1.3362E-13	25.4248	0.0053	0.7500	67.1903	1.4490	0.2500
0.0138	5.0639E-11	28.0359	0.0058	0.7500	74.8264	2.5250	0.2500
0.0078	1.3283E-13	28.8813	0.0067	0.7500	91.3716	3.2497	0.2500
0.0044	8.3430E-14	32.3002	0.0071	0.7500	1056997	5.2366	0.2500
0.0015	4.6353E-15	38.8165	0.0091	0.7500	154.2136	14.6752	0.2500

pO_2 (atm)	Capacitance R_{CPE1} (Fcm^2)	Capacitance R_{G2} (Fcm^2)
0.8449	1.0896E-04	9.4843E-03
0.7426	9.2976E-05	1.2732E-02
0.4558	9.3428E-05	1.4274E-02

pO_2 (atm)	Capacitance R_{CPE1} (Fcm^2)	Capacitance R_{G2} (Fcm^2)
0.1963	1.1150E-04	1.4055E-02
0.0204	2.0693E-04	2.1565E-02
0.0138	3.0686E-04	3.3745E-02
0.0078	3.2431E-04	3.5566E-02
0.0044	3.4513E-04	4.9543E-02
0.0015	4.3977E-04	9.5161E-02

ANNEX K. IMPEDANCE RESPONSE OF $YMn_{0.6}Ti_{0.3}O_3$ COMPOUND AT 700°C

pO_2 (atm)	L (Ωcm^2)	R1 (Ωcm^2)	R_{CPE1} (Ωcm^2)	t	p	R_{G1} (Ωcm^2)	t	p	R_{CPE2} (Ωcm^2)	t	p
0.8449	1.0343E-08	86.7547	9.0079	1.4980E-05	0,7500	22.8299	0.0144	0.2691	-	-	-
0.7426	1.9326E-09	87.5570	8.2201	1.3899E-05	0,7686	25.9353	0.0129	0.2502	-	-	-
0.4558	1.1222E-07	82.0833	7.7669	1.7278E-05	0,7505	25.0154	0.0200	0.2766	-	-	-
0.1963	7.8800E-13	80.2340	5.7378	1.0617E-05	0,8200	31.4026	0.0323	0.2604	-	-	-
0.0204	2.0662E-07	78.8080	5.0409	1.0887E-05	0,8358	44.5387	0.0648	0.2755	9.8169	0.0250	0.9110
0.0138	2.5391E-07	81.9376	5.3108	1.8253E-05	0,7871	35.9979	0.0380	0.2501	20.4531	0.0077	0.8093
0.0078	1.1815E-07	80.2731	3.4919	6.5083E-06	0,9114	50.3382	0.0779	0.2560	15.9817	0.0185	0.8687
0.0044	2.8293E-07	79.1916	3.3862	4.3194E-06	0,9499	47.0596	0.0667	0.2501	32.2099	0.0107	0.7784
0.0015	2.1203E-07	81.7998	2.5210	5.5647E-06	0,9486	78.5849	0.3184	0.2500	37.5112	0.0397	0.7845
0.0006	1.5441E-07	77.0061	1.7770	8.6251E-06	0,9471	94.6047	0.6822	0.2500	48.1041	0.0723	0.7812

pO_2 (atm)	Capacitance R_{CPE1} (Fcm^2)	Capacitance R_{G2} (Fcm^2)	Capacitance R_{CPE2} (Fcm^2)
0.8449	7.6841E-07	6.2902E-04	-

pO_2 (atm)	Capacitance R_{CPE1} (Fcm^2)	Capacitance R_{G2} (Fcm^2)	Capacitance R_{CPE2} (Fcm^2)
0.7426	9.0454E-07	4.9928E-04	-
0.4558	8.9130E-07	8.0100E-04	-
0.1963	1.2601E-06	1.0299E-03	-
0.0204	1.5846E-06	1.4551E-03	0.0218
0.0138	1.4990E-06	1,0563E-03	0.0050
0.0078	2.3004E-06	1.5471E-03	0.0153
0.0044	2.4009E-06	1.4172E-03	0.0079
0.0015	3.0368E-06	4.0513E-03	0.0444
0.0006	4.6457E-06	7.2115E-03	0.1024

ANNEX L. IMPEDANCE RESPONSE OF $YMn_{0.6}Ti_{0.3}O_3$ COMPOUND AT 800°C

pO_2 (atm)	L (Ωcm^2)	R1 (Ωcm^2)	R_{CPE1} (Ωcm^2)	t	p	R_{G1} (Ωcm^2)	t	p	R_{CPE2} (Ωcm^2)	t	p
0.8449	3.8038E-07	39.2258	1.3056	3.6801E-05	0.8163	4.9900	0.0016	0.3509			
0.7426	4.6015E-07	38.7881	1.3337	1.5185E-05	0.8824	5.4785	0.0020	0.3522			
0.4558	7.5555E-07	38.3181	1.7021	2.5496E-05	0.7982	6.2161	0.0025	0.3501			
0.1963	6.6731E-07	36.2914	1.8224	2.4954E-05	0.7971	5.2007	0.0014	0.3693	2.8164	0.0028	0.9017
0.0204	6.8626E-07	33.7895	0.7000	2.9597E-05	0.8388	13.2910	0.0180	0.2611	3.1009	0.0414	0.7699
0.0138	6.1220E-07	33.1414	0.7000	1.0657E-06	0.9467	15.3091	0.0265	0.2511	3.3965	0.0611	0.7503
0.0078	9.4290E-07	32.7413	0.7000	4.5260E-06	0.9435	16.7562	0.0369	0.2559	3.8660	0.0871	0.7505
0.0044	9.8437E-07	32.1896	0.7000	2.9490E-06	0.9500	19.3799	0.0611	0.2500	4.7675	0.1471	0.7500
0.0015	6.4727E-07	30.5519	0.7000	1.3017E-06	0.8812	24.6746	0.1567	0.2500	11.4676	0.2178	0.7905
0.0006	6.2300E-07	29.7250	0.7000	1.0550E-09	0.7660	29.9075	0.3274	0.2500	19.3260	0.3092	0.8907

pO_2 (atm)	Capacitance R_{CPE1} (Fcm^2)	Capacitance R_{G2} (Fcm^2)	Capacitance R_{CPE2} (Fcm^2)
0.8449	3.92664E-06	3.2596E-04	

pO_2 (atm)	Capacitance R_{CPE1} (Fcm^2)	Capacitance R_{G2} (Fcm^2)	Capacitance R_{CPE2} (Fcm^2)
0.7426	3.59448E-06	3.5747E-04	
0.4558	2.01108E-06	3.9741E-04	
0.1963	1.95698E-06	2.7625E-04	0.0017
0.0204	3.7239E-06	1.3526E-03	0.0224
0.0138	4.81308E-07	1.7308E-03	0.0362
0.0078	2.1194E-06	2.2018E-03	0.0606
0.0044	1.48057E-06	3.1510E-03	0.1306
0.0015	1.99722E-07	6.3499E-03	0.2775
0.0006	1.71048E-12	1.0947E-02	0.3850

ANNEX M. IMPEDANCE RESPONSE OF $YMn_{0.6}Ti_{0.3}O_3$ COMPOUND AT DIFFERENT TEMPERATURES AND DRY 10%H_2/Ar

Temperature (°C)	L (Ωcm^2)	R1 (Ωcm^2)	R_{G1} (Ωcm^2)	t	p	R_{CPE1} (Ωcm^2)	t	p	R_{CPE2} (Ωcm^2)	t	p
500	4.62E-22	1347.1394	554.0201	0.0036	0.3500	3464.6976	0.0035	0.8341	5625.9372	1.7495E-04	0.5000
600	1.02E-22	390.0811	317.0906	0.0001	0.3500	1062.1559	0.0019	0.6742	1376.9317	2.0377E-04	05000
650	4.86E-22	244.5213	207.3736	0.0001	0.3500	685.5388	0.0024	0,6190	786.8999	2.2637E-04	0.5001
700	2.09E-21	156.9377	109.9015	0,0001	0.3500	256.9462	0.0038	0.6712	461.1888	2.9573E-04	0.5000
750	2.24E-21	132.1390	89.8153	0,0000	0.3500	313.0859	0.0025	0.5766	315.7492	2.7993E-04	0.5003

Temperature (°C)	Capacitance R_{G2} (Fcm^2)	Capacitance R_{CPE2} (Fcm^2)	Capacitance R_{CPE2} (Fcm^2)
500	6.4712E-06	0.0057	8.7477E-05
600	4.4899E-07	0.0025	0.0001

650	4.6094E-07	0.0032	0.0001
700	5.1374E-07	0.0037	0.0001
750	5.3507E-07	0.0020	0.0001